A biochemical and biophysical study on cell division proteins from *Staphylococcus aureus* and biofilm proteins from *Bacillus subtilis*.

Simon Booth

Supervisor: Prof. R.J. Lewis

This thesis presented for the degree of
Doctor of Philosophy

Biosciences Institute
Newcastle University

July 2021

Abstract

Part I

Cell division in bacteria is tightly regulated by a multiprotein complex called the divisome. Proteins in the divisome couple cell division and growth, ensuring that a single copy of the chromosome is present in each resulting daughter cell, and preventing more than one instance of division from occurring at any one time. This thesis concerns a combination of biophysical and biochemical techniques used to study the cell division proteins DivIVA, Stk1 and GpsB from *Staphylococcus aureus*. A model of the solution molecular envelope of DivIVA is derived by small-angle X-ray scattering and compared to a previously proposed model of the protein from *Bacillus subtilis*. The molecular mechanisms of DivIVA oligomerization are probed through use of size-exclusion chromatography coupled multi-angle light scattering on various truncations of the protein. The structure of the N-terminal domain of *S. aureus* GpsB is solved and used to rationalise the interaction between GpsB and PBP4. Attempts are made to determine an interaction network between the cell division proteins and members of the peptidoglycan and wall-teichoic acid synthesis machinery by several biochemical and biophysical assays.

Part II

Biofilms are communities of sessile bacteria that form on a wide variety of natural and man-made surfaces, sometimes at a detriment to human health. Bacteria in biofilms are held together by a viscous extracellular matrix consisting of polysaccharides, lipids, proteins, and extracellular DNA (eDNA). Species of Bacillus are known to secrete two structurally similar endonucleases, Nuclease A and B (NucA & NucB), into their environment as a means of taking up eDNA either to enhance their genetic diversity, or for metabolic purposes, respectively. As a mechanism of protection from self-induced genome degradation, NucA is co-expressed with a proposed inhibitor, Nin. A combination of biophysical/chemical techniques are used to probe the interaction between NucA/B and Nin from *Bacillus subtilis*. *In vitro* studies show that NucA and NucB bind to Nin and that Nin inhibits their endonuclease activity. The affinity of the interactions between NucA or NucB and Nin are probed and found to be sub-nanomolar. The structures of NucA/NucB in complex with Nin are solved by X-ray crystallography, revealing the mechanism of inhibition by Nin, and allowing for the calculated dismantling of the complexes by site-directed mutagenesis.

Acknowledgements

Thanks firstly to Rick for letting me convince you I was worth taking on as a PhD student. It immediately became obvious in my first interactions with you that I'd stumbled across a down to earth, straight-talking, reasonable mentor; I'm glad to say I wasn't wrong in my predictions of you. Thanks for being so patient with me not only in the lab, but over my drawn-out writing over this last year and a half. The beer snobbery chats aren't over, I'm sure.

Thanks to all the past members of the Lewis lab: Arnaud, Vince, Rob, Lorraine, Sema, and Zoe for the constant support either in work or play, sometimes both.

Thanks to Tim for taking over as my official supervisor after Rick's departure from the university. Your understanding over the last year has been a major factor in getting this document over the line.

Thanks to the members of the SWON alliance, particularly Kasia and Victoria from the Foster group, for the fun and productive collaborations with DivIVA/GpsB/PBPs.

Thanks to Heath and Hannah for their collaborations on the Nuc/Nin project, making 10–15 point mutants I'm sure wasn't the most fun exercise in the world but thankfully it lead to something!

Thanks to Jamie and Henrik for guiding me through my small foray into the world of hardcore microbiology and microscopy, I hope I wasn't too much of a burden. Thanks, Henrik, for all your in-depth discussions about DivIVA.

Thanks to Claire in NICR and Simon in Sheffield for the mass spec data, and for being so patient with my lack of understanding of mass spec.

Thanks to all the Tuesday night-misbehavers and shenanigan-enablers: Orla, Alan, Amy, Tim, Nico, Dan. I miss you all dearly, but I can't say my liver does.

Thanks to my loving and supportive family, my mother, my father, and my sister Alex for your constant support and provision of respite throughout not only this chapter of my life, but all that preceded it.

In lieu of having an "*in spite of...*" section to this pre-amble, thanks to Rich for ensuring I was often reminded about life outside of this PhD, perhaps at a detriment to its progress at times.

Thanks to Christie for pushing me through the last few stages of this process and putting your own life aside sporadically in support of getting this over the line. I love you, darling.

”I should not like to leave an impression that all structural problems can be settled by X-ray analysis, or that all crystal structures are easy to solve. I seem to have spent much more of my life not solving structures than solving them.”

Dorothy Hodgkin, 1964

Table of contents

List of figures

Chapter 1.

Chapter 2.

Chapter 3.

Chapter 4.

Chapter 5.

Chapter 6.

List of tables

Abbreviations

Å	Ångstrom
A_{280}	Absorbance at 280 nm
ABC	ATP-binding cassette
AHL	Acyl-homoserine lactones
AIP	Auto-inducing peptides
ATP	Adenosine triphosphate
BCA	bicinchoninic acid
Bp	Base pairs
Bs	*Bacillus subtilis*
BSA	Bovine serum albumin
Bl	*Bacillus licheniformis*
C_{55}	undecaprenyl
CD	Circular dichroism
CDP	cytidine-5'-diphosphate
cm	Centimetre
Da	Dalton
D_{max}	Maximum particle dimension
DNA	Deoxyribonucleic acid
eDNA	Extracellular DNA
gDNA	Genomic DNA
dNTP	Deoxynucleotide
dH_20	Distilled water
DTT	Dithiothreitol
ε	Extinction coefficient
ECM	Extracellular matrix
EDTA	Ethylenediaminetetraacetic acid
EM	Electron microscopy
EPS	Exopolymeric substance
IEX	Ion-exchange chromatography
FP	Fluorescence polarisation
FT	Flow-through
eSTK	Eukaryotic-like Ser/Thr protein kinase

GFP	Green fluorescence protein
Glc2-DAG	gentiobiosyl-diacylglycerol
Glc*N*Ac	*N*-acetylglucosamine
Gro-P	*1*,3-*L*-α-glycerol-phosphate
HEPES	(4-(2-hydroxyethyl)-1-piperazineethanesulfonic acid
His_6	Hexahistidine
His-Me	Histidine-metal
IM	Inner membrane
IMAC	Immobilised metal-ion affinity chromatography
IPTG	Isopropyl β-*D*-1-thiogalactopyranoside
ITC	Isothermal titration calorimetry
Kb	Kilobase
KCl	Potassium chloride
K_D	Dissociation constant
kDa	Kilodalton
LB	Lysogeny broth
LCP	LytR-CpsA-Psr
LPS	Lipopolysaccharide
LTA	Lipoteichoic acid
Man*N*Ac	*N*-acetylmannosamine
MBP	Maltose-binding protein
meso-A_2pm	*meso*-diaminopimelic acid
MPD	2-Methyl-2,4-pentanediol
MR	Molecular replacement
mEGFP	Monomeric enhanced GFP
msfGFP	Monomeric superfolder GFP
MST	Microscale thermophoresis
Mur*N*Ac	*N*-acetylmuramic acid
M_W	Molecular weight
M_W^{app}	Apparent molecular weight
NA	Nutrient agar
NaCl	Sodium chloride
NaOH	Sodium hydroxide

NBS	Noc-binding sequences
NDM	New-Delhi metallo-β-lactamases
$NiCl_2$	Nickel chloride
NSD	Normalised spatial discrepancy
NTA	Nitrilotriacetic acid
OD_{600}	Optical density at 600 nm
OM	Outer membrane
OMP	Outer membrane protein
oriC	Origin of replication
PAGE	Polyacrylamide gel electrophoresis
PASTA	Penicillin-binding protein and serine/threonine kinase associated domain
PBP	Penicillin binding protein
PCR	Polymerase chain reaction
PDB	Protein data bank
PDB code/ID	Protein data bank accession number
PEG	Polyethylene glycol
PEP	Phosphoenolpyruvate
Pfu	*Pyrococcus furiosus*
PG	Peptidoglycan
P(r)	Distance distribution
Rbo-P	1,5-*D*-ribitol-phosphate
RMSD	Root mean square deviation
RNA	Ribonucleic acid
Rpm	Revolutions per minute
R_c	Cross-sectional radius of gyration
R_g	Radius of gyration
Sa	*Staphylococcus aureus*
SAXS	Small-angle X-ray scattering
SEC-SAXS	Size exclusion chromatography-coupled small angle x-ray scattering
SBS	SlmA-binding sequences
SDS	Sodium dodecyl sulphate
SDM	Site-directed mutagenesis

SEC-MALS	Size exclusion chromatography-coupled multi angle light scattering
Sp	*Streptococcus pneumoniae*
SPR	Surface plasmon resonance
TA	Teichoic acid
TB	Terrific broth
ter	Replication terminus
TEM	Transmission electron microscopy
TEV	Tobacco etch virus
Tris	Tris(hydroxymethyl)aminomethane
T_m	Melting temperature
UDP	Uridine diphosphate
UV	Ultra-violet
WTA	Wall teichoic acid
χ^2	Chi-squared

Standard three- and single- letter amino acid abbreviations are used throughout this thesis

Part I.

Biophysical and biochemical characterisation of cell division proteins from *Staphylococcus aureus*

Chapter 1.

Introduction: Cell division in bacteria

1.1 An overview of the bacterial cell envelope

Bacteria can be broadly classified into two groups, Gram-negative and Gram-positive, based on their response to the Gram stain (Bartholomew & Mittwer, 1952). Gram-negative cell envelopes consist of both an inner and an outer membrane (IM and OM, respectively), which encapsulate a relatively thin peptidoglycan (PG) layer a few nanometres (nm) thick (Nikaido, 2009). By contrast, Gram-positive bacteria have only a single membrane surrounded by a much thicker PG layer, ranging from 30 to 100 nm in thickness (Silhavy et al., 2010). It is this thick, external layer of PG in Gram-positive bacteria that allows for the retention of the Gram stain. A complication to the Gram-negative/positive nomenclature lies in certain species of bacteria classified as acid-fast, these are Gram-positive bacteria which stain weakly with the Gram stain (Bloch, 1953). Commonly studied bacteria within this classification are *Mycobacterium* species, such as *Mycobacterium tuberculosis* and *Mycobacterium bovis*, as well as some species of *Nocardia*, such as *Nocardia farcinica*. The cell walls of acid-fast bacteria are decorated with glycolipids in addition to peptidoglycan, it is these glycolipids present in the cell wall that form the molecular basis of the resistance of these species to Gram staining (Reynolds et al., 2009). It stands to reason that the Gram nomenclature for bacterial cells has remained an important classification since its development by Hans Christian Gram in 1884, as it provides important information about the gross structure of bacterial cell walls. The PG layer is a defining feature of bacteria, distinguishing them from archaea or eukaryotes. The tensile strength of PG allows bacteria to thrive in a variety of environments, indeed, targeting the proteins responsible for PG renewal in bacteria has been central to mankind's fight against infectious diseases (Lobanovska & Pilla, 2017). Whilst some chemical moieties in PG differ between species of bacteria, the general structure of PG comprises repeating disaccharides of *N*-acetylglucosamine (Glc*N*Ac) and *N*-acetylmuramic acid (Mur*N*Ac), cross-linked between Mur*N*Acs via short (four or five residue) peptide stems, to form a lattice-like arrangement (Vollmer et al., 2008a). The fifth, terminal *D*-alanine is normally lost during PG maturation. Some variations on this basic theme include additional short (one to five residue) peptide linkers between the peptide stems, which normally (but not exclusively) are cross-linked between the amino group from the sidechain of residue 3 and the carboxyl group of *D*-alanine at position 4 (a three to four cross-link). The direct cross-links typically also involve residues 3 and 4 (Figure 1.1).

Differences in the structure and regulation of PG and its synthesis are responsible for variations in cell integrity and morphology (Vollmer et al., 2008a; Turner et al., 2014), highlighting the importance of the PG layer to bacteria. The synthesis of PG is a complex multienzyme process initiated in the cytoplasm and subsequently linked to the inner (and outer) leaflet of the cell membrane. PG synthesis has been studied relatively extensively, particularly in the rod-shaped model organisms *Escherichia coli* and *Bacillus subtilis*, which are representatives of the Gram-negative and Gram-positive groups, respectively. Consequently, the anabolism of PG is fairly well understood (Lovering et al., 2012). The

coupling of PG hydrolysis and re-synthesis during cell division is essential for the cell to avoid an untimely death, however, the study of this synergy is a field that remains in its infancy.

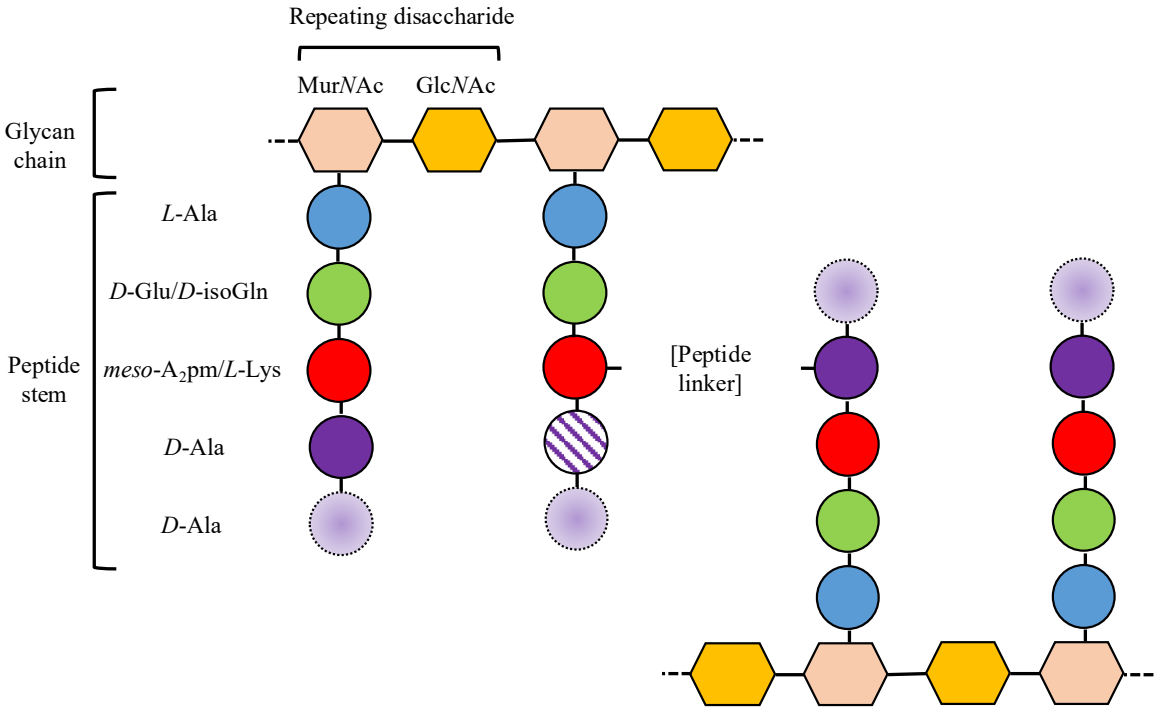

Figure 1.1: The general structure of peptidoglycan (PG). The general structure of the PG matrix is shown as a cartoon in which sugar moieties are represented as hexagons and the amino acids that comprise the peptide stems are shown as circles, each moiety is coloured independently. The cartoon represents the majority of Gram-negative/Gram-positive peptide stems, respectively. Variability in the presence of the *D*-Ala residues in mature PG at positions 4 (which is sometimes lost) and 5 (which is always lost) of the peptide stem is represented by a cross-hatched fill and a dashed outline with a gradient fill, respectively. The most common peptide linker in PG is formed between positions 3 and 4 of the peptide stem (as shown here). The chemical structure of the peptide cross-link varies, and may be composed of a direct link between residues in the peptide stem, or may be comprised of a peptide link, such as the penta-glycine linker present typically in *S. aureus*.

1.2 An overview of bacterial cell division

In the majority of cases, bacteria undertake a process of binary fission through which two identical daughter cells are produced from a parental cell, which involves the establishment of a site of division, elongation (in some cases), chromosome replication and segregation, generation and closure of a septum, and finally separation of the two cells at the septum. Cell division is thus an exceptionally complicated cycle of events requiring a multitude of spatial and temporal backstops for it to be undertaken successfully. While the fundamental events in this process are conserved across the entire bacterial kingdom, species-specific nuances are observed, often related to the structure of the cell envelope, variations in morphology, or the identity and nature of some of the regulators. Defining mid-cell is a critical step of division and is undertaken differently depending on the bacterial species. In rod-

shaped bacteria, such as *B. subtilis* and *E. coli*, the mid-cell is defined at the mid-point of the longest edge of the cell, where the septum forms in a ring across the shortest width of the cell (Figure 1.2).

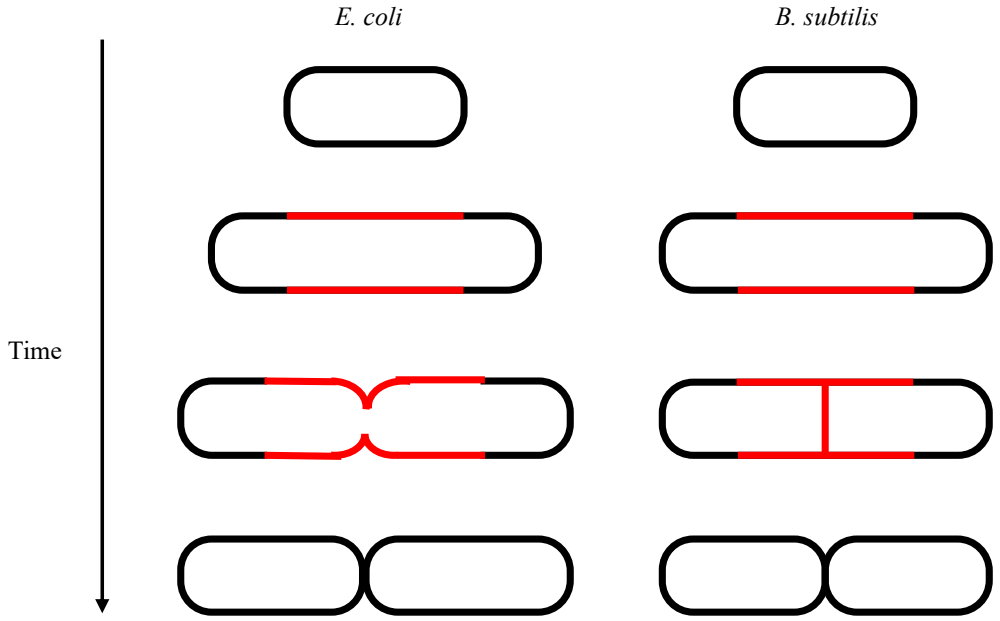

Figure 1.2: Examples of bacterial cell division in rod-shaped bacteria. Models of the rod-shaped model bacteria *E. coli* and *B. subtilis* are shown in black, with sites of new PG synthesis shown in red. *E. coli* and *B. subtilis* both divide by establishing septa at midcell, however, *E. coli* divides and generates new septal PG at the same time, whereas *B. subtilis* forms a complete septa prior to division. These modes of division are typical of their respective designation as Gram-negative or Gram-positive bacteria.

In spherical bacteria (cocci), such as the staphylococci, mid-cell is defined at the point at which there is the longest diameter of cross section of the spherical cell, and the septum forms around the circumference of the cell in a ring (Egan & Vollmer, 2013; Lutkenhaus, 1998; Turner et al., 2010) (Figure 1.2), and subsequent division planes are placed orthogonally to the previous because the PG "pie-crust" rings are important topological markers of past sites of division in *Staphylococcus aureus* (Turner et al., 2010). In ovococci, like the Gram-positive *Streptococcus pneumoniae* and Gram-negative *Neisseria gonorrhoeae*, both cell length and diameter considerations are important for determining mid-cell (Garcia et al., 2016) (Figure 1.3).

The location of septum formation is a good example of the level of control involved throughout; in many rod-shaped bacteria (such as *E. coli*) its position rarely varies in location beyond a few percent, resulting in progeny that rarely vary in volume outside of this margin (~4%) (Männik et al., 2012). Placement of the septum is aided by the Min and nucleoid occlusion systems, which both act as inhibitors of the septal ring progenitor protein, FtsZ (Rowlett & Margolin, 2013; Adams et al., 2014; Rowlett & Margolin, 2015; Wu & Errington, 2012). Some bacteria that lack the Min system, such as *Mycobacterium tuberculosis*, seem to utilize a different, albeit less-efficient system for determining

mid-cell as cell division of this species results in daughter cells of different sizes (Rowlett & Margolin, 2013). Septum formation and constriction of the cell into two daughter cells are common themes between both Gram-negative and Gram-positive bacteria, however, Gram-positive bacteria form a complete septum across the mid-cell before division occurs, whereas a Gram-negative bacterium divides while developing its septum simultaneously (Egan & Vollmer, 2013) (Figures 1.2 & 1.3). Whether cell elongation occurs during/prior to this process is also species specific and is not necessarily predictable by morphology and/or cell wall composition alone.

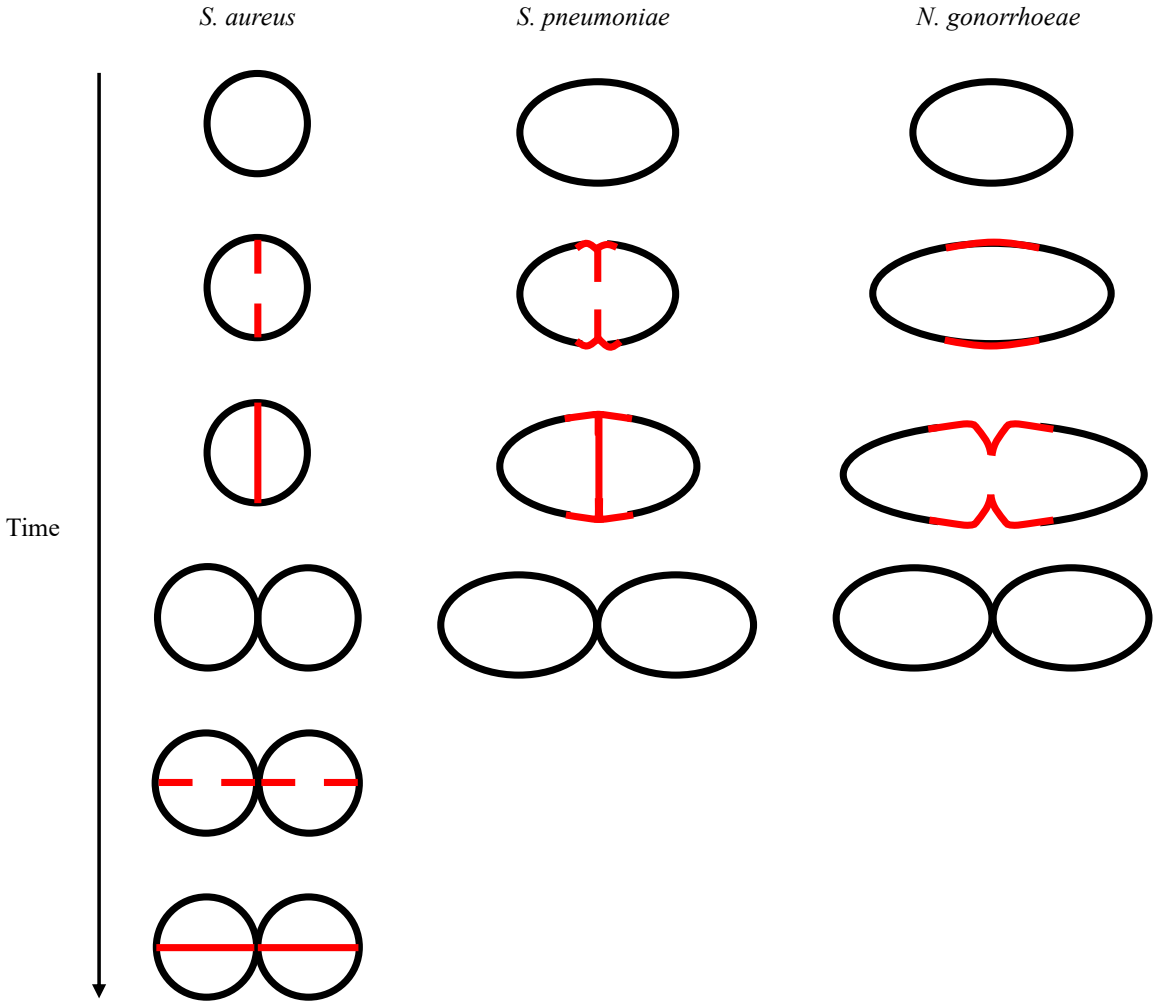

Figure 1.3: Examples of bacterial cell division in coccoid bacteria. The Gram-positive *S. aureus* and *S. pneumoniae*, and the Gram-negative *N. gonorrhoeae* are shown in black, sites of new PG synthesis shown in red. *S. aureus* and *S. pneumoniae* divide similarly to *B. subtilis* in that they both form complete septa prior to division, typical of Gram-positive bacteria. Typical of Gram-negative bacteria, *N. gonorrhoeae* forms its septum and divides simultaneously. In the case of *S. aureus*, successive divisions occur over orthogonal planes, an example of this is shown.

1.3 The Gram-negative cell envelope

The OM of Gram-negative bacteria is an asymmetrical bilayer (Figure 1.4) consisting of phospholipids and lipopolysaccharides (LPS), which assemble into the inner and outer leaflets of the membrane, respectively (Nikaido, 2009; Silhavy et al., 2010).

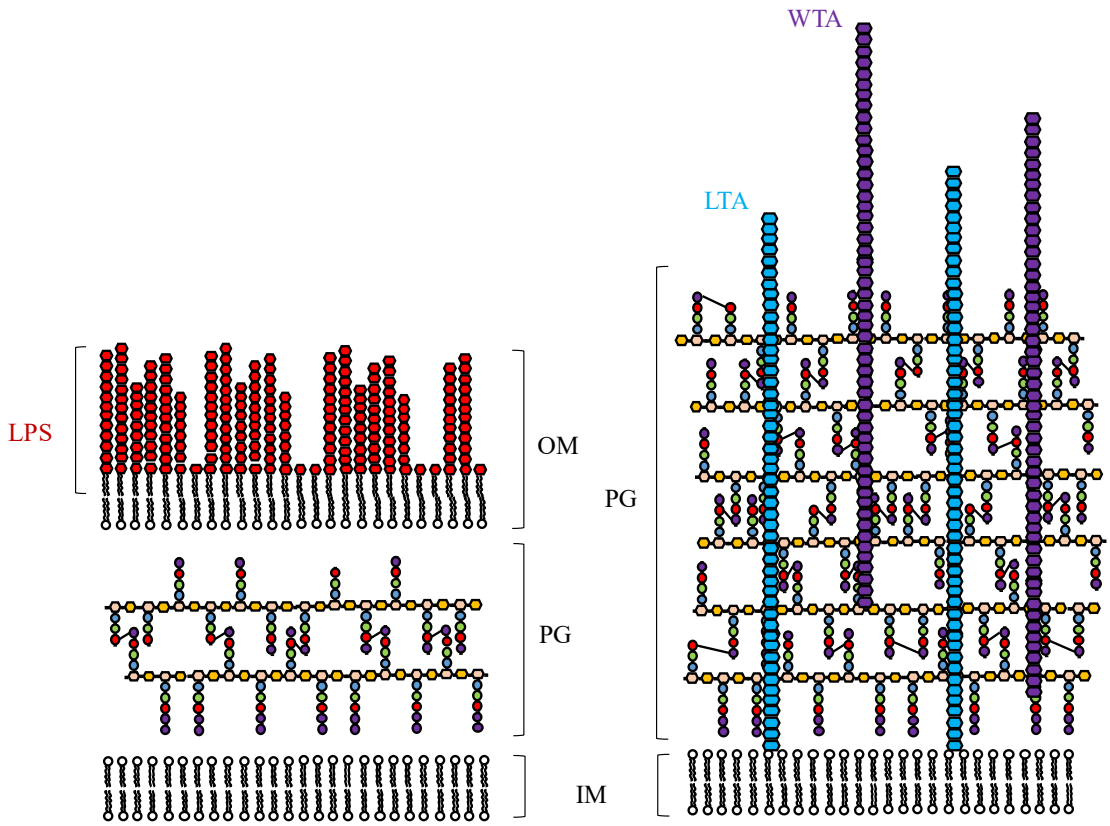

Figure 1.4: Comparison of the cell envelopes of Gram-negative (left) and Gram-positive (right) bacteria. The cell envelope of Gram-negative bacteria comprises an inner (IM) and outer membrane (OM) decorated with lipopolysaccharide (LPS), sandwiching a relatively thin layer of peptidoglycan (PG). By contrast, the cell envelope of Gram-positive bacteria is composed of a single cell membrane surrounded by a much thicker PG layer complemented with lipoteichoic acid (LTA) and wall teichoic acid (WTA). Cross-links between peptide stems are shown as three to four cross-links for the sake of simplicity. Not shown are the multitude of proteins that sit in the inner and OM of Gram-negative bacteria, nor those that reside in the membrane or the PG of Gram-positive bacteria. The components of PG are displayed using the same scheme as in Figure 1, with the nascent PG chain containing *D*-Ala at positions 4 and 5. The mature PG is represented without the *D*-Ala at position 5 and occasionally also without the *D*-Ala at position 4 to represent the natural variability of the peptide stem in the mature PG mesh.

Broadly speaking, the OM serves as a protective layer for Gram-negative bacteria, functioning as a semi-permeable barrier to the periplasm (Ruiz et al., 2006), and as an added layer of protection from environmental turgor (Silhavy et al., 2010). The OM accommodates a variety of outer membrane proteins (OMPs), which consist of porins, proteases, lipases, transporters and various receptors embedded into the OM (Rollauer et al., 2015). Unsurprisingly given their nomenclature, porins and

transporters are responsible for the diffusion/transport of small molecules into the periplasm, respectively (Achouak, 2001), and are responsible for the semi-permeable nature of the OM. Several members of the porin family of OMPs have been amenable to structural study by crystallography (Cowan et al., 1995; Weiss & Schulz, 1992; Glenwright et al., 2017) and the resulting structural models have had essential roles in the elucidation of molecular mechanisms of transport, highlighting the complexity of the OM. Just as with the other components of the envelope, the OM also requires remodelling during cell division. A more complete picture of the OM and its constituents is key to understanding how OM remodelling is regulated on a molecular level (Egan, 2018; Gray et al., 2015), however, this is outside of the scope of this thesis to address.

1.4 The Gram-positive cell envelope

1.4.1 Teichoic acids

As mentioned above, Gram-positive bacteria compensate for the lack of the protective/stabilising presence of the OM with a thicker layer of PG (Silhavy et al., 2010; Fischer & Tomasz, 2014). As well as the obvious difference in thickness, the PG layer of Gram-positive bacteria is distinguished from Gram-negative bacteria by its decoration with anionic glycopolymers called teichoic acids (TAs) (Brown et al., 2013; Percy & Gründling, 2014). TAs constitute 30-60% of the Gram-positive cell wall and are known to be important for cell integrity. TAs may act as a functional substitute for the OMPs present in Gram-negative bacteria as they are also capable of affecting permeability and integrity, and are responsible for host-pathogen interactions (Wanner et al., 2017). It follows that TAs are a virulence factor for Gram-positive pathogens and for this reason are of interest for study, as their synthesis pathways are also a potential target for future antibiotics (Swoboda et al., 2010; Farha et al., 2013). Mutations to TA biosynthesis pathways result in growth defects and aberrations in cell morphology in Gram-positive bacteria. There are two types of TA; wall teichoic acids (WTAs), which are covalently attached to the PG, and lipoteichoic acids (LTAs), which are attached to the cytoplasmic membrane and extend deep into the wall (Figure 1.4) (Formstone et al., 2008; Rausch et al., 2019). The TA chemical structure, as with PG, also varies from species to species and between strains of the same species.

WTAs are attached to PG through a phosphodiester bond between a well-conserved β-1→4 linked *N*-acetylmannosamine/*N*-acetylglucosamine (Man*N*Ac/Glc*N*Ac) disaccharide linkage unit and the Mur*N*Ac residues of the glycan chain of PG (Swoboda et al., 2010). Attached to the Man*N*Ac residues of the disaccharide linkage unit are either one or two 1,3-*L*-α-glycerol-phosphate (Gro-P) units, which themselves are attached to long chains of glycerol- or ribitol-phosphate repeats. In the majority of WTAs studied, the repeating chain consists of either Gro-P or 1,5-*D*-ribitol-phosphate (Rbo-P) repeats (Swoboda et al., 2010; Brown et al., 2013). The repeating chains attached to the Gro-P moiety of TAs are their main source of diversity and can differ even between different strains of the same species, for instance, *Bacillus subtilis* strain 168 has glycerol TA, while strain W23 has ribitol TA (Brown et al.,

2010). The polyGro-P/Rbo-P chains of WTAs are embellished with saccharides and *D*-alanine esters, the latter of which is a mechanism through which Gram-positive bacteria regulate surface charge (Malanovic & Lohner, 2016) (Figure 1.5). The diversity found in the polyGro-P/Rbo-P region of WTAs is thought to be a result of adaptations of Gram-positive bacteria to their specific environmental niches (Brown et al., 2013).

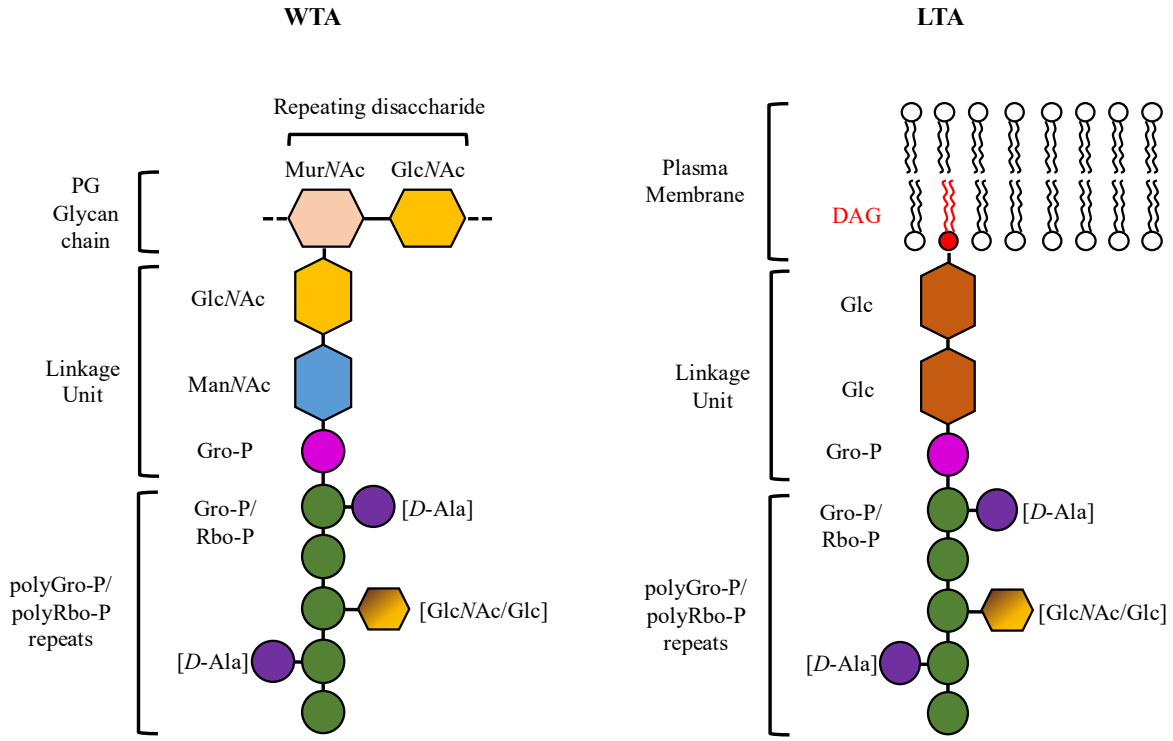

Figure 1.5: The general structure of the wall teichoic acid (WTA) and lipoteichoic acid (LTA). An example of the typical makeup of WTA is shown as a cartoon in which sugar moieties are displayed as hexagons and any non-sugar constituents as circles. The LTA structure shown here represents type I LTAs, the most common and well-studied type of LTA to-date. The identities of the repeating units/linkage units for WTA represent those of the best-studied WTAs. Despite being chemically identical, the GroP moiety in the linkage unit is coloured differently than the repeating units in order to highlight the repeating units as a region of diversity.

In LTAs, a lipid anchors the TA to the cell membrane and the lipid anchor is an example of a species-specific variable region in the molecule. In the majority of Firmicutes, including *S. aureus, B. subtilis*, and *L. monocytogenes*, the glycolipid anchor is made up of gentiobiosyl-diacylglycerol (Glc_2-DAG), with repeating units of Gro-P attached to C_6 of the terminal non-reducing Glc of Glc_2-DAG. This polyGro-P-Glc_2-DAG structure of LTAs is designated type I LTA (Figure 1.5). The more complex, lesser-studied forms of LTA are designated types II-V, a nomenclature that is likely to expand as more forms of LTA are discovered (Siegel et al., 2016; Percy & Gründling, 2014; Schneewind & Missiakas, 2014a). The study of LTA types II-V is a relatively new avenue of research, but it is outside of the scope of this thesis to discuss the nuances of their structural diversity, however, the general structure of all LTAs is that of an alditol-phosphate polymer attached to the membrane by a glycolipid anchor. The

polyGro-P chains of type I LTAs, analogous to WTAs, are also *D*-alanylated and glycosylated (Percy & Gründling, 2014) (Figure 1.5).

1.4.2 Teichoic acid synthesis

1.4.2.1 WTAs

The enzymes responsible for the construction of WTA are designated Tar or Tag enzymes dependent on the identity of the repeating polymer present in the specific species of bacteria from which the enzyme is located. For example, in *S. aureus,* the repeating polymer in WTA is Rbo-P, therefore, the enzymes involved in WTA synthesis are designated Tar, for teichoic acid ribitol. In *B. subtilis*, where the WTA is rich in Gro-P repeats, the WTA synthesis enzymes are designated Tag, for teichoic acid glycerol (Swoboda et al., 2010). Despite the difference in nomenclature between the two groups, the initial reactions of WTA synthesis are chemically identical. The first devoted step of WTA synthesis involves the transfer of Glc*N*Ac from UDP-Glc*N*Ac onto to an undecaprenyl (C_{55}) phosphate lipid carrier in the inner leaflet of the plasma membrane. This is catalysed by Tar/TagO, which catalyses the transfer of Glc*N*Ac from UDP-Glc*N*Ac onto the C_{55}, forming Glc*N*Ac-pyrophosphate-C_{55} (Karamata et al., 2002). Following attachment of Glc*N*Ac onto the lipid moiety, Tar/TagA catalyses the attachment of Man*N*Ac from UDP-Man*N*Ac onto C_4 of the Glc*N*Ac, forming the β-1→4 linked disaccharide (D'Elia et al., 2009). Tar/TagB catalyses the addition of the Gro-P linkage unit onto C_4 of the Man*N*Ac residue of the growing chain from cytidine-5'-diphosphate (CDP)-glycerol (Bhavsar et al., 2005). In those bacteria with polyGro-P polymer chains, such as the legacy *B. subtilis* strain 168, the next enzyme in the WTA synthesis pathway is TagF, which catalyses the sequential transfer of ~35 Gro-P units to the growing polymer chain (Schertzer & Brown, 2003; Sewell et al., 2009) (Figure 1.6a).

The CDP-glycerol utilised by Tar/TagB and Tar/TagF is generated by Tar/TagD, a cytidylyltransferase which activates Gro-P by the addition of CDP to Gro-P. Comparative enzymology studies on TarD and TagD from *S. aureus* and TagD from *B. subtilis* revealed differences in the enzyme activities and in the mechanisms of action between the two enzymes, however, TarD was able to complement a TagD mutation in *B. subtilis* (Badurina et al., 2003). TarF plays a divergent role in WTA synthesis in bacteria with polyRbo-P polymers, such as *S. aureus*, in these bacteria it is responsible for the addition of a single Gro-P unit to the Gro-P-Man*N*Ac-Glc*N*Ac-pyrophosphate-C_{55} moiety generated by TarB. The polymerisation of Rbo-P units into polyRbo-P is instead catalysed by the enzyme TarL in *S. aureus* (Brown et al., 2010) (Figure 1.6b). CDP-Rbo-P is generated by a pair of enzymes, TarJ and TarI, which catalyse the production of Rbo-P from ribulose-5-phosphate, and its subsequent activation into CDP-Rbo-P, respectively (Baur et al., 2009). Following their production, the polyGro-P/Rbo-P chains are decorated with either glucose or Glc*N*Ac sugars depending on the species or strain of bacteria in question (Swoboda et al., 2010). Study of TA glycosylation and its significance is still ongoing. In *S. aureus*, TarM catalyses the addition of Glc*N*Ac to the polyRbo-P chain (Xia et al., 2010) whereas TarQ

is responsible for the attachment of α-glucose to the polyGro-P chain in *B. subtilis* 168 (Swoboda et al., 2010).

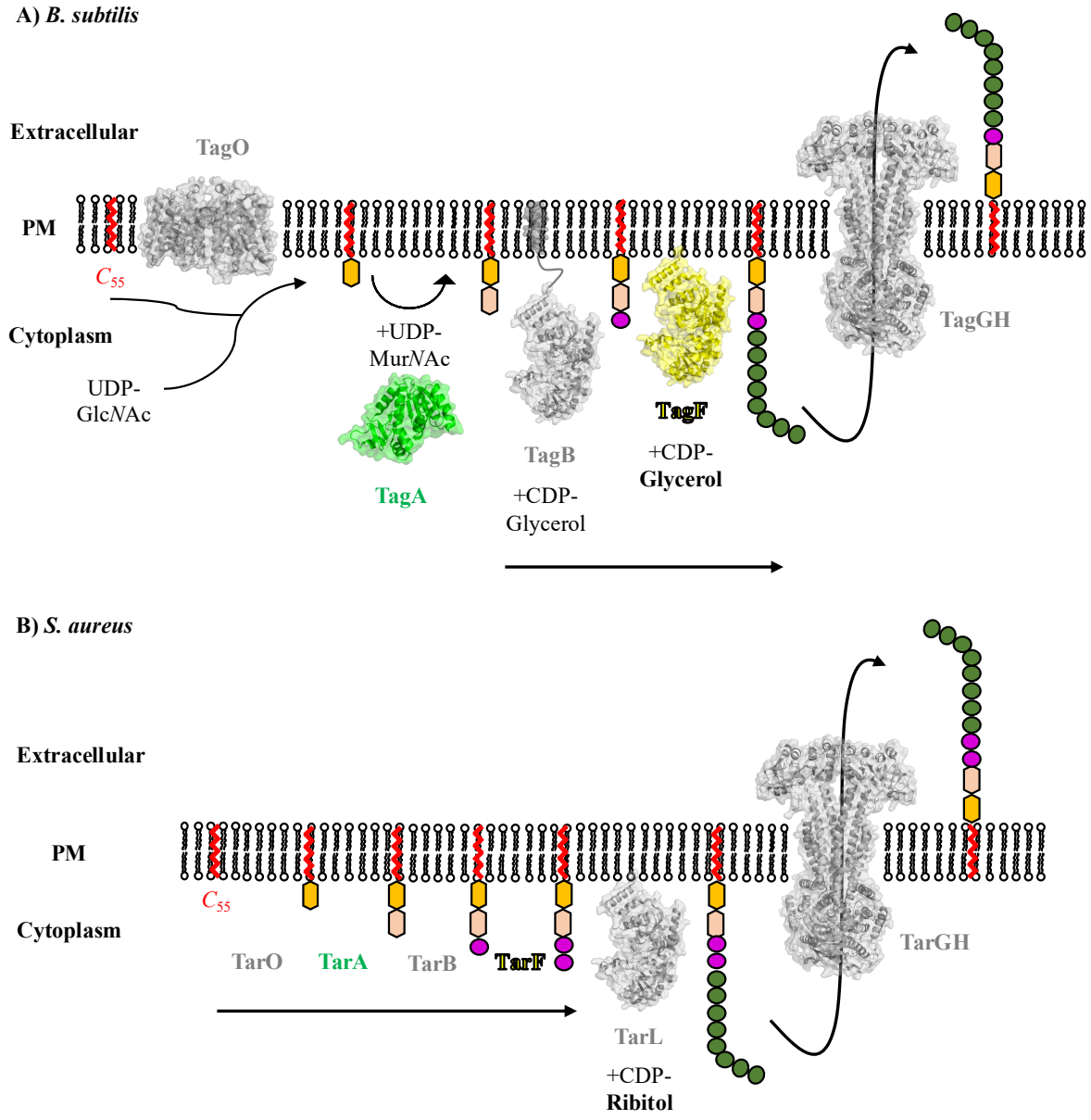

Figure 1.6: A structural overview of WTA construction in *B. subtilis* (A) and *S. aureus* (B). Of the membrane-associated WTA synthesis steps shown in this figure, currently only the structures of TarA (from *T. italicus*) and TagF (from *S. epidermidis*) are known (Kattke et al., 2019; Lovering et al., 2010). For the members of the WTA synthesis pathway for which there is no experimentally determined structural information, closest structural homologues from the PDB are rendered in their place and coloured grey. Here, *E. coli* MraY represents TagO (Chung et al., 2013), *S. epidermidis* TagF represents TagB and TarL (Lovering et al., 2010), and the ABC transporter MacB from *A. baumannii* represents TarGH (Okada et al., 2017).

Following its synthesis and glycosylation, WTA is then transported to the outside of the cell and attached to PG. The WTA precursor is transported outside of the cell by an ATP-binding cassette (ABC) transporter made up of Tar/TagG and TarH/TagH. Tar/TagG recognises the TA polymer and utilises

the energy generated by its ATPase domain to incite a conformational change in its associated transporter, Tar/TagH, which consequently flips the TA across the membrane (Lazarevic & Karamata, 1995) (Figure 1.6).

Once on the outer leaflet of the cell membrane, WTA is covalently attached to PG by a LytR-CpsA-Psr (LCP) family of enzymes (Gale et al., 2017; Kawai et al., 2011), which have been most extensively studied in *B. subtilis*. Genetic analyses have implicated TagT, TagU and TagV from *B. subtilis* in WTA attachment to PG, however, the mechanisms of action for these enzymes has not yet been elucidated (Brown et al., 2013). Homologues of TagT, TagU and TagV from *S. aureus* have been identified, designated LcpA (gene name *msrR*), LcpB (*SA0908*) and LcpC (*SA2103*). Deletions in all three LCP enzymes in *S. aureus* does not inhibit the production of WTA precursors, but prevents their attachment to PG (Chan et al., 2014; Dengler et al., 2012). Although some of the seemingly important components of the WTA attachment process are now known, there is obviously a great deal more work to be done to fully understand how WTA is attached to PG in different Gram-positive bacteria. Addition of *D*-alanine esters to the polyRbo-P/polyGro-P chain takes place following export of the WTA outside of the cell, however, whether *D*-alanylation occurs before or after attachment to PG is not currently known. Four enzymes encoded by the *dltABCD* operon are known to be responsible for attachment of *D*-alanine to WTA, and deletion of the operon results in a loss of *D*-alanine from WTA and LTA. DltA catalyses the intracellular attachment of *D*-alanine to a cofactor present in DltC, before DltC transfers the *D*-alanine across the membrane *via* the membrane proteins DltB and DltD by a currently unknown mechanism (Brown et al., 2013).

1.4.2.2 LTAs

Despite the similarities in structure and components between WTAs and LTAs, their synthesis pathways are quite different. Synthesis of type I LTA is initiated on the cytoplasmic leaflet of the cell membrane by YpfP, which catalyses the formation of Glc_2-DAG from UDP-Glc_2 and DAG (Kiriukhin et al., 2001). Unlike the WTA synthesis pathway, in which the polymer is produced in the cytoplasm and then flipped, Glc_2-DAG is flipped to the outer leaflet of the cell membrane at this stage by the flippase LtaA in *S. aureus*, and an unidentified flippase in *B. subtilis* (Gründling & Schneewind, 2007; Percy & Gründling, 2014). In *S. aureus*, the polyGro-P chain is synthesised by the integral membrane protein LtaS, which sequentially adds Gro-P to the growing chain of LTA by recycling Gro-P from the phosphatidylglycerol present in the plasma membrane (Percy & Gründling, 2014). Although *D*-alanylation is thought to be performed by the same DltABCD proteins as for WTA (Percy & Gründling, 2014), the mechanism of glycosylation is different. The initial stages of glycosylation occur in the cytoplasm, where a glycosyltransferase, GtlA, transfers the sugar moiety to be attached to the LTA to a C_{55}-phosphate carrier lipid on the cytoplasmic face of the membrane. The resultant sugar-phosphate-

C_{55} lipid is then flipped to the outside face of the membrane, where a second glycosyltransferase transfers the relevant sugar from the sugar-phosphate-C_{55} to the LTA (Percy et al., 2016).

1.5 Synthesis of peptidoglycan

1.5.1 Intracellular pathway

The cytosolic reactions of PG synthesis are undertaken chiefly by a family of ligases designated "Mur" (MurA, MurB, etc.); these enzymes are involved in the production of the PG precursor, Lipid II, in the inner leaflet of the IM (El Zoeiby et al., 2002). The first step in the cytosolic pathway of PG synthesis is undertaken by MurA, which catalyses the production of uridine diphosphate (UDP)-Glc*N*Ac-enolpyruvate from phosphoenolpyruvate (PEP), and UDP-Glc*N*Ac (Brown et al., 1995). The production of UDP-Glc*N*Ac-enolpyruvate is followed by its reduction into UDP-Mur*N*Ac, catalysed by MurB (Sylvester et al., 2001). Extension of UDP-Mur*N*Ac by sequential addition of the residues present in the stem peptide is taken on by the enzymes MurC-F to produce Park's nucleotide. In Gram-negative bacteria, Park's nucleotide comprises UDP-Mur*N*Ac, *L*-alanine (*L*-Ala), *D*-glutamine (*D*-Gln), *meso*-diaminopimelic acid (*meso*-A_2pm), *D*-alanine *(D*-Ala), *D*-Ala. Park's nucleotide is attached to undecaprenyl (C_{55}) diphosphate by MraY, resulting in a lipid PG precursor referred to as Lipid I (VanNieuwenhze et al., 2001). The final cytoplasmic enzymatic step involves the formation of the β-1→4 glycosidic bond of Mur*N*Ac with Glc*N*Ac via a glycosyltransferase (MurG) to produce Lipid II (de Kruijff et al., 2008), which is then flipped to the outside of the membrane of the cell by a flippase (Ruiz, 2016) (Figure 1.7).

The structure of each of the Mur enzymes from at least one species of bacteria have now been solved (El Zoeiby et al., 2002), a process that started with the structure of MurA in 1996 (Skarzynski et al., 1996). The structure of MurA was solved in complex with both its substrate UDP-Glc*N*Ac and the antibiotic Fosfomycin, revealing both the mechanism of action (Eschenburg et al., 2003) and the mode of inhibition of MurA. High resolution structures are now available for the remainder of the Mur enzymes, lending the entire cytoplasmic pathway of the process to rational drug design (El Zoeiby et al., 2002; Hrast et al., 2014).

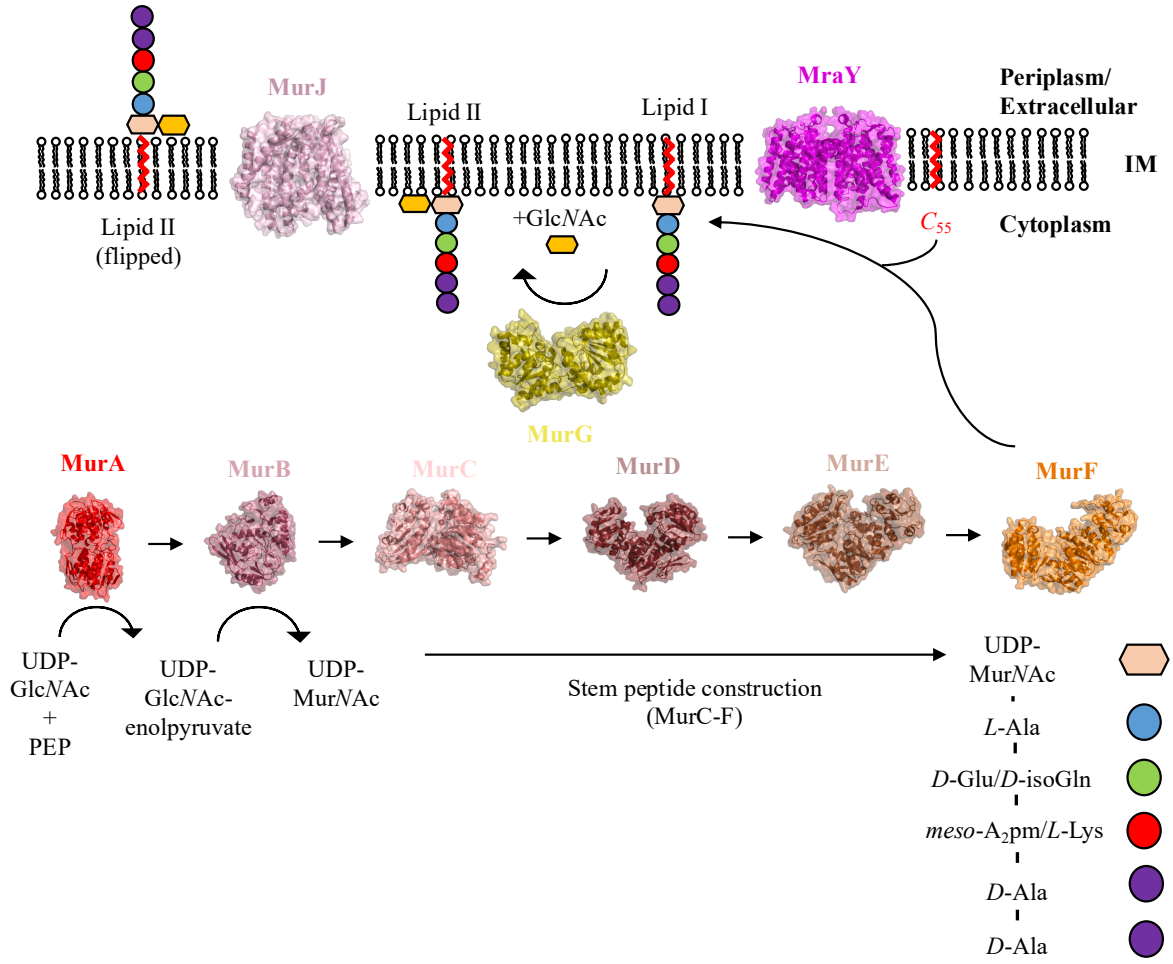

Figure 1.7: A structural overview of Lipid II construction. The structure of every enzyme involved in the cytoplasmic pathway of Lipid II synthesis has now been determined by X-ray crystallographic techniques. Here, the structures of every enzyme involved in Lipid II synthesis are displayed alongside the reaction(s) they are responsible for catalysing on either face of the cell membrane (IM). For the sake of consistency, the structures shown here are those derived from *E. coli* (Bertrand et al., 1997; Chung et al., 2013; Deva et al., 2006; Gordon et al., 2001; Ha et al., 2000; Jackson et al., 2009; Lees et al., 1996; Yan et al., 2000; Zheng et al., 2018).

1.5.2 Flipping lipid II across the plasma membrane

The identity of the flippase responsible for the transfer of lipid II across the cell membrane has been a subject of some debate for almost a decade. Three major candidates for the flippase were initially proposed, FtsW, RodA, and MurJ (Mohammadi et al., 2011; Sham et al., 2014; Sieger et al., 2013). All three proteins are integral membrane proteins, with 10 (FtsW/RodA) and 14 (MurJ) predicted transmembrane domains. All three proteins are highly conserved and essential (Boyle et al., 1997) for growth in both Gram-positive and Gram-negative bacteria, which would suggest that they do not play redundant roles in the cell. The first studies that appeared to observe FtsW as the lipid II flippase were *in vitro* experiments in which the ability of *E. coli* FtsW to flip fluorescently-labelled lipid II was measured using model membranes/liposomes (Mohammadi et al., 2011). These initial experiments suggested that FtsW was indeed capable of flipping lipid II whereas, under the same conditions, MurJ was not (Mohammadi et al., 2011). Follow-up experiments worked to identify the region of the protein

responsible for the flippase activity by removing transmembrane domains of FtsW and performing the same fluorescence-based flipping assays, with concomitant microscopy experiments on *E. coli* cells harbouring the same FtsW mutants (Mohammadi et al., 2014). The *in vitro* and *in vivo* experiments performed in this study suggested that FtsW likely acted through a pore-like mechanism (Mohammadi et al., 2014). At around the same time as these experiments, MurJ was proposed through a bioinformatics approach coupled with *in vivo* genetic analyses as an alternative lipid II flippase in *E. coli* (Ruiz, 2008). Intracellular PG precursors accumulated in *E. coli* harbouring MurJ mutations (Inoue et al., 2008), suggesting an inability of these strains to flip lipid II. More recent work now suggests that both FtsW and RodA function as PG polymerases (Taguchi et al., 2019; Meeske et al., 2016; Emami et al., 2017), swaying the flippase argument towards MurJ as the lipid II flippase. Aided by recent advancements in membrane protein crystallographic techniques (Caffrey, 2011; Landau & Rosenbusch, 1996), the crystal structure of MurJ from the extremophile *Thermosipho africanus* was solved in an inward conformation, allowing for the generation of an alternative access model of lipid II flipping based on a combination of *in silico* docking and *in vivo* experiments (Kuk et al., 2017). Subsequently, the structure of MurJ in several different conformations was solved, allowing for modelling of the mechanism of lipid II flipping (Kuk et al., 2019). The structure of MurJ from *E. coli* has also since been solved, and high-throughput mutagenesis performed, leading to the identification of sites for potential inhibitor development (Zheng et al., 2018).

1.5.3 Extracellular pathway

Following its transport onto the extracellular/periplasmic face of the cell membrane, Lipid II is polymerised by extracellular enzymes. The extracellular members of the peptidoglycan synthesis pathway are membrane-associated penicillin-binding proteins (PBPs), named for their affinity for penicillin. The PBPs are responsible for the polymerisation of the growing glycan chain, and/or by linking the peptide chains extruding from the glycan backbone; these are glycosyltransferase and transpeptidase activities, respectively (Egan et al., 2015). Some PBPs also have carboxypeptidase activity, these are responsible for the trimming of the peptide stem as a mechanism of regulating the number of cross-links formed in the cell wall and are responsible for cell shape maintenance in *E. coli* (Peters et al., 2016). PBPs can be separated into two groups, those that solely have transpeptidase activity (Class B PBPs), or bifunctional PBPs that possess both activities (Class A PBPs). Some examples of bifunctional PBPs include PBP1a, b and c in *E. coli*; PBP1, 2c and 4 in *B. subtilis*; and PBP1a, 2a and 1b in *Streptococcus pneumoniae* (Marie et al., 2003, 2010). Glycosyltransferases act early in the extracellular pathway to catalyse the polymerisation of the non-lipid region of lipid II into the nascent glycan chain (Egan et al., 2015), whilst downstream transpeptidases are responsible for the linking of the *D*-Ala residues of the extruding peptide chain to form the strong and stable peptidoglycan mesh (Sauvage et al., 2008) (Figure 1.8). The transpeptidase forms an acyl-enzyme intermediate with the *D*-Ala residue of the acceptor peptide, before being cross-linked to the donor peptide via an amino

group, which in Gram-positive organisms is glycine or lysine (Kim et al., 2015; Vollmer et al., 2008). Structural studies of PBPs have been performed extensively in several Gram-negative and Gram-positive species of bacteria and, as a result, the structural basis of their mechanism of action and inhibition is well-known.

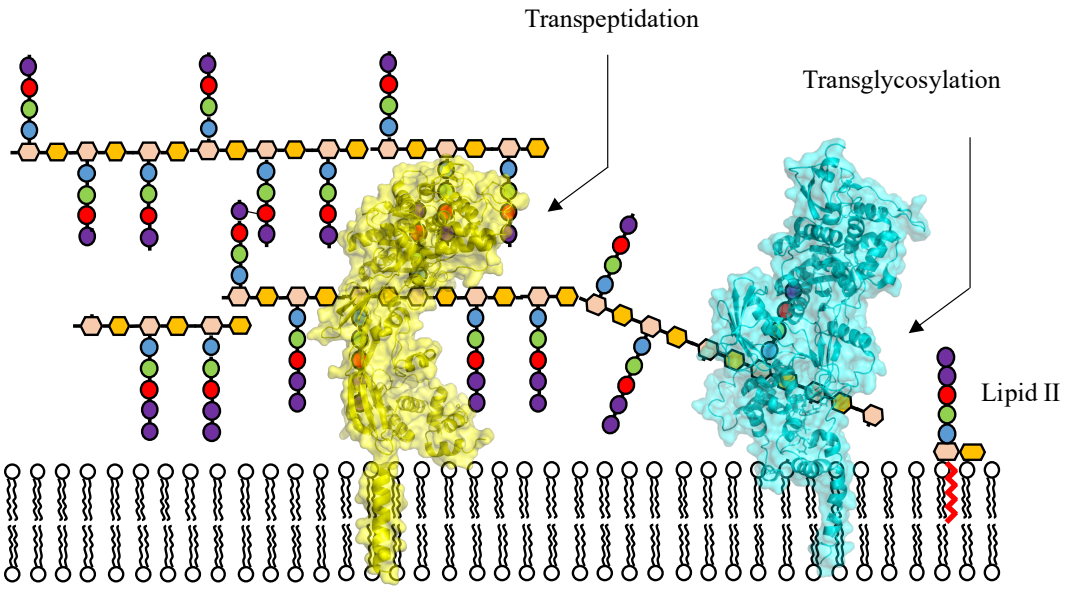

Figure 1.8: Polymerisation of the PG matrix in the extracellular/periplasmic space. PBPs are responsible for the polymerisation of the peptidoglycan matrix from the Lipid II precursors generated by the intracellular pathway. Here, the glycosyltransferase activity of PBPs is demonstrated by the bifunctional PBP1b from *E. coli*, shown in cyan (Sung et al., 2009). The transpeptidase activity of PBPs is demonstrated by PBP2b from *S. pneumoniae*, shown in yellow (Contreras-Martel et al., 2009).

1.5.4 Differences in PG between Gram-negative and Gram-positive bacteria

As well as the obvious difference in the respective thickness of the PG layer and associated macromolecules (TAs/surface proteins) described above, there are further subtle nuances between the precise chemical make-up of the PG of Gram-positive and Gram-negative bacteria. Chemical differences of the glycan chain between Gram-negative and Gram-positive species include variations in modifications such as glycosylation, phosphorylation, and deacetylation (Vollmer, 2008). In contrast to the lack of chemical diversity in the glycan chain, differences in the peptide stems of PG between Gram-negative and Gram-positive bacteria are far more common (Vollmer, 2008). Most peptide stems in the PG of Gram-negative bacteria follows the pattern *L*-Ala, *D*-glutamate (*D*-Glu), *meso*-A_2pm, followed by two *D*-Ala residues. In Gram-positive bacteria, however, the residues present in the stem peptide vary at positions two and three, at which D-*iso*glutamine (*D*-*iso*Gln) and *L*-lysine (*L*-Lys) are prevalent, respectively (Vollmer, 2008). In both Gram-positive and Gram-negative bacteria, *D*-Glu is initially added to the growing peptide stem by MurD at position two during construction of the peptide stem (Lovering et al., 2012; Vollmer et al., 2008). In those Gram-positive species where *D*-*iso*Gln is

found at position 2, *D*-Glu is enzymatically modified to *D-iso*Gln by an enzyme complex of MurT/GatD (Zapun et al., 2013). The structure of the MurT/GatD complex has been solved recently, revealing the mechanism of PG amidation by MurT, and also the mechanism through which GatD produces and channels the ammonia required for PG amidation to the MurT active site (Morlot et al., 2018).

1.6 Coordination of cell wall synthesis with cell division

1.6.1 The divisome

The collection of ~20–30 proteins responsible for regulating cell division has come to be known as the "divisome" (Figure 1.9). Proteins in the divisome ensure that (i) only one round of division occurs at a time, with one copy of the chromosome present in each cell; (ii) that cell wall synthesis is undertaken appropriately to circumvent lysis during septum formation; (iii) that cell separation occurs through the function of cell wall hydrolases (autolysins) (Egan & Vollmer, 2013). Investigation of the divisome has chiefly been undertaken in rod-shaped bacteria, yet there is still a lot to learn about divisome formation and organization in these bacteria as well as in other bacteria with different shapes, such as the spherical cocci. Some archaea with profound differences in morphology and cell division, such as the triangular *Haloferax volcanii* which divides by a process of ternary fission, also utilize some of the same proteins as in bacteria when regulating division (Walsh et al., 2019). The divisome is an attractive target for the generation of novel antimicrobials, as disruption of the machinery responsible for organizing cell division would ultimately result in a reduction and cessation of propagation. The function of the divisome to coordinate chromosome replication and segregation with cytokinesis is common to both Gram-negative and Gram-positive organisms, but the precise constituents of the divisome vary across species (Blaauwen et al., 2017).

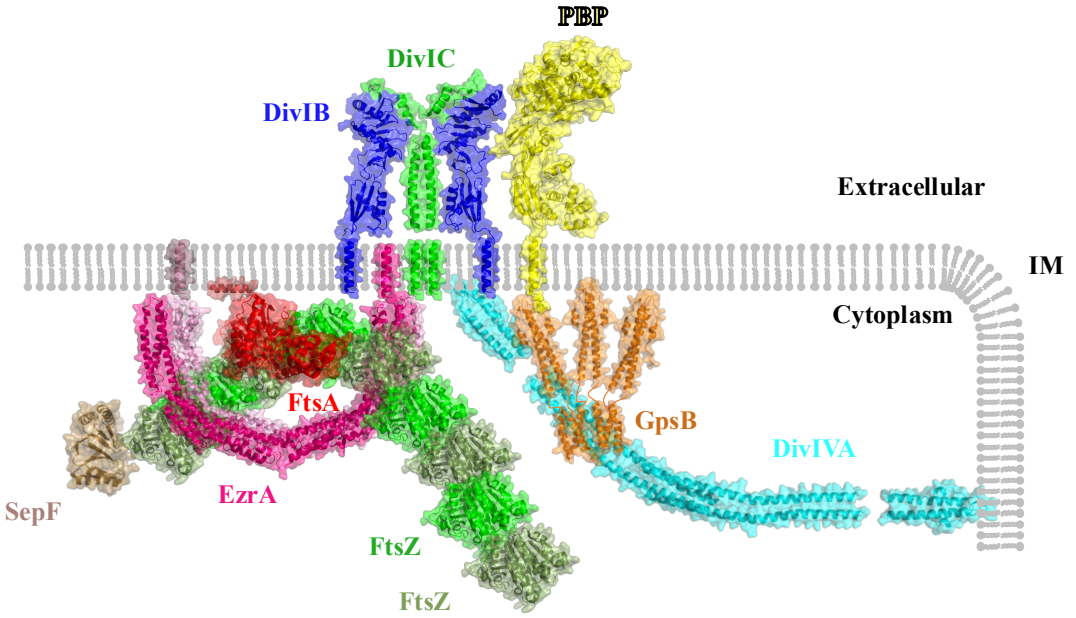

Figure 1.9: Structural model of the divisome. A selection of divisome proteins for which atomic structures have been determined are shown. Where structural data regarding protein-protein interactions are known, this figure reflects this. Where available, structures have been taken from the model organisms *B. subtilis* and *E. coli*, however, in the cases where there is a lack of structural data from these organisms, the structures with the greatest degree of sequence homology are shown. FtsZ is coloured alternately in green and splitpea to donate filament formation (Löwe et al., 1998), FtsA is shown in red (Fujita et al., 2014), an antiparallel EzrA dimer is coloured in hotpink and lightpink (Cleverley et al., 2014), SepF is shown in sand (Duman et al., 2013), a 2:2 complex of FtsQ/DivIB and FtsB/DivIC is shown in blue and tvgreen, respectively (Kureisaite-Cizience et al., 2018), a GpsB hexamer is shown in orange (Rismondo et al., 2016), a PBP (here represented by PBP2b from *S. pneumoniae*) is shown in yellow (Contreras-Martel et al., 2009). DivIVA is shown in cyan (Oliva et al., 2010).

1.6.2 FtsZ

The best-studied of the divisome proteins is FtsZ, and arguably it is the central protein to the function of the divisome. FtsZ, named after its mutants' abilities to cause *E. coli* cells to divide in a filamentous fashion at non-permissive temperatures (filamentous temperature sensitive) (Erickson, 1997), is a cytosolic protein known to accumulate at the site of division across all bacterial species (Lutkenhaus & Addinall, 1997). The discovery of FtsZ set the groundwork for much of the research conducted on the divisome in the past ~25 years. The crystal structure of FtsZ provided the first definitive evidence of a bacterial cytoskeleton, as FtsZ is a clear structural homologue of tubulin, despite sharing no significant amino acid sequence homology (Löwe & Amos, 1998). FtsZ polymerizes into filaments in a GTP-dependent manner, rapidly "treadmilling" in an agile and nimble ring-like structure, dubbed the "Z-ring," adjacent to the cytoplasmic face of the membrane. The Z-ring forms the scaffold onto which all proteins assemble that are responsible for modulating the cell envelope during cell division (Figure 1.9). Prior to the observation of the treadmilling of FtsZ, the Z-ring was thought to represent a semicontinuous ring at the mid-cell which constricted during septum formation. Z-ring formation relies

on both the formation of FtsZ filaments as well as the bundling of filaments through lateral interactions (Lutkenhaus & Addinall, 1997).

FtsZ consists of an N-terminal globular domain (the tubulin-like domain of FtsZ) and a conserved 'tail' at the C-terminus, both of which are essential for its function. The tubulin-like N-terminal domain is responsible for the polymerisation of FtsZ and is able to polymerise into filaments *in vitro* in absence of the C-terminal tail domain (Jindal & Panda, 2013). In the presence of GTP, FtsZ polymerises *in vitro* spontaneously without a requirement for any initiating proteins. The mechanism of treadmilling is thought to occur by FtsZ monomers dissociating from the "back" end (minus end) of the filament, their migration to and assembly at the "front" end (plus end) of the filament (Bisson-Filho et al., 2017). *In vitro*, filaments of FtsZ are thought to be comprised of ~40-50 subunits. Bundles of FtsZ filaments form *in vitro*, suggesting that the bundling of FtsZ filaments is an intrinsic property of the protein. The C-terminal peptide of FtsZ has been implicated as being important for filament bundling (Lan et al., 2008), however, this notion conflicts with structural studies of FtsZ by electron cryotomography, which suggest that the large spacing observed between filaments *in vivo* is not consistent with the direct interaction of FtsZ filaments (Szwedziak et al., 2014). More work is required to interrogate both the mechanism and relevance of lateral interactions between FtsZ filaments *in vivo*.

1.7 Z-ring placement regulation

1.7.1 The Min system

There are several molecular systems that oversee placement of the Z-ring, the Min system is a well-studied example of such a system. The Min system functions in an inhibitory manner, preventing formation of the Z-ring away from mid-cell. It follows that deletion of the Min system in rod-shaped bacteria such as *E. coli* results in populations of minicells, revealing the importance of the system for control of septal placement (Yu & Margolin, 1999). The Min system has been studied in most extensively in the rod-shaped models of Gram-negative and Gram-positive bacteria, *E. coli* and *B. subtilis* (Figure 1.10). In *E. coli*, the Min system consists of three proteins, MinC, MinD, and MinE, whereas in *B. subtilis*, the Min system consists of MinC, MinD, MinJ, and DivIVA (Rowlett & Margolin, 2013). In both species of bacteria, MinC is responsible for the disruption of FtsZ filament formation (Hu et al., 1999), whilst the remaining members of the Min system, MinD and MinE (or MinD, MinJ and DivIVA), are responsible for localising MinC such that Z-ring inhibition does not occur indiscriminately across the whole cell (Park et al., 2011; Raskin & de Boer, 1999; Renner & Weibel, 2012).

MinC consists of two domains, an N-terminal domain which appears to shorten existing FtsZ filaments *in vitro*, and a C-terminal domain implicated in the inhibition of filament bundling, possibly through

the disruption of lateral FtsZ interactions (Hu & Lutkenhaus, 2000). In *E. coli*, MinD and MinE oscillate between the two poles of the cell; MinD is responsible for the carriage of MinC, whereas MinE is responsible for the localisation of MinD to the poles. MinD is a ParA-family ATPase which binds to membranes in its dimeric, ATP-bound form. MinD dimers interact with the membrane through their C-terminal amphipathic helices (Lutkenhaus, 2012; Renner & Weibel, 2012). MinE is responsible for removing MinD from the membrane, which it does by stimulating the ATPase activity of MinD, resulting in both the breakdown of ATP and the MinD dimer (Park et al., 2011). MinE is attracted to the membrane as a result of both its interaction with MinD and through its N-terminal amphipathic helix. Fluorescently labelled MinE is observed to form a ring-like structure, sometimes referred to as the MinE-ring, or E-ring (Fu et al., 2001). *In vivo* the MinE ring follows MinD from mid-cell to the poles, resulting in a unidirectional movement of MinD towards the cell poles as a result of the action of MinE. The oscillation of MinCDE between poles in *E. coli* result in a low-density region of MinCDE at mid-cell, encouraging the placement of FtsZ filaments at this position in the cell (Rowlett & Margolin, 2013) (Figure 1.10).

In *B. subtilis*, MinC performs the same function as in *E. coli* as an FtsZ filament inhibitor. In contrast to the dynamic oscillatory nature of the Min system in *E. coli*, the Min system in *B. subtilis* forms a static structure at the cell poles (Jamroškovič et al., 2012). *B. subtilis* lacks MinE and, therefore, requires an alternative mechanism for localisation, a role filled by DivIVA and MinJ, which accumulate at the cell pole and recruit the MinCD complex (Rowlett & Margolin, 2013) (Figure 1.10).

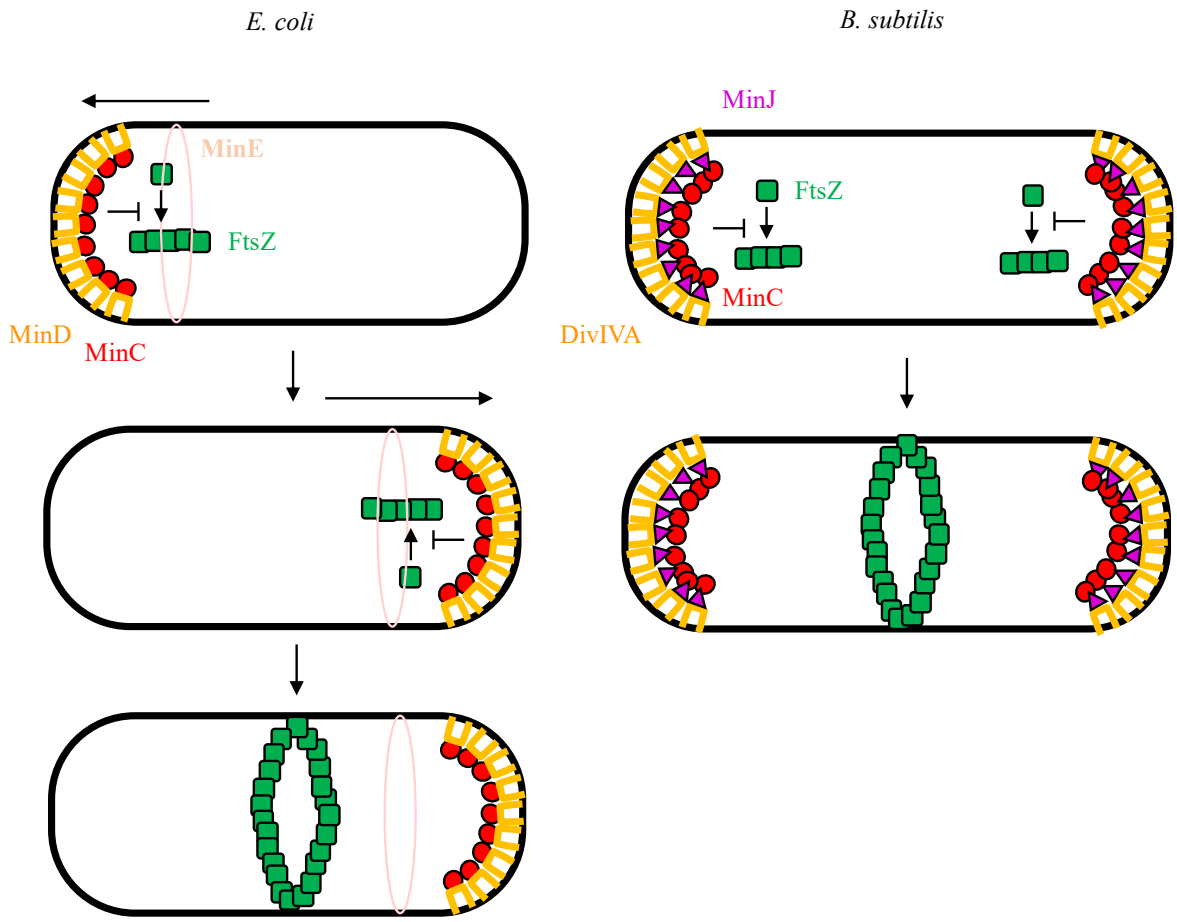

Figure 1.10: The Min system in *E. coli* and *B. subtilis*. In *E. coli*, the MinD traffics MinC between the cell poles, followed by the MinE ring. The oscillations of MinCDE between the two poles result in a low-density region at mid-cell, where Z-ring formation is allowed to occur. In *B. subtilis*, the Min system is static at the cell poles. The membrane-binding protein DivIVA recognises the negative curvature of the cell membrane at the poles and recruits MinJ, which in turn recruits MinC, preventing Z-ring formation at the cell poles and restricting it to mid-cell.

1.7.2 Nucleoid occlusion

Stringent regulation of septal closure such that the chromosome is not bisected prior to the completion of its duplication and segregation is a requirement for producing two genetically identical daughter cells; nucleoid occlusion is the mechanism through which bacteria achieve this. As is the case for many of the systems discussed in this thesis, nucleoid occlusion mechanisms have been studied best in *E. coli* and *B. subtilis*, where the proteins SlmA and Noc are responsible for this regulation, respectively (Schumacher, 2017). SlmA and Noc are both DNA-binding proteins that bind as dimers to palindromic DNA sequences (Noc-binding sequences (NBS), or SlmA-binding sequences (SBS)) on the chromosome (Cho et al., 2011; Tonthat et al., 2011). SlmA/Noc bind to many sites on the chromosomal DNA of their respective organisms, except for the regions including and surrounding the replication terminus (*ter*) (Adams et al., 2014).

SlmA binds to FtsZ *in vitro* (Cho et al., 2011), however, the mechanism of inhibition of FtsZ filamentation by SlmA is not currently defined. Two current models propose that SlmA either disrupts Z-ring formation by disrupting lateral interactions between filaments, or that SlmA dimers link together filaments with opposite directionalities, preventing any unidirectionality of the Z-ring (Wu & Errington, 2012). During chromosome replication and segregation, the replisome assembles at the origin of replication (*oriC*) and the chromosomes are replicated and segregated concomitantly. The *oriC* regions of the parental and daughter chromosome move to opposite cell poles and the *ter* region of the chromosome remains at mid-cell until replication is complete. As chromosome segregation and replication near completion and *ter* becomes the only region of the chromosome remaining at mid-cell, the concentration of SlmA decreases at mid-cell and inhibition of Z-ring formation is relieved (Figure 1.11). Intriguingly, no interactions have been determined between Noc and any other currently identified divisome protein, leaving the mechanism of septum inhibition by Noc open to further study (Adams et al., 2014; Schumacher, 2017).

In the rod-shaped bacteria described thus far, nucleoid occlusion factors are non-essential (Rowlett & Margolin, 2015), suggesting that the actions of other Z-ring placement regulators, such as the Min system, are sufficient to regulate septal placement in these bacteria. In many cocci, such as *S. aureus*, the Min system is absent, therefore, there is a greater dependence on nucleoid occlusion for correct septal placement. Indeed, deletion of the Noc homologue from *S. aureus* results in the formation of multiple Z-rings and bisection of the chromosome. In the absence of Noc, *S. aureus* is no longer able to divide in orthogonal planes, leading to the hypothesis that the plane of cell division undertaken by *S. aureus* is determined by the plane of chromosome segregation (Veiga et al., 2011). Precisely how the previous site of division is recognised on a molecular level is not yet understood and may involve nucleoid occlusion factors yet to be discovered.

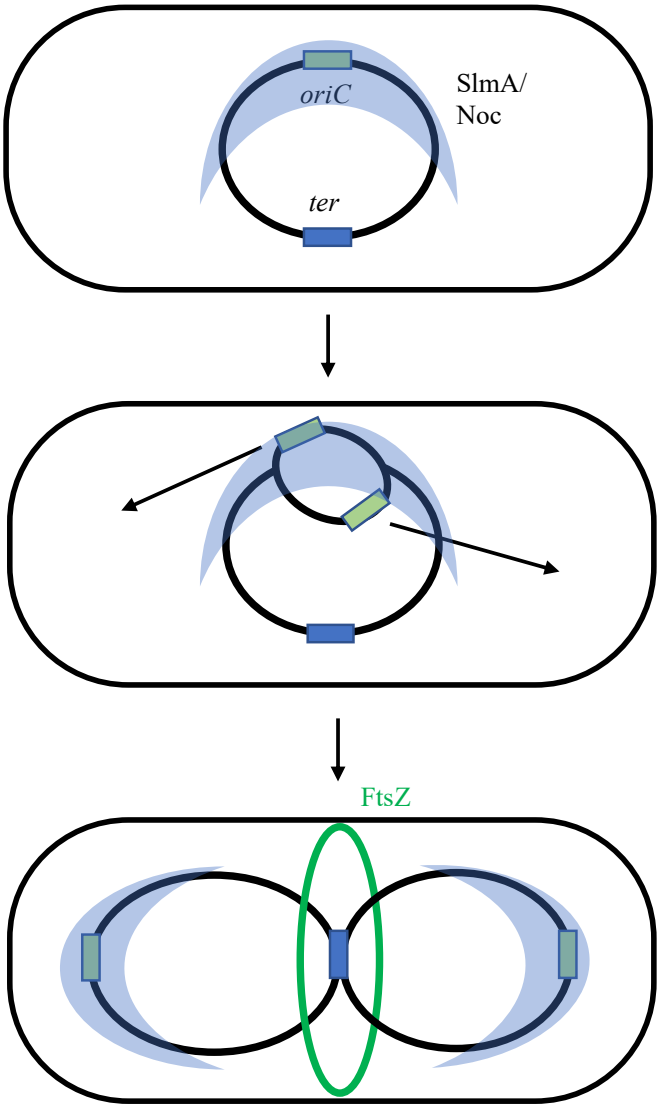

Figure 1.11: General mechanism of nucleoid occlusion. The nucleoid occlusion factors SlmA (*E. coli*) or Noc (*B. subtilis*) bind at many sites on the chromosome, apart from the replication termination region *ter*. In this figure the density of nucleoid occlusion factors are roughly depicted as a transparent crescent. As the chromosome is replicated and the parental and daughter *oriC* migrate to the cell poles, the inhibition of Z-ring formation is lifted as a result of a low-density region of SlmA/Noc at mid-cell. Whilst the mechanism of FtsZ inhibition by SlmA appears to be a result of a direct interaction, the mechanism inhibition of Z-ring formation by Noc has yet to be determined.

1.7.3 FtsZ-associated proteins

1.7.3.1 ZapA

An example of some positive regulators of Z-ring assembly are the FtsZ-associated proteins (Zaps). The majority of Zaps (ZapA, ZapB, ZapC, and ZapD) co-localise with FtsZ and stimulate Z-ring formation, though ZapE has an inhibitory role similar to MinC (Ortiz et al., 2016). ZapA is a conserved

cell division protein in both Gram-positive and Gram-negative bacteria that co-localises with FtsZ. ZapA contains a globular N-terminal domain and a coiled coil C-terminal domain (Low et al 2004). ZapA forms either dimers or tetramers in solution in a concentration-dependent manner. Tetramers of ZapA are made up of a 'head-on' arrangement of antiparallel dimers, which interlock at the coiled-coil regions at their C-termini (Low et al., 2004) (Figure 1.12). Recent work suggests that ZapA interacts with FtsZ via its N-terminal domain, generating a model in which tetramers of ZapA are able to form physical cross-links between FtsZ filaments (Roseboom et al., 2018) (Figure 1.12).

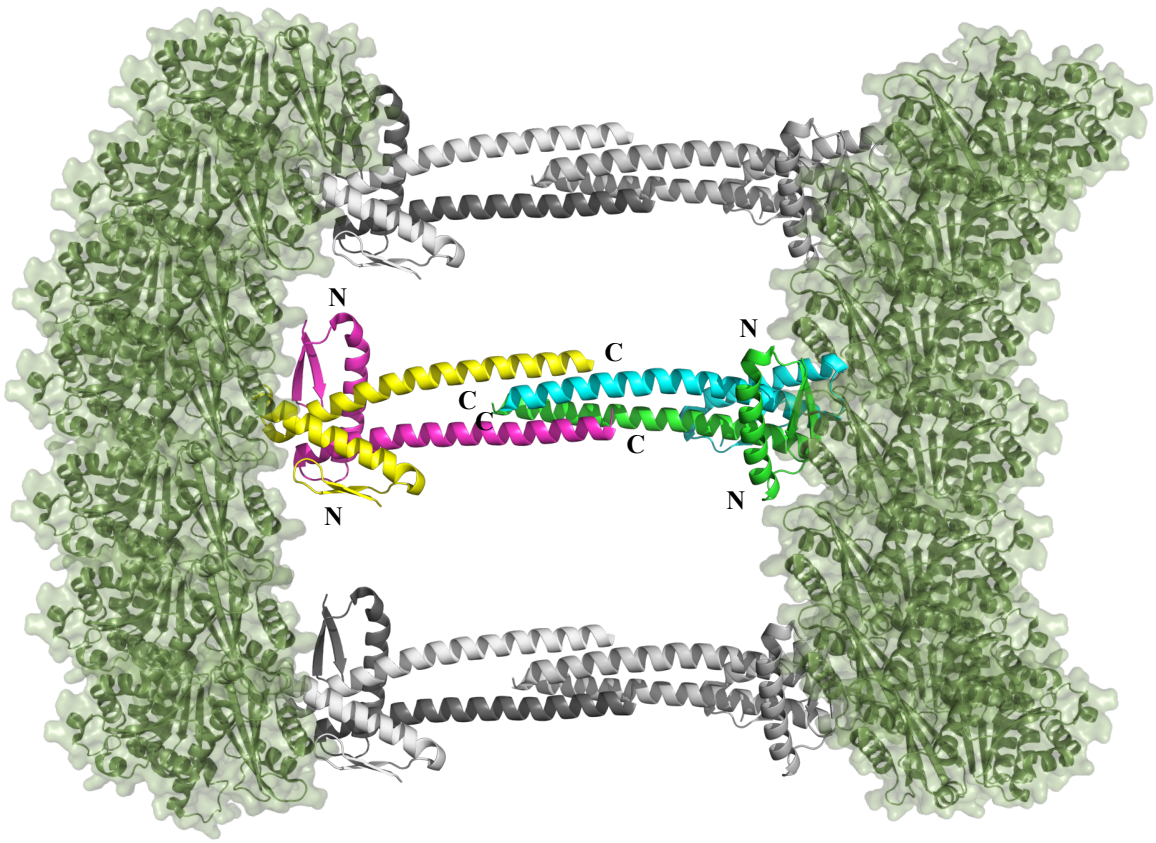

Figure 1.12: Proposed mechanism of FtsZ filament cross-linking by ZapA. The above model of ZapA/FtsZ interaction has been proposed in Rosenboom et al., 2018. Here, three tetramers of ZapA are rendered independently, one in which each ZapA monomer is rendered in a different colour and the four N- and C- termini labelled; two proximal ZapA tetramers are rendered in greyscale. Two filaments of FtsZ are shown in which the structure of FtsZ (Löwe et al., 1998) has been rendered and duplicated to reflect filament formation. ZapA is proposed in Rosenboom et al., 2018 to bind to FtsZ via its N-terminus, the model rendered here represents a general structural overview of the FtsZ/ZapA interaction, and is not based on precise structural information regarding the interaction.

The remainder of the Zaps (ZapB-E) are not conserved in all bacteria, and their presence is confined to the Gram-negative γ-bacteria (Ortiz et al., 2016). Co-sedimentation assays performed on ZapA and Zap B from *E. coli* revealed that ZapB interacts with the C-terminal coiled-coil domain of ZapA, likely stabilising the ZapA-FtsZ interaction (Galli & Gerdes, 2012). ZapB also interacts with a DNA-binding

protein involved in chromosome segregation, suggesting that ZapB may play a role in co-ordinating chromosome segregation and septum closure (Buss et al., 2017). ZapC and ZapD appear to play similar roles as ZapA, directly interacting with and cross-linking FtsZ filaments (Roach et al., 2016; Durand-Heredia et al., 2011).

1.7.3.2 FtsA

A well-studied protein-protein interaction of FtsZ is with FtsA, a well-conserved, actin-like ATPase, which self-organizes with FtsZ and tethers it to the membrane (Pichoff & Lutkenhaus, 2005). The FtsA-mediated membrane tethering is essential to ensure constriction of the membrane at the septum, as FtsZ does not interact with the membrane of its own accord. FtsA has been implicated in the ATP-dependent reorganisation of cell membranes, suggesting that FtsA has a more involved role in cell division than as a simple membrane tether for FtsZ. FtsA interacts with the cell membrane through a conserved C-terminal amphipathic helix, which may also be the region through which FtsA modulates membrane curvature (Conti et al., 2018). The crystal structure of FtsA and FtsZ in complex revealed that domain 2B of FtsA interacts with FtsZ in the region at the C-terminus of FtsZ. The same work identified that FtsA formed actin-like protofilaments that likely line up on the inside face of the membrane, tethering FtsZ filaments (van den Ent, 2000) (Figure 1.13).

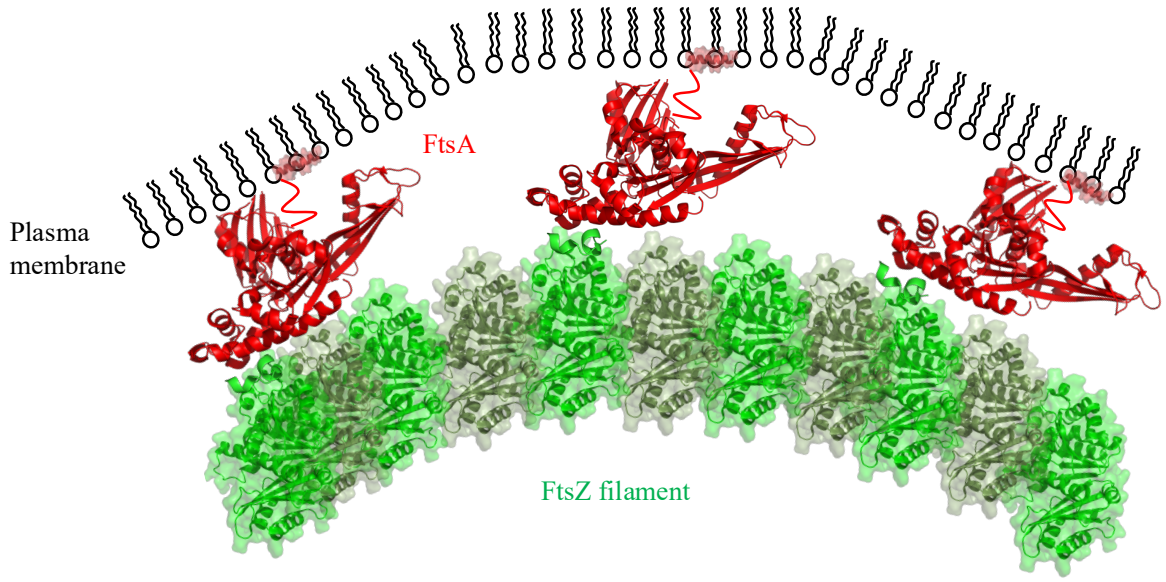

Figure 1.13: Model of FtsZ tethering to the membrane by FtsA. The above model of membrane tethering of FtsZ by FtsA has been proposed (van den Ent, 2000). Here an FtsZ filament is shown in alternating light and dark green subunits (Löwe et al., 1998), and FtsA is shown in red (van den Ent, 2000). The amphipathic helix of FtsA unresolved by X-ray crystallography is modelled as a single helix with a cartoon interpretation of the unresolved linker.

1.7.3.3 ZipA

ZipA works alongside FtsA in Gram-negative bacteria to tether FtsZ to the membrane, however, no such homolog is present in Gram-positive bacteria; SepF has been proposed to fulfil a similar function instead. The combination of the polymerized FtsZ, along with SepF/ZipA and FtsA, forms a structure called the proto-ring. As stated above, ZipA is involved in the regulation of divisome assembly and Z-ring placement in Gram-negative bacteria (Krupka et al., 2018). ZipA has been studied most extensively in *E. coli*, where it is essential (Hale & de Boer, 1997). ZipA is predominantly cytoplasmic, with a single transmembrane helix and a micro-domain in the periplasm. ZipA binds to FtsA and to FtsZ to tether both of them to the cell membrane (Pazos et al., 2018). The functional significance of ZipA was questioned by the discovery of a gain of function mutant of FtsA, which allowed for the bypassing of ZipA (Geissler et al., 2003), however, it has been suggested more recently that ZipA functions by protecting FtsZ from degradation by cytoplasmic proteases, a role that cannot be substituted for by FtsA (Pazos et al., 2013). The stimulatory or inhibitory effects of ZipA on Z-ring formation and FtsZ bundling are currently unknown; contradictory evidence for stimulatory (Chen et al., 2017) and inhibitory (Loose & Mitchison, 2014) roles for ZipA have been published. It has also been suggested that ZipA has neither a stimulatory nor an inhibitory effect on lateral interactions between FtsZ filaments, and that it simply acts as a passive membrane tether for FtsZ (Krupka et al., 2018). More work is clearly required to elucidate the functional significance of ZipA for divisome formation in Gram-negative bacteria.

1.8 Regulators of cell division and PG remodelling

Following the formation of the proto-ring, the 'late' division proteins start to assemble to promote downstream processes involved in the remodelling of the cell wall. Divisome assembly has perhaps been studied most extensively in *E. coli*; the proteins known to accumulate are FtsN, FtsI, FtsEX, FtsQ, FtsL, FtsB, FtsW, FtsK and PBP2B (Söderström & Daley, 2017; Aarsman et al., 2005). However, the conservation of many of these components is not necessarily maintained in Gram-positive bacteria, and the essentiality of the components is also not strictly conserved (Ortiz et al., 2016; Egan & Vollmer, 2013; Söderström & Daley, 2017).

1.8.1 DivIB/DivIC/FtsL

One example of a widely-conserved and essential subcomponent of the divisome is a trimeric complex of DivIB, DivIC and FtsL in Gram-positives (FtsQ, FtsB and FtsL in Gram-negatives, respectively). DivIB/FtsQ, DivIC/FtsB and FtsL are transmembrane proteins, each with a single transmembrane helix, and form a complex independent of other divisome proteins in *E. coli* and *B. subtilis* (Robson & King, 2006; Buddelmeijer & Beckwith, 2004). In *S. aureus* DivIB/FtsQ interacts with peptidoglycan through its extracellular PASTA domain and is required as a cell division checkpoint (Bottomley et al., 2014).

The extracellular portion of DivIB/FtsQ is also known to interact with PBPs, such as PBP2b in *B. subtilis* (Angeles et al., 2019), which may suggest that the DivIB/DivIC/FtsL (FtsQ/FtsB/FtsL) complex links the early intracellular stages of cell division with PG remodelling, a predominantly extracellular process (Boes et al., 2019). *In vitro* reconstitutions of the DivIB/DivIC/FtsL complex from *S. pneumoniae* have been performed and the full-length proteins isolated as complexes (Noirclerc-Savoye et al., 2013). The earliest structural studies of DivIB were performed on DivIB from *Geobacillus stearothermophilus*, wherein the domain organisation of DivIB was determined: DivIB contains three extracellular domains, α, β and γ. The structure of the β-domain of *G. stearothermophilus* DivIB has been solved by NMR, revealing a unique fold in this region of the protein (Robson & King, 2005). Structures of FtsQ from *E. coli* and *Yersinia enterocolitica* were later solved by X-ray crystallography, confirming the overall fold of the *G. stearothermophilus* DivIB structure and expanding on the NMR structure (van den Ent et al., 2008).

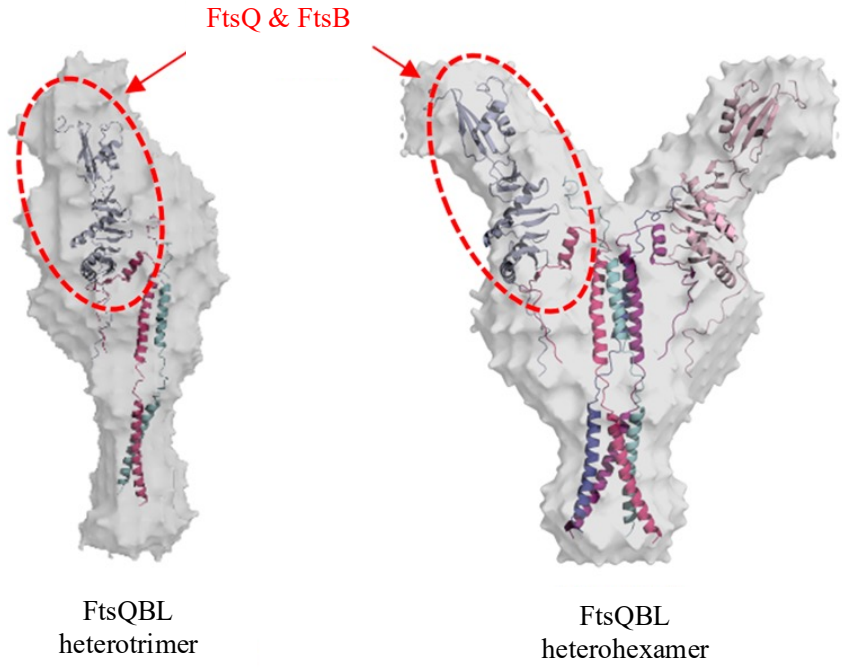

Figure 1.14: Model of FtsQ binding to FtsB and FtsL. SAXS and X-ray crystallographic studies of FtsQ and FtsB from *E. coli* have resulted in a model of their interaction on the inner membrane. The crystal structure of FtsQ and FtsB is enclosed within a red circle, the SAXS envelopes of the two observed oligomeric states of the FtsQBL are rendered as a grey transparent molecular envelope. Adapted from Choi *et al*., 2018.

Based on secondary structure analysis, DivIC and FtsL are predicted to be predominantly α-helical in their extracellular/periplasmic domains, with disordered intracellular domains. DivIC and FtsL form a complex independently of DivIB, predicted to be made up of a coiled-coil (Condon et al., 2018). Small-angle X-ray scattering (SAXS) analysis of a complex of DivIB, DivIC and FtsL from *S. pneumoniae* revealed that DivIB caps the coiled coil of DivIC and FtsL during complex formation, and may stabilise

the interaction between DivIC and FtsL (Masson et al., 2009). The structure of *E. coli* FtsQ in complex with a fragment of FtsB has recently been solved independently by two different groups. The structure of the FtsQB complex, coupled with SAXS experiments performed on the FtsQBL complex from *E. coli* has resulted in a model of complex formation on the periplasmic face of the intracellular membrane (Kureisaite-Ciziene et al., 2018) (Figure 1.14). Based on the essentiality of the interaction between FtsQ/DivIB with FtsB/DivIC, and their location of interaction on the outside surface of the cell, the structure of the complex should allow for the considered design of antibiotics, without a need to consider cell membrane traversal.

1.8.2 DivIVA

DivIVA is a member of the Gram-positive divisome with divergent roles in those bacteria that encode DivIVA orthologs. One feature common to all DivIVA homologs, however, is an apparent innate ability to sense membrane curvature (Lenarcic et al., 2009). The bulk of the published information about DivIVA comes from *B. subtilis* where, among other things, it functions as a topological marker for the Min system, a cell division inhibitor. X-ray crystallographic studies of the isolated N- and C-terminal domains of DivIVA revealed that it forms tetramers made up of an antiparallel arrangement of parallel coiled-coils (Oliva et al., 2010) (Figure 1.15).

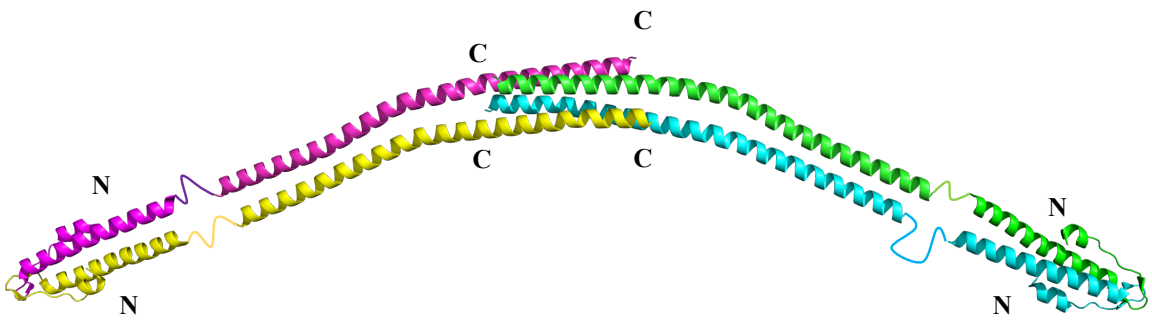

Figure 1.15: Structure of DivIVA from *B. subtilis*. Crystal structures of the N-terminus and C-terminus of DivIVA from *B. subtilis* were solved to 1.4 Å and 8 Å resolution, respectively, and the above model of DivIVA's structure assembled (Oliva et al., 2010). DivIVA forms an antiparallel "head-on" arrangement of parallel dimers, much like ZapA. Here DivIVA monomers are coloured separately and the N- and C- termini of the protein labelled to reflect the antiparallel nature of the protein. The regions of the protein unresolved by the crystal structures are drawn as a cartoon linker.

This model clashes somewhat with earlier EM studies suggesting that DivIVA forms higher-order oligomers, however, these structural studies were performed on mutants of DivIVA purposefully designed to alter oligomeric state and may not accurately represent the wild-type protein (Stahlberg et al., 2004). The crystal structure of the N-terminal domain of DivIVA also provided some insight into how membrane-binding might be possible; a conserved Phe-Arg motif oriented outwards from the protein is positioned to form hydrophobic and electrostatic interactions with the membrane, respectively

(Oliva et al., 2010). Since DivIVA interacts with several cytoplasmic proteins through its C-terminal domain, it may act somewhat promiscuously as a topological marker for several intracellular systems (Halbedel & Lewis, 2019). The situation is complicated as a result of DivIVA's divergent roles; for instance, *S. aureus* lacks MinC/D, and the interactions of DivIVA with divisome components in *S. aureus* have yet to be elucidated fully. Despite this, DivIVA shows similar localisation patterns in *S. aureus* as in *B. subtilis* (Pinho & Errington, 2004) (Figure 1.16), leaving the question of DivIVA's function in *S. aureus* open to interpretation.

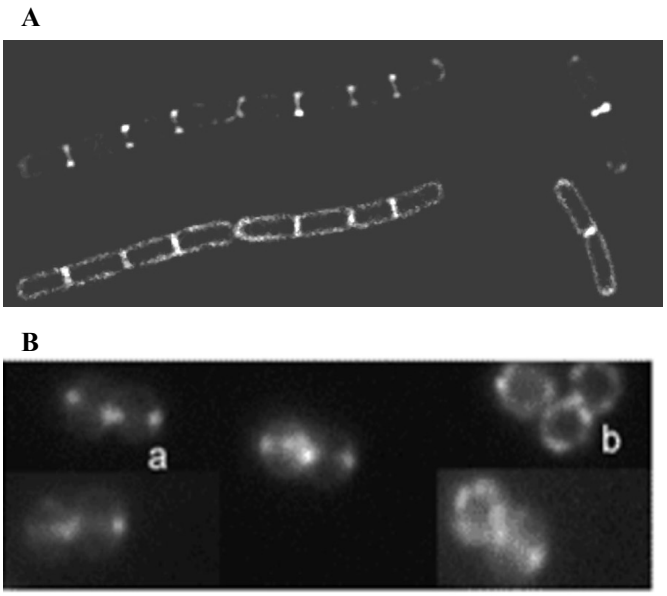

Figure 1.16: Localisation of DivIVA in A) *B. subtilis* and B) *S. aureus*. In wild-type *B. subtilis* cells, fluorescently-labelled DivIVA is observed to form punctate foci in the most negatively curved regions of membrane curvature, surround the fully-formed septum. This appears also to be the case in *S. aureus*, which shows similar localisation patterns of DivIVA at the septum. Figure adapted from Lenarcic *et al*., 2009, and Pinho & Errington, 2004.

1.8.3 GpsB

GpsB, a homolog of DivIVA present in Gram-positive organisms, is also involved in the coordination of PG synthesis at the septum (Cleverley et al., 2019). GpsB and DivIVA share sequence and structural homology at their N-termini, however, this homology between the two proteins decreases significantly in their C-terminal regions. The difference in C-terminal structure between the two proteins is responsible for the differences in oligomeric state between the two proteins. Integrative structural and biochemical studies on GpsB from *Listeria monocytogenes* and *B. subtilis* revealed that GpsB binds the cytoplasmic microdomains of PBPs and forms a hexamer in solution (Figure 1.17), generating a model through which GpsB likely coordinates the activities of PBPs (Cleverley et al., 2016; Rismondo et al., 2016).

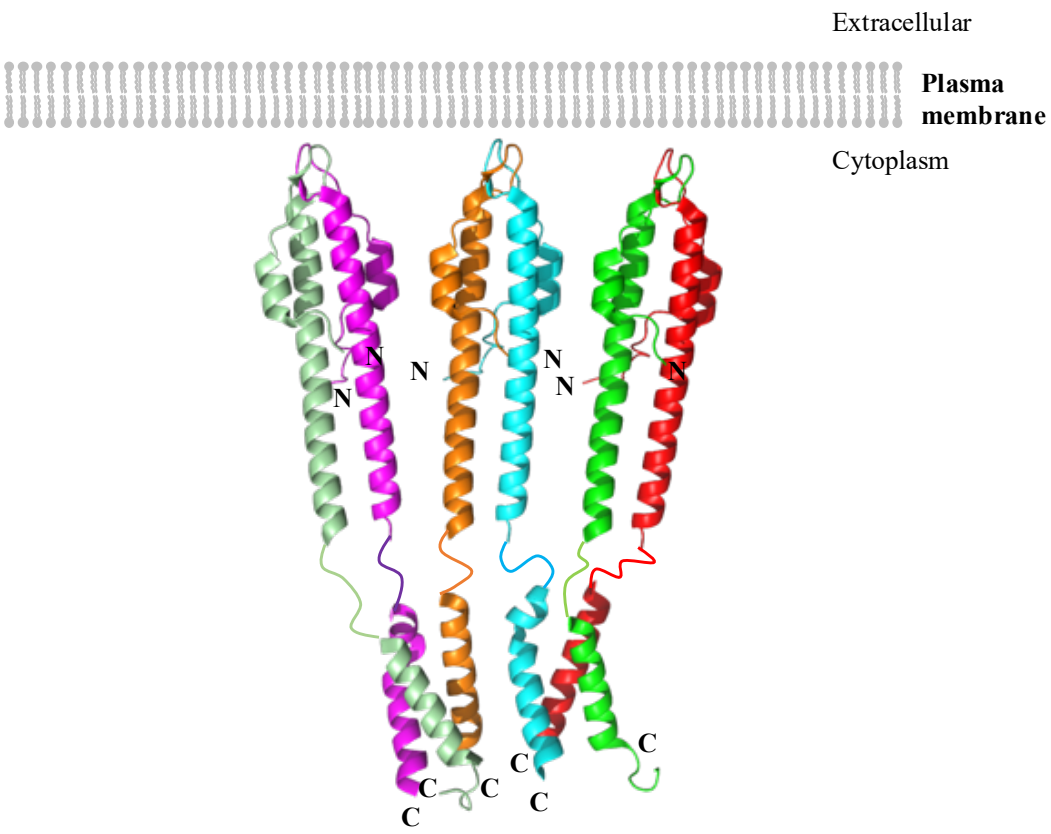

Figure 1.17: Domain organisation of GpsB. The structure of GpsB from *B. subtilis* has been solved through a combination of X-ray crystallography, SAXS, and SEC-MALS on several domains (Cleverley et al., 2016). The N-terminus and C-terminus of *Bacillus subtilis* GpsB was solved by X-ray crystallography to 2.8 Å and 1.2 Å resolution, respectively. SAXS studies on the full-length protein allowed for the above model to be generated using the high-resolution structural fragments. GpsB forms a hexamer in solution in a parallel orientation. Each monomer of GpsB is assigned its own colour and the N- and C- termini are labelled. The N-terminal domain of the protein is responsible for its interactions with membrane-associated cell division proteins.

Interactions between GpsB and PBPs from a wider range of Gram-positive bacteria including *B. subtilis*, *L. monocytogenes*, and *S. pneumoniae* have since been interrogated structurally and biochemically, leading to the identification of motifs required for binding (Halbedel & Lewis, 2019; Cleverley et al., 2019; Rismondo et al., 2016). A greater mechanistic understanding of the interactions between GpsB and PBP homologs in various species has aided the identification of novel interactions between GpsB and the PG remodelling enzymes YpbE and YrrS, leading to the conclusion that GpsB acts as an adaptor protein (Cleverley et al., 2019). Recent work on GpsB from *S. aureus* suggests a novel action of GpsB in the stimulation of lateral interactions between FtsZ filaments (Eswara et al., 2018). No interactions between FtsZ and GpsB have been detected in any other species of bacteria tested and, therefore, this finding could suggest a divergent role for GpsB in *S. aureus* (Eswara et al., 2018).

1.8.4 EzrA

Negative regulation is also necessary in order to prevent aberrant Z-ring formation; EzrA is an example of such a negative regulator in Gram-positive bacteria. EzrA was first identified in *B. subtilis*, and its co-locolisation with FtsZ was first observed by fluorescence microscopy (Levin et al., 1999). EzrA has a predicted TM helix at its N-terminus to link it, and potentially its interaction partners, to the membrane. *B. subtilis* EzrA inhibits the formation of FtsZ filaments *in vitro* and *in vivo*, and complete deletion of EzrA results in an increased frequency of FtsZ ring formation (Levin et al., 1999; Land et al., 2014; Singh et al., 2007). Recent studies in *S. aureus* and *B. subtilis* have implicated EzrA in the control of PG synthesis through direct interactions with PG synthases (Claessen et al., 2008; Steele et al., 2011). EzrA has been found by bacterial two-hybrid to interact with a multitude of divisome proteins in *S. aureus*, as well as the PG synthases PBP1, 2, and 3 (Steele et al., 2011). The crystal structure of EzrA from *B. subtilis* revealed that EzrA forms antiparallel dimers forming an overall crescent shape (Cleverley et al., 2014), with each monomer made up of repeating three-helical bundles that have structural homology to the spectrin repeat fold found in eukaryotic cytoskeletal proteins. The space within the arch of the crescent is sufficient to enclose an FtsZ filament, to sterically hinder the formation of lateral interactions between filaments (Cleverley et al., 2014) (Figure 1.9).

1.9 Eukaryotic-like Ser/Thr protein kinases and divisome components

Eukaryotic-like Ser/Thr protein kinases (eSTKs) are widespread in Gram-negative and Gram-positive bacteria and appear to have multiple roles both within and between species (Manuse et al., 2016). Whilst it is outside the scope of this thesis to discuss in detail all the eSTKs present in bacteria, one well-studied member of this family of protein is thought to have significant roles in cell division regulation. Originally identified in *Mycobacterium tuberculosis* and designated PknB (Kang, 2005), homologues of this kinase present in different species of bacteria have been given alternative names specific to their species, such as PrkC in *B. subtilis* (Libby et al., 2015), Stk1 in *S. aureus* (Débarbouillé et al., 2009), StkP in *S. pneumoniae* (Nováková et al., 2005), and PrkA in *L. monocytogenes* (Lima et al., 2011). All PknB homologues are bitopic membrane proteins consisting of an N-terminal intracellular kinase domain, a single transmembrane helix, followed by several C-terminal PASTA domains (Manuse et al., 2016). In *B. subtilis*, GpsB interacts with the intracellular domain of PrkC, stimulating its activity. DivIVA and EzrA have also been identified as essential for PrkC activity, suggesting that divisome components control the activity of PrkC in *B. subtilis* (Pompeo et al., 2015). Stk1 from *S. aureus* has been implicated in several regulatory systems in this organism (Débarbouillé et al., 2009; W. Zheng et al., 2018), however, its interactions with divisome components has not yet been tested.

1.10 Antibiotics targeting cell division/PG synthesis machinery

β-lactam antibiotics inhibit the transpeptidase action of PBPs by mimicking the structure of the terminal *D*-Ala-*D*-Ala residues of the glycan-attached peptide of PG, sequestering the active site serine in a covalent adduct and rendering the transpeptidase domain of the PBPs inactive (Waxman & Strominger, 1983). The inhibition of the cell wall synthesis machinery ultimately results in the lysis of the cell due to the inability of the bacteria to generate new cell wall material to replace the parts it has degraded; this is the major cause of cell death by β-lactam antibiotics (Waxman & Strominger, 1983). Secondary mechanisms of cell death have also been observed, however, in which nonlytic cells undergo cell death as a result of futile cycles of PG precursor synthesis, for instance (Cho et al., 2014). The introduction of β-lactams ushered in a golden age of antibiotics during which many diseases previously fatal became treatable. The overuse of antibiotics, combined with the short life cycle and rapid evolution of bacteria, has resulted in the generation of antibiotic-resistant strains of bacteria which, in certain clinical scenarios, often have fatal consequences (Lobanovska & Pilla, 2017). PG homeostasis and regulation thus remain an attractive target for antibiotic drug design.

Two major mechanisms of resistance to β-lactams have arisen: first, an accumulation of mutations in PBPs renders them insensitive to β-lactams and second, enzymes capable of degrading β-lactams, the β-lactamases (Peacock & Paterson, 2015), have evolved. For instance, methicillin resistance in methicillin-resistant *S. aureus* (MRSA) is caused by the introduction of the *mecA* gene coding for PBP2a, where the active site serine is located in a pocket that is occluded from β-lactams (Peacock & Paterson, 2015). A multitude of new PBP2a-targetting antibiotics have been developed, including the cephalosporin subgroup of β-lactams, ceftobiprole, and ceftaroline (Foster, 2017). These molecules appear to target both the PBP2a active site as well as a putative allosteric site (Lovering et al., 2012; Duplessis, 2011; Otero et al., 2013), but resistance to these new drugs has already emerged (Peacock & Paterson, 2015). β-lactam resistance is also caused by the evolution of new β-lactamases, which form acyl-enzyme intermediates with β-lactams as in PBPs, however, these enzymes can break open the β-lactam ring to form products that do not inhibit PBPs (Fernandes et al., 2013). β-lactamases were present in bacteria prior to the use of antibiotics in clinical and agricultural scenarios, but they have evolved into a very efficient β-lactam resistance mechanism thanks to increased selection pressure from antibiotic overuse by mankind (Bonomo, 2017; Hall & Barlow, 2004). The somewhat unfortunately named New-Delhi metallo-β-lactamases (NDMs) are one such example of this type of evolution, NDMs were first isolated and identified from a patient with a *Klebsiella pneumoniae* infection in 2009 (Yong et al., 2009) and have since become a cause of global concern (Nicolau et al., 2015). Antibiotics targeting NDMs are now necessary to combat the rise of superbugs which harbour these enzymes, and progress is being made toward this end.

The gap between antibiotic drug discovery and the development of antimicrobial resistance is becoming shorter with each iteration. In fact, reports of penicillin resistance in *E. coli* first appeared before penicillin was in general public use (Abraham, 1940). Alternative means of disrupting cell division to fight infection are, therefore, an attractive method of sidestepping this problem and there is potential for divisome components to provide the necessary novel target. Inhibitors of divisome components have shown promising preliminary results against bacterial infections, specifically in the case of FtsZ. An inhibitor of FtsZ, PC190723, causes cell elongation in *B. subtilis*, and cell enlargement in *S. aureus*, and is effective against MRSA strains (Andreu et al., 2010). Computational ligand docking of PC190723 has identified a potential site of action at an allosteric site away from the nucleotide binding region of FtsZ (Elsen et al., 2012; Haydon et al., 2008). This is the first viable mechanism found for alternative antibiotics targeting the divisome, but with the influx of structures becoming available for several divisome components, there is much promise for antibiotics targeting cell division to be developed to take back control from the march of infectious disease.

1.11 Aims of this study

As discussed in this chapter, investigation of the divisome has chiefly been undertaken in rod-shaped bacteria, namely *B. subtilis* and *E. coli*. Despite the progress in understanding discussed here, there is a lot to learn about divisome formation and organisation not only in these bacteria but in other bacteria with different shapes, such as the spherical cocci. From a translational standpoint, a lack of structural and functional information about lesser studied members of the cell division machineries presents a stumbling block in the antimicrobial pipeline and is thus a potentially lucrative area of research. To address some of these issues, several divisome proteins from *S. aureus* were purified and characterised structurally, biophysically, and biochemically. *S. aureus* DivIVA (*Sa*DivIVA) was expressed, purified and subjected to several structural, mutational and biochemical experiments to determine not only the structure of *Sa*DivIVA but also its potential role in the divisome. *S. aureus* GpsB (*Sa*GpsB) was purified and its interactions with members of the peptidoglycan polymerisation machinery and Stk1 probed, such that comparisons may be drawn between *Sa*GpsB and the well-studied homologues described above.

Chapter 2.

Materials and methods

2.1 Materials

2.1.1 Growth media

All media were purchased from Formedium unless stated otherwise. All media were prepared following the manufacturer's instructions using distilled water (dH_2O) and were autoclaved by technical staff in the Institute for Cell and Molecular Biosciences' autoclave facility. All small-scale cultures of *E. coli* were grown in lysogeny broth (LB), Lennox formulation; LB agar plates were supplemented with 15 g/L agar prior to autoclaving. Large-scale cultures of *E. coli* for protein expression were grown in terrific broth (TB). Cultures of *B. subtilis* were plated onto nutrient agar (NA). The compositions of the media used in this study are defined in Table 2.1. Where required for plasmid selection and maintenance, growth media were supplemented with antibiotics at the working concentrations shown in Table 2.2.

Table 2.1: Composition of growth media used in this study.

Media	Formulation
Lysogeny broth (LB) (Lennox modification)	10 g/L tryptone, 5 g/L yeast extract, 5 g/L NaCl
LB Agar (Lennox)	LB-Lennox plus 15 g/L agar
Terrific broth (TB)	12 g/L tryptone, 24 g/L yeast extract, 9.4 g/L KH_2PO_4, 2.2 g/L K_2HPO_4, 0.4 % (v/v) glycerol
Nutrient agar (NA)	5 g/L peptone, 1 g/L beef extract, 2 g/L yeast extract, 5 g/L NaCl, 15 g/L agar

Table 2.2: Working concentrations of antibiotics used in this study.

Antibiotic	Working Concentration (µg/mL)	Solvent
Ampicillin	100	H_2O
Kanamycin	50	H_2O
Chloramphenicol	30	100 % (v/v) ethanol
Spectinomycin	50	H_2O

2.1.2 General chemicals

All chemicals, unless stated otherwise, were purchased from ThermoFisher Scientific or Sigma-Aldrich.

2.1.3 Buffer preparation

All Tris buffers were prepared using Tris base powder and adjusted to the relevant pH with HCl at room temperature. HEPES buffers were prepared using HEPES free acid powder and the pH was adjusted with NaOH at room temperature.

2.2 Molecular biology

All molecular biology reagents/enzymes were purchased from Thermo Scientific, Promega, or New England Biolabs, unless otherwise stated.

2.2.1 Strains and plasmids

The bacterial strains utilised in this study are shown in Table 2.3. A list of the parental plasmids used as templates for cloning in this study are shown in Table 2.4.

Table 2.3: List of *E. coli* strains used in this study.

Strain	Description	Genotype
DH5α	Host strain, used for cloning and plasmid maintenance.	F⁻ *endA1 glnV44 thi-1 recA1 relA1 gyrA96 deoR nupG purB20* φ80d*lacZ*ΔM15 Δ(*lacZYA-argF*)U169, *hsd*R17(r_K^- m_K^+), λ⁻
BL21(DE3)	Protease-deficient general protein expression strain.	F⁻ *ompT hsdS*$_B$ (r_B^- m_B^-) *gal dcm lacY1* (DE3)
Rosetta™(DE3)	BL21(DE3) derivative used to enhance the expression of proteins that contain codons rarely used in *E. coli.*	F⁻ *ompT hsdS*$_B$ (r_B^- m_B^-) *gal dcm lacY1* (DE3) pRARE (Cam^R)
Lemo21(DE3)	BL21(DE3) harbouring pLemo, for expression of toxic, insoluble, or membrane proteins by titration of *L*-rhamnose into growth media.	*fhu*A2 [lon] *ompT gal* [*dcm*] Δ*hsdS*$_B$ (DE3) pLemo (Cam^R)
C43(DE3)	Derivative of C41(DE3), used for expression of recombinant toxic proteins.	F⁻ *ompT hsdS*$_B$ (r_B^- m_B^-) *gal dcm lacY1* (DE3)

2.2.2 *E. coli* competent cell preparation

Glycerol stocks of the desired cell line were used to inoculate 10 mL of LB, plus the relevant antibiotic if necessary, and left overnight at 37 °C with shaking at 180 rpm. Following overnight incubation, 100 mL of fresh LB was inoculated with 1 mL of saturated overnight culture and incubated at 37 °C, 180 rpm until an optical density at 600 nm (OD_{600}) of ~0.4 was reached, at which point cells were placed on ice for 30 minutes. The cells were subsequently collected (4,000 ×*g*, 5 mins, 4 °C), the cell pellet was resuspended gently in 25 mL of ice cold 0.1 M $MgCl_2$ and incubated for a further 30 minutes on ice. The cells were collected as before, the pellet resuspended in 25 mL of ice cold 0.1 M $CaCl_2$ and incubated again for 30 minutes on ice. The cells were collected as above and resuspended in 1.25 mL of ice cold 85 mM $CaCl_2$, 15 % (v/v) glycerol for freezing. Competent cells were transferred at 4 °C to sterile 1.5 mL microcentrifuge tubes in 50 µL aliquots, flash frozen in liquid N_2, and stored at -80 °C until required.

Table 2.4: List of parental plasmid vectors used in this study

Plasmid	Description	Antibiotic marker	Source
pOPINRSF	Overexpression vector carrying His_6-tag followed by HRV-3C protease site upstream of multiple cloning site.	Kanamycin	Ray Owens, unpublished
pMAT-11	Overexpression vector carrying MBP followed by TEV protease site upstream of multiple cloning site.	Ampicillin	Peränen et al., 1996
pET-22b(+)	Overexpression vector with N-terminal *pelB* signal sequence upstream of multiple cloning site. Carries non-cleavable C-terminal His_6-tag downstream of multiple cloning site.	Ampicillin	Novagen
pETDuet-1	Co-expression vector designed for the co-expression of two target genes.	Ampicillin	EMD Biosciences
pMV01	Expression vector for expression of msfGFP-fusion proteins. Contains *amyE* sequences up and downstream of multiple cloning site for homologous recombination into the *B. subtilis* chromosome.	Spectinomycin & Ampicillin	Henrik Strahl, unpublished
pBAD24	Expression vector for tight control of protein expression using glucose and arabinose.	Ampicillin	Guzman et al., 1995
pET-M11	Overexpression vector containing His_6-tag followed by TEV protease site upstream of multiple cloning site.	Kanamycin	Dümmler et al., 2005

2.2.3 Transformation of *E. coli* competent cells

Competent cell aliquots of 50 µL were supplemented with either 100 ng of plasmid DNA, or 5 µL of cloning reaction, and were incubated on ice for 20 minutes. The transformation mixture was heat shocked at 42 °C for 1 minute and was immediately placed back on ice for 2 minutes for recovery. Following recovery, the transformation mixture was supplemented with 250 µL of LB and was incubated at 37 °C, 180 rpm for one hour. The entire 300 µL mixture was spread evenly onto LB agar plates supplemented with the appropriate antibiotic(s); plates were left at 37 °C overnight for transformants to grow.

2.2.4 Purification of plasmids from *E. coli*

Glycerol stocks or single colonies of *E. coli* DH5α strains harbouring the plasmid destined for purification were used to inoculate 10 mL of LB plus the relevant antibiotic. Cultures were grown overnight at 37 °C with shaking at 180 rpm, following which the cells were collected by centrifugation (5,000 ×*g* for 20 minutes at room temperature). GeneJET plasmid miniprep kits (Thermo Scientific) were used to purify plasmids from cell pellets following the manufacturer's instructions. The purified plasmid concentration was determined by absorbance, measured at 260 nm (A_{260}) using a Nanodrop™ Lite (Thermo Scientific). All plasmids were stored at -20 °C until required.

2.2.5 Polymerase chain reaction

The polymerase chain reaction (PCR) was utilised to amplify genes, fragments of genes and entire plasmids for all cloning operations described in this thesis. A typical PCR reaction mixture, and exemplar cycling parameters, is shown in Tables 2.5 and 2.6, respectively. Annealing temperatures were altered in accordance with the melting temperature (T_m) of the primers, which were calculated using the New England Biolabs T_m calculator (https://tmcalculator.neb.com/#!/main), and denaturation temperatures were altered in accordance with the manufacturer's instructions for the polymerase in use. All PCRs were performed in a T100™ thermal cycler (Bio-Rad).

Table 2.5: A representative PCR reaction.

Component	Concentration
Polymerase Buffer	1 X
Polymerase	1 Unit
Primers	500 nM each
Template DNA	100 ng
dNTPs	0.2 mM
dH_2O	to 50 µL total

Table 2.6: Cycling parameters for a representative PCR reaction.

Temp	Time (min:sec)	No. of cycles
95-98 °C	1:00	1
95-98 °C	0:30	16-30
55-72 °C	0:30	
68-72 °C	0:30 per kbp	
68-72 °C	10:00	1

2.2.6 Restriction endonuclease-based cloning

All genes of interest were amplified by PCR (Section 2.2.5) using primers with 5'-overhangs that each contained a unique restriction site. The PCR product generated was purified using the GeneJET PCR Purification Kit (ThermoFisher Scientific) following the manufacturer's instructions. Purified amplicons and destination plasmids were digested independently with their relevant restriction enzymes following the manufacturer's protocols for the specific enzymes. Following their digestion, the products were separated by agarose gel electrophoresis on a 1 % (w/v) agarose gel in TAE buffer (40 mM Tris, 20 mM acetic acid, 1 mM EDTA, pH 8.3). Bands on the agarose gel corresponding to their expected length were excised from the gel with a sterile scalpel and purified using the GeneJET PCR Purification Kit (Thermo Scientific). The digested gene of interest was ligated at a 3:1 and 7:1 molar ratio of gene of interest:digested vector, using 25 ng of the digested vector. T4 DNA ligase (Thermo Scientific) was used following the manufacturer's instructions with regards to ligation mixture and incubation temperature/time. 5 µL of the ligation mixture was immediately transformed into

E. coli DH5α (Section 2.2.3). Two control reactions were performed in parallel, one in which digested vector alone was ligated/transformed, and another in which undigested parental plasmid was transformed at the same concentration as the digested vector used in the reaction. Colonies present on the reaction plate were used to inoculate 10 mL of LB plus antibiotic and the plasmids purified (Section 2.2.4). Successful cloning reactions were initially screened using restriction digests and apparently successful clones were verified by sequencing (Eurofins). An example of a restriction digest screen is shown in Figure 2.1.

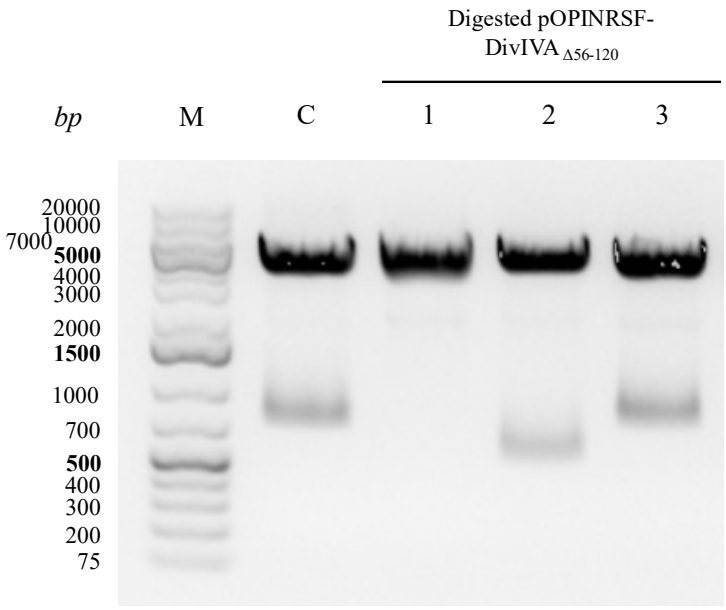

Figure 2.1: A representative example of a restriction digest screen for the presence of correct inserts. Plasmids purified from promising clones (1-3) were digested, alongside the template plasmid (C), with restriction enzymes flanking the insert (eg. *Nde*I/*Xho*I). The digestion mixes were electrophoresed on a 1 % (w/v) agarose gel. In the case of DivIVA $_{\Delta 56\text{-}120}$, shown here, a decrease in the length of the insert (~600 bp) was expected with respect to the template plasmid (~800 bp). In this case, colony 2 was confirmed by sequencing to be successful.

2.2.7 Restriction-free cloning strategy for N-terminal DivIVA truncation

Primers were designed to amplify *Sa*DivIVA$_{54\text{-}205}$, *Sa*DivIVA$_{91\text{-}205}$, and *Sa*DivIVA$_{121\text{-}205}$ from pOPINRSF-*Sa*DivIVA$_{FL}$ using the restriction-free (RF) cloning webserver (https://rf-cloning.org). Incorporation of the desired constructs into pOPINRSF by PCR and subsequent *Dpn*I digestion of parental plasmid was performed as previously described (van den Ent & Löwe, 2006). The cloning reaction was transformed into *E. coli* DH5α (Section 2.2.3), alongside the digested parent plasmid alone and undigested parent plasmid as negative and positive controls, respectively. Successful transformants were used to inoculate 10 mL of LB

plus antibiotic and grown at 37 °C for 16 hours before the plasmids were purified as described in Section 2.2.4. Purified plasmids were verified by DNA sequencing (Eurofins) before use.

2.2.8 In-Fusion™ cloning of DivIVA into pMV01

Primers were designed using the In-Fusion™ cloning tools webserver (https://www.takarabio.com/learning-centers/cloning/in-fusion-cloning-tools) to amplify *Sa*DivIVA from pOPINRSF-*Sa*DivIVA$_{FL}$, and to amplify and simultaneously linearise pMV01, generating complementary ends common to both PCR products. Following amplification, *Sa*DivIVA$_{FL}$ was ligated into linearised pMV01 and the parental plasmid *Dpn*I-digested following established protocols (Throop & Labaer, 2016). The cloning reaction was transformed into *E. coli* DH5α (Section 2.2.3); undigested parental plasmid and digested parent plasmid alone were used as controls. Plasmids were purified from successful transformants (Section 2.2.4) and verified by sequencing before use.

2.2.9 Site-directed mutagenesis

Site-directed mutagenesis (SDM) was performed using a modified version of the QuikChange (Agilent) protocol. Mutagenic primers were designed using the QuikChange primer design webserver (https://www.agilent.com/store/primerDesignProgram.jsp). PCR was performed not only to amplify the gene of interest but the remainder of the plasmid as well, to generate a large, linear DNA product consisting of the recombinant plasmid and the mutagenised gene of interest (Zheng, 2004). The successful generation of a PCR product was verified by agarose gel electrophoresis; a representative example is shown in Figure 2.2. 25 µL of methylated parental plasmid was supplemented with 1 µL of *Dpn*I (Thermo Scientific) and incubated at

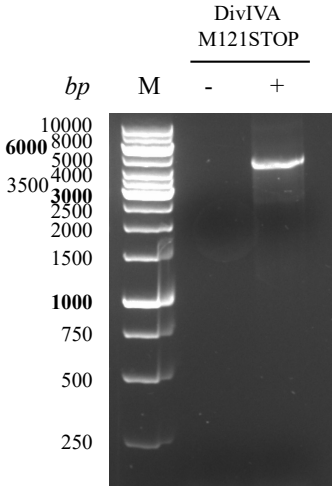

Figure 2.2: A representative agarose gel of an SDM reaction. A representative example of the product of an SDM reaction run on a 1 % (w/v) agarose gel is shown in lane +. For all SDM reactions, a reaction mixture was prepared without polymerase present as a control, this is shown in lane -.

37 °C for 2 hours, 5 µL of the digestion mixture was transformed into *E. coli* DH5α (Section 2.2.3). Mutant plasmids were verified by DNA sequencing before use.

2.2.10 Generation of MBP-fusions to *Sa*DivIVA

In the case of MBP-*Sa*DivIVA$_{FL}$, *Sa*DivIVA$_{FL}$ was amplified from pOPINRSF-*Sa*DivIVA$_{FL}$ with primers containing restriction sites appropriate for its insertion into pMAT-11 downstream of MBP and its cleavage sites (Appendix II). For MBP-*Sa*DivIVA$_{FL}$-MBP, following successful incorporation of *Sa*DivIVA$_{FL}$ into pMAT-11, a double MBP fusion was generated in which the MBP sequence was amplified from pMAT-11 with the addition of *Nco*I and *Xho*I to either end of the amplicon. Amplification of the pMAT-11-*Sa*DivIVA$_{FL}$ was then undertaken to generate a linearised plasmid with *Nco*I/*Xho*I sites corresponding to the 5'- and 3'- ends of the MBP amplicon, allowing for the restriction-based insertion of MBP onto the c-terminus of *Sa*DivIVA$_{FL}$ (Figure 2.3).

2.2.11 Preparation of glycerol stocks for *E. coli* strains

Verified strains of *E. coli* were grown overnight in LB supplemented with the appropriate antibiotic(s) at 37 °C, 180 rpm. 700 µL of saturated overnight cultures were supplemented with 300 µL of sterile 100 % (v/v) glycerol and flash-frozen in liquid nitrogen. Glycerol stocks were stored at -80 °C until needed.

2.2.12 Transformation of *B. subtilis*

B. subtilis strains intended for transformation were streaked onto fresh nutrient agar plates supplemented with appropriate antibiotics ~16 hours prior to the beginning of the transformation. Cells were scraped from the plate and used to inoculate conical flasks containing 10 mL of transformation medium (Table 2.7). Cells were grown at 37 °C for 3 hours with shaking before 10 mL of dilution medium (Table 2.7) was added to the flask and incubated for a further 2 hours. 400 µL of cells were subsequently transferred to 2 mL round-bottomed microcentrifuge tubes containing either 10 µL of plasmid DNA or 2 µL of genomic DNA and these cultures were incubated with shaking for 1 hour at 37 °C. Cells were collected (16,000 ×*g*, 1 min, room temperature) and the supernatant discarded. Cells were resuspended in ~100 µL of LB and plated onto nutrient agar supplemented with antibiotic, if necessary, and the plates were incubated at 37 °C overnight. Successful transformants were resuspended in 100 µL of LB and re-plated onto nutrient agar. To integrate DivIVA-msfGFP into the chromosome, colonies were plates onto NA plates in the presence/absence of 1 % (w/v) xylose to screen for successful transformants.

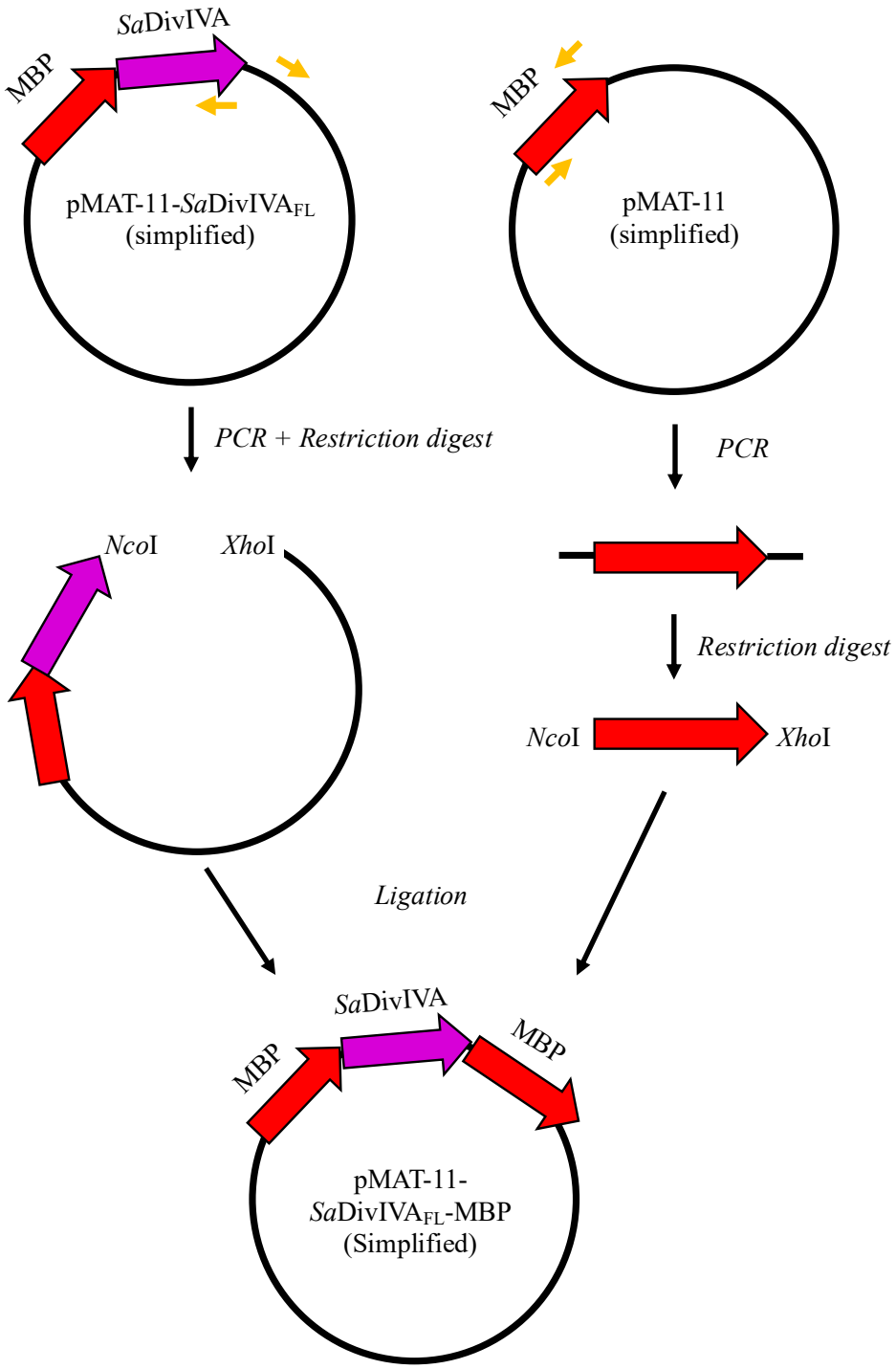

Figure 2.3: Method of construction of pMAT-11-*Sa*DivIVA$_{FL}$-MBP. Primers were designed (orange) to amplify pMAT-11-*Sa*DivIVA$_{FL}$ such that the linearised plasmid product could be digested with restriction enzymes. Simultaneously, MBP from pMAT-11 was amplified with 5' overhangs identical to those introduced to pMAT-11-*Sa*DivIVA$_{FL}$. Ligation of the two products of PCR and restriction digestion results in a plasmid with two MBP genes, in frame with *Sa*DivIVA$_{FL}$ and on either end of the *Sa*DivIVA$_{FL}$ gene.

Table 2.7: Composition of media used for transformation of *B. subtilis*.

	Transformation medium	Dilution medium
Component	Concentration	Concentration
$(NH_4)_2SO_4$	15 mM	15 mM
K_2HPO_4	80 mM	80 mM
KH_2PO_4	44 mM	44 mM
Sodium citrate	4 mM	4 mM
$MgSO_4$	8 mM	8 mM
Glucose	26 mM	26 mM
Casamino acids	0.02 % (w/v)	0 % (w/v)
Tryptophan	0.1 mM	0 mM
$(NH_4)_5[Fe(C_6H_4O_7)_2]$	2 μM	0 μM

2.3 Protein purification

2.3.1 Expression

Either a streak of colonies from freshly transformed cells, or a scraping of a glycerol stock, were used to inoculate 100 mL of LB supplemented with the appropriate antibiotic(s) and left to grow to saturation overnight at 37 °C, 180 rpm. 10 mL of saturated overnight culture was used to inoculate each litre of sterile TB media and bacteria were grown at 37 °C, 200 rpm to an OD_{600} of ~0.8. Protein expression was induced by the addition of IPTG to a final concentration of 1 mM and the cells were grown at 20 °C for ~16 hours. Cells were collected by centrifugation (4,000 ×*g* for 30 minutes at 4 °C) and cell pellets were either lysed immediately or flash-frozen in liquid N_2 and stored at -20 °C until needed.

2.3.2 Preparation of cell-free extracts for soluble proteins

Cells were resuspended in resuspension buffer (30 mM Tris.HCl pH 8, 300 mM NaCl), supplemented with a few crystals of bovine pancreas DNAse I (Roche) and one cOmplete™ EDTA-free protease inhibitor cocktail tablet (Roche) per 50 mL of cell suspension. Cells were lysed by single passage through a cell disruptor (Constant Systems) at 20 kpsi. Insoluble

material was separated from soluble material by centrifugation at 30,000 ×*g* for 30 minutes at 4 °C. Samples were taken of both the soluble and insoluble material for analysis by sodium dodecyl sulphate-polyacrylamide gel electrophoresis (SDS-PAGE) (Section 2.3.9).

2.3.3 Immobilised metal affinity chromatography

Cell-free extracts were applied at 1 ml.min^{-1} to a 5 ml HisTrap FF column (GE Healthcare) attached to an ÄKTAprime FPLC system. After loading, the column was washed with Immobilised Metal Affinity Chromatography (IMAC) buffer A (50 mM Tris.HCl pH 8, 500 mM NaCl, 20 mM imidazole) at 5 ml.min^{-1} until the A_{280} returned to baseline. Bound proteins were eluted in step gradients of IMAC buffer B (50 mM Tris.HCl pH 8, 500 mM NaCl, 800 mM imidazole). A representative example of an IMA chromatogram is shown in Figure 2.4.

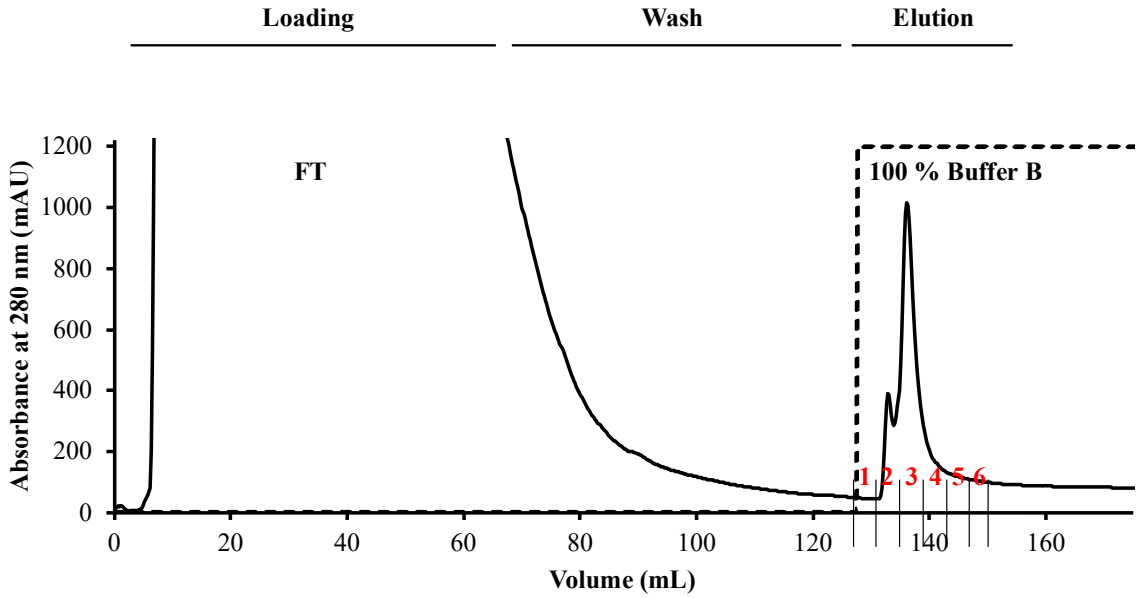

Figure 2.4: A representative chromatogram from an IMAC purification step. Cell-free extract was loaded onto the HisTrap FF column at 1 mL.min^{-1} and the flow-through (FT) from the column collected (Loading). Once all of the cell-free extract was loaded onto the column, the column was washed with IMAC buffer A until the A_{280} returned to baseline (Wash). Following the wash, IMAC buffer B was passed over the column and the eluted protein collected into 4 mL fractions (Elution).

2.3.4 Cleavage of recombinant tags

Proteins were mixed at a 1:50 (w:w) ratio of protease to recombinant protein, and the cleavage mixture was dialysed ~100-fold at 4 °C overnight into 25 mM Tris.HCl pH 8, 150 mM NaCl, 1 mM DTT. Following overnight cleavage, the mixture was re-applied to the HisTrap column and the flow-through and eluent collected in batch to perform a reverse-IMAC. Pre-cleavage samples were analysed alongside flow-through and eluent from the reverse-IMAC step on

SDS-PAGE (Section 2.3.9) to verify successful cleavage (Figure 2.5). If successful, flow-through from the second IMAC purification was concentrated for further purification.

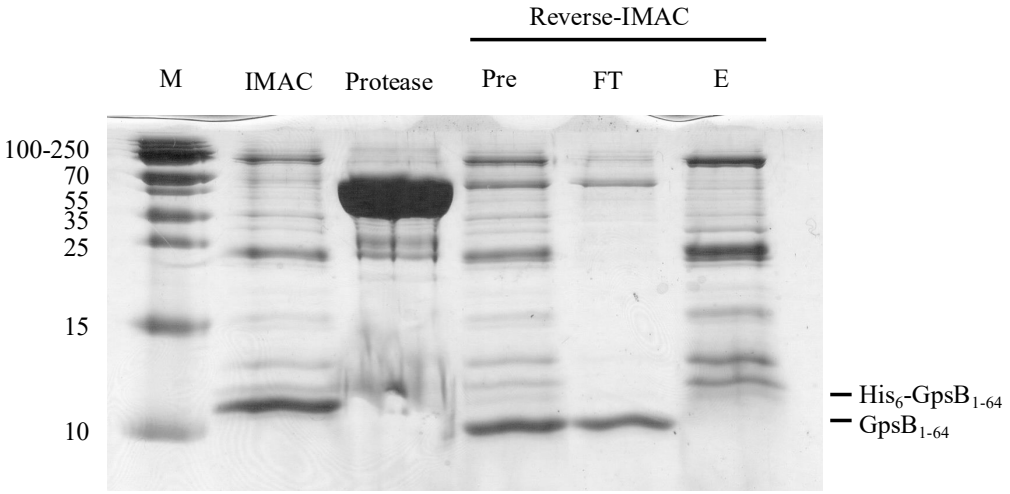

Figure 2.5: A representative example of cleavage & reverse-IMAC. The cleavage step for $GpsB_{1-64}$ is shown as a representative example of cleavage and reverse-IMAC as a purification step. Here all samples have been loaded onto a 17 % Tris-Tricine SDS-PAGE system. Following elution from IMAC, the elution is dialysed and cleaved with the relevant protease overnight. After overnight incubation with the protease, the cleavage mixture (Pre) was loaded onto the IMAC column for the second time and the cleaved protein with no His_6-tag passes through the column (FT). Any uncleaved material and IMAC contaminants were retained on the column and elute as usual (E).

2.3.5 Ion-exchange chromatography

Proteins were either dialysed into ion-exchange chromatography (IEX) buffer A (25 mM HEPES.NaOH pH 7.5) overnight or diluted in IEX buffer A such that the final concentration of NaCl was less than 50 mM. Following NaCl dilution, proteins were loaded onto at 1 $ml.min^{-1}$ a 5 mL HiTrap Q (GE Healthcare) attached to an ÄKTAprime FPLC system. The column was washed with IEX buffer A until the A_{280} returned to baseline. Proteins were eluted from the column by a gradient of 0 - 100 % IEX buffer B (25 mM HEPES.NaOH pH 7.5, 1 M NaCl) over a volume of 100 mL.

2.3.6 Preparative size-exclusion chromatography

Following their respective penultimate purification step, protein samples were concentrated by ultrafiltration using Amicon Ultra-15 concentrators (Millipore) at a molecular weight cut-off several kDa smaller than the target. Protein samples were injected at volumes ≤5 mL onto HiLoad 16/60 prep grade columns (GE Healthcare) packed either with Superdex 75 or 200 resin, depending on the molecular weight of the protein of interest and desired resolution. Columns were attached to ÄKTApurifier FPLC systems and run at a constant flow rate of 1

ml.min^{-1}. Protein was collected from the column in 2 mL fractions and elution was monitored at A_{280} nm. Final purity of target proteins was assessed by SDS-PAGE (Section 2.3.9).

2.3.7 Sodium dodecyl sulphate-polyacrylamide gel electrophoresis

Glycine-sodium dodecyl sulphate-polyacrylamide gel electrophoresis (SDS-PAGE) gels of different percentages were constructed using a Mini-PROTEAN® Tetra Cell (Bio-Rad). The components of stacking and resolving gels are listed in Table 2.8. Analytes were mixed with 6x SDS loading dye and heated to 100 °C for 2 minutes immediately prior to loading. Proteins were electrophoresed at 150 V for 45 minutes. Gels were stained using Coomassie blue for 1 h and de-stained in 20 % (v/v) ethanol, 10 % (v/v) acetic acid. For proteins with molecular weights smaller than 30 kDa, a Tricine-SDS-PAGE gel system was utilised, and the procedure for making and running the gels performed as previously described (Schägger, 2006).

Table 2.8: Standard recipe for SDS-PAGE gels used in this study.

	Resolving gel	**Stacking gel**
Component	Concentration	Concentration
Acrylamide/bis-acrylamide, 19:1	10-15 %	6 %
Tris-HCl, pH 8.8	0.375 M	0 M
Tris-HCl, pH 6.8	0 M	0.125 M
SDS	0.1 % (w/v)	0.1 % (w/v)
Ammonium persulphate	0.1 % (w/v)	0.1 % (w/v)
TEMED	0.1 % (v/v)	0.1 % (v/v)

2.3.8 Determination of protein concentration by absorbance at 280 nm (A_{280})

In the majority of cases, protein concentration was determined by A_{280}. Concentrated pure protein was diluted in the same buffer used for purification and A_{280} measured using a Nanodrop™ Lite spectrophotometer (Thermo Scientific) such that the absorbance reading was within the accurate range of the instrument (0.08 – 2 absorbance units). Protein concentration was calculated using sequence-derived extinction coefficients calculated with the ProtParam webserver (https://web.expasy.org/protparam/).

2.3.9 Determination of protein concentration by bicinchoninic acid assay

In cases where determination of protein concentration by A_{280} was rendered unreliable by the lack of any tryptophan or tyrosine residues, protein concentrations were determined using the bicinchoninic acid (BCA) Protein Assay Kit (Pierce™). BCA assays were performed in

microplates following the manufacturer's standard protocol and the concentrations determined by comparison to a standard curve prepared in parallel using known concentrations of bovine serum albumin (BSA). A representative standard curve used to calculate protein concentration is shown in Figure 2.6.

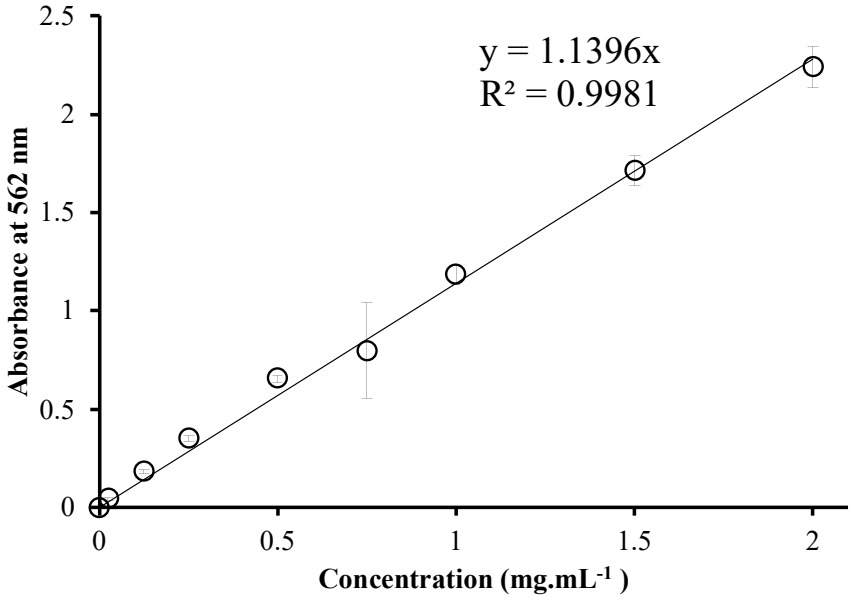

Figure 2.6: A representative BCA standard curve. Known concentrations of BSA were subjected to a BCA assay alongside target proteins in order to generate a standard curve from which the unknown concentrations of protein could be estimated. The equation used to calculate protein concentration is shown as well as the R^2 measure of the fit of the data to the trendline.

2.3.10 Generation of liposomes

Lipids were dissolved at 10 mg.ml^{-1} in chloroform and incubated at 37 °C until homogeneous. Chloroform was evaporated overnight in a vacuum chamber, ensuring the removal of all solvent. The mass of the resultant lipid cake was quantified, and the lipid cake resuspended in PBS buffer to 10 mg.mL^{-1}. The suspension was incubated in a sonicating water bath for 10 minutes, or until homogenised. The resuspended lipid cake was then sonicated using a probe sonicator with 1 second pulses for 10 minutes on ice to generate multilamellar vesicles. Liposomes were stored at -20 °C until required.

2.4 Characterisation of protein samples

2.4.1 Native-polyacrylamide gel electrophoresis

Samples for native-polyacrylamide gel electrophoresis (native-PAGE) analysis were mixed with 5x native-PAGE sample buffer (65 mM Tris.HCl pH 8.5, 20 % (v/v) glycerol, 0.01 % (w/v) bromophenol blue) and loaded onto a 10 % acrylamide gel. Native-PAGE gels were prepared as for SDS-PAGE (Section 2.3.9), but in the complete absence of SDS. Gels were electrophoresed at 150 V for 2 hours, or until the dye front reached the bottom of the gel. Gels were stained and de-stained as for SDS-PAGE (Section 2.3.9)

2.4.2 Circular dichroism

Concentrated proteins were diluted to 10 µM in dH_2O or sodium phosphate buffer and circular dichroism (CD) spectrum measurements performed in a JASCO J8-10 spectropolarimeter, with a 1 mm pathlength quartz cuvette (Hellma Analytics). Samples were scanned from 190 nm to 260 nm at 10 $nm.min^{-1}$ with a bandwidth of 2 nm and a response time of 8 seconds. 10 CD scans were performed per sample at 20 °C and the runs averaged. A buffer spectrum run in the same cuvette on the same day was subtracted from the protein spectrum for analysis. For thermal melts, samples were denatured either from 4 °C or 20 °C to 90 °C at a rate of 2 °C per minute and the CD signal was monitored at 222 nm. CD spectra were analysed using the BeStSel webserver (http://bestsel.elte.hu/index.php) or using the DichroWeb webserver (http://dichroweb.cryst.bbk.ac.uk/html/home.shtml), using the CDSSTR analysis programme.

2.4.3 Analytical size-exclusion chromatography

Samples were injected at 100-500 µL onto a Superdex 200 increase 10/300 GL (GE Healthcare) attached to an ÄKTApurifier FPLC system. Samples were analysed at a flow rate of 0.75 $mL.min^{-1}$. Protein elution was monitored by absorbance at 280 nm and if necessary, fractions of 500 µL were collected for analysis by SDS/native-PAGE.

2.4.4 Size exclusion chromatography-coupled multi angle light scattering

Size exclusion chromatography-coupled multi angle light scattering (SEC-MALS) samples were loaded at 0.5 $mL.min^{-1}$ onto a Superdex 200 increase 10/300 GL column equilibrated in 20 mM Tris.HCl pH 8, 150 mM KCl, 1 mM DTT attached to an ÄKTA Pure (GE Healthcare). The eluent from the size-exclusion column was passed through a DAWN Heleos II EOS 18-angle laser photometer and an Optilab® T-rEX™ differential refractometer (Wyatt

Technology). Light scattering, differential refractive index data were analysed, and the molecular weights calculated using ASTRA® 6 (Wyatt Technology).

2.4.5 Size exclusion chromatography-coupled small angle X-ray scattering

All size exclusion chromatography-coupled small angle X-ray scattering (SEC-SAXS) experiments were performed at Diamond Light Source (Oxfordshire, UK) on beamline B21. Samples were applied onto a Superdex 200 increase 10/300 GL column equilibrated in 20 mM Tris.HCl pH 8.0, 150 mM KCl, 1 mM DTT and the eluent passed through the experimental cell. SAXS data were recorded at 12.4 keV over 3 second frames at a detector distance of 4.014 m.

2.4.6 One-dimensional processing of SAXS data

Retention time was plotted as a function of scattering intensity in ScÅtter (BIOISIS) and CHROMIXS (Panjkovich & Svergun, 2018) and monodisperse regions of the elution profile were identified by use of the Rg estimation tool present in both software packages. Subtraction of the average scattering profile of buffer from that of the protein was performed independently in ScÅtter and CHROMIXS, generating plots of average sample scattering intensity (I(Q)) against scattering vector (Q). To ensure there were no major differences in the subtraction of buffer scattering from sample, the scattering curves generated in both programs were compared against each other using DATCMP (ATSAS) and found to be identical with a χ^2 of 1. All subsequent scattering curves generated in this thesis were generated by buffer subtraction in ScÅtter.

2.4.7 Dummy atom modelling

Twenty independent rounds of DAMMIF (Franke & Svergun, 2009) were performed to generate twenty dummy-atom models that fit the scattering data with a range of χ^2 values. Dummy-atom models were compared in DAMSEL, and those with a normalised spatial discrepancy (NSD) greater than the average NSD + 2σ were discarded. Dummy atom models were superimposed in DAMSUP, averaged in DAMAVER , and low-frequency dummy atoms removed in DAMFILT (Franke & Svergun, 2009). For refinement, a DAMSTART file was generated from DAMMIF runs and used for refinement in DAMMIN (Svergun, 1999) following the same procedure as with DAMMIF, ultimately generating a dummy-atom model of the most-likely solution structure from the scattering data. Molecular envelopes were generated in UCSF Chimera using its inbuilt molmap command.

2.4.8 Lysine methylation of *Sa*DivIVA$_{1-120}$

The lysines in *Sa*DivIVA$_{1-120}$ were methylated using the JBS Methylation Kit (Jena Biosciences) following the manufacturer's instructions. A sample of pre-methylation and post-methylation *Sa*DivIVA$_{1-120}$ was analysed by intact protein mass spectrometry (Simon Thorpe, University of Sheffield) and the number of methylated lysines determined from the difference in masses.

2.4.9 Crystallisation screening and data collection

Proteins were concentrated to above 10 mg.mL^{-1} and screened using a Mosquito (TTP Labtech) against a range of commercially available crystallisation screens (PACT, JCSG+, Morpheus, INDEX, MPD Suite) (Gorrec, 2009; Newman et al., 2005) using the sitting-drop vapour diffusion method. 96-well MRC crystallisation plates (Molecular Dimensions) were used for all initial screens, with drop ratios of 1:1 and 2:1 of protein:reservoir per condition. Where required, optimisations of any crystal hits were performed using the hanging drop vapour diffusion method in 24-well Linbro plates (Molecular Dimensions) plates. Crystallisation trials were routinely incubated at 20 °C, however, for *Sa*DivIVA$_{1-120}$, crystallisation trials were also incubated at 4 °C. Any hits were screened for diffraction in-house using a gallium liquid METALJET™ X-ray generator equipped with a Photon II detector (Bruker AXS GmbH). Two images were collected during screening, at relative phi angles of 0 ° and 90 °, to allow for indexing of the reciprocal lattice. Full datasets from the best diffracting samples were collected at Diamond Light Source (Oxfordshire). The specific experimental parameters used during data collection are described in their relevant chapters.

2.4.10 Structure solution and refinement

Diffraction data were routinely indexed and integrated in DIALS (Beilsten-Edmands et al., 2020), and scaled and merged in AIMLESS (Evans & Murshudov, 2013). Initial phases were approximated in PHASER (McCoy et al., 2007). Model building was performed automatically in ccp4build (Winn et al., 2011) or buccaneer (Cowtan, 2006), after which rounds of refinement were performed in Coot (Emsley & Cowtan, 2004) and REFMAC5 (Murshudov et al., 2011) until refinement reached convergence. Validation of the model was performed in MolProbity (Williams et al., 2018) and Coot. The precise strategy used for each protein is described in their respective chapters.

2.5 Biochemical techniques

2.5.1 Isothermal titration calorimetry

All ITC experiments were carried out in a MicroCal iTC200 (Malvern Panalytical). Samples were buffer exchanged into ITC buffer (25 mM HEPES pH 7.5, 150 mM NaCl) with a PD MiniTrap G-25 (GE Healthcare) immediately prior to analysis. 20 samples of 2 µL were titrated into a cell volume of 200 µL. Samples were stirred at 750 rpm and the cell kept at a temperature of 20 °C throughout. Data was analysed and binding constants determined using the MicroCal PEAQ ITC Analysis software (Malvern Panalytical) using a 1:1 binding model.

2.5.2 Surface plasmon resonance

Surface plasmon resonance (SPR) experiments were performed in a Biacore X-100 (GE Healthcare) with a running buffer of 25 mM HEPES.NaOH pH 7.5, 150 mM NaCl. Proteins were immobilised onto a NTA chip (GE Healthcare) pre-charged with a 1-minute pulse of 0.5 mM $NiCl_2$ onto both flow cells. His_6-tagged ligand was passed over the experimental flow cell during capture for 1 minute at 10 µL.min^{-1}. The analyte was passed over both flow cells at 30 µL.min^{-1} and the response from the reference cell subtracted from the experimental cell to assess whether non-specific binding to the chip surface had occurred. Data were analysed and fit to binding models using the Biacore evaluation software (GE Healthcare) and the K_D and error calculated.

2.5.3 Microscale thermophoresis

Microscale thermophoresis (MST) experiments were performed in a Monolith NT.115 (NanoTemper GmbH, Germany). Experiments were performed by preparing serial dilutions of unlabelled protein against constant concentrations of fluorescently labelled peptide/protein in premium capillaries. Where applicable, proteins were labelled with either Monolith NT Protein Labelling Kit BLUE-NHS or Monolith NT His-tag Labelling Kit RED-tris-NTA following the manufacturer's instructions. 20 % LED power was used to measure fluorescence and MST powers of 40-80 % were used for the temperature gradient. Binding was measured by monitoring changes in normalised fluorescence following the introduction of the local temperature gradient in the capillary. Data were analysed and fit to binding models using the MO.Affinity Analysis software and the K_D and error calculated.

2.5.4 Fluorescence polarisation

Fluorescence polarisation (FP) experiments were performed in 10 mM Tris.HCl, 250 mM NaCl, 0.1 % Triton X-100. Serial dilutions of unlabelled protein were prepared against a constant concentration of fluorescently labelled peptide (20 nM). Binding experiments were prepared in triplicate in a 386-well plate and fluorescence polarisation monitored in a PHERAstar FS (BMG Labtech). The excitation wavelength was 485 nm, and fluorescence emission was recorded above 520 nm. To calculate K_{DS}, the data were fit to a 1:1 non-linear regression model in SigmaPlot 14 using the Hill equation:

$$P = P_{min} + P_{\max.}\left(\frac{[Protein]}{K_D + [Protein]}\right)$$

2.5.5 Phosphorylation reactions

Phosphorylation reactions were performed at a kinase concentration of 3.7 μM with the substrate protein at 37 μM. The phosphorylation reaction was initiated by addition of 5 mM ATP and 5 mM $MgCl_2$. Proteins were phosphorylated in a buffer of 10 mM HEPES pH 7.5. Phosphorylation mixtures were incubated at 37 °C for 30 minutes and analysed by native PAGE (Section 2.4.1) or mass spectrometry (Simon Thorpe, University of Sheffield).

2.6 Microscopy

2.6.1 Fluorescence microscopy experiments

E. coli DH5α strains harbouring the relevant plasmids were grown overnight in 3 mL of LB supplemented with the relevant antibiotic(s). Overnight cultures were diluted 1:100 into fresh LB plus antibiotic and grown to an OD_{600} of ~0.2/3. Cultures were induced with 0.2 % (w/v) arabinose and incubated for 5 minutes; induction was ceased by the addition of 0.4 % (w/v) glucose. Strains of *B. subtilis* intended for microscopy experiments were grown overnight at 30 °C. Overnight cultures were diluted 1:100 into fresh LB containing 0.1 % (w/v) glucose and incubated at 37 °C until the OD_{600} of the culture reached ~0.2, cultures were induced with 0.03 % (w/v) xylose and immediately stained. Membranes were stained with 2 μg/ml FM5-95 (Molecular Probes) for 5 minutes immediately prior to microscopy experiments. Samples were immobilized on microscope slides covered with a 1.2% agarose film and imaged immediately. Fluorescence microscopy was carried out using a Zeiss Axiovert 200M equipped with a Nikon

Eclipse Ti system with a CFI Plan Apochromat DM 100x oil objective, an Intensilight HG 130 W lamp, a C11440-22CU Hamamatsu ORCA camera, and NIS elements software, version 4.20.01. Images were analysed using Fiji (Schindelin et al., 2012).

2.6.2 Negative-stain electron microscopy

Protein samples for analysis at a range of concentrations from 0.01 – 1 mg.mL^{-1} were deposited onto glow-discharged 300 mesh carbon-coated copper grids and excess liquid wicked off with filter paper. The grids were washed with distilled water and blotted with filter paper three times before staining with 0.2% uranyl acetate, blotting and air-drying. Grids were visualised in a Hitachi HT7800 120kV TEM and the images analysed using Fiji (Schindelin et al., 2012).

Chapter 3.

Characterisation of *S. aureus* DivIVA by integrative structural and biochemical methods.

3.1 Background and aims

As mentioned in Section 1.8.2, DivIVA is a protein with divergent roles in those bacteria that encode it. The majority of the published work on DivIVA has come from *B. subtilis*, where it has been shown that DivIVA is attracted to regions of membrane curvature in the cell, acting as a topological marker and coordinating septal placement through interactions with members of the Min system (Strahl & Hamoen, 2012; Lenarcic et al., 2009; Jamroškovič et al., 2012; Booth & Lewis, 2019). All of the structural work to-date performed on DivIVA has also come from *B. subtilis*, where a high-resolution structure of the N-terminus, and a low-resolution structure of the C-terminus have been solved by X-ray crystallography, allowing for the generation of a model of the full-length protein (Oliva et al., 2010). Comparatively very little is known about *S. aureus* DivIVA, aside from an understanding that the deletion of *divIVA* has no immediately obvious phenotypic effect on cell division (Pinho & Errington, 2004).

The work presented in this Chapter attempts to address the deficit of information available regarding *Sa*DivIVA. Integrative structural studies are applied to *Sa*DivIVA to confirm the structural model proposed for *Bs*DivIVA is also applicable to *Sa*DivIVA. *Sa*DivIVA is fragmented into various truncated forms in an attempt to understand the significance of the different regions of the protein for structure and function. The interaction of *Sa*DivIVA with liposomes and other cell division proteins is explored, and the localisation of *Sa*DivIVA *in vivo* is explored.

3.2 Expression and purification of *Sa*DivIVA constructs

All recombinant plasmids were verified by sequencing before use. Plasmid vectors containing *Sa*DivIVA constructs were transformed into *E. coli* Rosetta(DE3) for expression (Section 2.2.3). Cell-free extracts containing full-length *Sa*DivIVA (*Sa*DivIVA$_{FL}$) were purified in two steps by IMAC and gel filtration (Sections 2.3.1 – 2.3.3, 2.3.6). Cleavage of *Sa*DivIVA$_{FL}$'s His_6-tag was attempted on several occasions with differing ratios of protease:*Sa*DivIVA$_{FL}$, however, on no occasion did cleavage go to completion, and separation of uncleaved and cleaved proteins was not possible, rendering cleavage of the His_6-tag non-viable. A representative size-exclusion chromatogram and associated SDS-PAGE analysis, the final step in the purification of *Sa*DivIVA$_{FL}$, is shown in Figure 3.1. All proteins presented in this chapter

were purified following the same strategy, unless stated otherwise, and purity was verified as ≥95 % pure by SDS-PAGE in all cases before any further analysis.

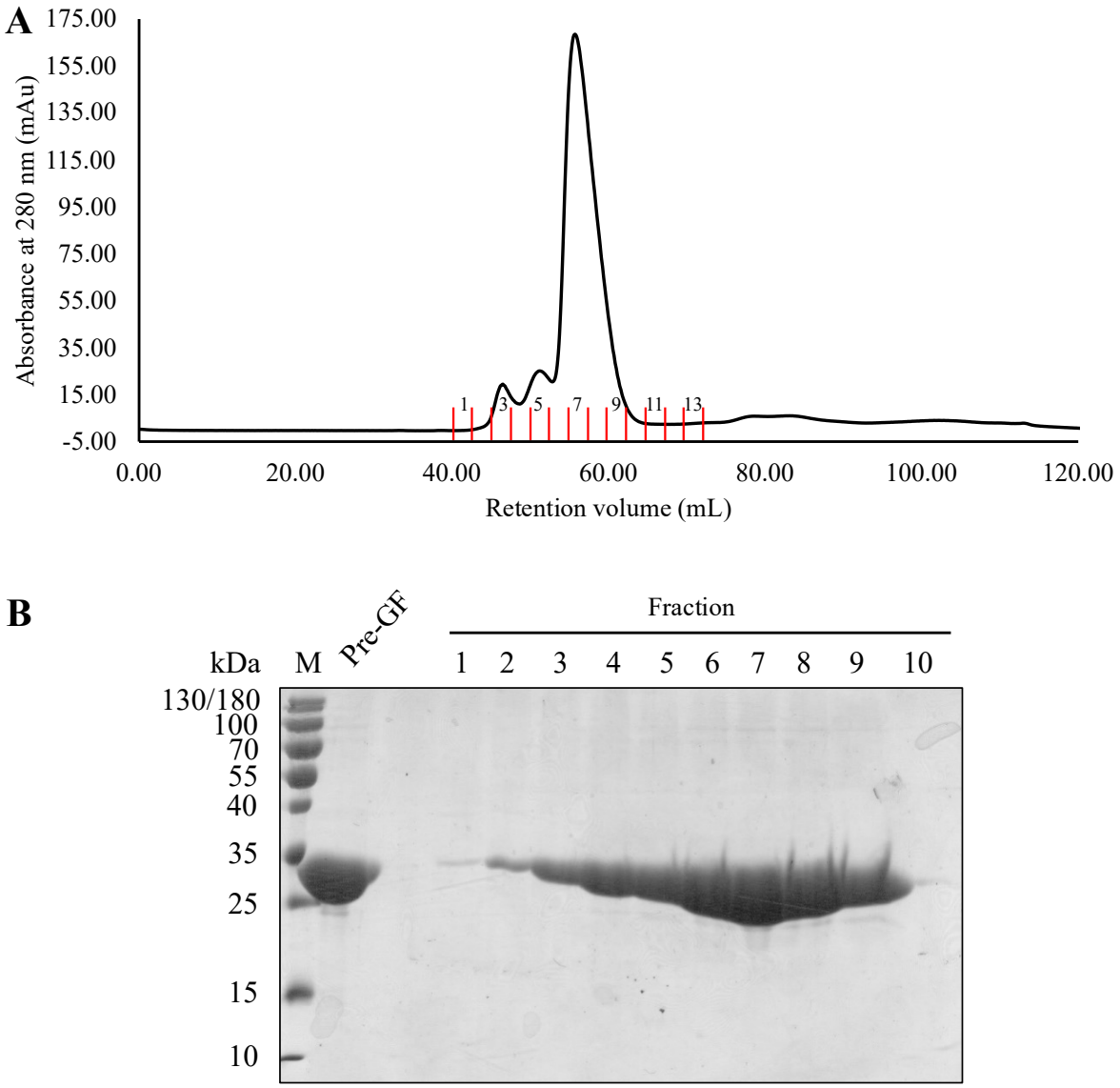

Figure 3.1: Representative purification of *Sa*DivIVA$_{FL}$. A) A typical gel filtration chromatogram of *Sa*DivIVA$_{FL}$ loaded onto a HiLoad Superdex 200 16/60 pg. **B)** A representative SDS-PAGE of *Sa*DivIVA$_{FL}$, the major band on the gel is *Sa*DivIVA (M_w = 25.3 kDa). Based on these data, fractions 6-9 were pooled and concentrated.

3.3 Secondary structure analysis of *Sa*DivIVA$_{FL}$

Circular dichroism (CD) was performed (Section 2.4.2) on *Sa*DivIVA$_{FL}$ to ensure that the predicted helical nature of the protein was preserved following purification. *Sa*DivIVA$_{FL}$ has a CD spectrum typical of a protein with a large proportion of alpha-helical secondary structure (Figure 3.2). Fitting of the CD data using the BeStSel server (Micsonai et al., 2015) (Figure 3.2) resulted in an alpha-helical percentage of 72.7 %. Secondary structure prediction in

XtalPred (Slabinski et al., 2007) using the sequence of *Sa*DivIVA resulted in an alpha helical content estimate of 79 %. The secondary structure prediction of *Sa*DivIVA$_{FL}$, coupled with the secondary structure of its homologue from *B. subtilis*, appears to confirm that *Sa*DivIVA$_{FL}$ is folded as expected *in vitro*.

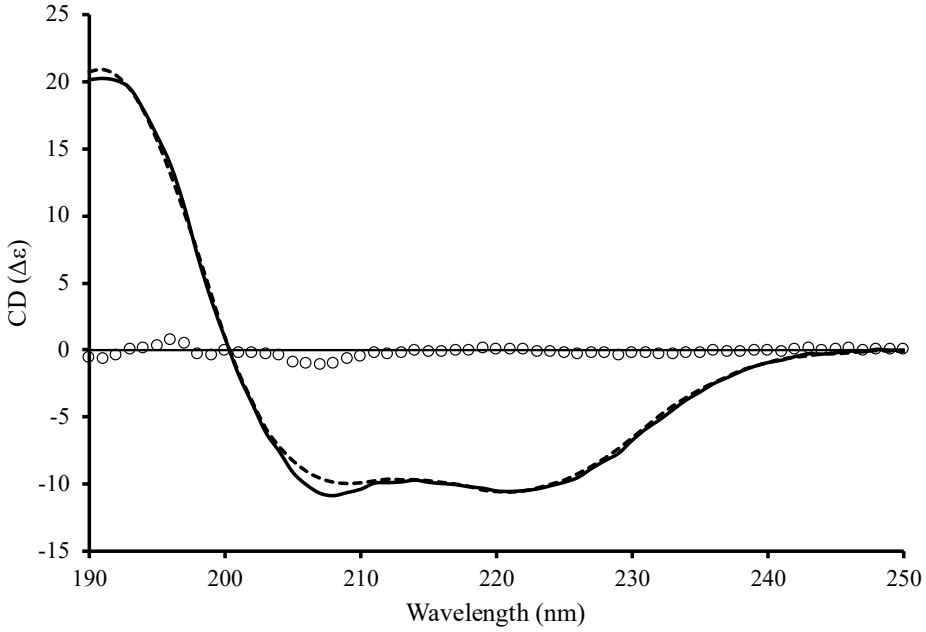

Figure 3.2: CD spectrum of *Sa*DivIVA$_{FL}$. The experimental CD spectrum is plotted as a solid black line, the CD spectrum fit by BeStSel is plotted as a dashed line. The residuals between the experimental and fitted data are plotted as black circles.

3.4 Solution characteristics and molecular envelope of full-length *Sa*DivIVA

Purified *Sa*DivIVA$_{FL}$ was analysed by SEC-MALS (Section 2.4.4). *Sa*DivIVA$_{FL}$ eluted from SEC-MALS as a monodisperse species at an apparent molecular weight (M_w^{app}) of ~113 kDa (Figure 3.3). Monomers of full-length *Sa*DivIVA are 25.3 kDa, rendering full-length *Sa*DivIVA a tetramer in solution. To probe the solution structure further, *Sa*DivIVA$_{FL}$ was analysed by SEC-SAXS (Section 2.4.5). Retention time was plotted as a function of scattering intensity in ScÅtter (BIOISIS) and CHROMIXS (Panjkovich & Svergun, 2018) and monodisperse regions of the elution profile were identified by use of the R_g estimation tool present in both software packages. Subtraction of the average scattering profile of buffer from that of protein was performed independently in ScÅtter and CHROMIXS, generating plots of average sample scattering intensity (I(Q)) against scattering vector (Q). To ensure there were no major differences in the subtraction of buffer scattering from sample, the scattering curves

generated in both programs were compared against each other using DATCMP (Petoukhov et al., 2012) and found to be identical with a χ^2 of 1 (not shown). All subsequent scattering curves presented in this chapter were generated by buffer subtraction in ScÅtter.

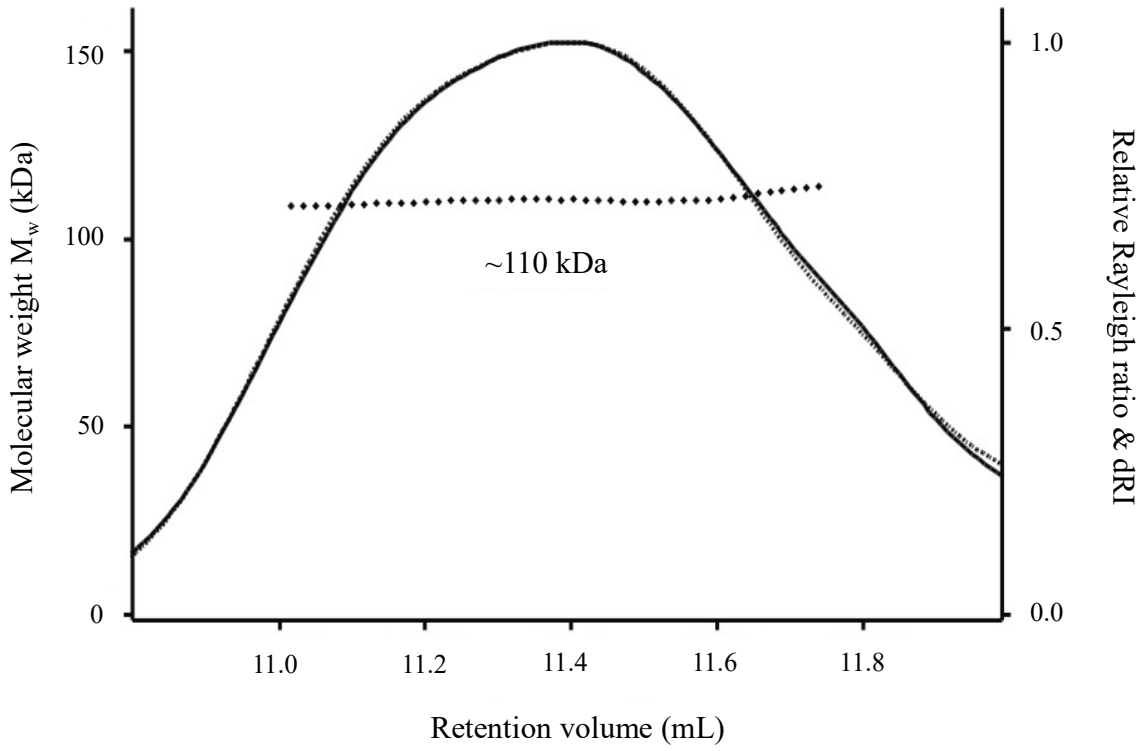

Figure 3.3: SEC-MALS analysis of *Sa*DivIVA$_{FL}$. *Sa*DivIVA eluted from SEC-MALS with a M_w^{app} of ~110 kDa, a tetramer made up of 25 kDa monomers. The molecular weight calculated from MALS is shown as diamonds across the elution.

A summary of the structural parameters calculated from direct reciprocal analysis of the SAXS data are presented in Table 3.1, and a graphical summary of the analyses shown in Figure 3.4; the analyses and statistics presented in this chapter conform to current best practices in the field of macromolecular SAXS (Jacques et al., 2012). The disparity between the radius of gyration (R_g) and cross-sectional radii (R_c) values calculated from the SAXS data suggest that *Sa*DivIVA$_{FL}$ is elongated or rod-like, having a thin cross-section compared to its total size. The presence of two distinct linear regions in the plot of ln (I(Q)×Q) vs Q^2 (Figure 3.5a) is indicative of two regions within the particle with differing cross-sectional radii (Table 3.1). The Porod exponent for *Sa*DivIVA$_{FL}$ sits directly between that of a highly compact/globular (Porod exponent of 4), and entirely flexible/random-coil (Porod exponent of 2) protein, consistent with that of an elongated molecule. Kratky analysis of the scattering data (Figure 3.4f) does not fit

expected trends for either globular or completely unfolded proteins, indicating that the particle is elongated, flexible, or has multiple domains.

Table 3.1: A summary of the structural parameters calculated from the SAXS data collected for $SaDivIVA_{FL}$

	$SaDivIVA_{FL}$
Reciprocal space analysis	
I(0) (cm^{-1})	0.322
R_g (Å)	90.4
qR_g max	1.06
R_c	
Q^2-range used ($Å^{-2}$)	$3.0\times10^{-4} - 6.0\times10^{-4}$
R_c (Å)	34.5
Q^2-range used ($Å^{-2}$)	$2.3\times10^{-3} - 3.1\times10^{-3}$
R_c (Å)	14.8
Porod exponent (P^x)	2.8
Real space analysis	
I(0) (cm^{-1})	0.322
R_g	90.8
D_{max} (Å)	300
Q-range used for fitting ($Å^{-1}$)	0.0057 – 0.3373
χ^2	1.493

The distance distribution (P(r)) of *Sa*$DivIVA_{FL}$ was generated by performing an indirect Fourier transform of the scattering data in GNOM, aided by predictions of maximum particle dimension (D_{max}) using ScÅtter, Bayesapp and DATGNOM (Petoukhov et al., 2007). Modelling the P(r) curve with a D_{max} of 300 Å results in the best fit to the scattering data, with a χ^2 value close to 1, as well as a good agreement between the structural parameters calculated in reciprocal and real space (Table 3.1). The P(r) distribution is one of a rod-like particle, in that the global maximum of the P(r) distribution is skewed towards smaller interatomic distances and slopes downwards from its apex to D_{max}. This contrasts with typical P(r) distributions of globular proteins, which follow Gaussian distributions. Of interest in the P(r) distribution of *Sa*$DivIVA_{FL}$ is the local maximum present at 150 Å, the presence of which is not explained by the reciprocal space analysis of the data (Figure 3.4c).

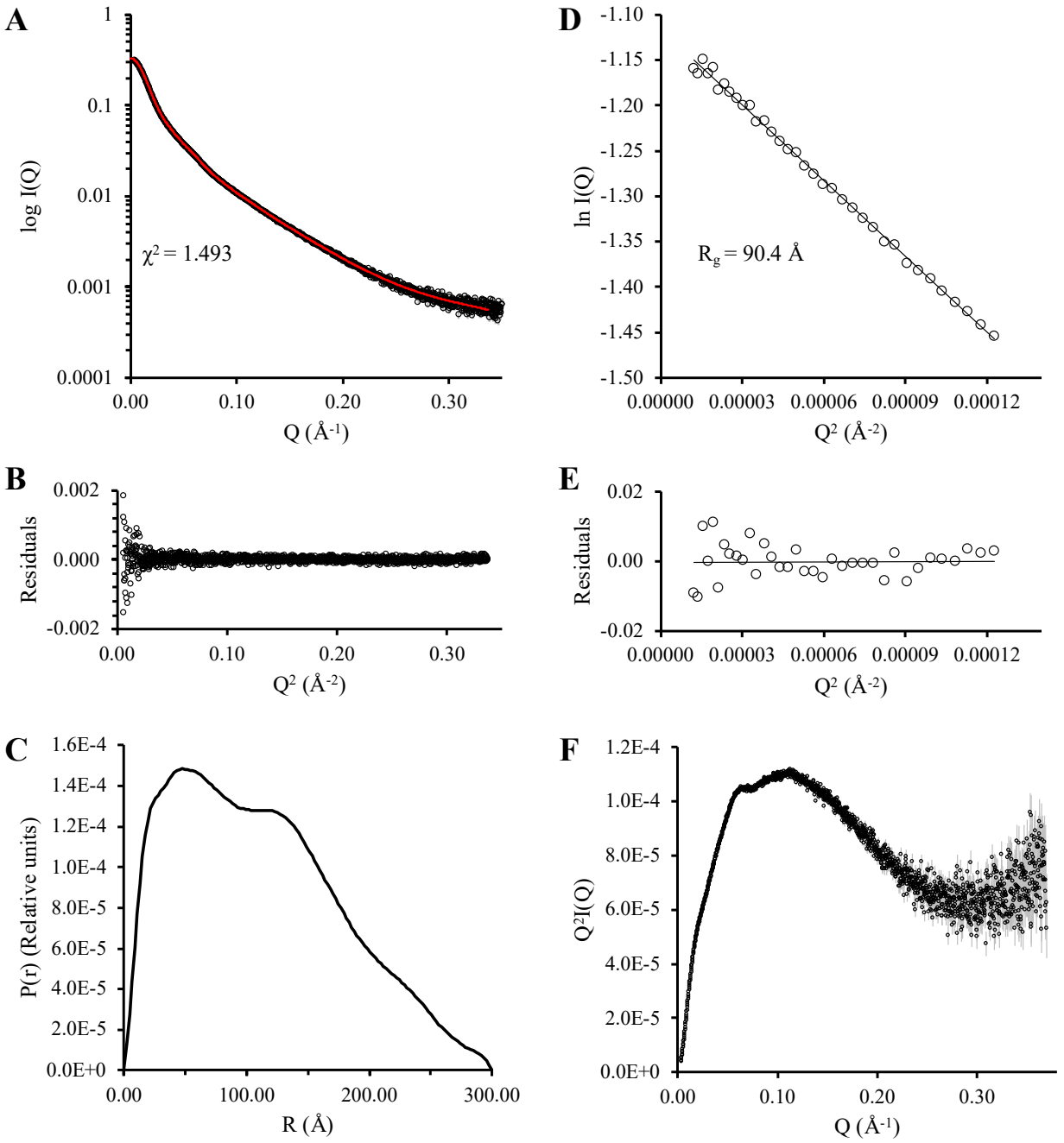

Figure 3.4: SAXS analysis of *Sa*DivIVA$_{FL}$. A) The buffer-subtracted scattering data calculated for *Sa*DivIVA$_{FL}$ is shown as black circles with error bars as grey lines. The calculated scattering curve generated from the Fourier transform of the P(r) distribution shown in C is plotted as a red line. The χ^2 evaluated from the fit between the calculated scattering curve and the experimental curve demonstrates the quality of this model of the P(r). **B)** Residual plot of the fit between the calculated scattering curve and the experimental scattering curve plotted in A. **C)** P(r) distribution calculated in GNOM from the scattering curve shown in A. **D)** Guinier plot of *Sa*DivIVA$_{FL}$ highlighting the range of data used to calculate R_g. **E)** Residual plot of the fit of the data to the trendline used to calculate R_g from the scattering data. **F)** Kratky plot of the data showing the rod-like/multi-domain nature of *Sa*DivIVA$_{FL}$.

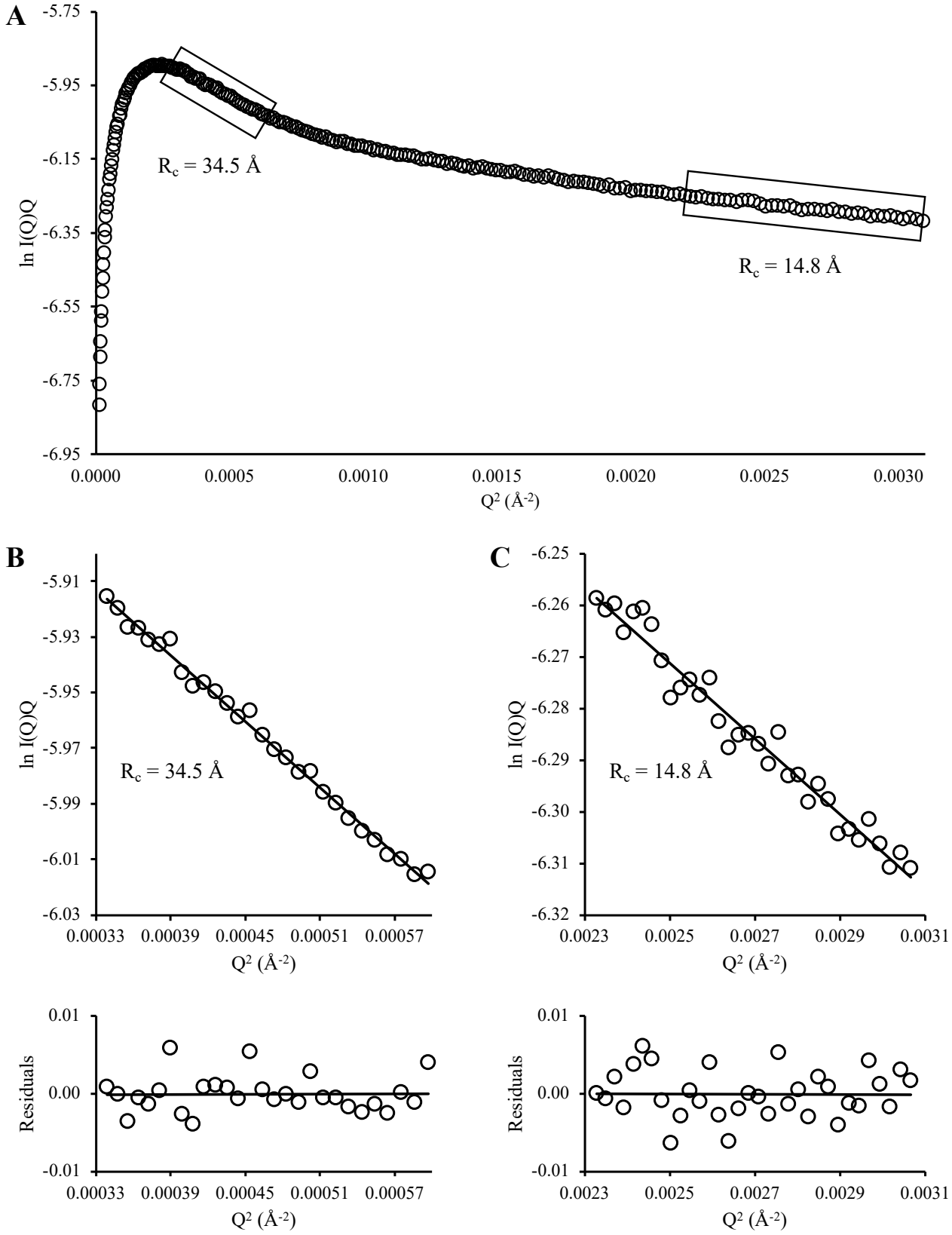

Figure 3.5: Determination of the two cross-sectional radii for *Sa*DivIVA$_{FL}$. A) Modified Guinier plot of the SAXS data presented in Figure 3.4a used to calculate R_c for elongated particles. The two distinct linear regions of the plot are enclosed within black boxes. **B)** The range of data used to determine the R_c for the first linear region with the corresponding residual plot of the fit. **C)** Determination of the R_c for the second linear region with its corresponding residual plot.

To gain a three-dimensional insight into particle shape, dummy-atom modelling was performed with the scattering data (Section 2.4.7), the parameters and statistics for this can be found in Table 3.2. The molecular envelope generated for *Sa*DivIVA$_{FL}$ is that of an elongated particle, with a ~100° bow at the centre of its major axis (Figure 3.6). The local maximum present at ~150 Å in the P(r) curve of *Sa*DivIVA$_{FL}$ is rationalised by the wishbone-like envelope; the distances between the kink at the centre of the molecule and the extremities of the molecule fall roughly within 150 Å, rationalising the increase in probability for this interatomic distance in the P(r). The molecular envelope generated is not dissimilar to the model of *Bs*DivIVA with the small exception that the magnitude of the kink is more pronounced in the *Sa*DivIVA$_{FL}$ envelope and as such, the high-resolution structural fragments of *Bs*DivIVA can be fit *a priori* into the molecular envelope of *Sa*DivIVA$_{FL}$.

Table 3.2: Parameters and statistics for the generation of the dummy-atom model of SaDivIVA$_{FL}$

	SaDivIVA$_{FL}$
DAMMIF (default parameters, 10 calculations)	
Q-range used for fitting (Å^{-1})	0.0057 – 0.337
Symmetry, anisotropy assumptions	P1, none
NSD (standard deviation)	0.987 (0.053)
χ^2 range	2.384 – 3.554
DAMMIN (default parameters)	
Q-range used for fitting (Å^{-1})	0.0057 – 0.337
Symmetry, anisotropy assumptions	P1, none
χ^2	1.131

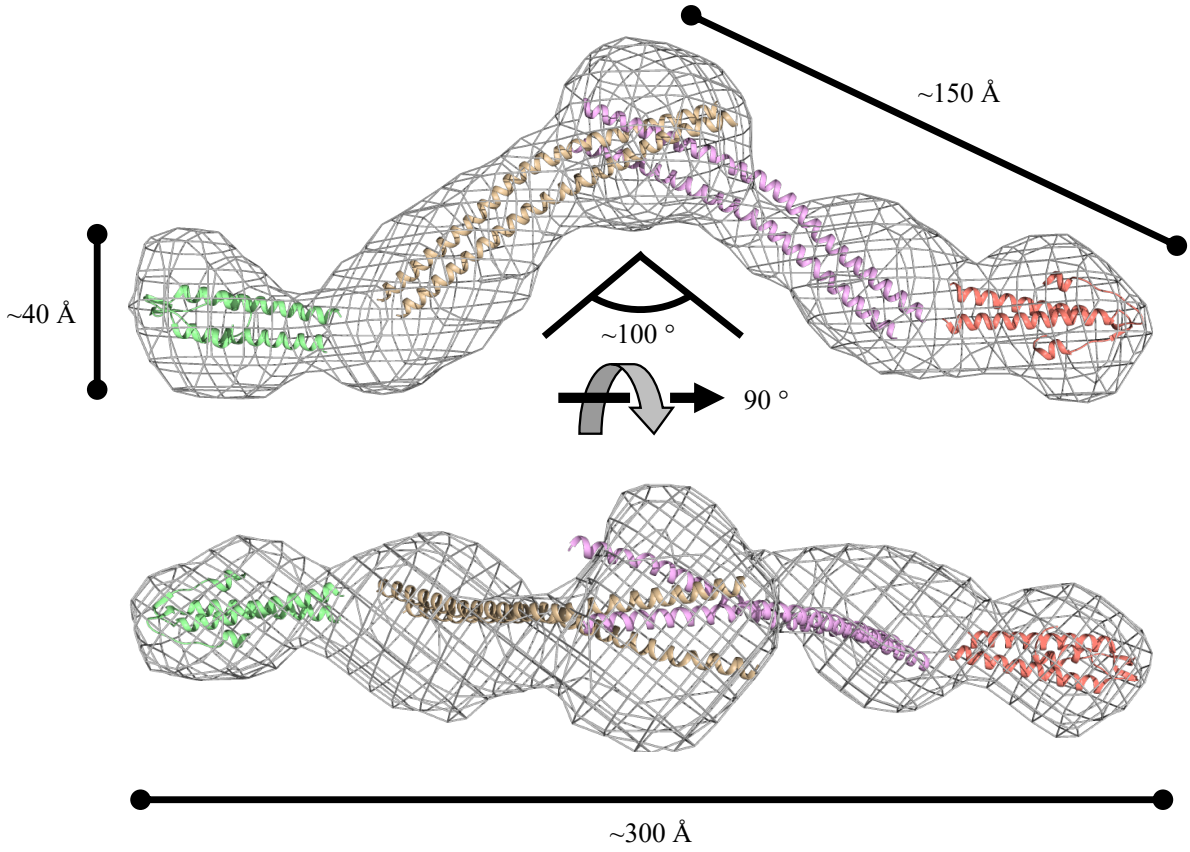

Figure 3.6: The molecular envelope of *Sa*DivIVA$_{FL}$. The low-resolution molecular envelope of *Sa*DivIVA is represented as a wire mesh. Into the mesh, the crystal structures of the fragments of *Bs*DivIVA from Oliva et al., 2010 (40.24 % sequence identify to *Sa*DivIVA across all residues) have been manually docked *a priori*. Rough distances between dummy atoms were calculated in PyMOL and correspond to structural features observed in the P(r) distribution of this molecule.

3.5 Probing the oligomerisation model of *Sa*DivIVA biophysically

3.5.1 C-terminal truncations of *Sa*DivIVA

As an initial test of the solution model of *Sa*DivIVA (Figure 3.6), truncations from the C-terminus of *Sa*DivIVA were generated by the introduction of stop codons into the pOPINRSF-*Sa*DivIVA plasmid (Section 2.2.9). Truncations were chosen by sequence alignment of *Sa*DivIVA against *Bs*DivIVA (Figure 3.7); as *Bs*DivIVA is the protein from which the model of tetramerisation is derived, it provides a good approximation of the domain boundaries relevant to tetramerisation. The low resolution structure of the C-terminal fragment of *Bs*DivIVA (Oliva et al., 2010) was also used alongside the sequence alignments as a rough guide for generating the truncation mutants. Three truncation mutants were generated, *Sa*DivIVA$_{1\text{-}120}$, *Sa*DivIVA$_{1\text{-}165}$, and *Sa*DivIVA$_{1\text{-}187}$ to probe the C-terminal tetramerisation domain, with the hypothesis that removal of some or all of this domain would result in the breakdown of the tetrameric oligomer based on the model of tetramerisation at the C-terminus.

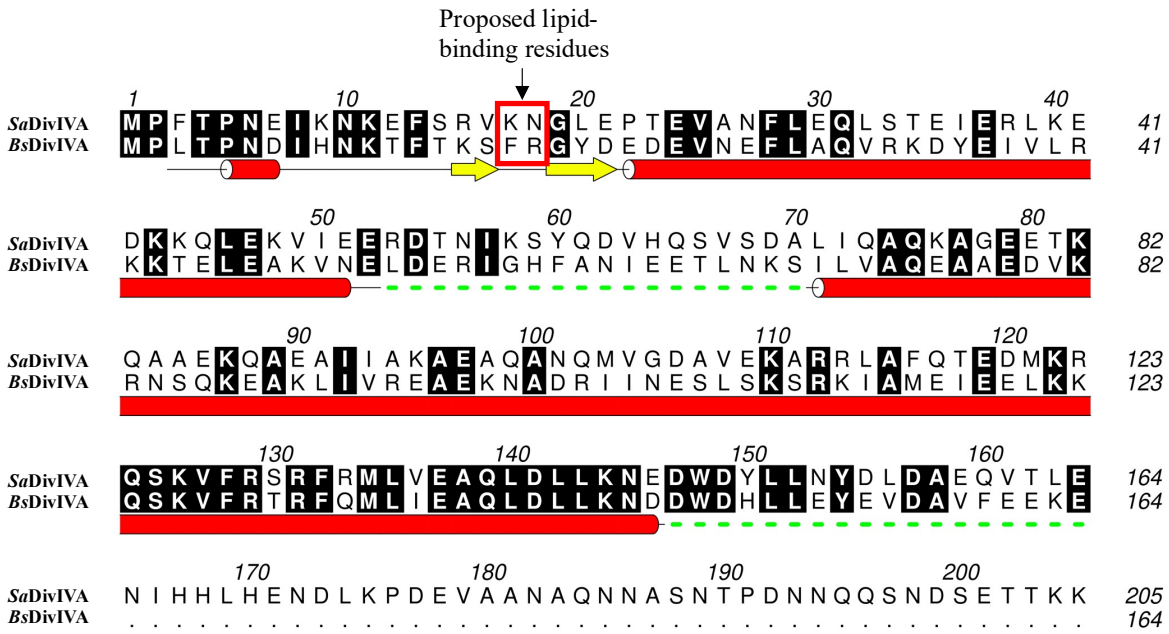

Figure 3.7: Sequence alignment of *Sa*DivIVA against *Bs*DivIVA. The sequences of *Sa*DivIVA and *Bs*DivIVA were aligned in ClustalOmega (Sievers et al., 2011) and identical residues highlighted in black using ALINE (Bond et al., 2009). Experimentally determined secondary structure from the crystal structures of *Bs*DivIVA is shown below the sequence of *Bs*DivIVA, where red cylinders represent alpha-helices, yellow arrows represent beta strands, black lines represent loops, and green dashed lines represent regions of unknown structure. A region of significant sequence identity (62.75 %) is seen between residues 110 and 164 of the two proteins. The sequence identity between *Bs*DivIVA and *Sa*DivIVA across all residues is 40.24 %.

To test this hypothesis, SEC-MALS was first performed on the *Sa*DivIVA truncations, as above with *Sa*DivIVA$_{FL}$. SEC-MALS analysis of *Sa*DivIVA$_{1\text{-}165}$ and *Sa*DivIVA$_{1\text{-}187}$ revealed a decrease in M_w^{app} as the proteins eluted from the column (Figures 3.8a and 3.8b). This is indicative of a dissociation of oligomers with dilution over the column, likely a result of decreased stability of the tetramer in solution. As it is a requirement for the determination of structural information by SAXS that the sample exists in a monodisperse state, the acquisition of any structural information on these constructs by SAXS is not possible, and these constructs were abandoned as a consequence. *Sa*DivIVA$_{1\text{-}120}$ eluted on SEC-MALS as a monodisperse species with a M_w^{app} corresponding to a dimer (Figure 3.8c), allowing for the further study of this construct by SAXS.

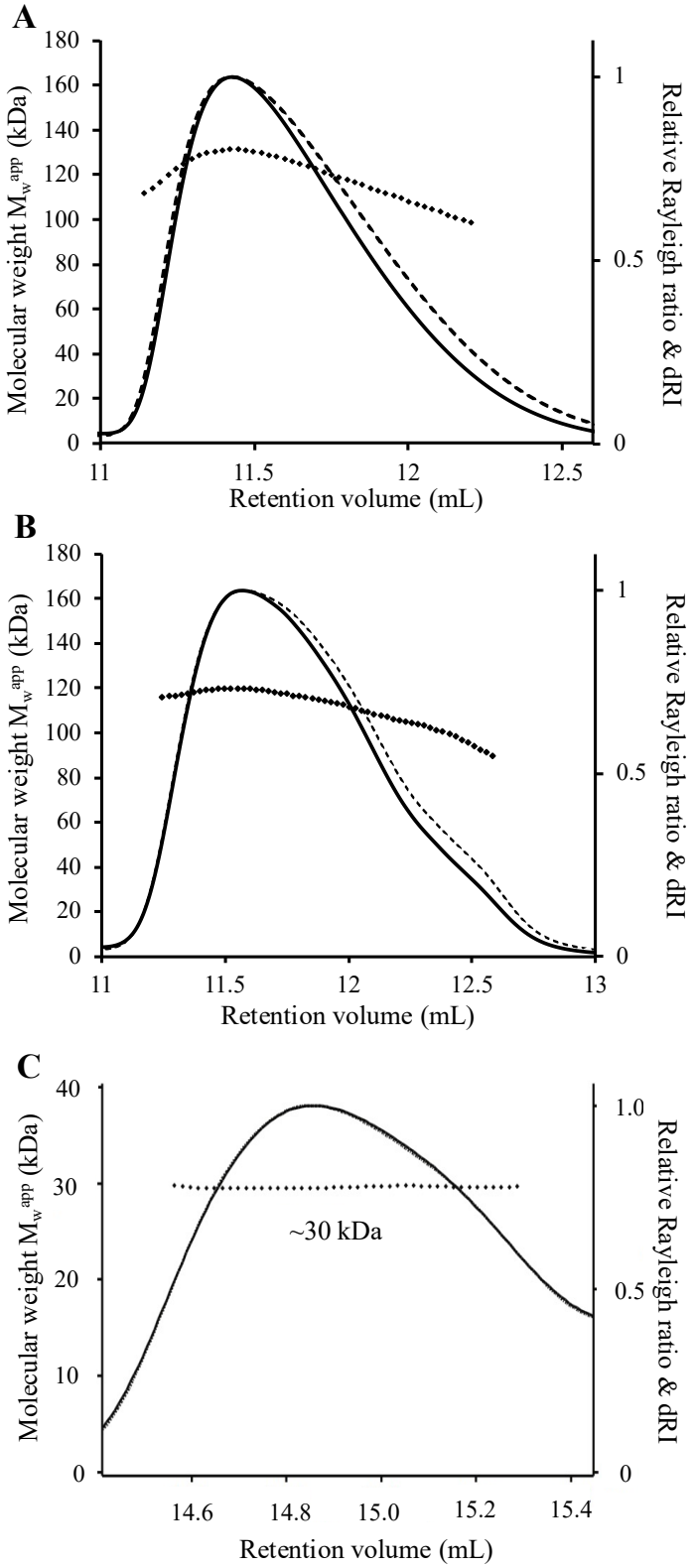

Figure 3.8: SEC-MALS analysis of *Sa*DivIVA $_{1\text{-}187}$, *Sa*DivIVA $_{1\text{-}165}$, and *Sa*DivIVA $_{1\text{-}120}$. A) SEC-MALS analysis of *Sa*DivIVA $_{1\text{-}187}$. The sloping of the M_w calculated from MALS indicates polydispersity in the sample. **B)** SEC-MALS profile of *Sa*DivIVA $_{1\text{-}165}$. A similar dissociation of species across the elution is seen as for *Sa*DivIVA $_{1\text{-}187}$. **C)** SEC-MALS profile of *Sa*DivIVA $_{1\text{-}120}$. A single species is present at a M_w^{app} of ~30 kDa, representative of a dimer of 15 kDa monomers.

SEC-SAXS analysis was performed on *Sa*DivIVA$_{1-120}$ and the data processed following the same procedure for *Sa*DivIVA$_{FL}$. The structural parameters calculated from the SAXS data are shown in Table 3.3, and the scattering data are presented graphically in Figure 3.9. The same disparity between R_g and R_c is present in this protein as in *Sa*DivIVA$_{FL}$, consistent with a rod-like particle. In contrast to *Sa*DivIVA$_{FL}$, a single R_c is present in this construct, corresponding to the lesser of the two R_c values calculated for *Sa*DivIVA$_{FL}$ (Figure 3.10). This similarity likely indicates that residues 1-120 of *Sa*DivIVA comprise the thinner region of the full-length protein, which aligns well with the dimeric state of the construct by SEC-MALS, confirming that *Sa*DivIVA$_{1-120}$ forms a thinner dimeric coiled-coil like structure. The Kratky plot of *Sa*DivIVA$_{1-120}$ is similar to *Sa*DivIVA$_{FL}$ in that the sample does not conform to profiles for globular or completely unfolded proteins (Figure 3.9f), a feature that is corroborated by the Porod exponent of this construct (Table 3.3). The P(r) distribution is statistically best modelled with a D_{max} of 150 Å and is typical of an ideal rod in solution (Figure 3.9c)

Table 3.3: Structural parameters calculated from the SAXS data for *Sa*DivIVA$_{1-120}$

	SaDivIVA$_{1-120}$
Reciprocal space analysis	
I(0) (cm^{-1})	0.135
R_g (Å)	43.4
qR_g max	0.87
R_c	
Q^2-range used ($Å^{-2}$)	$1.6\times10^{-3} - 2.3\times10^{-3}$
R_c (Å)	16.0
Porod exponent (P^x)	2.9
Real space analysis	
I(0) (cm^{-1})	0.140
R_g (Å)	44.89
D_{max} (Å)	150
Q-range used for fitting ($Å^{-1}$)	0.0035 – 0.3373
χ^2	1.56

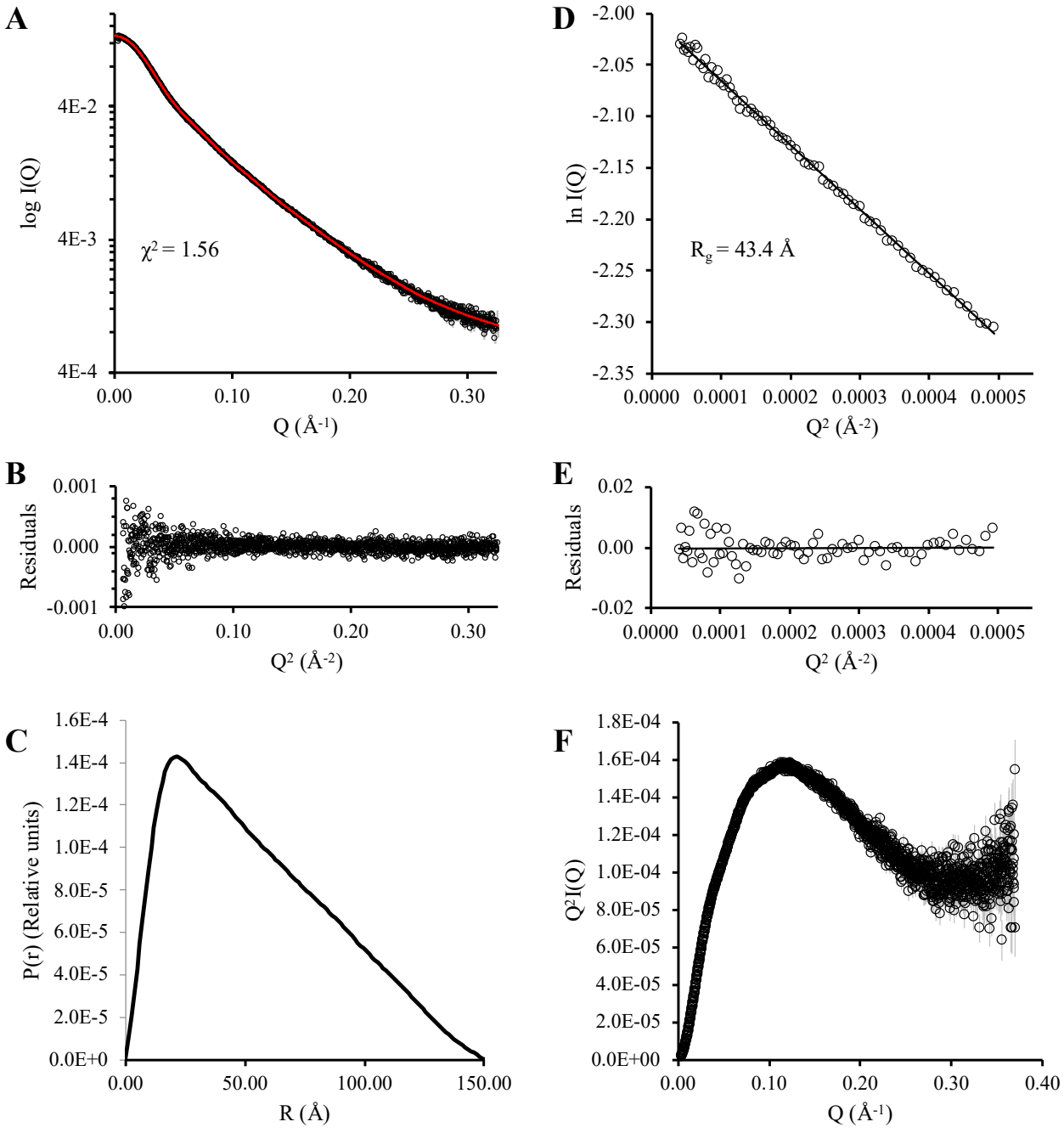

Figure 3.9: SAXS analysis of *Sa*DivIVA $_{1\text{-}120}$. A) The subtracted scattering data for *Sa*DivIVA $_{1\text{-}120}$ calculated in ScÅtter are shown as black circles, error bars are shown in grey. The calculated scattering curve generated from the Fourier transform of the P(r) distribution shown in C is plotted in red. **B)** Residual plot of the fit of the calculated scattering curve to the experimental scattering curve. **C)** P(r) distribution calculated from the indirect Fourier transform of the scattering data in ScÅtter. **D)** Guinier plot of *Sa*DivIVA $_{1\text{-}120}$ highlighting the range of data used to calculate R_g. **E)** Residual plot of the estimation of R_g from the scattering data. **F)** Kratky plot of the data showing the elongated nature of *Sa*DivIVA $_{1\text{-}120}$, error bars are shown in grey.

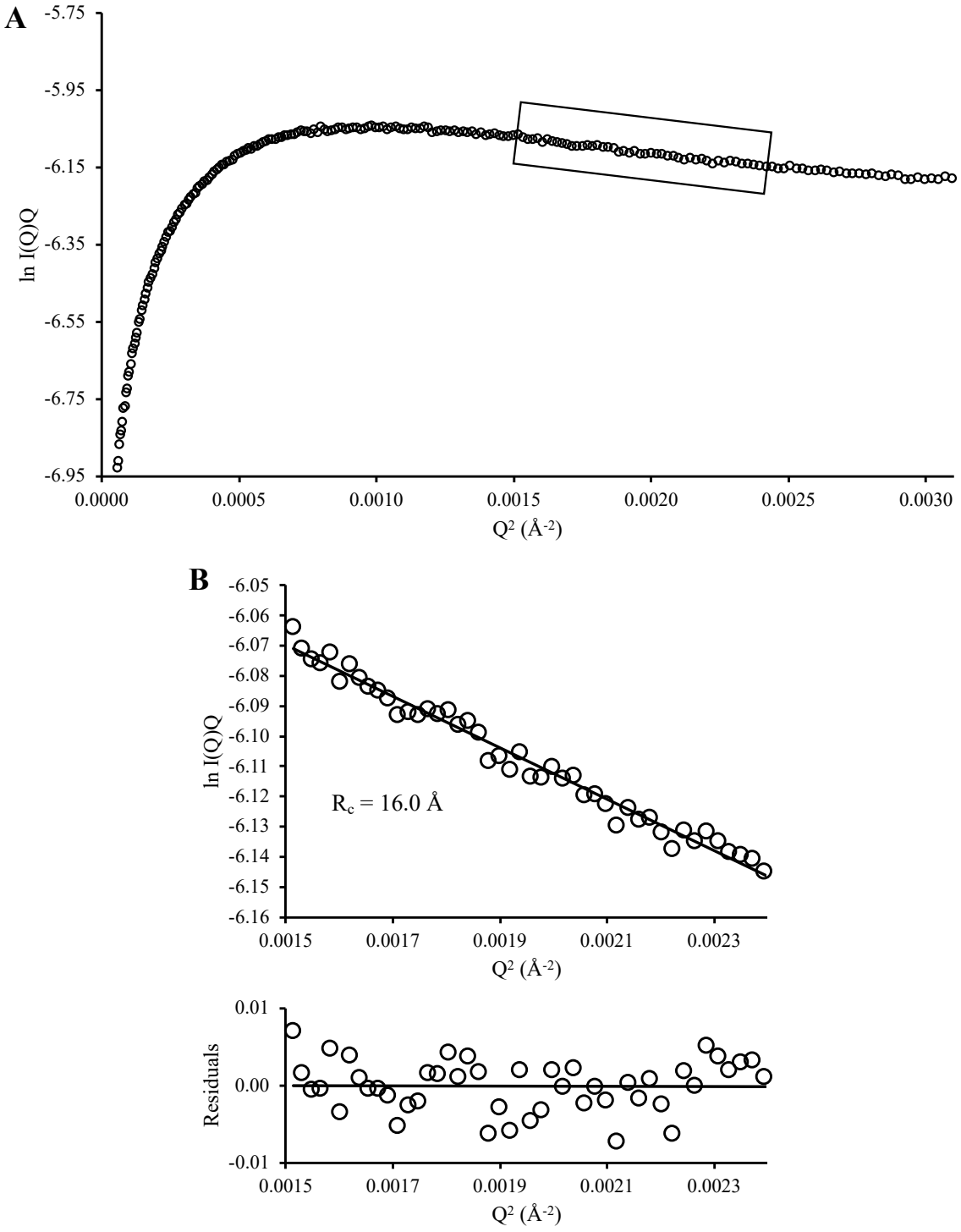

Figure 3.10: Determination of the cross-sectional radius of *Sa*DivIVA$_{1\text{-}120}$. A) Modified Guinier plot of *Sa*DivIVA$_{1\text{-}120}$ used to calculate R_c. The two distinct linear regions seen for *Sa*DivIVA$_{FL}$ are not observed for *Sa*DivIVA$_{1\text{-}120}$, indicating the presence of a single R_c value for this construct. The range of data used for the analysis is enclosed within a black box. **B)** The fit to the data used for the determination of the R_c with its corresponding residual plot.

Dummy atom modelling of the SAXS data and calculation of the molecular envelope was performed as for *Sa*DivIVA$_{FL}$ and the parameters and statistics for the modelling are presented in Table 3.4. Manual docking of the molecular envelope of SaDivIVA$_{1\text{-}120}$ *a priori* into the

dummy-atom model of *Sa*DivIVA$_{FL}$ fits with the model of tetramerisation at the C-terminus of *Sa*DivIVA (Figure 3.11). The larger R_c value seen for *Sa*DivIVA$_{FL}$, but absent from *Sa*DivIVA$_{1-120}$, is therefore likely to comprise the tetrameric region of *Sa*DivIVA$_{FL}$.

Table 3.4: Parameters and statistics for the dummy atom modelling of *Sa*DivIVA$_{1-120}$

	SaDivIVA$_{1-120}$
DAMMIF (default parameters, 10 calculations)	
Q-range used for fitting (Å^{-1})	0.0057 – 0.337
Symmetry, anisotropy assumptions	P1, none
NSD (standard deviation)	0.812 (0.022)
χ^2 range	1.234 – 1.663
DAMMIN (default parameters)	
Q-range used for fitting (Å^{-1})	0.0057 – 0.337
Symmetry, anisotropy assumptions	P1, none
χ^2	1.622

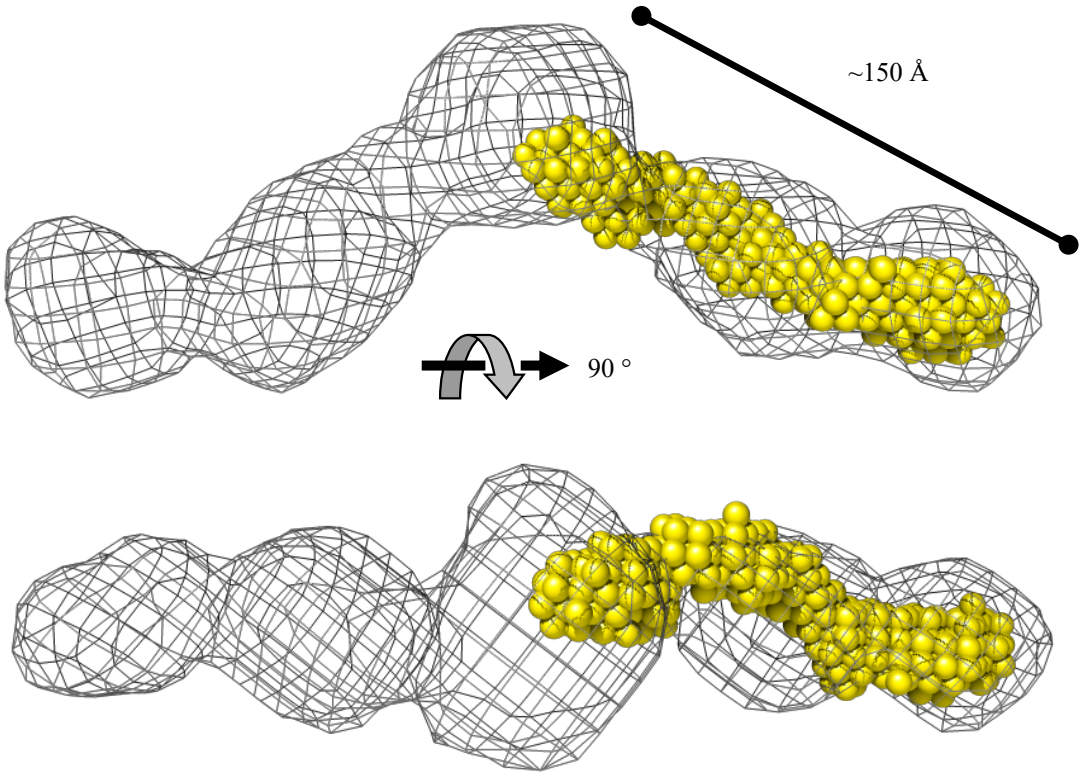

Figure 3.11: The molecular envelope of *Sa*DivIVA$_{1-120}$. The molecular envelope of *Sa*DivIVA$_{1-120}$ is rendered as yellow dummy atoms. The molecular envelope of *Sa*DivIVA$_{FL}$ is rendered as a mesh and the envelope of *Sa*DivIVA$_{1-120}$ modelled into the envelope of *Sa*DivIVA$_{FL}$.

3.5.2 N-terminal truncations of *Sa*DivIVA

To follow-up the work on the C-terminal truncation mutants, constructs of *Sa*DivIVA were generated in which the N-terminal end of the protein was truncated. Truncations were chosen to remove as much as possible of the N-terminus of *Sa*DivIVA whilst retaining a tetramer in solution. Three N-terminal truncations of *Sa*DivIVA, *Sa*DivIVA$_{54\text{-}205}$, *Sa*DivIVA$_{91\text{-}205}$ and *Sa*DivIVA$_{121\text{-}205}$ were cloned by restriction-free cloning (Section 2.2.7) to remove the N-terminal residues. Despite expressing and purifying as expected in *E. coli*, all C-terminal constructs bar *Sa*DivIVA$_{54\text{-}205}$ were excluded during SEC and eluted in the void volume of the column, demonstrating that these constructs formed soluble aggregates, rendering them unsuitable for any further analysis. *Sa*DivIVA$_{54\text{-}205}$, however, eluted as expected by gel filtration and was analysed as with the other constructs of *Sa*DivIVA by SEC-MALS/SAXS following the same methodologies.

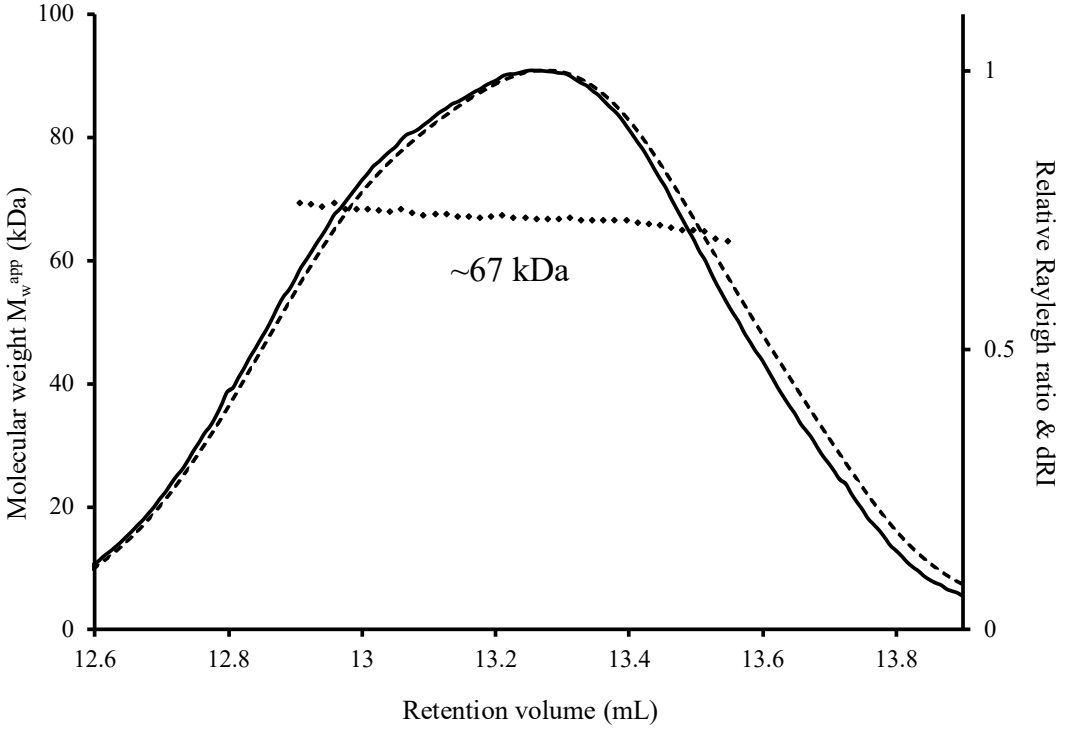

Figure 3.12: SEC-MALS analysis of *Sa*DivIVA$_{54\text{-}205}$. *Sa*DivIVA eluted from SEC-MALS with a M_w^{app} of ~67 kDa, a tetramer made up of 17 kDa monomers. The molecular weight calculated from MALS is shown as diamonds across the elution, as with *Sa*DivIVA$_{FL}$ and *Sa*DivIVA$_{1\text{-}120}$, the sample is monodisperse by SEC-MALS.

*Sa*DivIVA$_{54\text{-}205}$ eluted as a monodisperse species on SEC-MALS with a M_w^{app} of ~67 kDa, consistent with that of a tetramer, as monomers of this construct have a M_w of 17.4 kDa (Figure 3.12). This SEC-MALS result confirms that the N-terminal region of the protein is not

responsible for tetramerisation, consistent with the crystal structure of the N-terminal fragment of *Bs*DivIVA (Oliva et al., 2010). The structural parameters for *Sa*DivIVA$_{54-205}$ calculated from SEC-SAXS analysis are presented in Table 3.5 and a graphical summary of the SAXS data is shown in Figure 3.13. As with all other constructs of *Sa*DivIVA studied, the SAXS data fit the model of an elongated/rod-like protein. The calculated R_c of *Sa*DivIVA$_{54-205}$ is larger than that of its dimeric truncation counterpart, *Sa*DivIVA$_{1-120}$, however, it is smaller than the larger of the two R_cs calculated for *Sa*DivIVA$_{FL}$, a discrepancy that is not addressed by the reciprocal space analysis of the data alone. The similarity between the Kratky plot and Porod exponent of *Sa*DivIVA$_{54-205}$ and the other constructs studied demonstrates that the protein behaves similarly to the other constructs in solution as an elongated particle. Modelling the P(r) curve with a D_{max} of 222 Å results in a good agreement between the reciprocal/real space structural parameters and a χ^2 value of 1.1. The P(r) distribution follows the general trend of an elongated particle, however, the peak of the curve is shifted towards a larger interatomic distance than in the other constructs studied. This shifting of the P(r) is rationalised by the larger R_c of this construct, and that the width of construct is larger.

Table 3.5: Structural parameters calculated for *Sa*DivIVA$_{54-205}$ calculated from the SAXS data

	SaDivIVA$_{54-205}$
Reciprocal space analysis	
I(0) (cm^{-1})	0.0695
R_g (Å)	56.8
qR_g max	1.127
R_c	
Q^2-range used ($Å^{-2}$)	$1.3\times10^{-3} - 2.24\times10^{-3}$
R_c (Å)	26.1
Porod exponent (P^x)	2.9
Real space analysis	
I(0) (cm^{-1})	0.0700
R_g	59.39
D_{max} (Å)	222
Q-range used for fitting ($Å^{-1}$)	0.0063 – 0.3344
χ^2	1.1

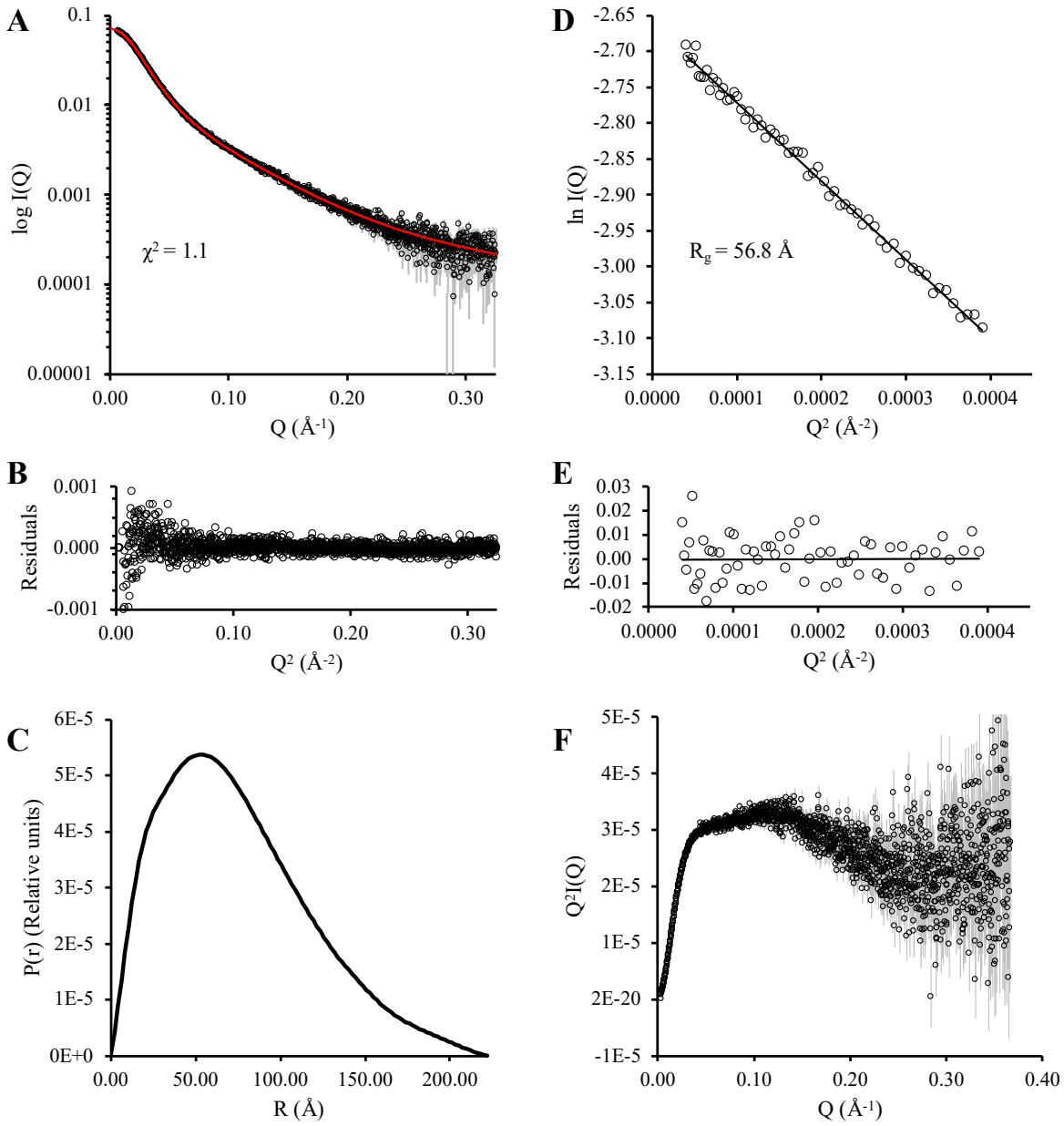

Figure 3.13: SAXS analysis of *Sa*DivIVA $_{54-205}$. A) The buffer-subtracted scattering data generated by ScÅtter is plotted as black circles (error bars shown in grey); The calculated scattering curve generated from the Fourier transform of the P(r) distribution shown in C is plotted in red. **B)** Residual plot of the fit to the calculated scattering curve from the experimental scattering curve. **C)** P(r) distribution calculated from the indirect Fourier transform of the scattering data in GNOM. **D)** Guinier plot of *Sa*DivIVA $_{54-205}$ highlighting the range of data used to calculate R_g. **E)** Residual plot of the estimation of R_g from the scattering data. **F)** Kratky plot of the data showing the rod-like/multi-domain nature of *Sa*DivIVA $_{54-205}$.

Dummy-atom modelling was performed as for the other *Sa*DivIVA constructs, the statistics for which are shown in Table 3.6. The molecular envelope of *Sa*DivIVA$_{54-205}$ generated by dummy atom modelling of the SAXS data is that of an elongated particle similar to the full-length protein and with the presence of a kink in its centre. Docking of the full-length protein and this N-terminal truncation mutant demonstrates the similarity of the two constructs (Figure 3.14).

Table 3.6: Parameters and statistics for the dummy atom modelling of *Sa*DivIVA$_{54-205}$

	SaDivIVA$_{54-205}$
DAMMIF (default parameters, 20 calculations)	
Q-range used for fitting (Å^{-1})	0.0063 – 0.334
Symmetry, anisotropy assumptions	P1, none
NSD (standard deviation)	1.019 (0.036)
χ^2 range	1.302 – 1.397
DAMMIN (default parameters)	
Q-range used for fitting (Å^{-1})	0.0063 – 0.334
Symmetry, anisotropy assumptions	P1, none
χ^2	1.305

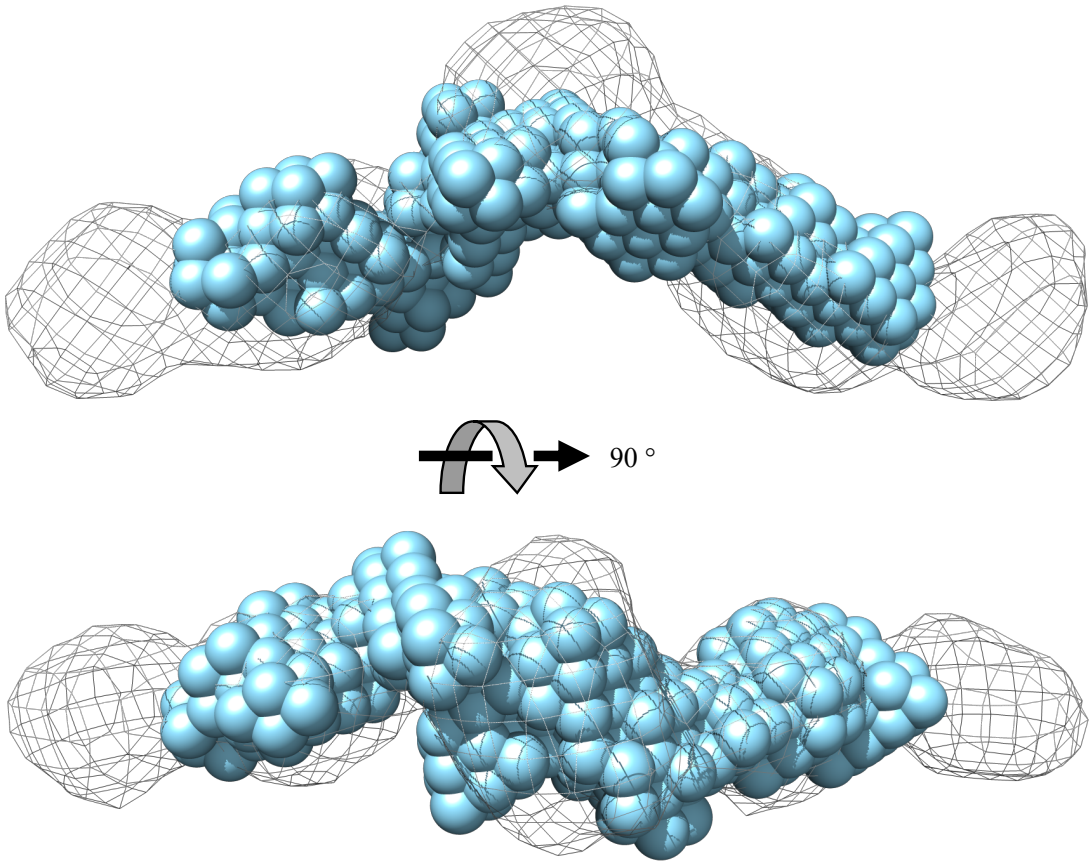

Figure 3.14: The molecular envelope of *Sa*DivIVA $_{54-205}$. The molecular envelope of *Sa*DivIVA $_{FL}$ is rendered as a wire mesh and the molecular envelope of *Sa*DivIVA $_{54-205}$ is rendered as blue dummy atoms.

3.5.3 Internal deletions in the linker region of *Sa*DivIVA

With the boundaries of the N-terminal domain and the C-terminal tetramerisation domain of *Sa*DivIVA known, mutants were generated in which the region between the tetramerisation domain and the N-terminal domain were deleted. Based on the data collected for *Sa*DivIVA so far, removal of the region between residues 54 and 120 should result in the formation of a tetramer with a shorter overall length. The deletion constructs were designed to retain the correct helical register of *Sa*DivIVA so as not to disturb the correct formation of coiled coils in the protein. Two constructs of DivIVA were generated from the pOPINRSF-*Sa*DivIVA$_{FL}$ plasmid (Section 2.2.6) with this in mind: *Sa*DivIVA$_{\Delta 58\text{-}119}$ and *Sa*DivIVA$_{\Delta 57\text{-}120}$. Prior to the removal of these internal regions of *Sa*DivIVA, predictions were made using the COILS server (Lupas et al., 1991) of the boundaries for the coiled-coil regions of *Sa*DivIVA, ensuring that that the coiled-coil regions of the protein were unperturbed.

*Sa*DivIVA$_{\Delta 58\text{-}119}$ and *Sa*DivIVA$_{\Delta 57\text{-}120}$ were expressed and purified by IMAC as described for *Sa*DivIVA$_{FL}$. During gel filtration, *Sa*DivIVA$_{\Delta 58\text{-}119}$ was excluded by the column and eluted in the void volume, rendering this protein unsuitable for any further analysis. The residues deleted in this construct may disrupt the helical register of the protein, resulting in the aberrant protein folding/formation of soluble aggregates reflected in the gel filtration trace. In the case of *Sa*DivIVA$_{\Delta 57\text{-}120}$, however, a single peak away from the void volume was observed by gel filtration, suggesting that this construct removes the required section of the protein without disturbing the correct formation of alpha-helices/coiled coils in the remainder of the protein.

SEC-MALS analysis of *Sa*DivIVA$_{\Delta 57\text{-}120}$ reveals a monodisperse species with a M_w^{app} of ~69 kDa, a tetrameric arrangement of 18.3 kDa monomers (Figure 3.15). SEC-SAXS analysis was performed on this construct as described for all other constructs, the structural parameters for which are presented in Table 3.7 and a graphical summary of the data collected presented in Figure 3.16. The magnitude of the disparity between R_g and R_c for this construct is less than might be expected for a rod-like particle and the Porod exponent is closer to that of a globular protein than seen for the other constructs analysed.

Table 3.7: Structural parameters calculated for *Sa*DivIVA$_{\Delta 57\text{-}120}$ calculated from the SAXS data

	SaDivIVA$_{\Delta 57\text{-}120}$
Reciprocal space analysis	
I(0) (cm^{-1})	0.127
R_g (Å)	50.32
qR_g max	1.288
R_c	
Q^2-range used (Å^{-2})	$1.44\times10^{-3} - 2.40\times10^{-3}$
R_c (Å)	28.7
Porod exponent (P^x)	3.1
Real space analysis	
I(0) (cm^{-1})	0.130
R_g	50.47
D_{max} (Å)	170
Q-range used for fitting (Å^{-1})	0.0112 – 0.315
χ^2	1.24

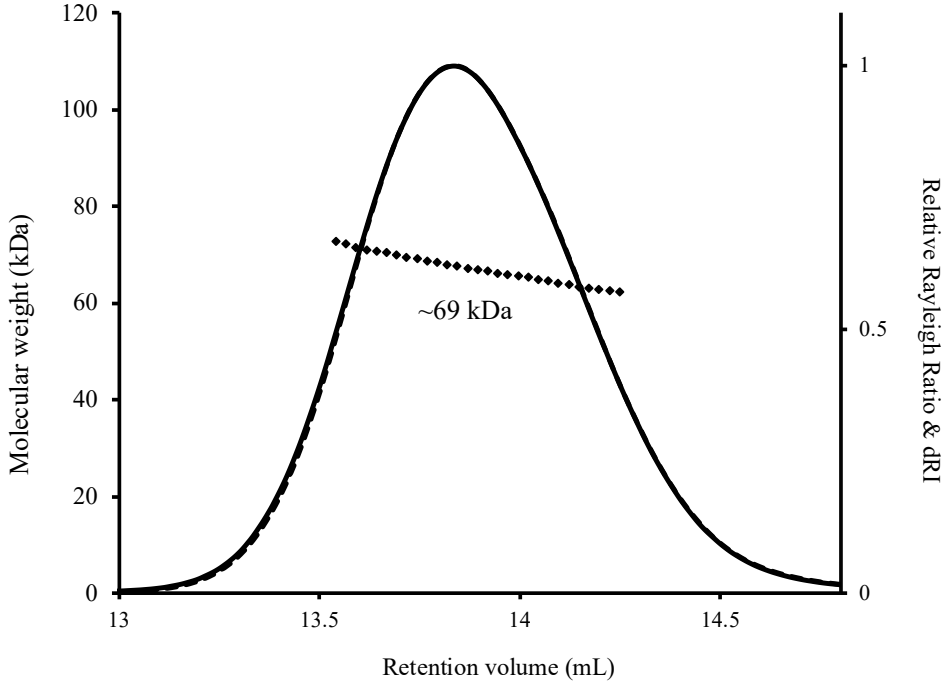

Figure 3.15: SEC-MALS analysis of *Sa*DivIVA$_{\Delta 57\text{-}120}$. *Sa*DivIVA$_{\Delta 57\text{-}120}$ eluted from SEC-MALS with a M_w^{app} of ~69 kDa, corresponding to a tetramer of 18 kDa monomers. The molecular weight calculated from MALS is plotted as diamonds across the elution.

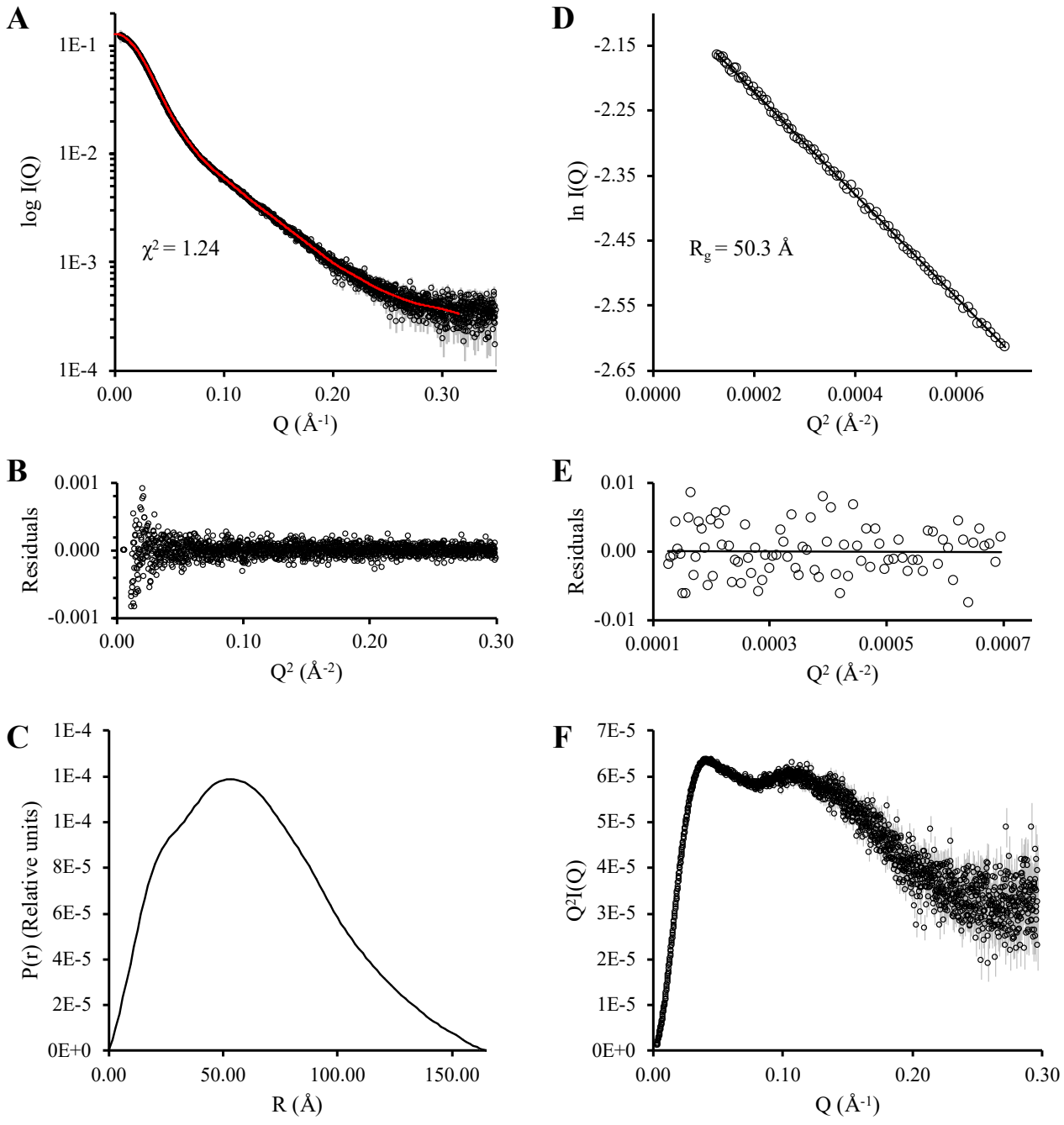

Figure 3.16: SAXS analysis of *Sa*DivIVA $_{\Delta 57\text{-}120}$. A) Plotted as black circles is the buffer-subtracted scattering data for *Sa*DivIVA $_{\Delta 57\text{-}120}$. The calculated scattering curve generated from the indirect Fourier transform of the P(r) distribution shown in C is plotted in red. **B)** The residual plot of the fit of the experimental scattering curve to the calculated scattering curve. **C)** The P(r) distribution calculated from the indirect Fourier transform of the scattering data in ScÅtter. **D)** Guinier plot of *Sa*DivIVA $_{\Delta 57\text{-}120}$ highlighting the range of data used to calculate R_g. **E)** Residual plot of the estimation of R_g from the scattering data. **F)** Kratky plot of the data showing the multi-domain nature of *Sa*DivIVA $_{\Delta 57\text{-}120}$.

Modelling of the P(r) distribution with a D_{max} of ~170 Å results in a good fit to the scattering data (Figure 3.16c), revealing *Sa*DivIVA$_{\Delta 57\text{-}120}$ to be roughly 130 Å shorter than the full-length construct of the protein. The general shape of the molecule as described by the P(r) distribution is a relatively globular one, which may be explained by the kinked structure of *Sa*DivIVA; it is consistent with the model of oligomerisation that the closer proximity of the two N-terminal domains to the C-terminal tetramerisation domain result in a molecule less elongated/rod-like and a denser particle overall. Dummy-atom modelling of *Sa*DivIVA$_{\Delta 57\text{-}120}$ was performed and the molecular envelope shown in Figure 3.17, the parameters and statistics for the generation of the molecular envelope are presented in Table 3.8. As predicted by the one-dimensional analysis of the SAXS data thus far, the particle conforms to a global description of a rod, but is more distorted than elongated, resulting in a more compact particle overall.

Table 3.8: Parameters and statistics for the dummy atom modelling of *Sa*DivIVA$_{\Delta 57\text{-}120}$

	SaDivIVA$_{\Delta 57\text{-}120}$
DAMMIF (default parameters, 10 calculations)	
Q-range used for fitting (Å^{-1})	0.0114 – 0.1817
Symmetry, anisotropy assumptions	P1, none
NSD (standard deviation)	0.834 (0.024)
χ^2 range	1.131 – 1.152
DAMMIN	
Q-range used for fitting (Å^{-1})	0.0114 – 0.1817
Symmetry, anisotropy assumptions	P1, none
χ^2	1.138

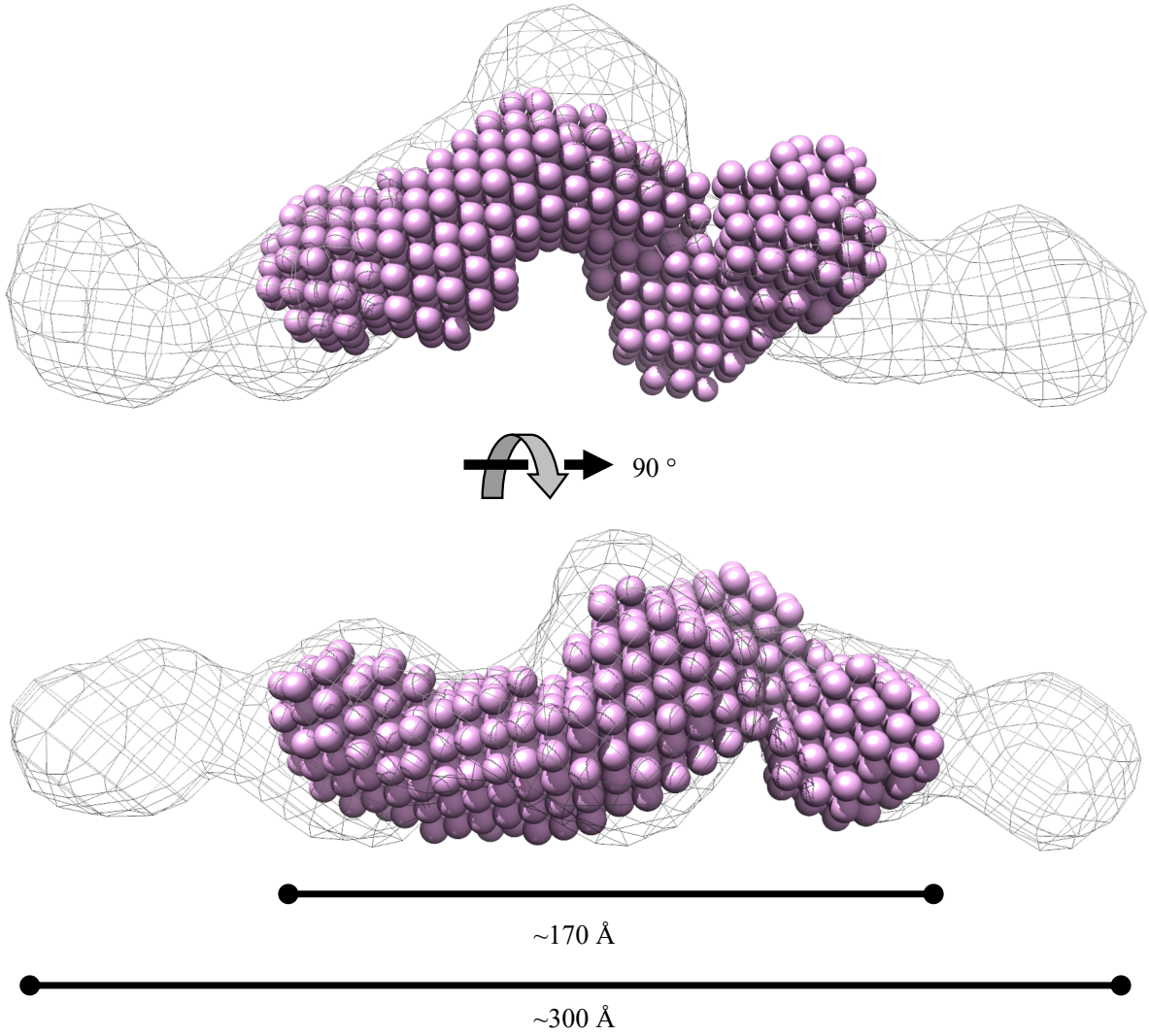

Figure 3.17: The molecular envelope of *Sa*DivIVA $_{\Delta 57\text{-}120}$. The molecular envelope of *Sa*DivIVA $_{FL}$ is rendered as a wire mesh, and the dummy-atom model generated for *Sa*DivIVA $_{\Delta 57\text{-}120}$ is rendered as purple spheres.

3.5.4 Secondary structure analysis of *Sa*DivIVA truncation mutants

CD was used as a quality control step for each truncation mutant of *Sa*DivIVA to confirm that no loss/disruption of secondary structure occurred as a result of any mutations/truncations. All truncations of *Sa*DivIVA share a similar alpha-helical trace by CD (Figure 3.18a). This confirms that none of the aforementioned modifications have perturbed substantially the helical nature of the protein. Alongside its use as a quality control step for the truncations, CD was also used to compare the stability of the truncated proteins against wild-type *Sa*DivIVA. CD thermal melts were performed on every construct of *Sa*DivIVA and used as a rough measure of the stability of the proteins. *Sa*DivIVA$_{FL}$ is the most stable construct of *Sa*DivIVA studied with a melting temperature (T_m) of 42 °C (Figure 3.18b). A decrease in T_m is seen for *Sa*DivIVA$_{54\text{-}205}$ and *Sa*DivIVA$_{\Delta 57\text{-}120}$ of approximately 5 °C, whilst a decrease of 20 °C is seen

for *Sa*DivIVA$_{1-120}$. Both the N- and C-terminal regions of *Sa*DivIVA appear to contribute to the overall stability of the protein, however, complete loss of the tetramerisation domain has the most pronounced effect on the stability of the protein.

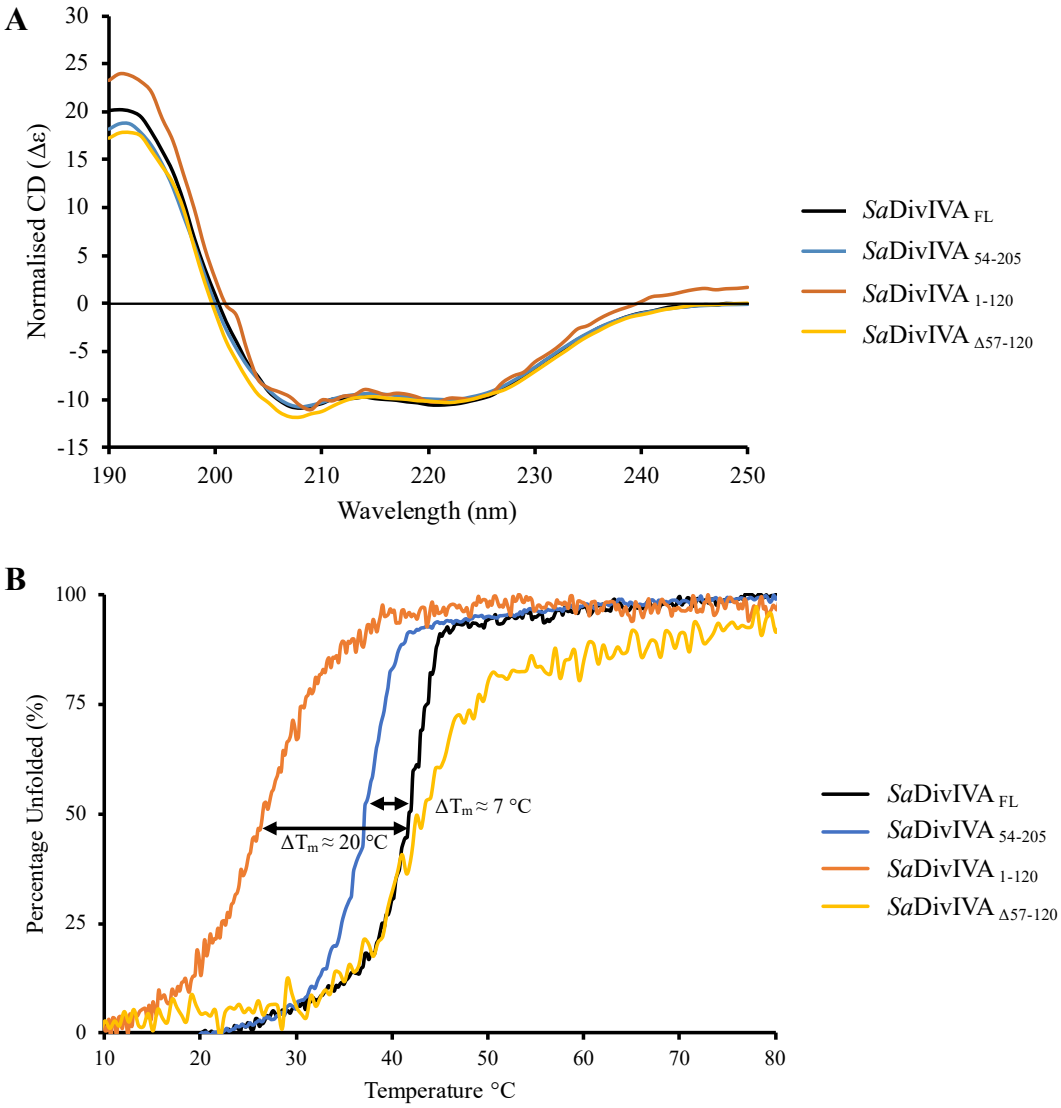

Figure 3.18: CD analysis of *Sa*DivIVA truncations. A) The experimental CD spectra for each truncation mutant compared to the spectrum for *Sa*DivIVA$_{FL}$. The general profile of the spectra for each protein matches that of *Sa*DivIVA$_{FL}$. **B)** CD thermal melts performed on the truncation mutants of *Sa*DivIVA. CD signals were measured at 222 nm as a function of temperature increase inside the experimental chamber.

3.5.5 MBP-fusions of *Sa*DivIVA

To test the oligomerisation model proposed in solution on the full-length protein, fusions were made to maltose-binding protein (MBP) and subjected to the same SEC-MALS/SAXS analysis as for all other constructs of *Sa*DivIVA. MBP was fused to the N- and C-terminus of *Sa*DivIVA, generating MBP-*Sa*DivIVA and MBP-*Sa*DivIVA-MBP (Section 2.2.10). The

presence of a single protease cleavage site between the N-terminal MBP and *Sa*DivIVA allowed for the purification of both MBP-*Sa*DivIVA-MBP and *Sa*DivIVA-MBP simultaneously. Whilst MBP-*Sa*DivIVA expressed well and purified successfully in a two-step purification by IMAC followed by gel filtration (Section 2.3.1 - 2.3.3, 2.3.6), MBP-*Sa*DivIVA-MBP did not express well in *E. coli*, and what little protein was isolated by affinity chromatography precipitated heavily and was unable to be purified further. This may be a result of the position of the MBPs at the C-terminus sterically hindering the formation of the tetrameric arrangement of helices, exposing the hydrophobic core of the bundle and seeding aggregation. Constructs of *Sa*DivIVA with MBP fused to their C-termini were abandoned as a result of this observation.

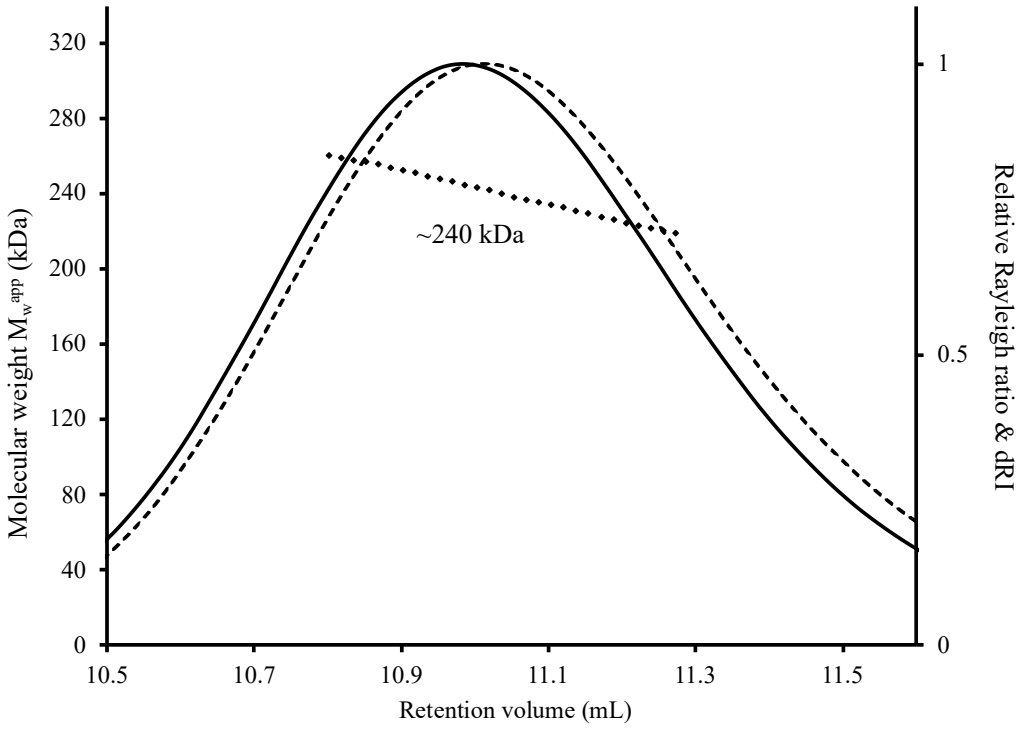

Figure 3.19: SEC-MALS analysis of MBP-*Sa*DivIVA. MBP-*Sa*DivIVA eluted from SEC-MALS with a M_w^{app} of ~240 kDa. There is a dissociation seen in the M_w over the column, indicating that this construct is not as stable as the other constructs studied, which may account for this discrepancy.

By SEC-MALS, MBP-*Sa*DivIVA eluted with a M_w^{app} of ~240 kDa, below the expected M_w of 276 kDa, as monomers of MBP-*Sa*DivIVA$_{FL}$ have a M_w of 69 kDa. The MALS profile for MBP-*Sa*DivIVA showed a slight decrease in oligomer across the elution, potentially indicating a slight loss in stability for the tetramer with the MBP at the N-terminus of *Sa*DivIVA (Figure 3.19). Nonetheless, SEC-SAXS analysis was performed on MBP-*Sa*DivIVA$_{FL}$ and the structural parameters calculated from this are presented in Table 3.9. There is a pronounced

increase in R_g for MBP-*Sa*DivIVA compared to *Sa*DivIVA$_{FL}$, to be expected for the addition of four large globular proteins to the particle. As with *Sa*DivIVA$_{FL}$, there is the presence of two distinct linear regions in the modified Guinier plot, suggesting the presence of two distinct R_cs. Both R_cs for MBP-*Sa*DivIVA are increased when compared to *Sa*DivIVA$_{FL}$, likely a result of the presence of the MBPs skewing the average radius towards larger values. MBP-*Sa*DivIVA generates a P(r) curve which, when compared to the P(r) of *Sa*DivIVA$_{FL}$, reveals a shifting of the local maximum at 150 Å in *Sa*DivIVA$_{FL}$ to ~250 Å in MBP-*Sa*DiviVA$_{FL}$, as well as an increase in D_{max} by 125 Å (Figure 3.21).

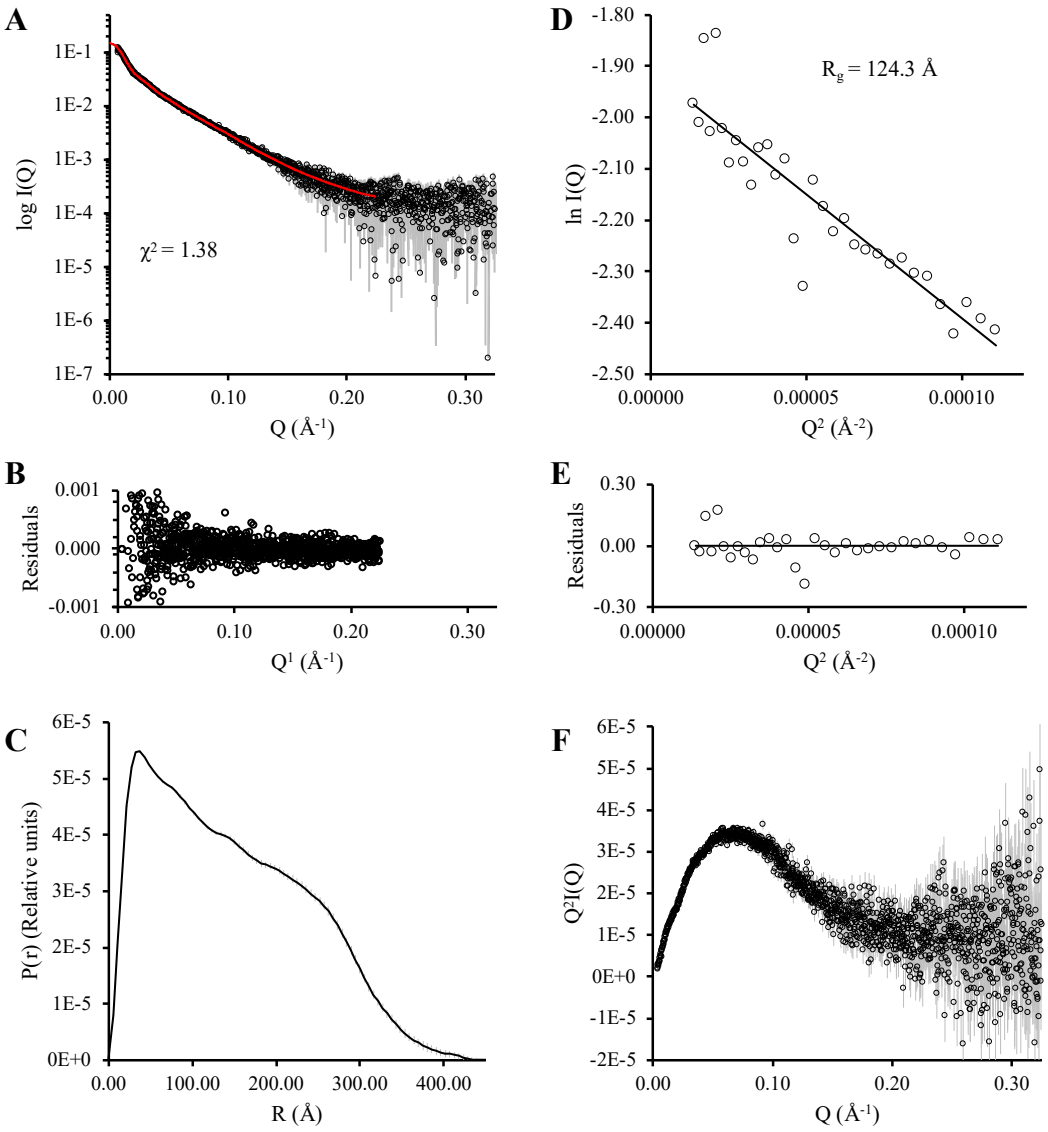

Figure 3.20: SAXS analysis of MBP-*Sa*DivIVA. A) The subtracted scattering data for MBP-*Sa*DivIVA calculated in ScÅtter is plotted as black circles. The calculated scattering curve generated from the Fourier transform of the P(r) distribution shown in C is plotted in red. **B)** The residual plot of the fit of the experimental scattering curve to the calculated scattering curve. **C)** P(r) distribution calculated from the indirect Fourier transform of the scattering data in GNOM. **D)** Guinier plot of MBP-*Sa*DivIVA highlighting the range of data used to calculate R_g. **E)** Residual plot of the estimation of R_g from the scattering data. **F)** Kratky plot of the scattering data from A.

Table 3.9: Structural parameters calculated for MBP-*Sa*DivIVA from the SAXS data

	MBP-SaDivIVA
Reciprocal space analysis	
I(0) (cm^{-1})	0.15
R_g (Å)	124.3
qR_g max	1.1566
R_c	
Q^2-range used ($Å^{-2}$)	$1.3\times10^{-4} - 4.0\times10^{-4}$
R_c (Å)	40.7
Q^2-range used ($Å^{-2}$)	$5.4\times10^{-4} - 1.2\times10^{-3}$
R_c (Å)	17.0
Porod exponent (P^x)	3.4
Real space analysis	
I(0) (cm^{-1})	0.14
R_g	119.4
D_{max} (Å)	445
Q-range used for fitting ($Å^{-1}$)	0.0037 – 0.223
χ^2	1.38

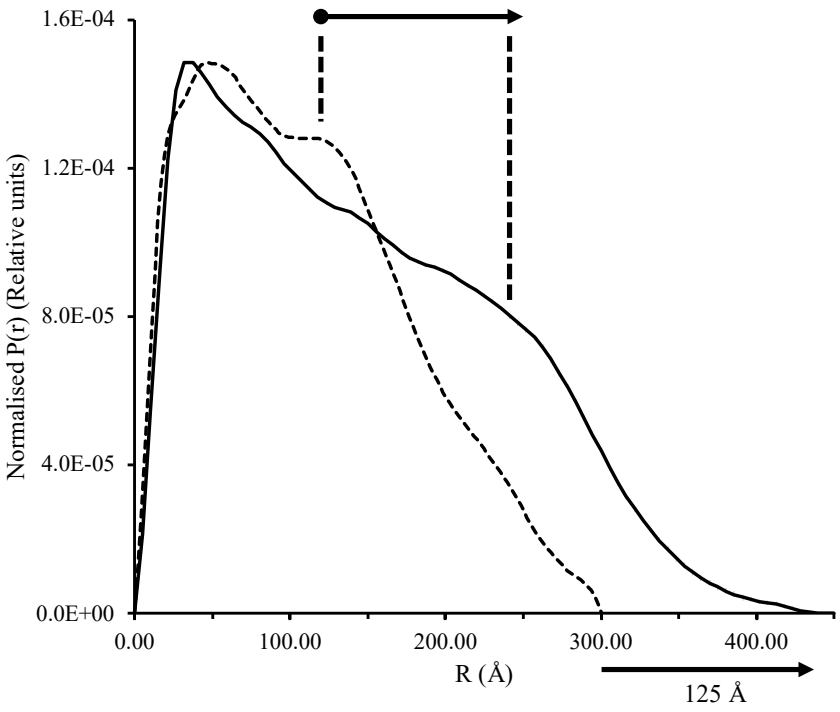

Figure 3.21: Comparison of the P(r) distributions of MBP-*Sa*DivIVA$_{FL}$ and *Sa*DivIVA$_{FL}$. The P(r) distribution of MBP-*Sa*DivIVA$_{FL}$ is shown as a solid black line, the P(r) distribution of *Sa*DivIVA$_{FL}$ is shown as a dashed black line. The D_{max} of MBP-*Sa*DivIVA$_{FL}$ is approximately 125 Å longer than that of *Sa*DivIVA$_{FL}$. The local maximum present at 125 Å in the P(r) distribution of *Sa*DivIVA$_{FL}$ is no longer present in the P(r) distribution of MBP-*Sa*DivIVA$_{FL}$.

3.6 Negative-stain electron microscopy of *Sa*DivIVA$_{FL}$

To verify the calculated dimensions of *Sa*DivIVA$_{FL}$ by SAXS, negative-stain EM was employed to visualise *Sa*DivIVA$_{FL}$ particles in real space (Section 2.6.2). EM analysis of *Sa*DivIVA$_{FL}$ reveals particles with a range of orientations (Figure 3.22). By manually picking elongated particles, general statements about the length the particles can be made. The elongated particles were measured using Fiji (Schindelin et al., 2012), using the scale bar as calibrant, and were found to have lengths of 25-35 nm, which agree with the estimation of D_{max} from SAXS of 300 Å (30 nm). Those with particles with shorter calculated lengths are likely lying obliquely to the plane of the grid, resulting in the appearance of a a shorter particle. The conformational diversity of *Sa*DivIVA$_{FL}$ seen in these negative stain electron micrographs may contribute to the recalcitrance of SaDivIVA$_{FL}$ to crystallisation.

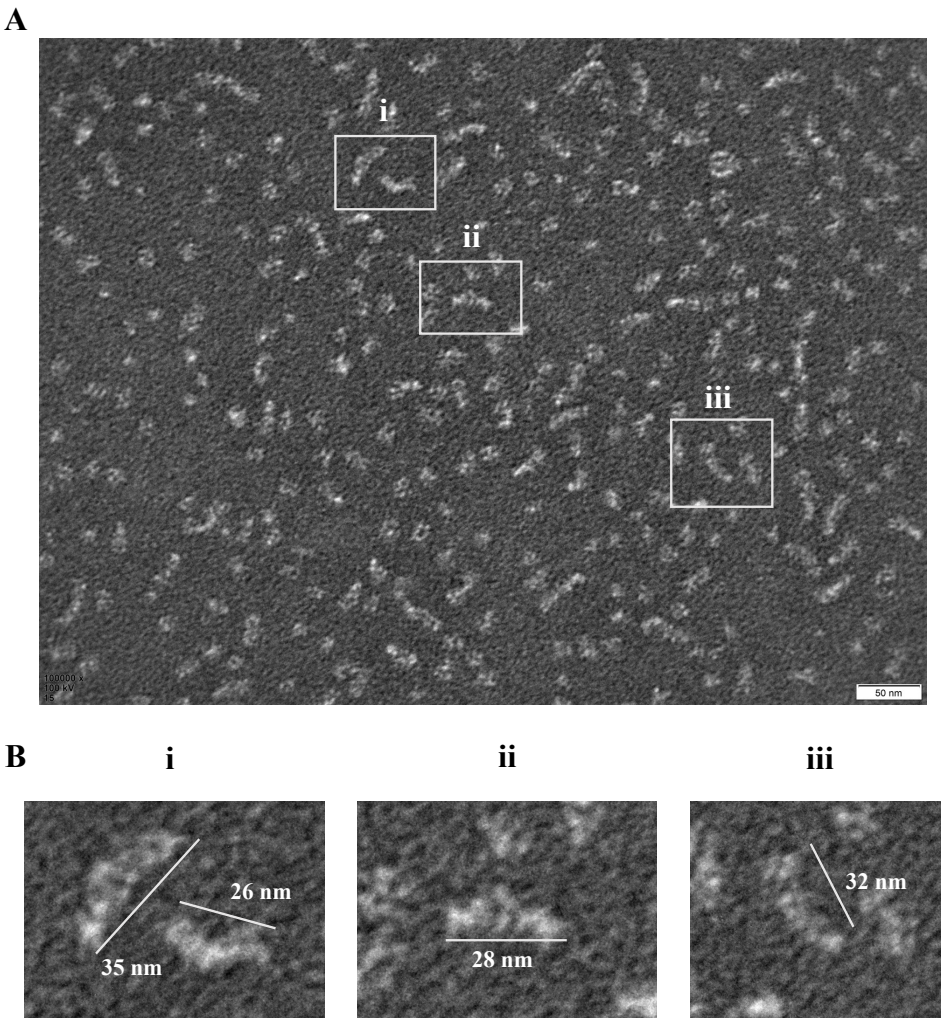

Figure 3.22: Negative-stain EM of *Sa*DivIVA$_{FL}$. A) Representative EM grid containing *Sa*DivIVA$_{FL}$ particles. The diversity in orientations of *Sa*DivIVA$_{FL}$ in solution is represented by the range of particle shapes present on the grid. **B)** Zoomed images of the EM grid from A with distances calculated in Fiji using the scale bar in **A**.

3.7 Crystal structure of *Sa*DivIVA$_{1-57}$

A construct of *Sa*DivIVA encapsulating the N-terminal domain alone, *Sa*DivIVA$_{1-57}$, was generated by site-directed mutagenesis following the same methodologies as for the C-terminal truncations presented in Section 3.5.1. The construct boundaries were picked to mimic the known structures of the N-terminal domain of *Bs*DivIVA (PDB code 2WUJ; Oliva et al., 2010) and of the DivIVA paralogue GpsB from *B. subtilis* (PDB code 4UG3; Rismondo et al., 2016). *Sa*DivIVA$_{1-57}$ was expressed, purified, crystallised, and its structure solved by Dr. Vincenzo Rao (Newcastle University). The fold of *Sa*DivIVA$_{1-57}$ is identical to all currently solved DivIVA and GpsB structures to-date, with an RMSD between it and its most closely related homologue, *Bs*DivIVA (PDB code 2WUJ), of 1.8 Å over all C_α atoms. The general structure of *Sa*DivIVA is a homodimer of parallel helices whose N-termini cross over each other and fold back onto the coiled coil (Figure 3.23a). Although the overall fold of the N-terminus of *Sa*DivIVA is in essence identical to *Bs*DivIVA, the residues at the lipid-binding interface are not. The residues thought to be responsible for the interaction of *Bs*DivIVA with the plasma membrane, Phe17 and Arg18 (Oliva et al., 2010), are replaced by Lys18 and Asn19 in *Sa*DivIVA (Figure 3.23bc).

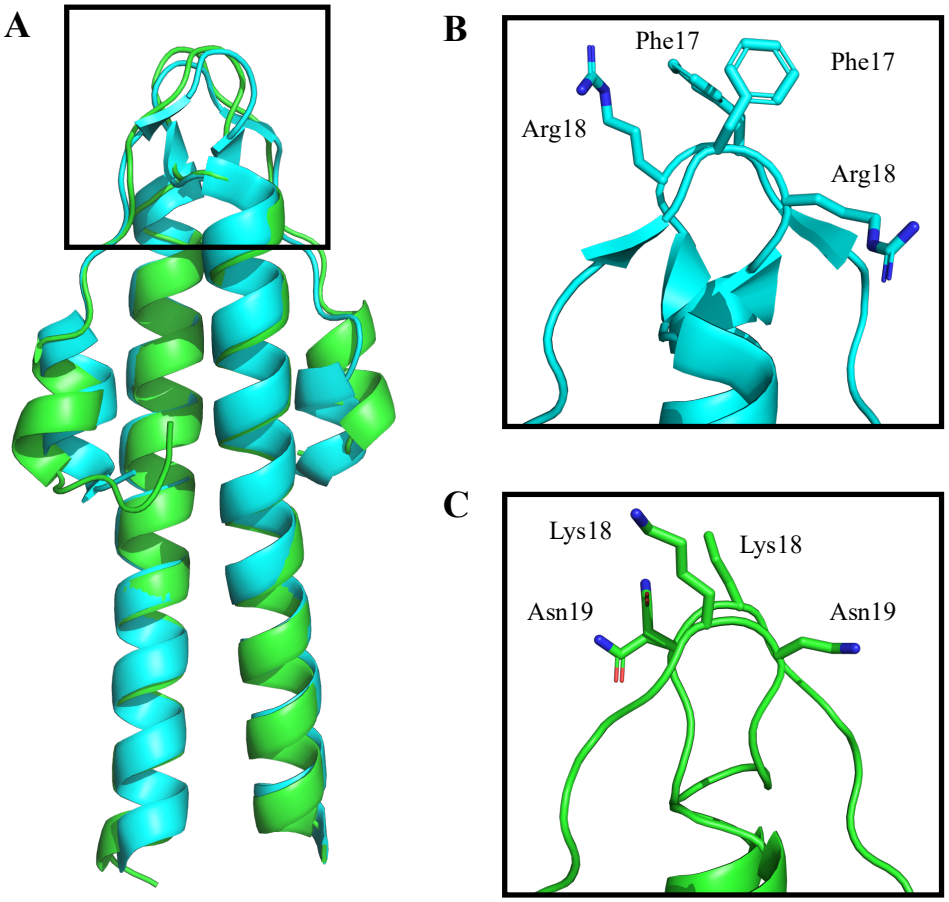

Figure 3.23: Crystal structure of the N-terminus of *Sa*DivIVA. A) Superposition of the structure of the N-termini of *Sa*DivIVA (green) against *Bs*DivIVA (cyan) (PDB id 2WUJ: Oliva et al., 2010) showing the structural similarity between the two proteins. The proposed lipid binding residues are enclosed in a black box. The structures were superimposed in PyMol (Schrödinger). **B)** Zoomed structure of the lipid-binding region of *Bs*DivIVA, highlighting the position of Phe17 and Arg18, thought to be responsible for membrane binding in *Bs*DivIVA. **C)** Zoomed structure of the same region displayed in B but for *Sa*DivIVA.

3.8 Crystallisation and structure determination of *Sa*DivIVA$_{1\text{-}120}$

*Sa*DivIVA$_{1\text{-}120}$ was screened for crystallisation conditions as described in section 2.4.9. Initial sub-diffraction quality hits were found initially at 20 °C from the JCSG+ screen (Molecular Dimensions), in 0.1 M HEPES pH 7.5, 70 % MPD. The initial hits in this condition were optimised by varying the pH and MPD concentration, however, no diffraction quality crystals were obtained. The initial condition was optimised further through use of the Additive Screen (Hampton Research), using the initial hit condition as the basis for the screen. Whilst several rod-like crystals were generated, no diffraction quality crystals were acquired through either of these means. As a rescue strategy for crystallisation, the lysine residues of *Sa*DivIVA$_{1\text{-}120}$ were methylated (Section 2.4.8) (Walter et al., 2006). Methylated *Sa*DivIVA$_{1\text{-}120}$ was analysed by Electrospray Ionisation-Mass Spectrometry (ESI-MS) and compared against unmethylated *Sa*DivIVA$_{1\text{-}120}$ (Simon Thorpe, University of Sheffield), and all 14 lysine residues present in

*Sa*DivIVA$_{1-120}$ were found to be methylated (data not shown). Methylated protein was screened for crystallisation conditions as for unmethylated protein, and crystallisation experiments stored at 20 °C and 4 °C. After one year, crystals were found at 4 °C. Eight crystals were harvested with nylon loops, flash-frozen in liquid nitrogen and diffraction data were collected at beamline I24 of the Diamond Light Source. Of the eight hits present, one diffracted at 3.6 Å, allowing for the construction of a low-resolution structure. Data collection and refinement statistics for *Sa*DivIVA$_{1-120}$ are shown in Table 3.10.

Table 3.10 Data collection and refinement statistics for *Sa*DivIVA$_{1-120}$.

	***Sa*DivIVA$_{1-120}$**
Wavelength (Å)	0.969
Resolution range (Å)[a]	80.55 – 3.60 (3.94 – 3.60)
Space group	$P\ 1\ 2_1\ 1$
Unit cell dimensions	
***a*, *b*, *c* (Å)**	56.29, 38.90, 81.98
α, β, γ (°)	90, 100.74, 90
Total reflections[a]	14818 (3614)
Unique reflections[a]	4187 (983)
Multiplicity[a]	3.5 (3.7)
Completeness (%)[a]	99.4 (99.6)
Mean I/σI[a]	6.5 (3.1)
Wilson B-factor (Å^2)	79.84
R_{merge}[a]	0.08 (0.28)
$R_{p.i.m.}$[a]	0.05 (0.17)
$CC_{1/2}$[a]	0.998 (0.977)
R_{work} (%)	0.29
R_{free} (%)[b]	0.35
Number of non-hydrogen atoms	1702
macromolecules	1702
solvent	0
Protein residues	216
RMS(bonds)	0.013
RMS(angles)	1.68
Ramachandran favored (%)	85.38
Ramachandran allowed (%)	12.26
Ramachandran outliers (%)	2.36
Clashscore	8.3
Average B-factor	227
macromolecules	227
solvent	N/A

[a]Values in parentheses denote highest resolution shell.
[b]5% of reflections were selected randomly for determination of R_{free}

The structure of the N-terminus of *Sa*DivIVA$_{1-120}$ is identical to *Sa*DivIVA$_{1-57}$, but with extended C-termini which diverge with increasing distance from the N-terminus (Figure 3.24). The divergence of the two C-terminal helices is likely a result of crystal packing, as crystal contacts are made between adjacent *Sa*DivIVA$_{1-120}$ molecules (Figure 3.25), likely facilitating crystallisation. The structure of *Sa*DivIVA$_{1-120}$ reveals that linker region present between the N-terminus of *Sa*DivIVA and the C-terminal tetramerisation domain is structured, and is made up of a continuous alpha-helix. The crystal packing of *Sa*DivIVA$_{1-120}$ may even suggest a minor role for residues 73-120 of *Sa*DivIVA$_{1-120}$ in tetramerisation.

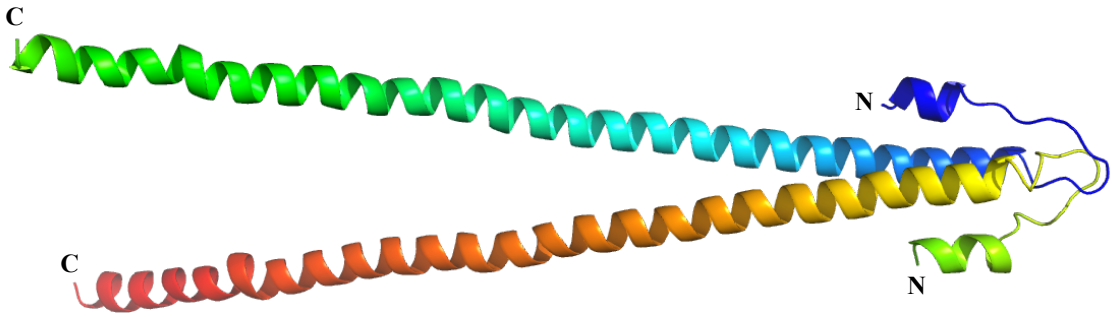

Figure 3.24: Crystal structure of *Sa*DivIVA $_{1-120}$. The low-resolution structure of *Sa*DivIVA $_{1-120}$ is rendered as a cartoon coloured in rainbow, with the N- and C-termini of each *Sa*DivIVA $_{1-120}$ monomer labelled.

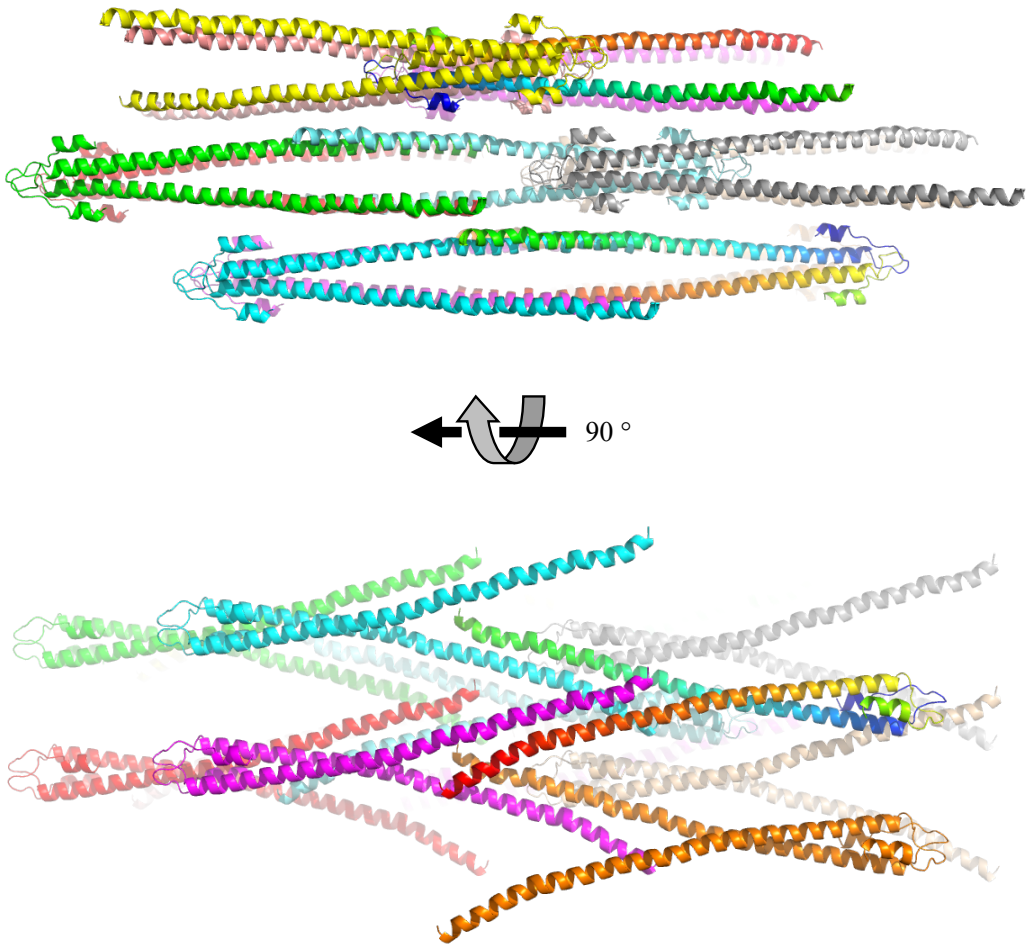

Figure 3.25: Crystal packing of *Sa*DivIVA $_{1\text{-}120}$. The crystal lattice of *Sa*DivIVA $_{1\text{-}120}$ is rendered with each *Sa*DivIVA $_{1\text{-}120}$ dimer rendered in a different colour. Each *Sa*DivIVA $_{1\text{-}120}$ dimer is connected to two other dimers through crystal contacts at the C-terminus of the protein.

3.9 Attempts to crystallise other *Sa*DivIVA constructs

All *Sa*DivIVA constructs presented in this chapter were screened against a variety of commercial screens (Section 2.4.9) in an attempt to find conditions sufficient for crystallisation. Other than the two successful cases presented here, no diffraction-quality crystals were generated. In the vast majority of cases, no crystals grew at all despite the screening of variables such as temperature, protein concentration, the use of several crystallisation screens, and rescue strategies such as lysine methylation or *in situ* protease degradation. The recalcitrance of *Sa*DivIVA proteins to crystallisation is perhaps a result of its inherent flexibility, as seen in the EM studies of the full-length protein and the SAXS analysis of all constructs presented in this chapter.

3.10 Rigid-body modelling of *Sa*DivIVA

Despite uncovering the general dimensions of the molecule of interest, the information provided by SAXS dummy atom modelling is limited by its inherently low resolution. Integrative modelling techniques such as rigid-body modelling of high-resolution structures render SAXS a far more powerful technique than when used *ab initio*. Rigid-body modelling is a particularly useful technique in cases where structures of entire proteins are not known but subdomains or fragments of the protein are, for example, where multidomain proteins are linked by flexible regions that render the full-length protein recalcitrant to crystallisation. In cases such as these, the fragments/subdomains of the protein can be modelled as rigid bodies and the missing fragments of the structures predicted with dummy atom models, resulting in a more accurate depiction of the protein in solution than with the fragments of the structure alone.

Rigid body modelling of *Sa*DivIVA$_{FL}$ was performed in CORAL (Schneidman-Duhovny et al., 2012), with the structure of *Sa*DivIVA$_{1-57}$ and the C-terminus of *Bs*DivIVA defined as rigid bodies, and the remainder of the protein sequence defined as unknown structure. The interfaces between the N-terminal dimers and the tetramerisation interface at the C-terminus were enforced through the contacts function in CORAL. The model generated by CORAL fits the crescent shape of the molecular envelope of *Sa*DivIVA$_{FL}$ well, with a χ^2 of 1.35. In the rigid-body model shown here, the proposed lipid-binding N-termini of the molecule bending inwards in an arch towards the center of the molecule (Figure 3.26). The C-terminal dummy-atom residues are somewhat randomly oriented, which may reflect their disordered nature in solution.

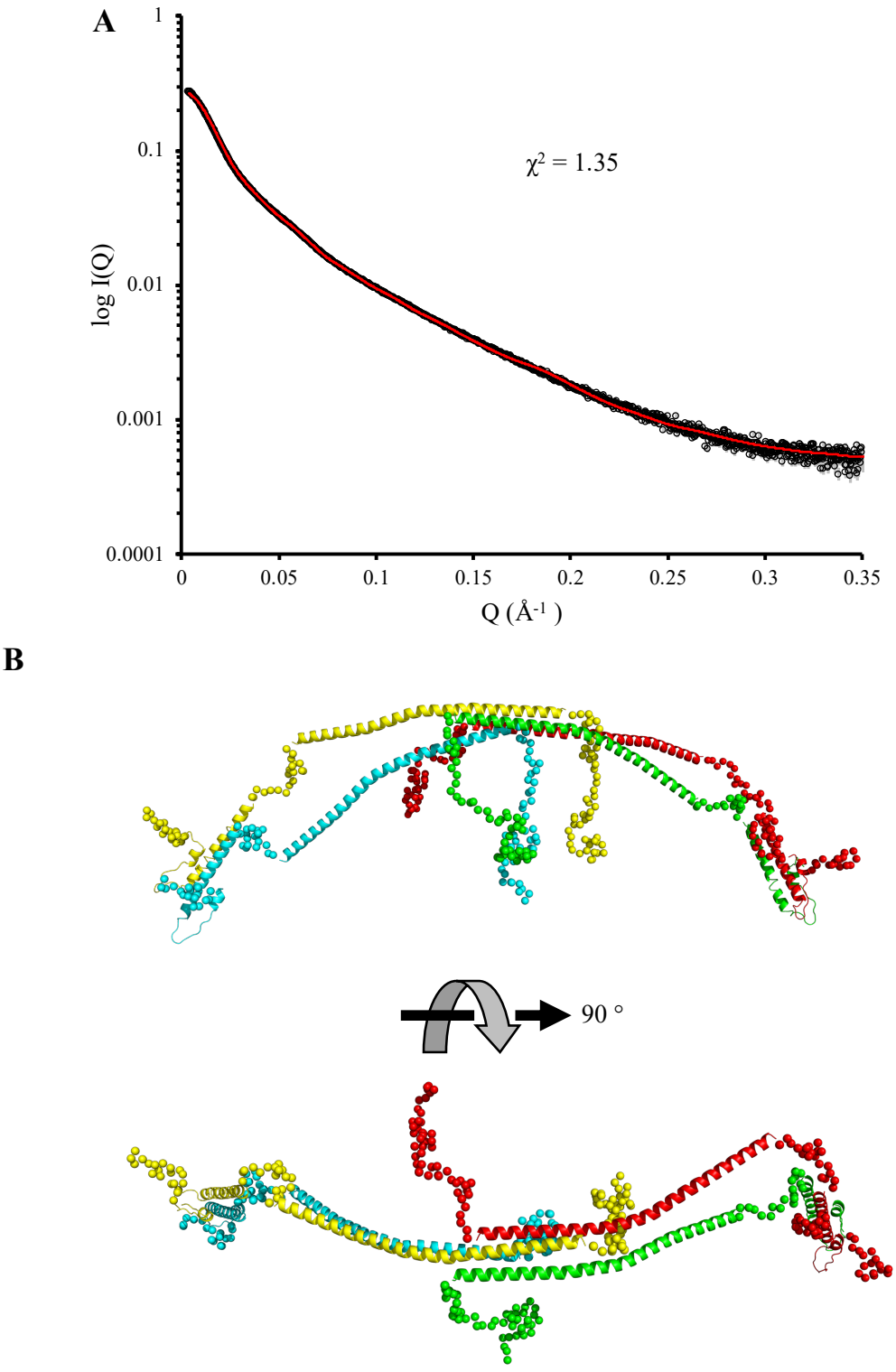

Figure 3.26: Rigid-body modelling of *Sa*DivIVA. A) The scattering data for *Sa*DivIVA $_{FL}$ is represented as black circles with error bars in grey. Shown as a red line is the fit generated by CORAL of the rigid-body model to the experimental SAXS data. **B)** The rigid-body model generated by CORAL of *Sa*DivIVA $_{FL}$. Rigid bodies from high-resolution crystal structures are shown as ribbon diagrams, missing fragments of the structure are shown as dummy atoms. Each monomer of *Sa*DivIVA $_{FL}$ is coloured separately. Single contacts between each of the helices in the C-terminal tetrameric bundle were enforced in order to ensure the tetrameric interface of *Sa*DivIVA was kept intact during modelling, as well as the dimeric interface between the coiled coil at the n-terminus of the protein.

3.11 Testing the interactions of *Sa*DivIVA with cell wall synthesis proteins

The interactions of *Sa*DivIVA against several proposed interacting proteins from *S. aureus* were tested by a variety of biochemical and biophysical assays. Targets for binding assays were chosen based on bacterial two-hybrid experiments performed by the Foster lab (University of Sheffield), in which preliminary interactions between DivIVA and members of the wall-teichoic acid synthesis machinery (SA2103 and SA0908) and peptidoglycan synthesis machinery (PBP1 and PBP4) were identified by bacterial two-hybrid analysis (unpublished). As *Sa*DivIVA is a cytoplasmic protein, and the proposed binding partners identified are all bitopic membrane proteins, the region of interaction is limited to the short intracellular regions of the proposed binding partners. In lieu of overcoming the obstacles involved in expressing and purifying full-length membrane proteins for the sake of a short region of potential interaction, soluble fluorescent peptides comprising the intracellular regions of the bitopic targets were synthesised with fluorescein attached to their N-termini as a means to monitor their interactions with *Sa*DivIVA via a variety of techniques.

3.11.1 Fluorescence polarisation

The presence of the fluorescent probe allowed for the study of DivIVA:peptide interactions by FP (Section 2.5.4). As shown in Figure 3.27a, no interactions between DivIVA and any of the fluorescent peptides tested against were observed utilising this method. If an interaction between *Sa*DivIVA$_{FL}$ and the respective peptide had been observed, an increase in fluorescence polarisation would have resulted as a function of *Sa*DivIVA$_{FL}$ concentration, until a point at which all binding sites were saturated, and the fluorescence polarisation reached a plateau. The lack of any increase in fluorescence polarisation even at the highest concentrations of *Sa*DivIVA$_{FL}$ indicate either an immeasurably low K_D, or no binding at all, and may suggest that *Sa*DivIVA$_{FL}$ does not interact with these proteins *in vivo*.

3.11.2 Microscale thermophoresis

As for FP, the fluorescent moiety attached to the peptides allowed for the study of their interactions by MST (Section 2.5.3) without any other labelling of the proteins or peptides under study. No change in the thermophoresis of any of the labelled peptides was observed as a function of *Sa*DivIVA$_{FL}$ concentration (Figure 3.27b), indicating that there was no detectable change in the size, charge or solvation entropy of the fluorescent probe. As there is a ~20-fold size difference between *Sa*DivIVA$_{FL}$ and the peptides used in these experiments, this would

strongly suggest that no binding is occurring, and therefore no measurable change in thermophoresis would occur.

3.11.3 Surface plasmon resonance

As a third and final verification of the lack of binding of *Sa*DivIVA$_{FL}$ to any of its proposed interaction partners *in vitro*, SPR was used to test for interactions (Section 2.5.2). In these experiments, *Sa*DivIVA$_{FL}$ was immobilised onto a Ni-NTA chip with the His$_6$-tag at the N- or C-terminus of the protein to ensure any binding region of *Sa*DivIVA$_{FL}$ was not occluded by the chip surface. N- or C-terminally immobilised *Sa*DivIVA$_{FL}$ proteins were screened against all the aforementioned peptides. In all cases there was no change in response on passing the peptides over the experimental cell, indicative of a lack of binding (Figure 3.27c and 3.27d).

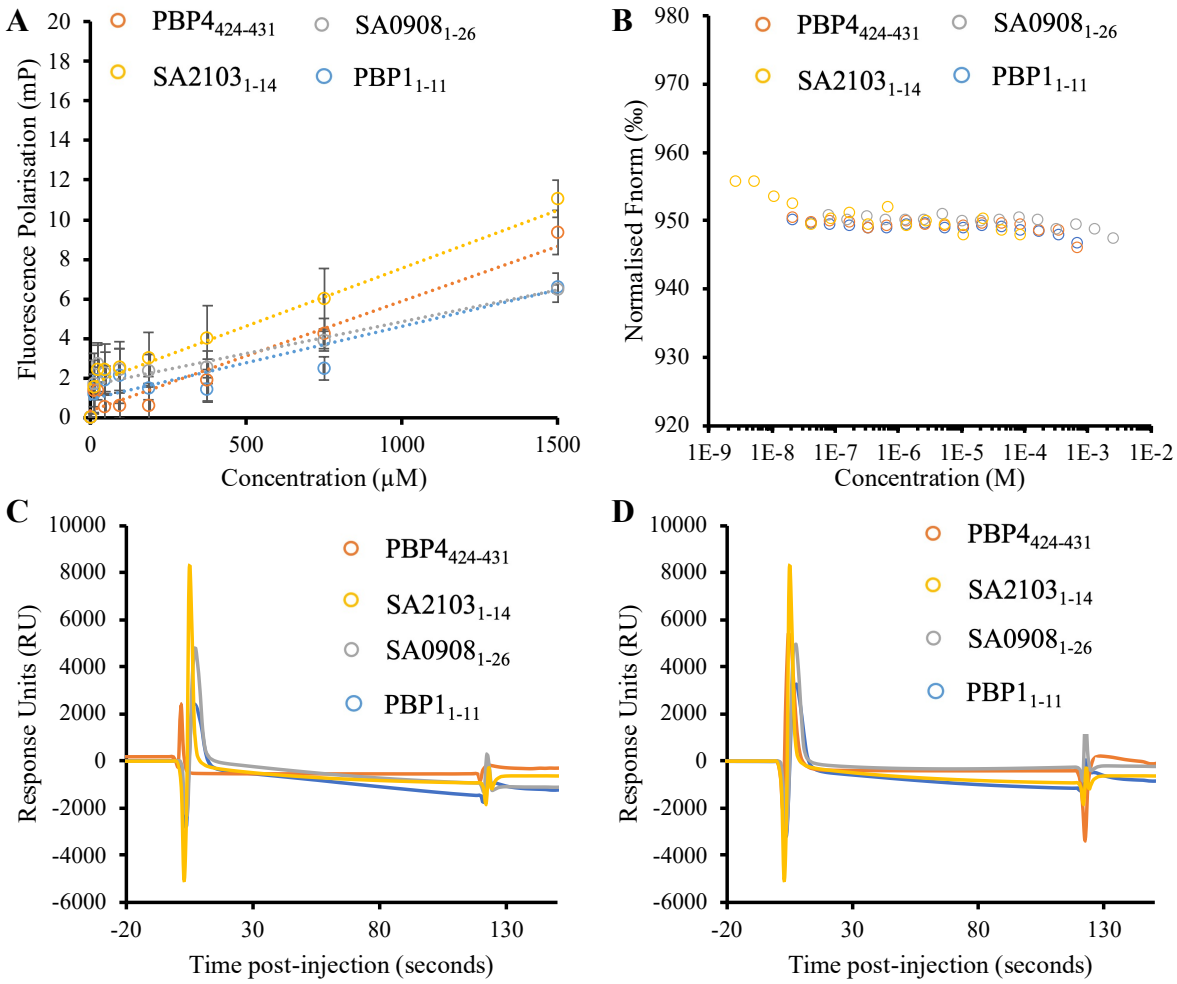

Figure 3.27: Interaction studies of *Sa*DivIVA against members of the cell division machinery. A) Fluorescence polarisation of *Sa*DivIVA$_{FL}$ against PBP4$_{424-431}$, PBP1$_{1-11}$, SA0908$_{1-26}$, and SA2103$_{1-14}$ from *S. aureus*. **B)** MST assay of *Sa*DivIVA$_{FL}$ against the same peptides as in A, demonstrating the lack of any change in thermophoresis as a function of *Sa*DiviVA$_{FL}$ concentration. **C/D)** SPR sensorgram of N- **(C)** or C- **(D)** terminally immobilised *Sa*DivIVA$_{FL}$ against the same peptides screened in A and B.

3.12 Protein-liposome interaction studies by surface plasmon resonance

Phospholipid binding of *Sa*DivIVA was tested for *in vitro* by SPR. As with the peptide interaction studies described above, *Sa*DivIVA was immobilised onto a Ni-NTA chip (Section 2.5.2) with the His_6-tag at the N- or C-terminus of the protein, to ensure that the immobilisation of the protein onto the surface did not hinder the accessibility of the liposomes to any lipid-binding region of *Sa*DivIVA$_{FL}$. Liposomes containing a 3:1 ratio of phosphatidylethanolamine (PE) to phosphatidylglycerol (PG), *E. coli* lipid extract (containing PE, PG and cardiolipin), and PE alone were prepared (Section 2.3.10) and passed over the immobilised *Sa*DivIVA$_{FL}$ (Figure 3.28). No increase in response was seen for any of the combinations of protein:liposome, indicating a lack of binding of liposomes of these compositions to immobilised *Sa*DivIVA$_{FL}$.

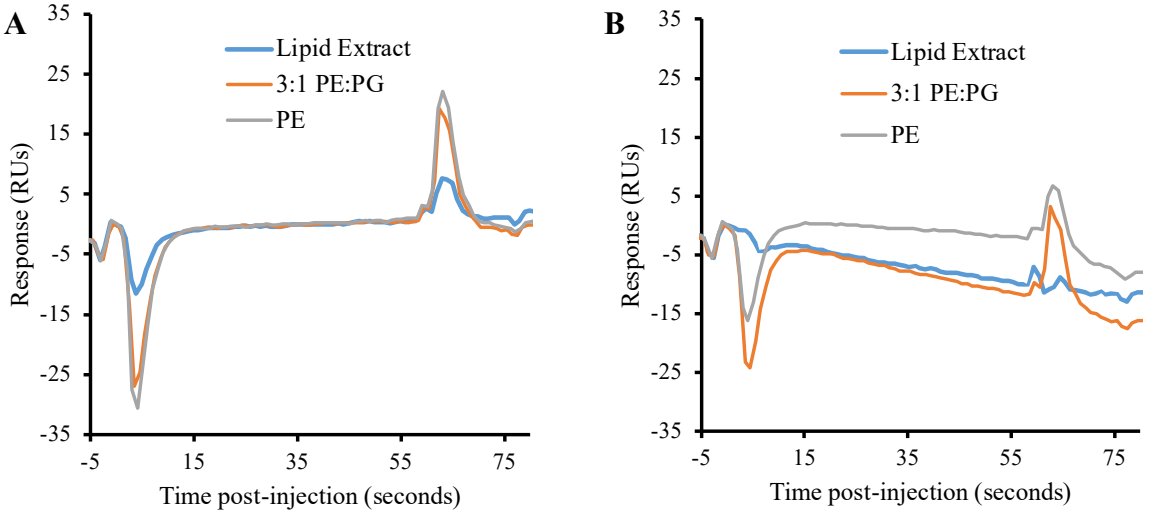

Figure 3.28: Interaction studies between *Sa*DivIVA and liposomes. N-terminally **(A)** or C-terminally **(B)** immobilised *Sa*DivIVA$_{FL}$ was screened against liposomes with varying phospholipid compositions.

3.13 *Sa*DivIVA binding to model membranes *in vivo*

As a mechanism by which to study the structure-function relationship between *Sa*DivIVA oligomerisation and membrane binding *in vivo*, fusions were generated between *Sa*DivIVA and Green Fluorescent Protein (GFP). *Sa*DivIVA was fused to monomeric superfolder GFP (msfGFP) using the pMV01 plasmid provided by Henrik Strahl (Newcastle University) (Section 2.2.6) and expressed in *E. coli* DH5α cells. The localisation of the fluorescent fusion protein was visualised by fluorescent microscopy techniques (Section 2.6.1) with supervision from Jamie Grimshaw (Newcastle University). A lipophilic fluorescent dye, FM 5-95, was used to fluorescently-label the plasma membranes of the bacterial cells studied. *Sa*DivIVA-msfGFP was observed to be diffusely localised in the cytoplasm, as shown in Figure 3.29.

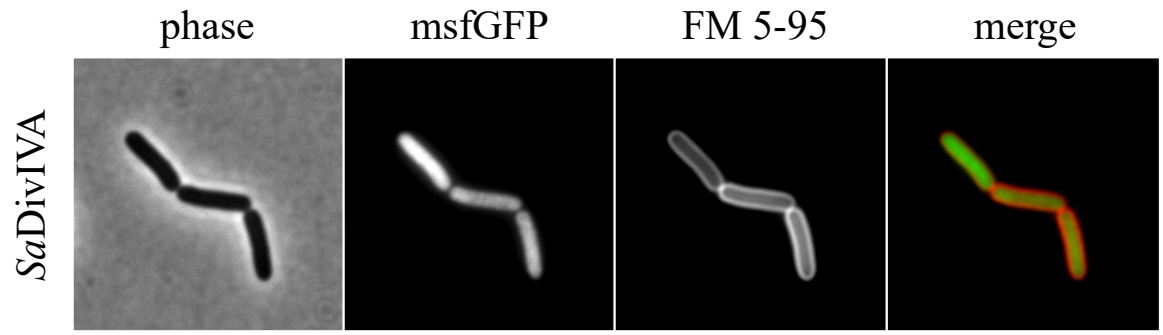

Figure 3.29: Localisation of *Sa*DivIVA-msfGFP in *E. coli* cells. *E. coli* DH5α cells harbouring pMV01-*Sa*DivIVA-msfGFP were expressed in mid-log phase and visualised by fluorescence microscopy. The lipophilic fluorescent dye FM 5-95 was used to fluorescently label the plasma membranes of *E. coli*.

To address the issue of any differences in membrane composition or differences in division morphology that are specific to *E. coli*, *B. subtilis* strain 168 was used to study the membrane binding of *Sa*DivIVA. The same construct as for the *E. coli* localisation experiments was used for *B. subtilis*, the *Sa*DivIVA-msfGFP fusion was inserted into the *amyE* locus of *B. subtilis* and the native copy of *Bs*DivIVA deleted from the genome (Section 2.2.12). *Sa*DivIVA-msfGFP was found to be cytoplasmic in *B. subtilis* cells with and without their native copy of *Bs*DivIVA (Figure 3.30ab). To further probe differences in membrane composition between *S. aureus* and *B. subtilis*, the same experiment was performed in *B. subtilis* cells lacking phosphatidylserine decarboxylase (*psd*). Removal of *psd* prevents *B. subtilis* from being able to synthesise phosphatidylethanolamine (PE), a phospholipid absent from the membrane of *S. aureus* (Hayami et al., 1979). Under these conditions, *Sa*DivIVA-msfGFP remained cytoplasmically localised (Figure 3.30b), suggesting that the presence of PE in the membrane of *B. subtilis* is likely not the reason for the lack of membrane localisation.

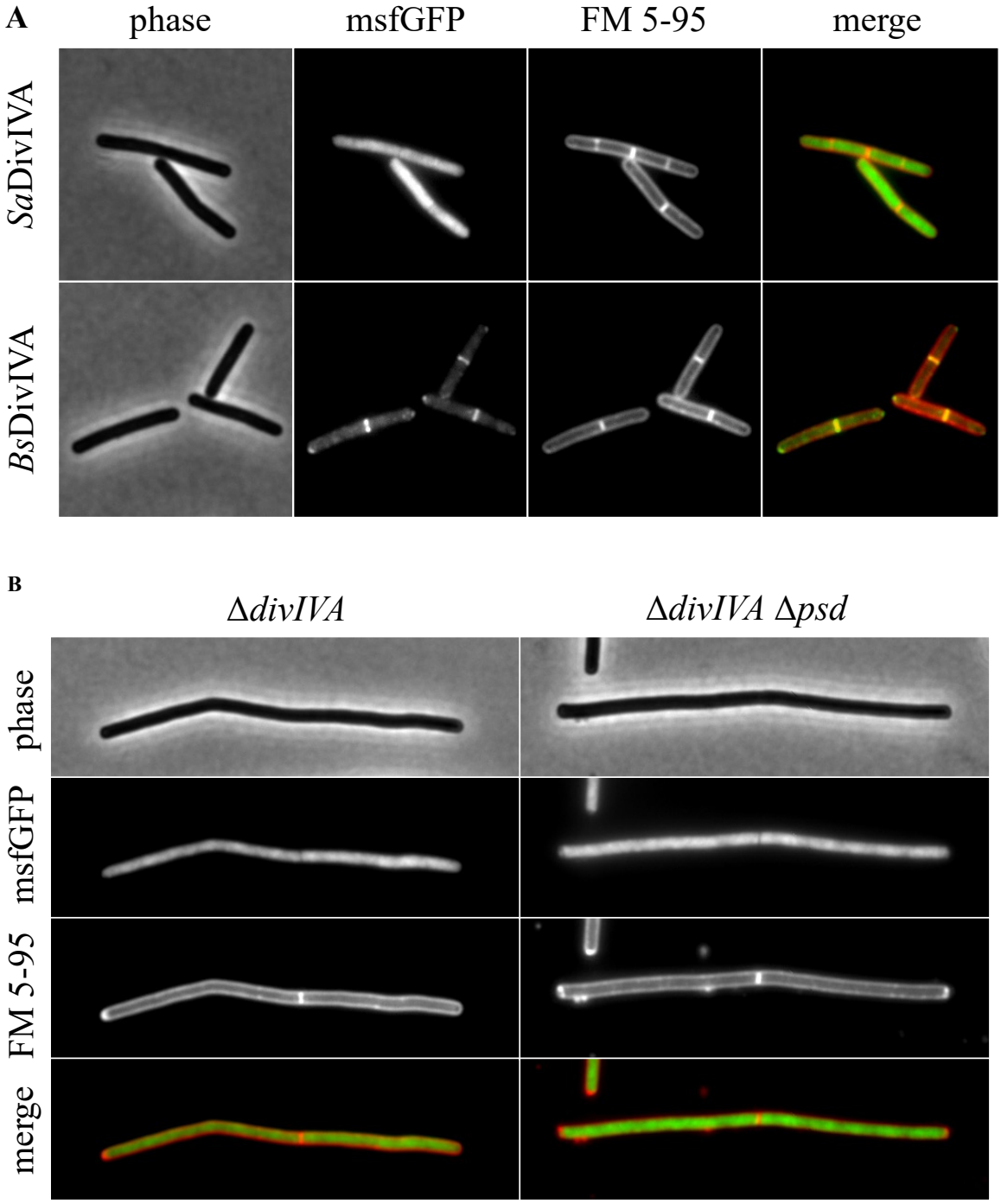

Figure 3.30: Localisation of *Sa*DivIVA-msfGFP in *B. subtilis* cells. A) Localisation of *Sa*DivIVA-msfGFP (top row) in *B. subtilis* 168. *Sa*DivIVA-msfGFP was found to be cytoplasmic in *B. subtilis* cells, in contrast to the behaviour of *Bs*DivIVA-msfGFP, which localises to the membranes and accumulates at the division septa (bottom row). The lipophilic fluorescent dye FM 5-95 was used to fluorescently label the plasma membranes of *B. subtilis*. **B)** Localisation of *Sa*DivIVA-msfGFP in *B. subtilis* ΔdivIVA and ΔdivIVAΔpsd.

3.14 Localisation studies of *Sa*DivIVA in *S. aureus*

In order to study the localisation of *Sa*DivIVA constructs in a more native environment, mEGFP fusion proteins of *Sa*DivIVA$_{FL}$, *Sa*DivIVA$_{\Delta 57\text{-}120}$, and *Sa*DivIVA$_{1\text{-}58}$ were constructed and visualised by fluorescent microscopy techniques in *S. aureus* by Dr Kasia Wacnik (University of Sheffield). Sites of active peptidoglycan synthesis were fluorescently labelled through use of the fluorescent D-amino acid HADA. *Sa*DivIVA$_{FL}$-mEGFP was observed to form punctate foci in *S. aureus*, with some localisation occurring at the septa of dividing cells (Figure 3.31). By contrast, *Sa*DivIVA$_{\Delta 57\text{-}120}$ and *Sa*DivIVA$_{1\text{-}58}$ are mostly diffusely located in the cytoplasm. The contrast between the constructs seen here may suggest that individual domains of *Sa*DivIVA are insufficient for localisation within the cell, and that the full-length protein is required for localisation, however, no experiments were performed using the C-terminus alone, therefore comparable work with the C-terminus of *Sa*DivIVA alone would be necessary in order to substantiate this claim. The length of *Sa*DivIVA also appears to play an important role in localisation, as shown by the decrease in observed foci for *Sa*DivIVA$_{\Delta 57\text{-}120}$.

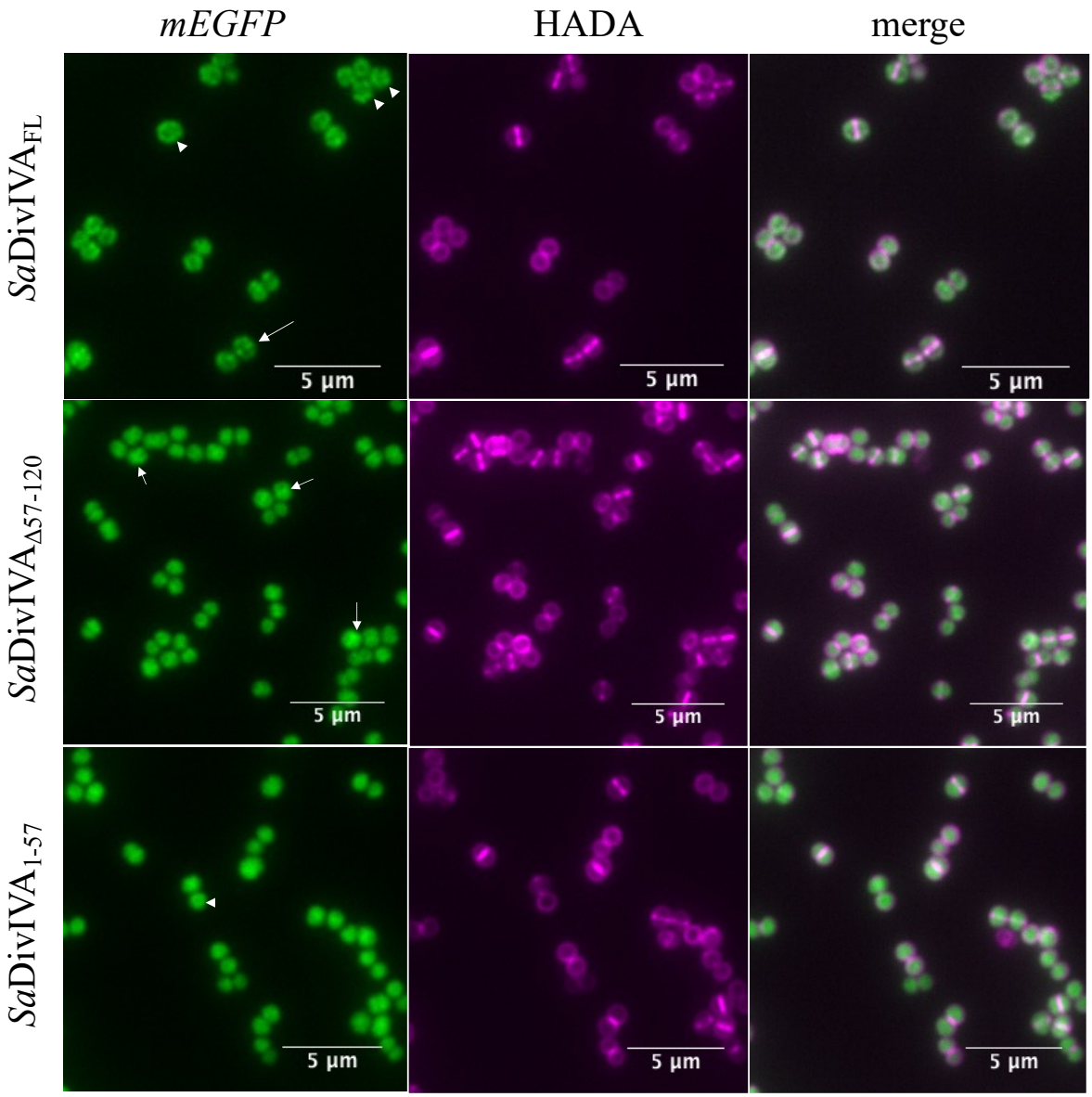

Figure 3.31: Localisation of *Sa*DivIVA-mEGFP in *S. aureus*. Localisation of *Sa*DivIVA GFP fusion proteins in *S. aureus*. The fluorescent D-amino acid HADA was used to fluorescently label the sites of active peptidoglycan synthesis. *Sa*DivIVAFL-mEGFP (top row) is observed to localise at punctate foci, with some localisation at division septa in *S. aureus* cells, indicated by white arrows. *Sa*DivIVA $_{\Delta 57\text{-}120}$-mEGFP (middle row), and *Sa*DivIVA $_{1\text{-}57}$-mEGFP (bottom row), however, form way fewer punctate foci, and are generally observed to have a more cytoplasmic distribution.

3.15 Discussion

3.15.1 *Sa*DivIVA forms a 'head-on' arrangement of parallel dimers in solution

SEC-MALS and SEC-SAXS experiments were conducted on several constructs of *Sa*DivIVA to probe the structure of the protein in solution. All of the SEC-MALS/SAXS experiments performed support the conclusion that the model of oligomerisation proposed for *Bs*DivIVA is also applicable to *Sa*DivIVA in solution. Docking of the higher resolution structures of

*Bs*DivIVA into the molecular envelope generated for *Sa*DivIVA$_{FL}$ presents a strong case for the arrangement of coiled coils in solution (Figure 3.6) and all experiments conducted to test this model support this argument. Removal of the C-terminal region of *Sa*DivIVA results in disruption of tetramer formation, indicating that the C-terminal tetramer proposed in the model of *Bs*DivIVA (Oliva et al., 2010) (and shown in Figure 3.6) is likely present in solution, and is not a result of a crystallisation artefact. The dissociation seen by SEC-MALS analysis of *Sa*DivIVA$_{1-165}$ and *Sa*DivIVA$_{1-187}$ (Figure 3.8) may indicate that the region between residues 165 and 205 contributes to the overall stability of the oligomer, but is not absolutely essential for higher order oligomerisation, whereas the region between residues 120 and 165 contains the residues essential for tetramerisation.

Based on the disruption of the tetrameric state in *Sa*DiviVA$_{1-165}$ and *Sa*DivIVA$_{1-187}$ it is likely that the entire region from residue 120 to the C-terminus of the protein contributes in some essential way to tetramer formation, and that the entirety of the region from residue 120 onwards functions in synergy with these looser interactions at the extreme ends of the C-terminus. The rigid body model produced of *Sa*DivIVA$_{FL}$ suggests that the C-terminus of the protein immediately following the tetramerisation domain is disordered. The disorder is consistent with the molecular envelope generated for *Sa*DivIVA, which does not contain enough space for the extra 41 residues present at the C-terminus of *Sa*DivIVA compared to *Bs*DivIVA; it may be that the C-terminal residues are not visible in the molecular envelope of *Sa*DivIVA$_{FL}$ as they are disordered and therefore averaged out in dummy atom modelling. Only one minor truncation to the N-terminus of *Sa*DivIVA, *Sa*DivIVA$_{54-205}$, resulted in tetramer formation, any more drastic truncations from the N-terminus of *Sa*DivIVA caused the formation of soluble aggregates.

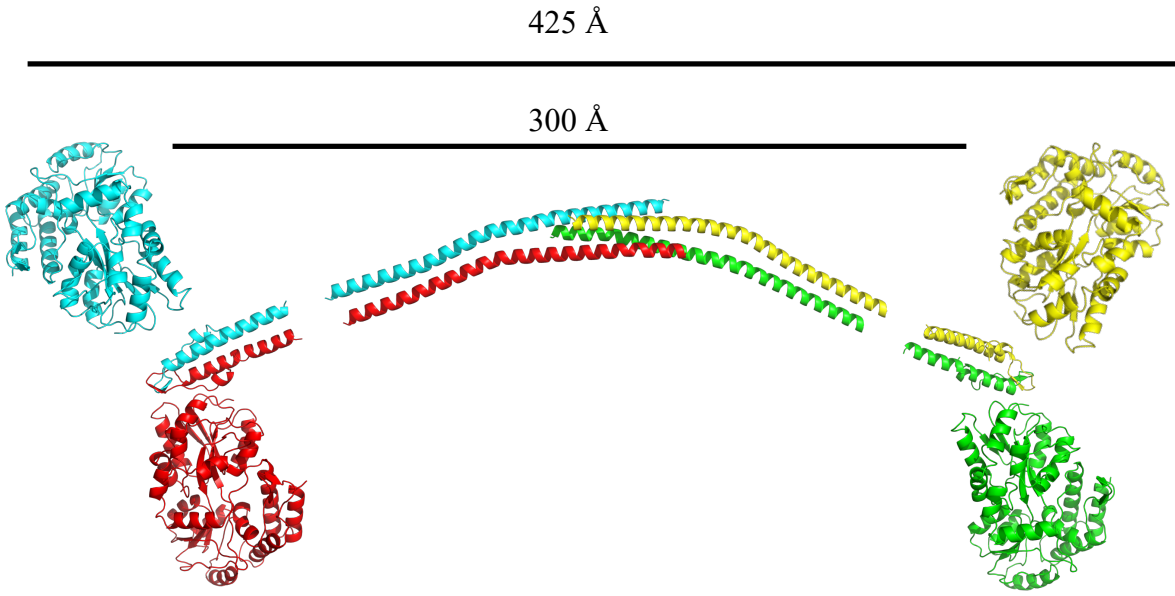

Figure 3.32: Model of tetramerisation of *Sa*DivIVA likely represented by the SAXS data for MBP-*Sa*DivIVA. The increase in interatomic distances seen in the P(r) distribution at ~280 Å likely correspond to the inter-MBP distances at the extreme ends of the molecule. The increase in D_{max} of ~125 Å roughly corresponds to the addition of two 50 Å MBP molecules at the ends of the particle.

The crystal packing of SaDivIVA$_{1\text{-}120}$, as well as the observed abberant folding behaviour of *Sa*DivIVA on N-terminal truncation suggests that the region of the protein between residues 54 and 120 is involved in the stabilisation of the tetramer, or that the C-termini may wrap over one another further towards the N-terminal ends than suggested in the model proposed in Figure 3.6. This is incompatible, however, with the data collected for *Sa*DivIVA$_{\Delta 57\text{-}120}$ in which a stable tetramer was observed despite the deletion of these residues. It is likely that the other truncation mutants forming soluble aggregates simply exposed hydrophobic residues in the coiled-coil region between residues 54 and 120, and this caused the aggregation in these samples. The increase in D_{max} seen for MBP-*Sa*DivIVA and the shifting of the local maximum of *Sa*DivIVA$_{FL}$ to larger interatomic distances (Figure 3.21) is indicative of the presence of MBP at opposing ends of the particle, consistent with the N-terminal ends of *Sa*DivIVA being present at opposite ends of the molecule; a model of this is shown in Figure 3.32. Taken together, all of the aforementioned data build a convincing case for the model of DivIVA tetramerisation.

3.15.2 *Sa*DivIVA does not interact with PBP1, PBP4, SA0908, or SA2103 *in vitro*.

A combination of biochemical assays were used to assess the interaction of *Sa*DivIVA with a variety of cell division-relevant proteins. Despite bacterial two-hybrid data identifying

interactions between *Sa*DivIVA and these proteins, *Sa*DivIVA was not found to bind to any of these proposed binding partners *in vitro*. The discrepancy between the *in vivo* and *in vitro* data may reflect a shortcoming in the bacterial two-hybrid assay in that it essentially measures proximity of the two proteins of interest in the cell. A positive result by bacterial two-hybrid relies upon two domains of adenylate cyclase, designated T25 and T18, to come into close proximity and to catalyse the production of cyclic adenosine monophosphate (cAMP) from adenosine triphosphate (ATP). The cAMP generated is then able to diffuse out into the cytoplasm, inducing expression of lactose/maltose operons, which can be detected for by use of several colorimetric assays (Karimova et al., 1998). The positive results seen in bacterial two-hybrid studies against *Sa*DivIVA include several membrane proteins. As *Sa*DivIVA is thought to be associated with the membrane (Lenarcic et al., 2009), it is likely that these proteins are often in close proximity in the cell, regardless of the presence of an interaction. It is also possible that the experimental parameters used to test binding *in vitro* do not entirely represent the environment required for binding, and a combination of protein-protein and protein-lipid interactions may be required in order for *Sa*DivIVA to interact measurably with its proposed binding partners. To date, no DivIVA proteins from any other Gram-positive organism have been found to interact with any of the membrane-associated cell wall synthesis proteins discussed in this chapter, therefore, our findings that these proteins do not interact *in vitro* are actually in agreement with what is already known about DivIVA and the results from bacterial two-hybrid are more likely a result of a false-positive interaction.

3.15.3 The interaction of *Sa*DivIVA with cell membranes

Interaction studies between *Sa*DivIVA and liposomes with various lipid compositions indicate that *Sa*DivIVA does not indiscriminately bind lipid membranes measurably *in vitro*. This is consistent with the results of the localisation studies performed in *E. coli* and *B. subtilis*, in which *Sa*DivIVA is not found to localise to membranes at all. This does raise an interesting question about whether or not *Sa*DivIVA binds membranes at all, or whether the experimental setup for each of the experiments performed here is lacking in some aspect. Despite the effort taken to ensure the membrane composition of *B. subtilis* replicates that of *S. aureus*, there are still differences in the membrane composition and morphology between the two bacteria, and this may reflect a shortcoming in these experiments. In contrast to the studies performed in *B. subtilis* and *E. coli*, some punctate foci are seen for *Sa*DivIVA$_{FL}$ in *S. aureus*. It is possible that

a currently unknown factor present in *S. aureus* is responsible for the localisation of *Sa*DivIVA-$_{FL}$, such as a binding partner or kinase, which would explain the inability to identify any indiscriminate membrane-binding for *Sa*DivIVA in this study.

In the crystal structure of the N-terminal domain of *Bs*DivIVA (Oliva et al., 2010), the residues implicated in the binding of the protein to the membrane sit on the crossed-loops of the structure, with the solvent-exposed phenylalanine residues (Phe17) proposed to embed into the hydrophobic core of the membrane, and the adjacent arginine residues (Arg18) suggested to stabilise the interaction through electrostatic interactions with the surface of the membrane (Oliva et al., 2010). In *Sa*DivIVA$_{1-54}$, Lys18 and Asn19 replace Phe17 and Arg18; it is possible that the lack of a suitably hydrophobic residue in place of Phe17 in *Sa*DivIVA and the loss of positive charge from the equivalent to Arg18 suggests that the model of membrane binding proposed for *Bs*DivIVA may not apply for *Sa*DivIVA. Further investigation of this issue by site-directed mutagenesis is necessary to thoroughly test this hypothesis.

3.15.4 A structural mechanism of *Sa*DivIVA membrane binding

The biological significance of *Sa*DivIVA remains unclear. The antiparallel dimer of dimers model presented here orients the proposed lipid-binding domains of *Sa*DivIVA at opposing ends of the molecule. As DivIVA is known to bind to regions of negative curvature (Lenarcic et al., 2009), the presence of the lipid-binding domains at opposite ends of the molecule could support a model wherein efficient membrane-binding occurs only when both ends of the molecule are able to interact with the membrane. This model would favour the localisation of DivIVA at more negatively curved membranes, as the ability of both lipid-binding domains to interact with the membrane would be enhanced. An argument has been made that the curvature radius of *B. subtilis* is larger than the experimentally determined length of *Bs*DivIVA, rendering this model of binding of single DivIVA molecules at regions of curvature unlikely (Lenarcic et al., 2009; Strahl & Hamoen, 2012). Thus far the only alternative model proposed for the binding of DivIVA to negative membrane curvature, dubbed the 'molecular bridging' model, was proposed as a result of Monte-Carlo simulations (Lenarcic et al., 2009). In these simulations, the localisation of stacks of spheres with dimensions approximating the length of *Bs*DivIVA within an area approximating a *B. subtilis* cell were modelled, with weak interactions defined between the stacks and the membrane. This model proposes that DivIVA molecules require an interaction with each other in order to bridge the curvature radius of the septum and localise at the curvature of the cell, this is corroborated by TEM images of

*Bs*DivIVA in which filaments of the protein can be seen (Stahlberg et al., 2004), a feature that is not observed for *Sa*DivIVA (Figure 3.22). An experimental assay for the affinity of DivIVA proteins against membranes at differing magnitudes of negative curvature would be a powerful experiment to elucidate the mechanism of binding to negative membrane curvature. Unfortunately, the lack of such an assay represents a methodological barrier that is outside of the scope of this thesis to address. *Sa*DivIVA$_{\Delta 57\text{-}120}$ was generated in an effort to test the single molecule binding model of DivIVA to regions of negative curvature, with the rationale that a shorter version of the protein would be less able to 'measure' regions of negative curvature. The observed decrease in observed foci for *Sa*DivIVA$_{\Delta 57\text{-}120}$ construct in *S. aureus* may provide preliminary evidence supporting this theory.

Chapter 4.

The interactions of the cell division proteins GpsB, PBP4, and Stk1 from *S. aureus*

4.1. Background and aims

As discussed in Section 1.8.3, GpsB has been implicated in coordinating PBP activity in the majority of Firmicutes studied to date by an essential interaction between its N-terminal domain and the intracellular microdomains of PBPs (Cleverley et al., 2019; Lewis, 2017; Rismondo et al., 2016; Halbedel & Lewis, 2019; Booth & Lewis, 2019). Unlike its counterparts in *B. subtilis*, *S. pneumoniae* and *L. monocytogenes*, no interactions between *S. aureus* GpsB (*Sa*GpsB) and its four PBPs have been described, despite a directed effort to identify them (Steele et al., 2011); instead, *Sa*GpsB was reported to form a complex with FtsZ (Eswara et al., 2018) that has not been observed in any other species. The distance of the Z-ring from the cell membrane compared with the proximity of GpsB's PBP-binding domain to the cell membrane would suggest that, on steric grounds, a direct *Sa*GpsB:*Sa*FtsZ complex is unlikely (Halbedel & Lewis, 2019); if the reported interaction is not artefactual, it may require an as-yet undiscovered third party to bridge *Sa*GpsB and *Sa*FtsZ, or may depend on a surface in *Sa*GpsB that is not involved in regulating PBPs. GpsB's place as a member of the divisome in *S. aureus* is obviously far from established, leaving the study of this protein open to a wealth of potential discoveries. Following the well-established methods already applied to the study of GpsB homologues from *L. monocytogenes*, *S. pneumoniae*, and *B. subtilis* (Rismondo et al., 2016; Cleverley et al., 2019; Halbedel & Lewis, 2019a) may shed some light on the interactions between cell wall synthesis proteins and GpsB in *S. aureus*.

As discussed in Section 1.9, proteomic, genetic, and biochemical studies have revealed that DivIVA and GpsB are phosphorylated by eSTKs in several organisms (Hempel et al., 2012; Fleurie et al., 2014; Pompeo et al., 2015). Despite confirming the presence of phosphorylation events, none of the aforementioned work has identified any consequences of phosphorylation on cell division regulation because of a lack of any obvious phenotypic differences in eSTK gene knockouts and the absence of structural and biochemical data. Both proteins, in all species studied, contain a significant number of potential phosphorylation sites, with *Sa*GpsB containing 13 serine residues and 7 threonine residues (15.4 % of its primary structure) and *Sa*DivIVA containing 11 serine and 10 threonine residues (10.3 % of its primary structure). Sequence alignment of GpsB homologues from *L. monocytogenes*, *S. pneumoniae*, *S. aureus*, and *B. subtilis* reveals that Ser9 of *Sa*GpsB is a conserved residue, apart from in *L. monocytogenes*, where a threonine is present in place of a serine; both residue types are able to be phosphorylated by eSTKs. Thr21 has some conservation across GpsB homologues,

excluding *S. pneumoniae*. Thr4 and Ser66 are conserved across DivIVA orthologues, although in the majority of DivIVA orthologues, threonine is present in place of Ser66.

As a response to the gaps in knowledge identified above regarding *Sa*GpsB and its place as part of the wider divisome of *S. aureus*, this Chapter concerns the structural investigation of *Sa*GpsB, its interaction with PBP4 from *S. aureus* (*Sa*PBP4), and the phosphorylation of DivIVA and GpsB from *S. aureus* using the purified cytoplasmic domain of the *S. aureus* eSTK Stk1.

4.2. The structure of *Sa*GpsB and its interaction with *Sa*PBP4

4.2.1. Expression and purification of *Sa*GpsB constructs

Plasmid vectors harbouring GpsB constructs were generated by Dr Vincent Rao prior to my entry into the lab, but were verified by sequencing before use. Plasmids were transformed into competent *E. coli* (Section 2.2.3) and expressed as described in Section 2.3.1. Expression and purification of three constructs of full-length *Sa*GpsB (*Sa*GpsB$_{FL}$) was attempted, an N-terminally His$_6$-tagged *Sa*GpsB$_{FL}$, a C-terminally His$_6$-tagged *Sa*GpsB$_{FL}$, and an N-terminally GST-tagged *Sa*GpsB$_{FL}$. For each expression construct of *Sa*GpsB described above, insufficient yields or purity of *Sa*GpsB$_{FL}$ were achieved to allow for study by X-ray crystallography or even FP. Sufficiently pure *Sa*GpsB$_{FL}$ was obtained through use of the N-terminally His$_6$-tagged construct, however, protein yields were far from sufficient, as shown in Figure 4.1.

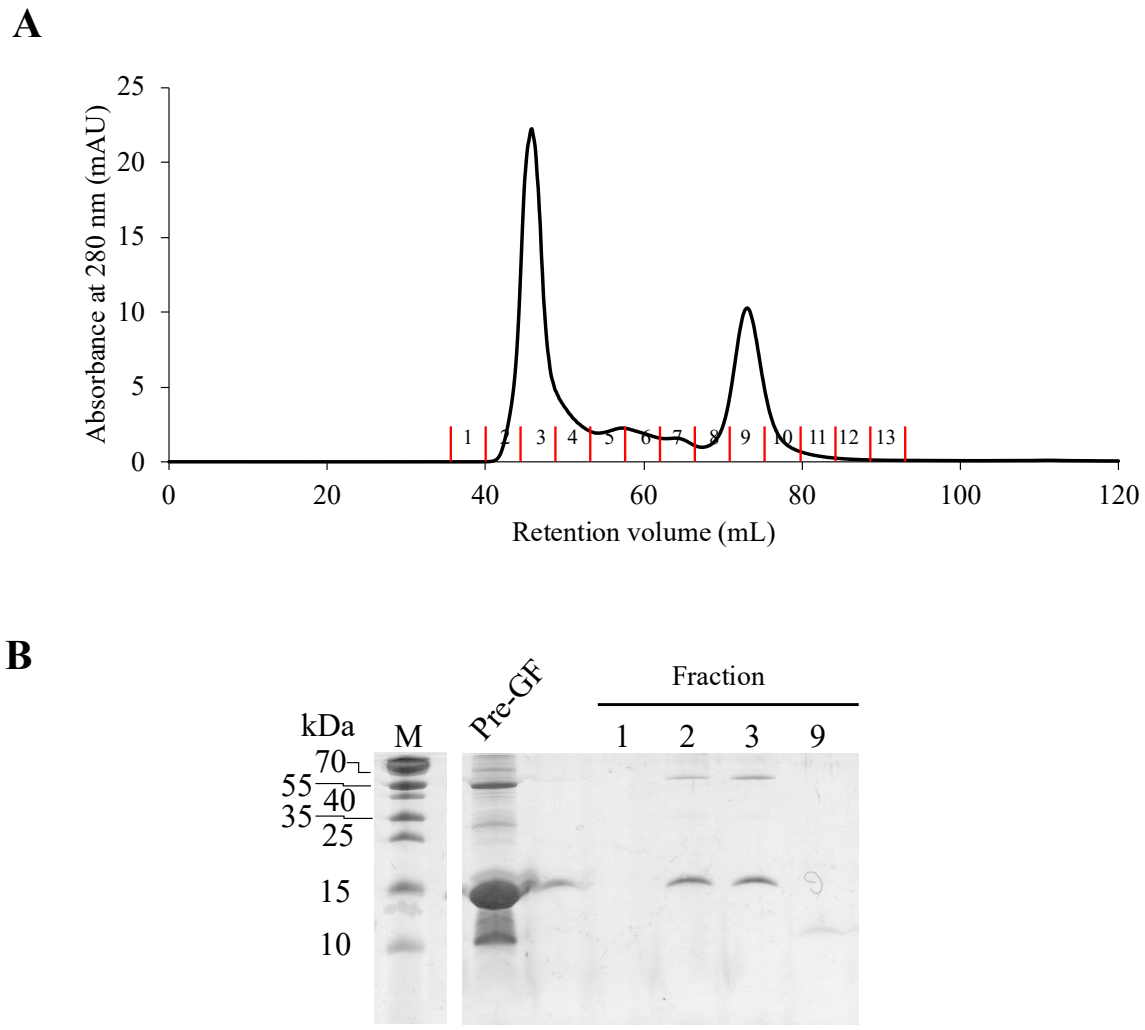

Figure 4.1: Representative purification of *Sa*GpsB$_{FL}$. A) A typical gel filtration chromatogram of *Sa*GpsB$_{FL}$ loaded onto a HiLoad Superdex 75 16/60 pg. *Sa*GpsB$_{FL}$ elutes at ~45 mL, which corresponds roughly to a hexameric molecule of *Sa*GpsB$_{FL}$ (hexameric MW = 79.2 kDa). **B)** A representative SDS-PAGE of *Sa*GpsB$_{FL}$. The major band running just below the 15 kDa molecular weight marker (lane M) corresponds to *Sa*GpsB$_{FL}$ (monomeric MW = 13.2 kDa). Based on these data, fractions 2-3 were pooled and concentrated.

As a result of the difficulty involved in producing *Sa*GpsB$_{FL}$, interaction and structural studies concerning *Sa*GpsB$_{FL}$ were abandoned and the data presented in this Chapter were mostly generated using the N-terminal domain of *Sa*GpsB encompassing residues 1 to 64 (*Sa*GpsB$_{1-64}$), which mimics much of the prior work undertaken on GpsB homologues in *B. subtilis*, *L. monocytogenes* and *S. pneumoniae* (Rismondo et al., 2016; Cleverley et al., 2019, 2016). All *Sa*GpsB constructs described in this Chapter were purified by successive steps of IMAC, proteolytic cleavage of N-terminal His$_6$-tags by human rhinovirus 3C protease, and size-exclusion chromatography (Sections 2.3.3, 2.3.4, and 2.3.6). A representative size-exclusion chromatogram, the final purification step for *Sa*GpsB$_{1-64}$, and associated SDS-PAGE analysis, is shown in Figure 4.2. In the size exclusion purifications of both *Sa*GpsB$_{FL}$ and *Sa*GpsB$_{1-64}$ an

additional protein band at approximately 55 kDa can be seen that co-purified with *Sa*GpsB$_{FL}$ (Figure 4.1); given this species is present in both cases it is more than likely an *E. coli* contaminant and was not considered further as it was well-separated size exclusion purifications of *Sa*GpsB$_{1-64}$ (Figure 4.2).

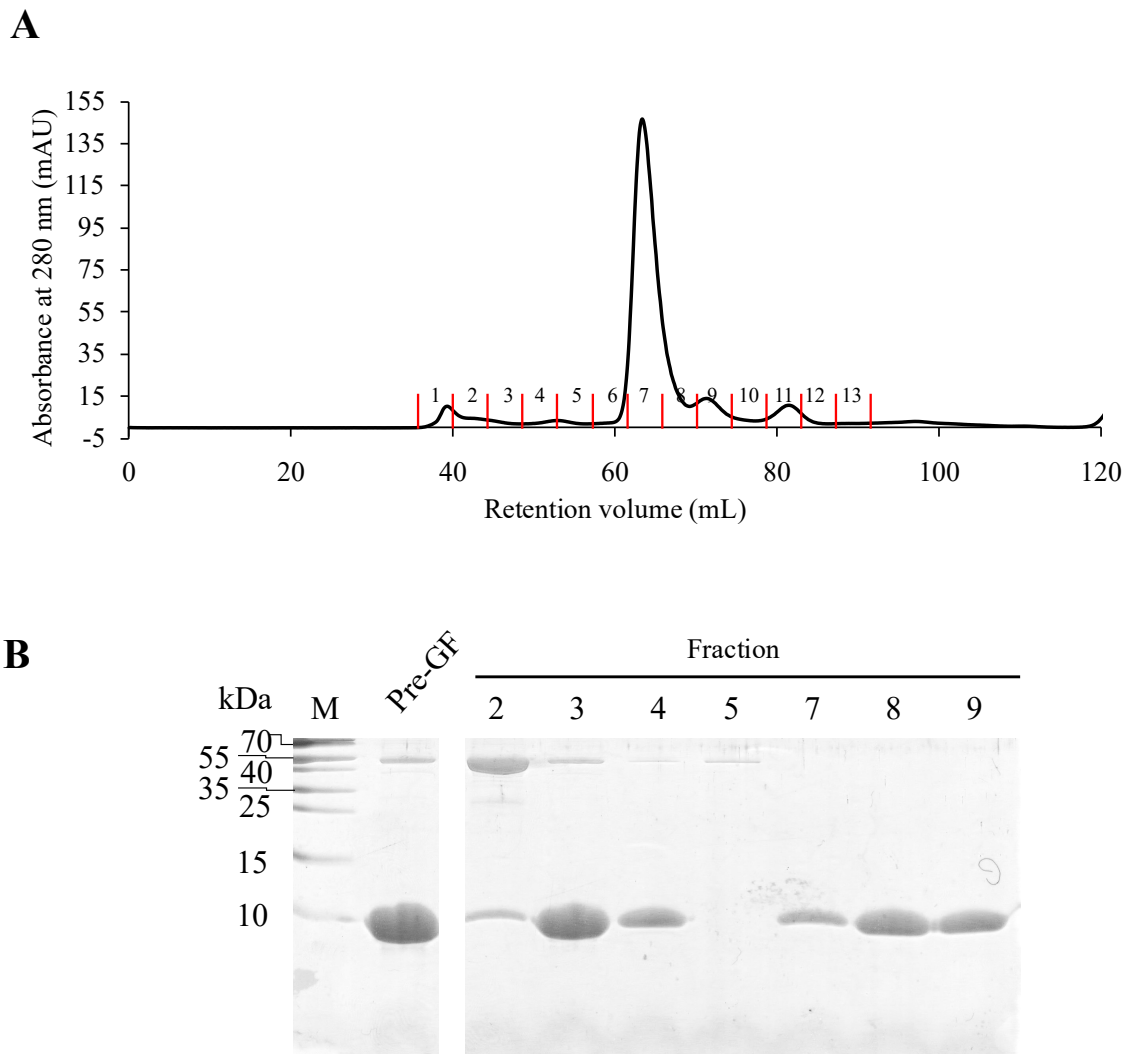

Figure 4.2: Representative final purification step of *Sa*GpsB$_{1-64}$. A) A typical gel filtration chromatogram of *Sa*GpsB$_{1-64}$ from a HiLoad Superdex 75 16/60 pg column. *Sa*GpsB$_{1-64}$ elutes at ~65 mL, which corresponds approximately to a dimeric molecule of *Sa*GpsB$_{1-64}$ (dimeric MW = 15.2 kDa). **B)** A representative SDS-PAGE of *Sa*GpsB$_{1-64}$, the major band running just below the 10 kDa molecular weight marker (lane M) corresponds to *Sa*GpsB$_{1-64}$ (monomeric MW = 7.6 kDa). Based on these data, fractions 7-9 were pooled and concentrated.

4.2.2. The crystal structure of *Sa*GpsB$_{1-64}$

Purified *Sa*GpsB$_{1-64}$ was subjected to crystallisation trials (Section 2.4.9) and crystals appeared after one week in a crystallisation solution containing 0.1 M MES/imidazole pH 6.5, 0.2 M 1,6-hexanediol, 0.2 M 1-butanol, 0.2 M (*RS*)-1,2-propanediol, 0.2 M 2-propanol, 0.2 M 1,4-

butanediol, 0.2 M 1,3-propanediol, 12.5 % (w/v) PEG 1000, 12.5 % (w/v) PEG 3350, and 12.5% (v/v) MPD. The crystals were harvested with nylon loops, and flash-frozen in liquid nitrogen before diffraction data were collected at beamline I24 of the Diamond Light Source. The structure of *Sa*GpsB$_{1-64}$ was solved by molecular replacement using the structure of the N-terminal domain of *Bs*GpsB (PDB code 4UG3; Sections 2.4.10; Rismondo et al., 2016) as the search model. Rounds of model building and refinement were interspersed (Section 2.4.10) until the structure was refined and validated to convergence using a combination of REFMAC5, PDB-REDO, and MolProbity (Murshudov et al., 2011; Joosten et al., 2014; Williams et al., 2018). The data collection and refinement statistics for *Sa*GpsB$_{1-64}$ are shown in Table 4.1.

Table 4.1: Data collection and refinement statistics for *Sa*GpsB$_{1-64}$.

	***Sa*GpsB$_{1-64}$**
Wavelength (Å)	0.97896
Resolution range (Å)[a]	47.6 - 2.3 (2.4 - 2.3)
Space group	$P\,1\,2_1\,1$
Unit cell dimensions	
***a*, *b*, *c* (Å)**	53.08, 37.17, 77.18
α, β, γ (°)	90, 102.03, 90
Total reflections[a]	24368 (2395)
Unique reflections[a]	13304 (1302)
Multiplicity[a]	1.8 (1.8)
Completeness (%)[a]	98.6 (98.6)
Mean I/σI[a]	6.91 (3.09)
Wilson B-factor (Å^2)	21.3
R_{merge}[a]	0.05 (0.21)
$R_{p.i.m.}$[a]	0.05 (0.21)
$CC_{1/2}$[a]	0.99 (0.85)
R_{work} (%)	0.19
R_{free} (%)[b]	0.22
Number of non-hydrogen atoms	2074
macromolecules	1968
solvent	106
Protein residues	239
RMS(bonds) (Å)	0.008
RMS(angles) (Å)	1.54
Ramachandran favored (%)	98.70
Ramachandran allowed (%)	1.30
Ramachandran outliers (%)	0.00
Clashscore	7.71
Average B-factor (Å^2)	34.64
macromolecules	35.11
solvent	25.91

[a]Values in parentheses denote highest resolution shell.

[b]5% of reflections were selected randomly for determination of R_{free}

The overall fold of *Sa*GpsB$_{1-64}$ is identical to that of its homologues from *B. subtilis*, *L. monocytogenes*, and *S. pneumoniae* (PDB codes 4UG3, 4UG1, and 6GQA, respectively; Rismondo et al., 2016; Cleverley et al., 2019), as well as to the N-terminal domain of its paralog, *Sa*DivIVA (Section 3.7). The RMSDs between chain A of *Sa*GpsB$_{1-64}$ and other GpsB homologues/paralogues were calculated using gesamt (Krissinel, 2012) and are shown in Table 4.2. The structure of *Sa*GpsB$_{1-64}$ is that of a short parallel coiled-coil, whose N-termini cross over and fold back onto the external face of the coiled coil (Figure 4.3).

Table 4.2: RMSD calculations between *Sa*GpsB$_{1-64}$ and GpsB homologues/paralogues.

Structure	*Sp*GpsB (6GQA)	*Bs*GpsB (4UG3)	*Lm*GpsB (4UG1)	*Bs*DivIVA (2WUJ)	*Sa*DivIVA
No. of aligned residues	55	55	55	50	50
RMSD (Å)	1.13	1.46	1.26	1.25	1.67
Sequence identity (%)	38	41	33	32	18

A slight kink is present in one of the two dimers present in the asymmetric unit of *Sa*GpsB$_{1-64}$ (Figure 4.3). The lack of a kink in both dimers, combined with its absence in any of the other known GpsB structures, would suggest that this feature is an artefact of crystal packing rather than of any biological relevance. Examination of the kinked dimer of this structure reveals three C-terminal residues, Val54, Glu58 and His61 are involved in interactions with three residues at the N-terminus of a symmetry-mate, Met23, Thr22 and Glu20 (Figure 4.4). The interactions of these residues between symmetry mates in this structure have likely positively influenced crystal packing, allowing for the crystallisation of *Sa*GpsB$_{1-64}$, underlining the unpredictable nature of macromolecular crystallisation.

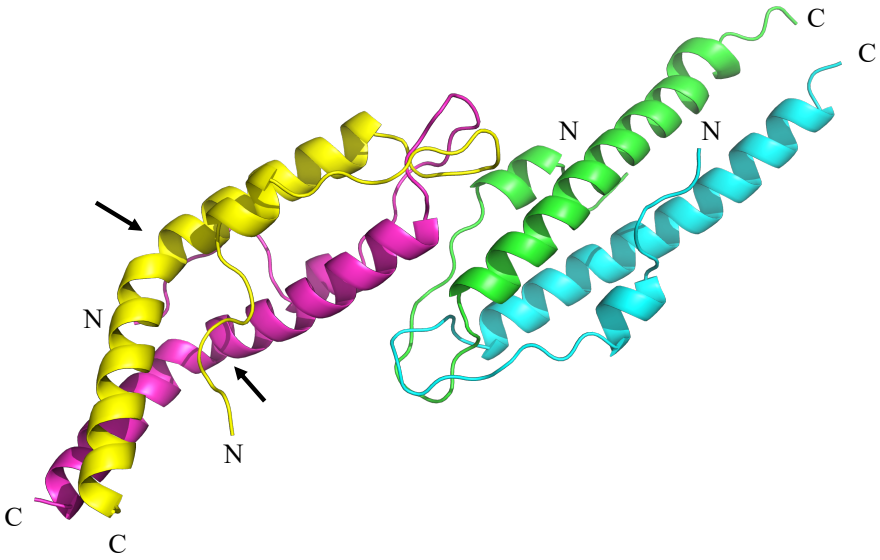

Figure 4.3: The crystal structure of *Sa*GpsB$_{1-64}$. The structure of *Sa*GpsB$_{1-64}$ is displayed as a cartoon with each monomer of GpsB displayed in a different colour. Each asymmetric unit in the crystal structure of *Sa*GpsB$_{1-64}$ contains 4 monomers.

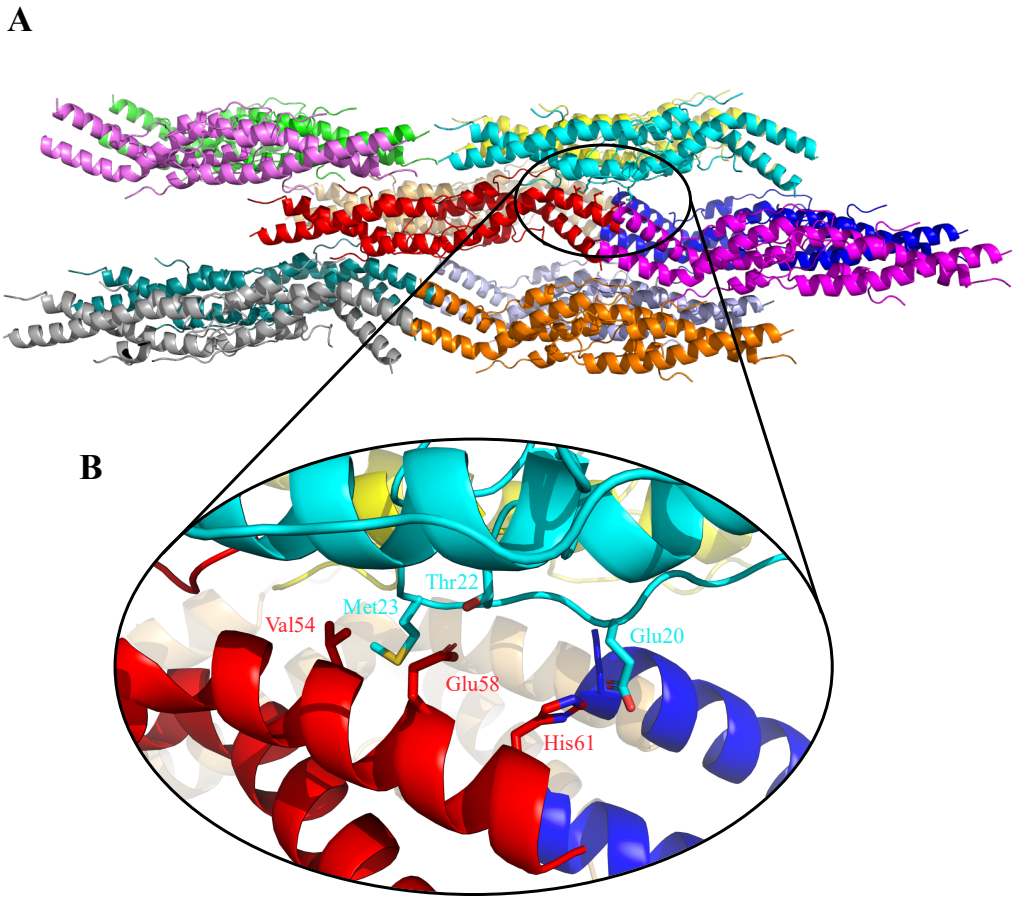

Figure 4.4: Interactions between symmetry mates in GpsB. A) The local packing environment of *Sa*GpsB$_{1-64}$, each symmetry mate is rendered in a different colour. **B)** Close-up of the kinked C-terminal region of *Sa*GpsB$_{1-64}$, highlighting residues Val54, Glu58, and His61, which form interactions with Met23, Thr22, and Glu20 of their symmetry mate.

The structure of *Sa*GpsB presented here highlights an issue in the work examining the *Sa*GpsB:*Sa*FtsZ interaction (Eswara et al., 2018). In this body of work, the authors suggested, based on size-exclusion chromatography alone, that a single amino acid mutation to *Sa*GpsB (*Sa*GpsB^{Leu35Ser}) locked *Sa*GpsB into a dodecameric state, rendering the protein inactive (Figure 5B, Eswara et al., 2018). Examination of the structure of *Sa*GpsB$_{1-64}$ reveals Leu35 to be within the hydrophobic core of the protein (Figure 4.5) and all the sidechains within 5 Å of Leu35 are hydrophobic; it thus follows that mutation of Leu35 to a polar residue is highly likely to result in aberrant protein folding. Eswara *et al* attempted to address this issue with CD analysis, comparing wild-type *Sa*GpsB with *Sa*GpsB^{Leu35Ser}, however, the CD spectra presented (Supplementary Figure 1, Eswara et al., 2018) (Appendix I) are extremely noisy and only covered a range of wavelengths between 200 and 280 nm, rather than the typically utilised range of 180/190 nm to 280 nm. Valuable CD data for predominantly alpha-helical proteins is found at ~195 nm, where a global maximum is typically observed, the lack of any data in this region renders any quantitative analyses of secondary structure inaccurate (Kelly et al., 2005). It is also somewhat concerning that the mutation from leucine to serine produced an apparent ~3 kDa shift in mass on SDS-PAGE (Figure 5A, Eswara et al., 2018) (Appendix I). It could be presumed, therefore, that any changes in *Sa*GpsB function identified in the Eswara study as a result of the Leu35Ser mutation are more likely a result of a protein folding-artefact rather than of any biological relevance. Due to time constraints, a Leu35Ser version of *Sa*GpsB was not purified during this project, however, a more thorough structural and biophysical analysis of a Leu35Ser substitution either in *Sa*GpsB$_{1-64}$ or *Sa*GpsB$_{FL}$ is necessary to analyse in greater depth the claims of Eswara et al., 2018.

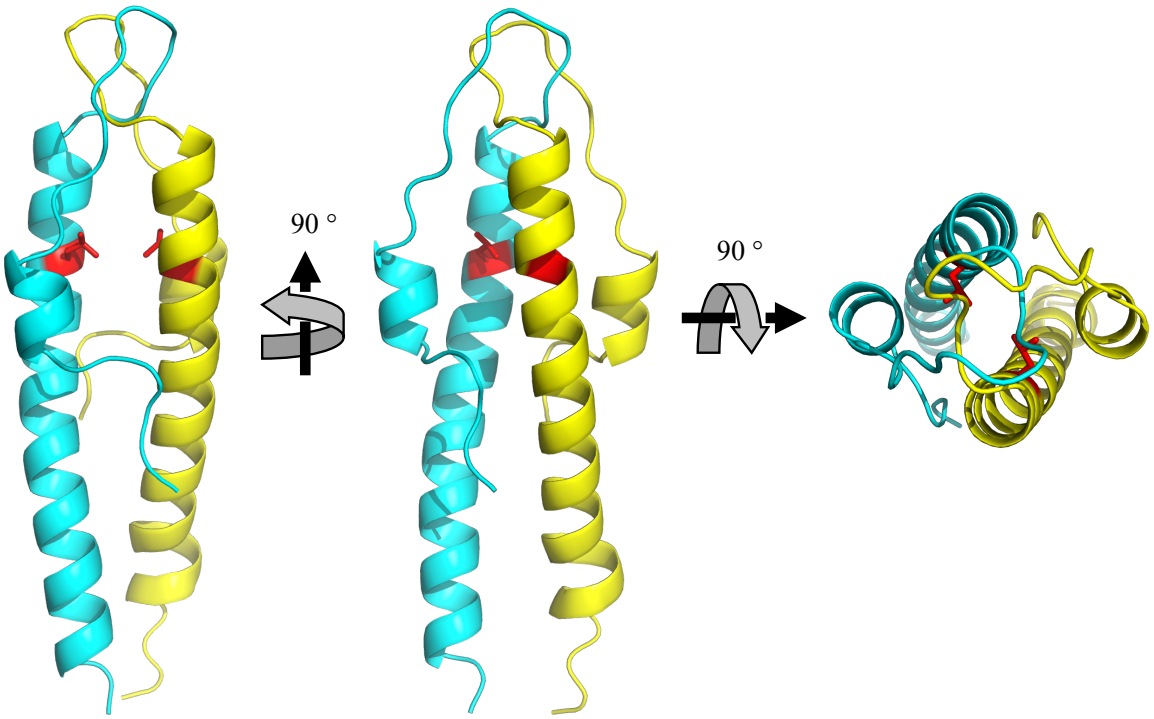

Figure 4.5: Leu35 is buried in the structure of *Sa*GpsB$_{1\text{-}64}$. The structure of *Sa*GpsB is rendered in three different orientations as a cartoon, with chain A and B rendered in cyan and yellow, respectively. Leu35 is rendered as sticks and is coloured red. Leu35 is clearly buried in the centre of *Sa*GpsB$_{1\text{-}64}$, therefore any changes to its polarity or size are likely to have substantive negative effects on *Sa*GpsB's structure.

Previous structural studies on GpsB homologues have identified arginine-rich binding motifs present on the intracellular micro-domains of PBPs, responsible for their charge-based interaction with GpsB (Cleverley et al., 2019). Superposition of *Sa*GpsB$_{1\text{-}64}$ with the PBP-bound structure of its closest-related homologue from *S. pneumoniae* (*Sp*PBP2a and *Sp*GpsB, respectively, PDB code 6GQN; Cleverley et al., 2019) would suggest that *Sa*GpsB harbours the residues necessary for a similar mode of interaction (Figure 4.6). Generation of a vacuum electrostatic surface map of *Sa*GpsB$_{1\text{-}64}$ reveals a negatively charged cavity that would be suitable for binding positively charged amino acids (Figure 4.7a), similar to the GpsB homologues from *B. subtilis*, *S. pneumoniae*, and *L monocytogenes* (Rismondo et al., 2016; Cleverley et al., 2019). Of the four PBPs encoded by *S. aureus*, PBP4 (*Sa*PBP4) is the only PBP with an arginine-rich intracellular micro-domain, suggesting that it may bind to *Sa*GpsB. In this instance, however, the intracellular domain of *Sa*PBP4 is at the C-terminus of the protein, whereas all the other PBPs and other proteins demonstrated to bind to GpsB in *L. monocytogenes*, *B. subtilis* and *S. pneumoniae* have their GpsB-binding microdomains at their N-termini (Cleverley et al., 2019; Rismondo et al., 2016; Halbedel & Lewis, 2019; Booth & Lewis, 2019). The other three *Sa*PBPs are membrane-anchored at their N-termini, with each

intracellular microdomain containing fewer arginines, and are therefore less likely to interact with *Sa*GpsB.

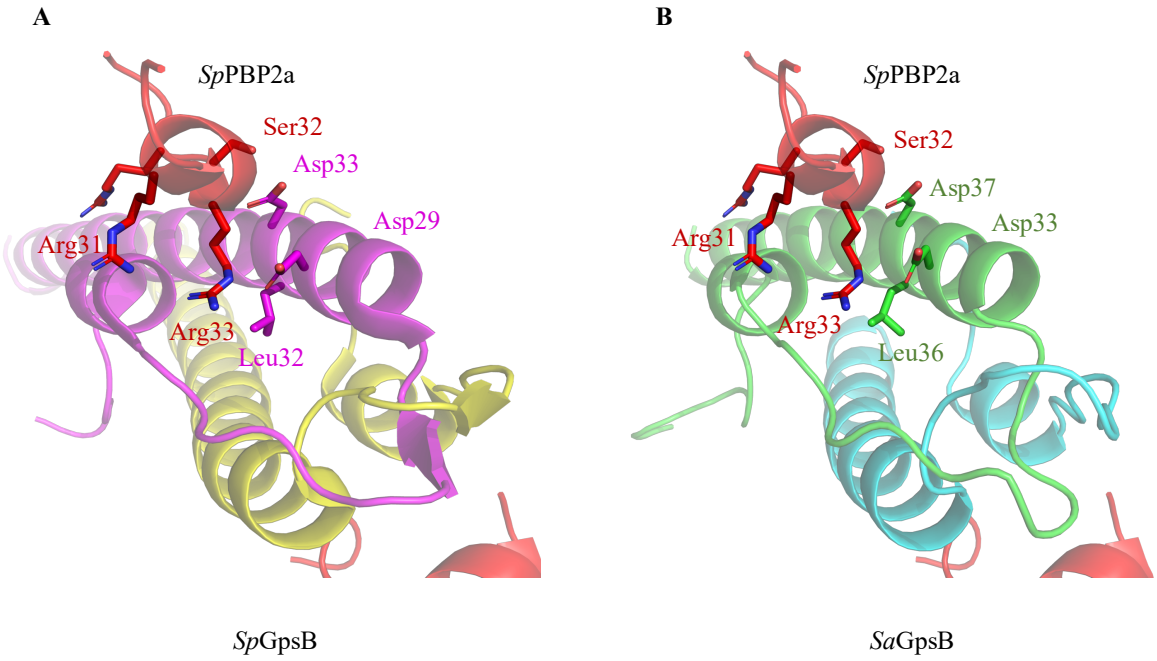

Figure 4.6: Superimposition of the peptide-bound structure of *Sp*GpsB:*Sp*PBP2a with *Sa*GpsB$_{1\text{-}64}$. The structure of chains A & B of *Sa*GpsB and *Sp*GpsB were superimposed in PyMol and either **A)** *Sp*GpsB, or **B)** *Sa*GpsB, rendered. *Sa*PBP2a appears to have the potential to form all the necessary interactions to *Sa*GpsB to bind to *Sa*GpsB. The interactions between Arg36 and its binding partner are exclusively with mainchain carbonyls, not depicted here for clarity.

A theoretical model of a putative *Sa*GpsB:*Sa*PBP4 interaction was generated in Molrep (Vagin & Teplyakov, 1997) using the sequence of the intracellular *Sa*PBP4 microdomain, and the *Sp*PBP2a peptide present in the peptide-bound *Sp*GpsB structure (PDB code 6GQN; Cleverley et al., 2019) as a structural template. The *in-silico* model presented here (Figure 4.7) reveals two arginine residues on *Sa*PBP4, Arg425 and Arg428, with the potential to bind in the negatively charged putative binding pocket of *Sa*GpsB (Figure 4.7). In order to assess the potential of these proteins to interact in the manner envisaged, their interaction was quantified by fluorescence polarisation adopting the procedures already used and validated for the other GpsB orthologues and their respective binding partners (Cleverley et al., 2019, 2016; Rismondo et al., 2016).

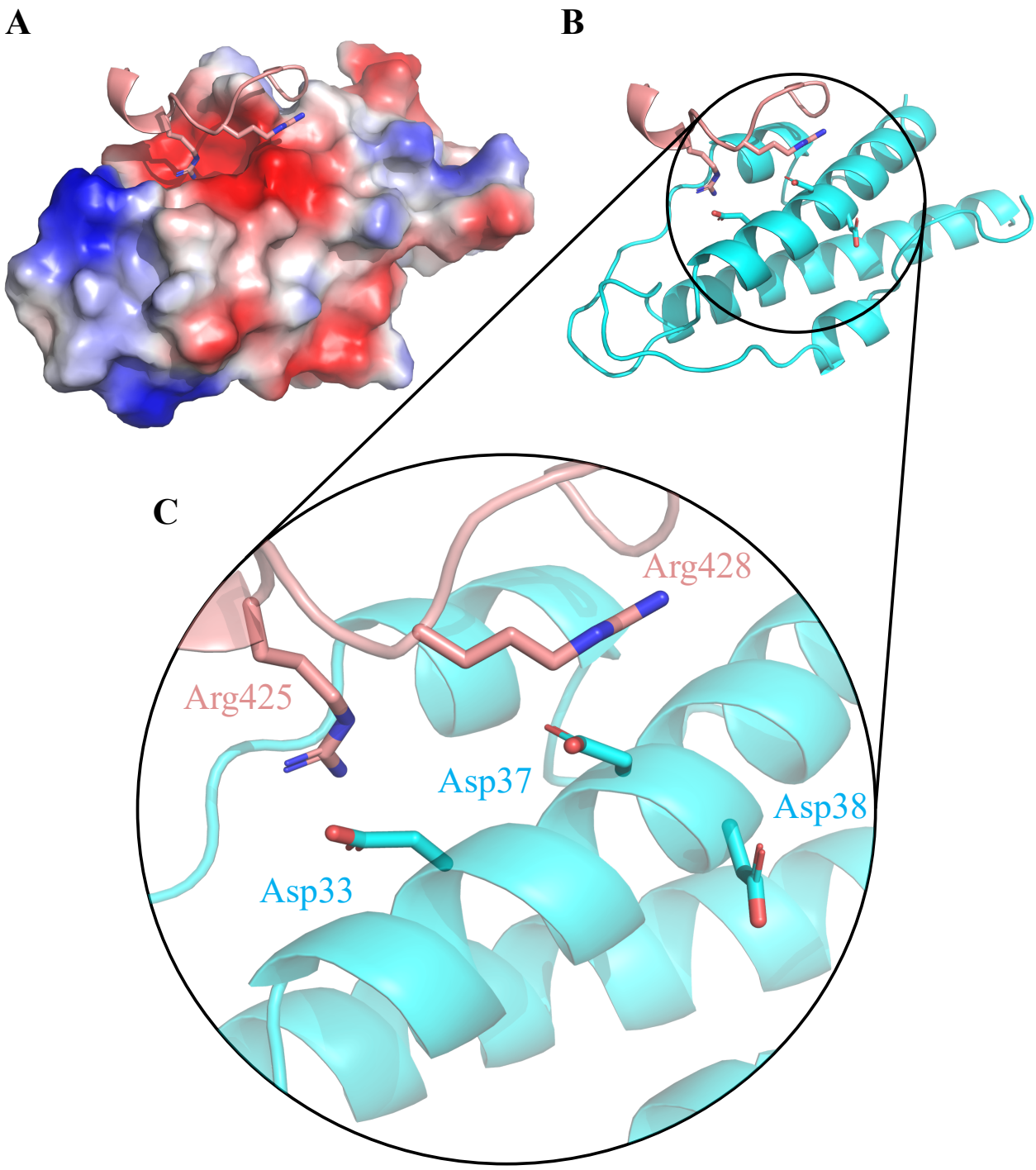

Figure 4.7: An *in silico* model of an *Sa*GpsB:*Sa*PBP4 complex and positions of proposed key residues in the binding pocket of *Sa*GpsB. A) The vacuum electrostatic surface of *Sa*GpsB$_{1\text{-}64}$ calculated and rendered by PyMol is shown, where blue and red denote positively-charged and negatively-charged regions, respectively. The *in silico* model of the *Sa*PBP4 intracellular domain is shown in salmon pink. **B)** A cartoon diagram of the proposed *Sa*GpsB:*Sa*PBP4 complex. **C)** A zoomed-in view of the proposed interface between *Sa*GpsB and the *in silico* model of *Sa*PBP4.

4.2.3. Validating the *Sa*GpsB:*Sa*PBP4 interaction model biochemically

With the *in-silico* model of the *Sa*GpsB$_{1-64}$ and *Sa*PBP4 complex in mind, the interaction between the two was tested using fluorescence polarisation (Section 2.5.4) using the same fluorescent peptide of *Sa*PBP4 as described for *Sa*DivIVA (Section 3.11.1). Binding was detected between *Sa*GpsB$_{1-64}$ and *Sa*PBP4, with a calculated K_D of 23 ± 2 μM (Figure 4.8). The K_D value calculated for *Sa*GpsB$_{1-64}$ and *Sa*PBP4 are comparable to those of previous studies on GpsB homologues and their respective PBP binding partners, which mostly occupy a range between ~30 μM and 370 μM, with an exception in *Sp*GpsB and *Sp*PBP2b, where binding was too weak to determine a K_D accurately (Cleverley et al., 2019). It is also highly likely that the K_D values reported here, as well as by Cleverley and Rismondo (Cleverley et al., 2019; Rismondo et al., 2016), are likely to be overestimated for two reasons. First, the target PBP is embedded in the cell membrane and restricted to (likely slow) movement in a 2-D plane and not free to diffuse in a 3-D cuvette. Second, because of the difficulty in obtaining GpsB$_{FL}$ proteins at high enough concentrations for FP measurements, these experiments have been conducted only with the N-terminal domain of GpsB proteins and any co-operative or avidity effect on binding the target from hexameric GpsB$_{FL}$ is lost. In the *in-silico* model generated for *Sa*GpsB and *Sa*PBP4, the residues Asp33, Asp37, and Asp38 are placed within a negatively charged pocket of *Sa*GpsB, and may therefore each contribute to binding to the positively charged arginine residues of the PBP4 peptide. In an attempt to validate the model of binding proposed *in silico*, three single mutations were introduced into this negatively charged binding pocket of *Sa*GpsB$_{1-64}$, Asp33Ala, Asp37Ala, and Asp38Ala (Figure 4.7c) through site-directed mutagenesis (Section 2.2.9).

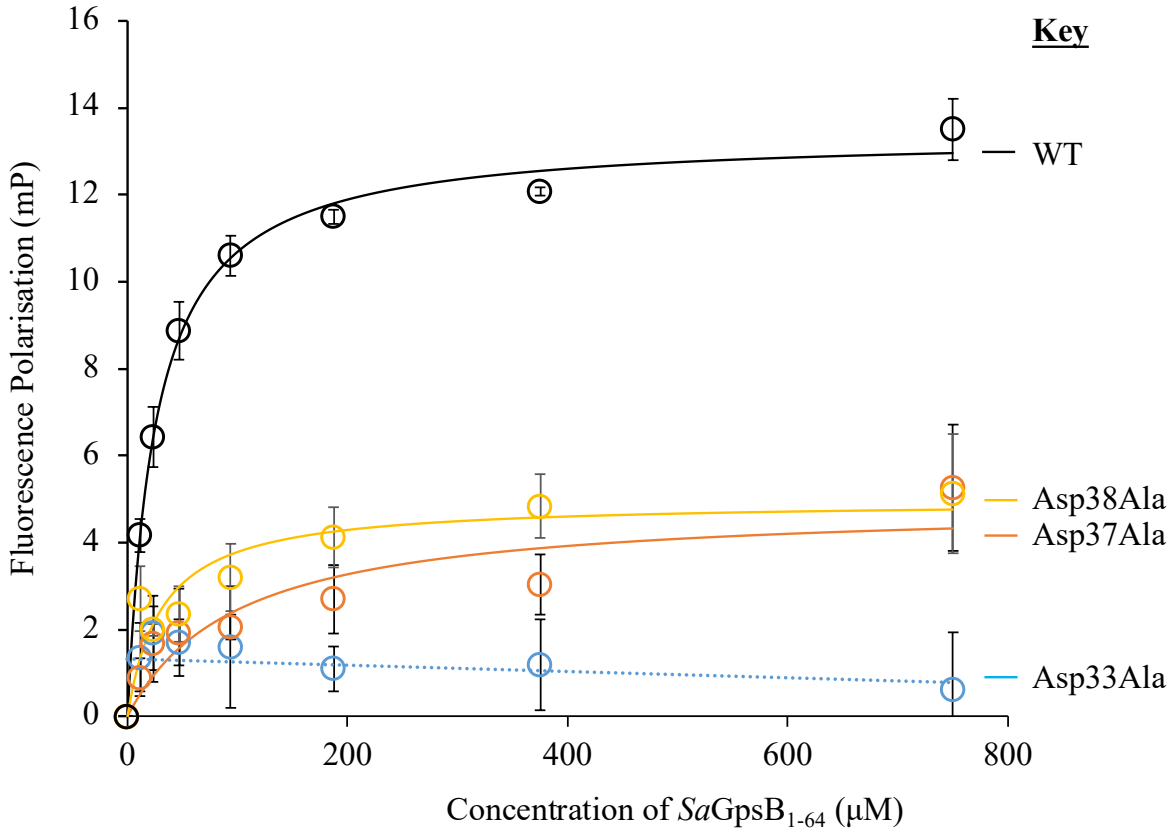

Figure 4.8: Effect of mutations to the putative binding pocket of *Sa*GpsB on binding between *Sa*GpsB and *Sa*PBP4. Fluorescence polarisation of wild-type and mutant *Sa*GpsB$_{1-64}$ against the fluorescently-labelled intracellular microdomain of *Sa*PBP4. Error bars are shown in grey, the non-linear regression line generated by SigmaPlot and used to calculate the K_D is shown as a black line. Each binding curve is shown in a different colour with its respective mutation given in the key on the right of the graph. Where non-linear regression curves have been calculated, these are shown in a colour corresponding to the data from which they were calculated. In the case of Arg33Ala, where a non-linear regression curve could not be calculated, a straight line has been plotted using the data points. The data shown here are means of 3 independent measurements and the error bars represent the standard deviations of the mean.

The binding of mutated *Sa*GpsB$_{1-64}$ proteins to the fluorescent *Sa*PBP4 peptide was tested by FP and of the three mutations generated, Asp33Ala had the most significant impact on binding, rendering a K_D incalculable by non-linear regression analysis. Asp37Ala and Asp38Ala had less pronounced effects on binding, with respective K_Ds of 100 ± 52 μM and 31 ± 13 μM (Figure 4.8). The binding data generated for these constructs confirms some aspects of the model proposed in Figure 4.7. In the *Sa*GpsB$_{1-64}$ structure, Asp33 and Asp37 are placed most centrally in the negatively charged pocket and are structural homologues of Asp29 and Asp33 from *Sp*GpsB (Figure 4.6). Equivalent inhibitory effects on PBP peptide binding have been observed for homologous mutations to GpsB homologues, for instance, an Asp33Ala mutation to *Sp*GpsB rendered binding between it and *Sp*PBP2a below the detection limit of FP analysis,

compared to a wild-type K_D of 80 μM (Cleverley et al., 2019), it stands to reason based on the model presented here that these mutations to *Sa*GpsB would have a similar effect on binding. The Asp38Ala mutation has a reduced effect on the binding affinity between *Sa*GpsB and *Sa*PBP4, which may also be explained by comparing the structures of *Sa*GpsB with all currently-solved GpsB homologues. The structural homologue of *Sa*GpsBs Asp38 in *Sp*GpsB is Asp34 (Figure 4.9), which does not form any interactions with *Sp*PBP2a in the crystal structure. Similar comparisons can be made between *Sa*GpsB and *Bs*GpsB, where the structural homologue of Asp33 in *Sa*GpsB is Asp31 in *Bs*GpsB; an Asp31Ala mutation to *Bs*GpsB results in immeasurably weak binding between *Bs*GpsB and *Bs*PBP1, which in their wild-type forms have a K_D of 100 μM. In the absence of any diffracting crystals of *Sa*GpsB:*Sa*PBP4 complexes, the effect of the mutations tested in this study would appear to validate the model of binding proposed in Section 4.2.2. Unfortunately, a lack of any clear phenotype associated with a *Sa*PBP4 or *Sa*GpsB deletion means the impact of the mutations to *S. aureus* has not been studied prior to the identification of any synthetic-lethal coupling. Should such a synthetic-lethal coupling become available, the work described here may provide useful insight into the function of *Sa*GpsB as a regulator of cell wall synthesis in spherical bacteria.

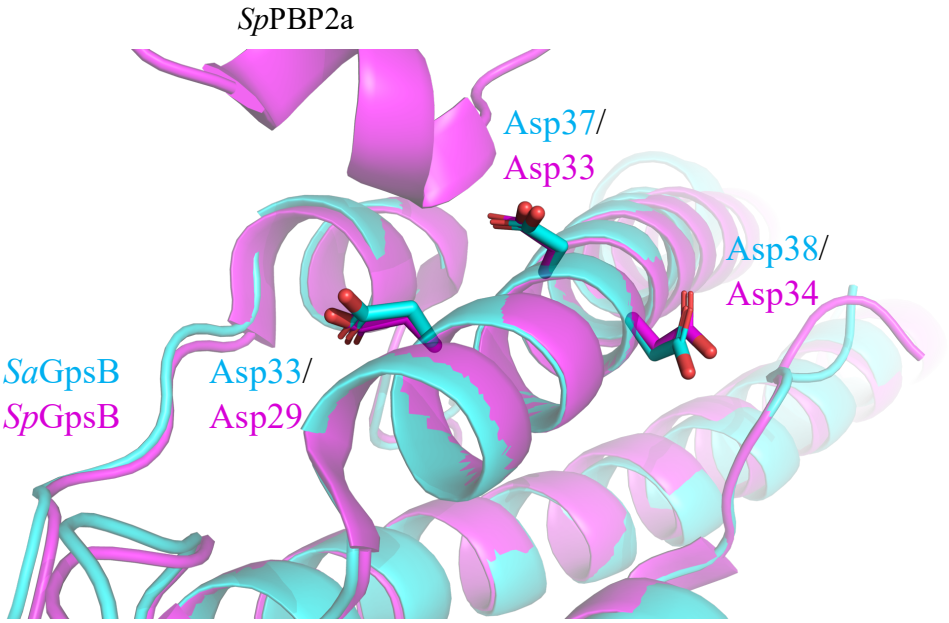

Figure 4.9: Superposition of Asp33, Asp37 and Asp38 from *Sa*GpsB with their respective Asps in *Sp*GpsB. *Sa*GpsB and *Sp*GpsB are rendered as cyan and magenta cartoons, respectively. Asp33, Asp37, and Asp38 in *Sa*GpsB are superimposable with Asp29, Asp33, and Asp38 from *Sp*GpsB.

4.3 Probing phosphorylation of *Sa*GpsB and *Sa*DivIVA *in vitro*

Conservation of potentially phosphorylatable residues in both GpsB and DivIVA supports the possibility that the function(s) of these two proteins are regulated by phosphorylation, and suggests that these residues may be important for signalling events mediated by phosphorylation across several organisms (Fleurie et al., 2014; Pompeo et al., 2015; Rued et al., 2017). As discussed in Section 1.9, the eSTK Stk1 may play a role in phosphorylation of *Sa*GpsB, as is the case with Stk1 and *Sa*GpsB homologues (Pompeo et al., 2015; Fleurie et al., 2014; Hirschfeld et al., 2020). Examination of the structures of the N-terminal domains of *Sa*DivIVA and *Sa*GpsB reveal conserved surface-exposed serines/threonines residues on each protein, potentially accessible to a protein kinase (Figure 4.10). A single structurally conserved residue, Thr4 for *Sa*DivIVA and Ser9 for *Sa*GpsB, is present between the two homologues.

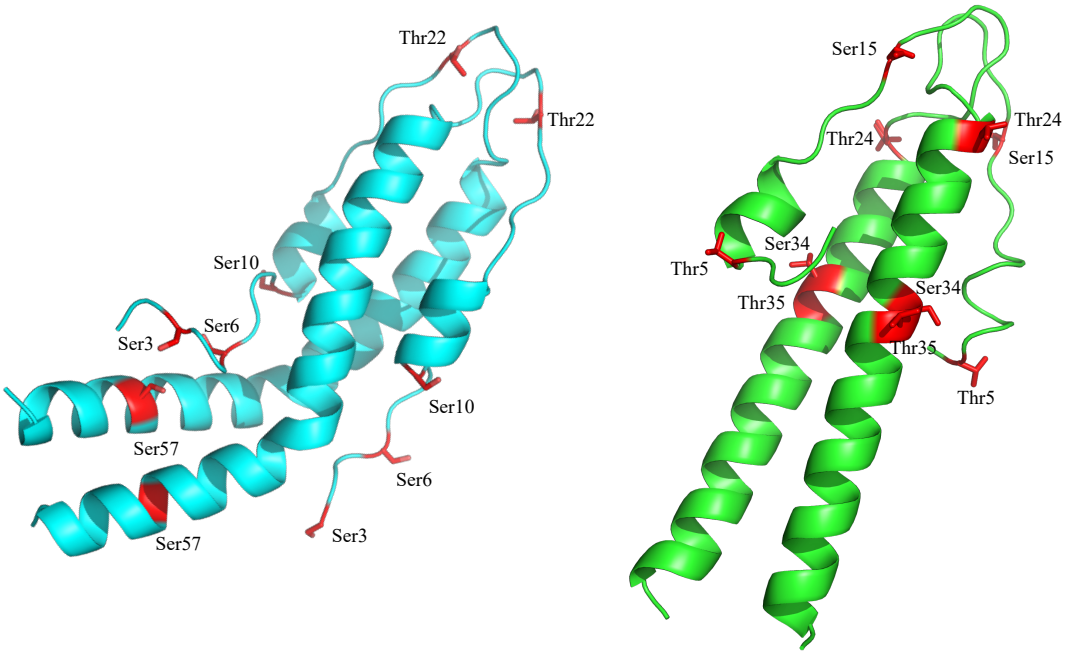

Figure 4.10: Potential sites of phosphorylation on *Sa*GpsB$_{1-64}$ and *Sa*DivIVA. The structures of *Sa*GpsB$_{1-64}$ (left) and *Sa*DivIVA (right) are shown in blue and green, respectively. Serine and threonine residues are rendered as sticks and are coloured in red. In both structures there are several surface-exposed serines and threonines with the potential for phosphorylation.

4.3.1 Purification of Stk1

The intracellular kinase domain of Stk1 (residues 1-291; Stk1$_{1-291}$) was cloned from *S. aureus* gDNA using restriction-based methods (Section 2.2.6) into the *Nco*I/*Xho*I sites of pETM-11 (Dümmler et al., 2005). Stk1$_{1-291}$ was expressed in the Lemo21(DE3) strain of *E. coli* (Section

2.3.1) and purified by IMAC, His_6-tag cleavage/reverse-IMAC, and gel filtration (Sections 2.3.3, 2.3.4, and 2.3.6). The purity of $Stk1_{1-291}$ was assessed electrophoretically (Section 2.3.9) before its concentration to ~10 $mg.ml^{-1}$. Immediately following concentration, $Stk1_{1-291}$ was flash-frozen in liquid nitrogen and stored at -80 °C until required. A representative size-exclusion chromatogram of $Stk1_{1-291}$, the final purification step for this protein, and the associated SDS-PAGE analysis, is shown in Figure 4.11.

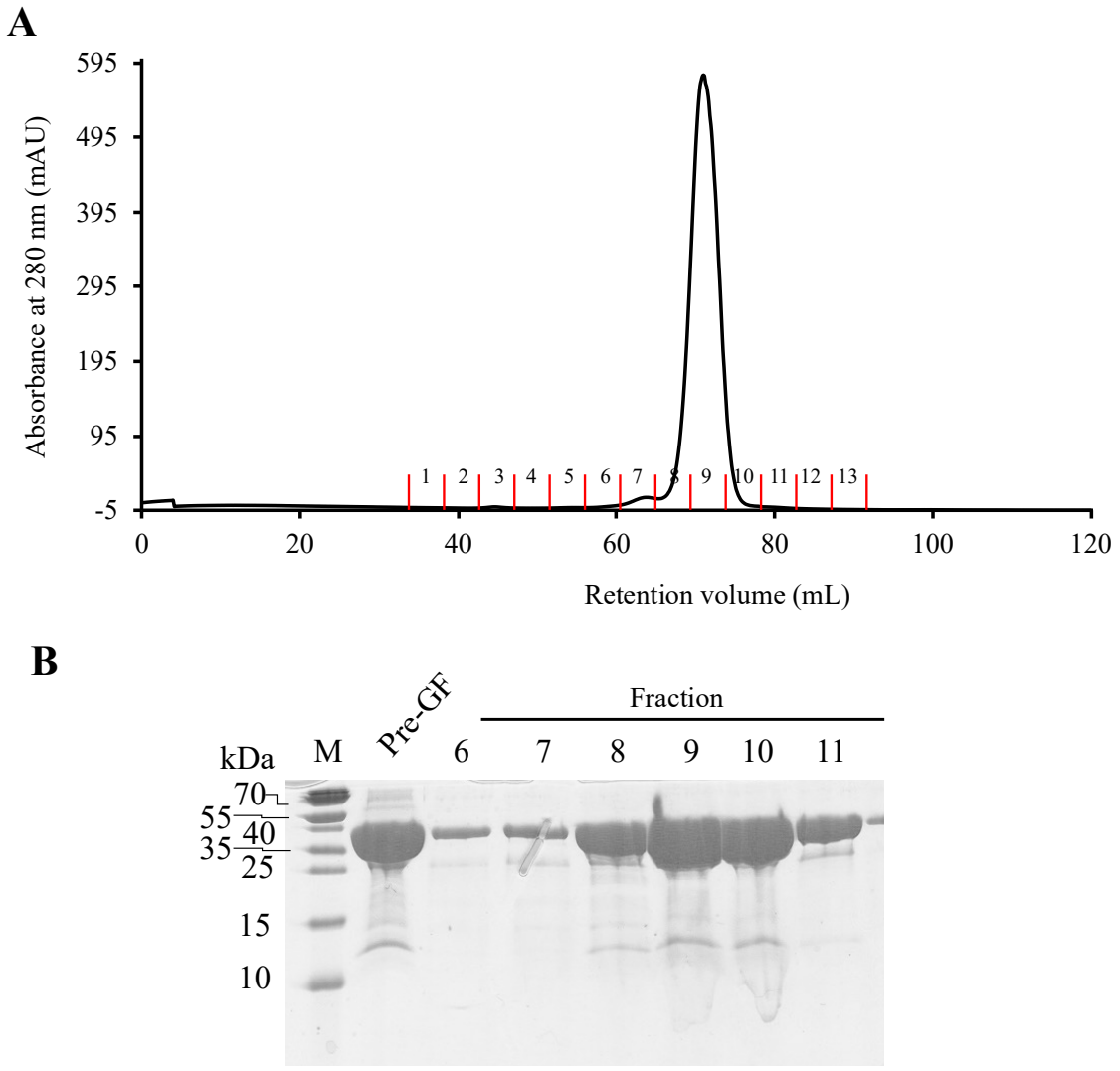

Figure 4.11: Purification of $Stk1_{1-291}$. A typical gel filtration chromatogram of $Stk1_{1-291}$ loaded onto a HiLoad Superdex 200 16/60 pg. **B)** A representative SDS-PAGE analysis of $Stk1_{1-291}$, the major band running between the 35 kDa and 40 kDa molecular weight marker (lane M) corresponds to $Stk1_{1-291}$ (monomeric MW = 33.2 kDa). Based on these data, fractions 8-10 were pooled and concentrated.

4.3.2 Phosphorylation of *Sa*DivIVA and *Sa*GpsB by Stk1$_{1\text{-}291}$.

*Sa*DivIVA$_{FL}$ or *Sa*GpsB$_{FL}$ were phosphorylated by Stk1$_{1\text{-}291}$ as described in Section 2.5.5. In an initial test for phosphorylation, the proteins were incubated with Stk1$_{1\text{-}291}$ at a ten-fold molar excess, and mixtures were assessed by native-PAGE (Section 2.4.1). Any obvious change to the electrophoretic profile of *Sa*DivIVA$_{FL}$/*Sa*GpsB$_{FL}$ was taken as an indication of a change to surface charge and/or surface shape, most likely a direct consequence of phosphorylation. Whilst no obvious change in electrophoretic mobility was observed for *Sa*DivIVA$_{FL}$, a subtle change in electrophoretic mobility was seen for *Sa*GpsB$_{FL}$; some discrete bands were identifiable for *Sa*GpsB$_{FL}$ in the absence of Stk1$_{1\text{-}291}$, however, following incubation with Stk1$_{1\text{-}291}$, *Sa*GpsB$_{FL}$ was seen as a smear on native-PAGE (Figure 4.12). Native-PAGE analysis of *Sa*DivIVA$_{FL}$ and *Sa*GpsB$_{FL}$ would suggest that *Sa*DivIVA$_{FL}$ was not phosphorylated by Stk1$_{1\text{-}291}$ but *Sa*GpsB$_{FL}$ was. Alternatively, the addition of a low number of phosphoryl groups on the multimeric *Sa*DivIVA$_{FL}$ may be insufficient to produce a change in the physicochemical properties of the protein significant enough to be observed by native-PAGE.

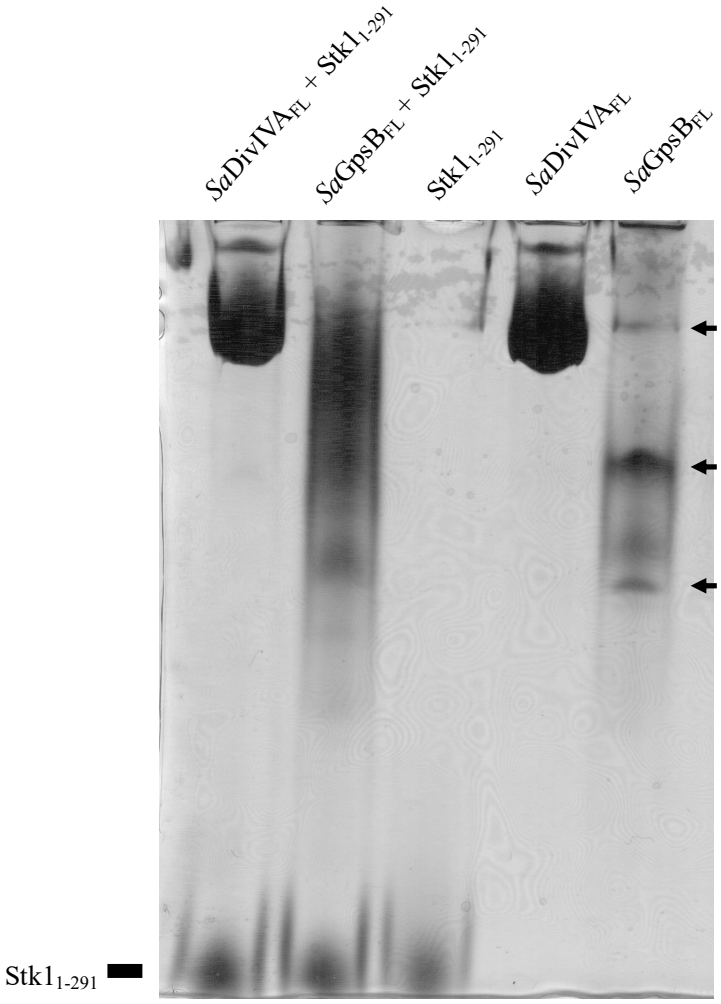

Figure 4.12: Native-PAGE analysis of *Sa*GpsB$_{FL}$ and *Sa*DivIVA$_{FL}$ phosphorylation by Stk1$_{1-291}$. *Sa*DivIVA$_{FL}$ and *Sa*GpsB$_{FL}$ were run on a native-PAGE gel in the presence and absence of Stk1$_{1-291}$ following a phosphorylation reaction. Although no obvious difference was seen between *Sa*DivIVA in the presence and absence of Stk1$_{1-291}$, there was a modest change in the profile of *Sa*GpsB$_{FL}$, which ran as a smear following incubation with Stk1$_{1-291}$, whereas in the absence of Stk1$_{1-291}$, some discrete bands are visible (marked with arrows)

Following the data seen for *Sa*GpsB, and in lieu of any immediate access to mass-spectrometry equipment, the rough domain location of phosphorylation sites on *Sa*GpsB was probed initially by repeating phosphorylation reactions with *Sa*GpsB$_{1-64}$ as a substrate for Stk1$_{1-291}$. Incubation of *Sa*GpsB$_{1-64}$ with Stk1$_{1-291}$ at a ten-fold molar excess resulted in a more obvious and discrete change in the electrophoretic profile of *Sa*GpsB$_{1-64}$, causing *Sa*GpsB$_{1-64}$ to migrate further into the gel matrix, suggesting the presence of at least one phosphorylation site at the N-terminus of *Sa*GpsB$_{FL}$ (Figure 4.13). Unfortunately, at the time of these experiments, no stable C-terminal domain of *Sa*GpsB was available, and therefore the reciprocal experiment to this one with the C-terminal domain of *Sa*GpsB was not performed.

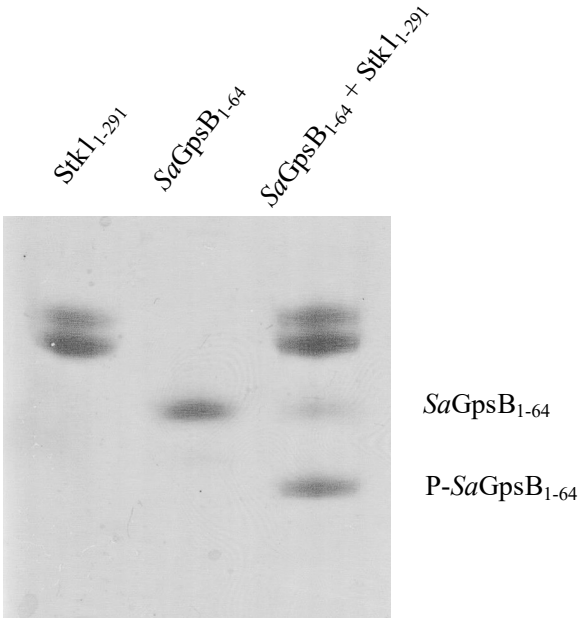

Figure 4.13: Native-PAGE analysis of *Sa*GpsB$_{1-64}$ in the presence/absence of Stk1$_{1-291}$. *Sa*GpsB$_{1-64}$ was phosphorylated by Stk1$_{1-291}$ and analysed by native-PAGE as for *Sa*GpsB$_{FL}$. A clear change is seen in the electrophoretic profile of *Sa*GpsB$_{1-64}$ following the phosphorylation reaction, and a second band is seen to be migrating faster following phosphorylation.

To confirm the hypotheses above, ESI-MS was used to confirm the presence of phosphoryl groups on *Sa*DivIVA$_{FL}$, *Sa*GpsB$_{FL}$, and *Sa*GpsB$_{1-64}$, where any mass increases of multiples of ~80 Da to the proteins would indicate the incorporation of successive phosphoryl groups. The samples, prepared as above in the presence and absence of Stk1$_{1-291}$, were sent for ESI-MS analysis (Simon Thorpe, University of Sheffield). In both the presence and absence of Stk1, the observed accurate mass of *Sa*DivIVA (25,392 Da) matched the predicted mass of the protein after cleavage of the His$_6$-tag (25,392 Da) and, in agreement with the native-PAGE data, it could be concluded that *Sa*DivIVA was not phosphorylated by Stk1$_{1-291}$ under these reaction conditions (Figure 4.14).

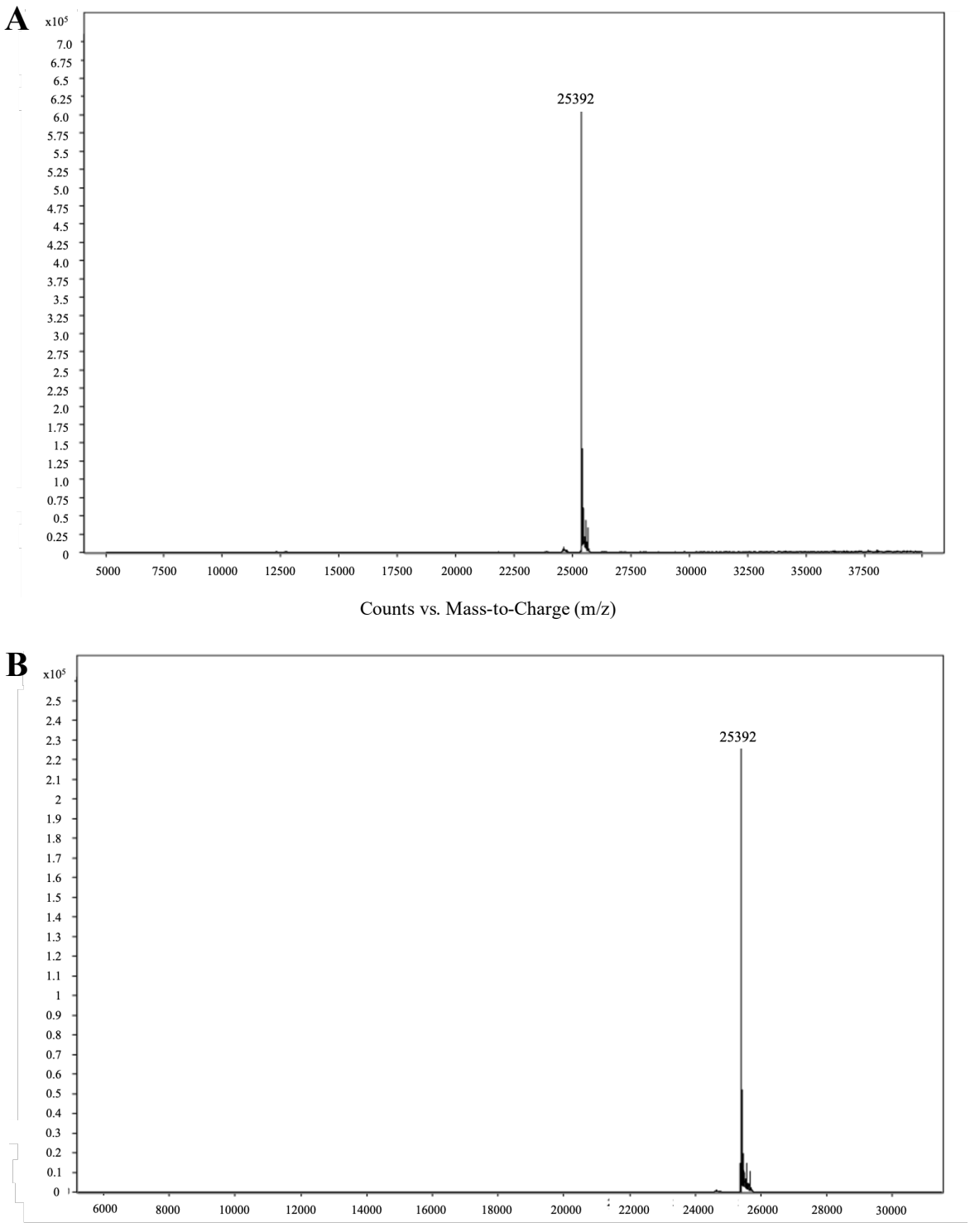

Figure 4.14: MS analysis of *Sa*DivIVA$_{FL}$ A) before and B) after incubation with Stk1$_{1-291}$. The accurate masses of *Sa*DivIVA$_{FL}$ prior to incubation with Stk1$_{2-291}$ and after incubation with Stk1$_{2-291}$ were acquired by ESI-MS. After incubation with Stk1$_{2-291}$ the mass of *Sa*DivIVA$_{FL}$ remained unchanged suggesting that no phosphorylation had occurred under these experimental conditions.

In the absence of $Stk1_{1\text{-}291}$, the observed accurate masses of *Sa*$GpsB_{FL}$ (13,714.1 Da) and *Sa*$GpsB_{1\text{-}64}$ (7,566.7 Da) matched their respective predicted mass (13173.75 and 7567.54 Da) following cleavage of the His_6-tag, however, the observed accurate mass of *Sa*$GpsB_{FL}$ in the presence of $Stk1_{1\text{-}291}$ revealed two additional peaks in the mass spectrum (13,253.9 Da and 13,333.8 Da) with increases in mass relative to unmodified *Sa*$GpsB_{FL}$ of 79.8 Da and 159.7 Da (Figure 4.15), suggesting strongly that *Sa*$GpsB_{FL}$ was phosphorylated on up to two sites. Similarly, and consistent with the native-PAGE experiments, accurate mass measurement by mass spectrometry of *Sa*$GpsB_{1\text{-}64}$ revealed a 79.96 Da increase in mass (from 7566.75 Da to 7646.71 Da) on phosphorylation by $Stk1_{1\text{-}291}$ (Figure 4.16), supporting the presence of a single phosphorylation site in the N-terminal domain of *Sa*GpsB and one in either the linker or in the C-terminal domain of *Sa*GpsB.

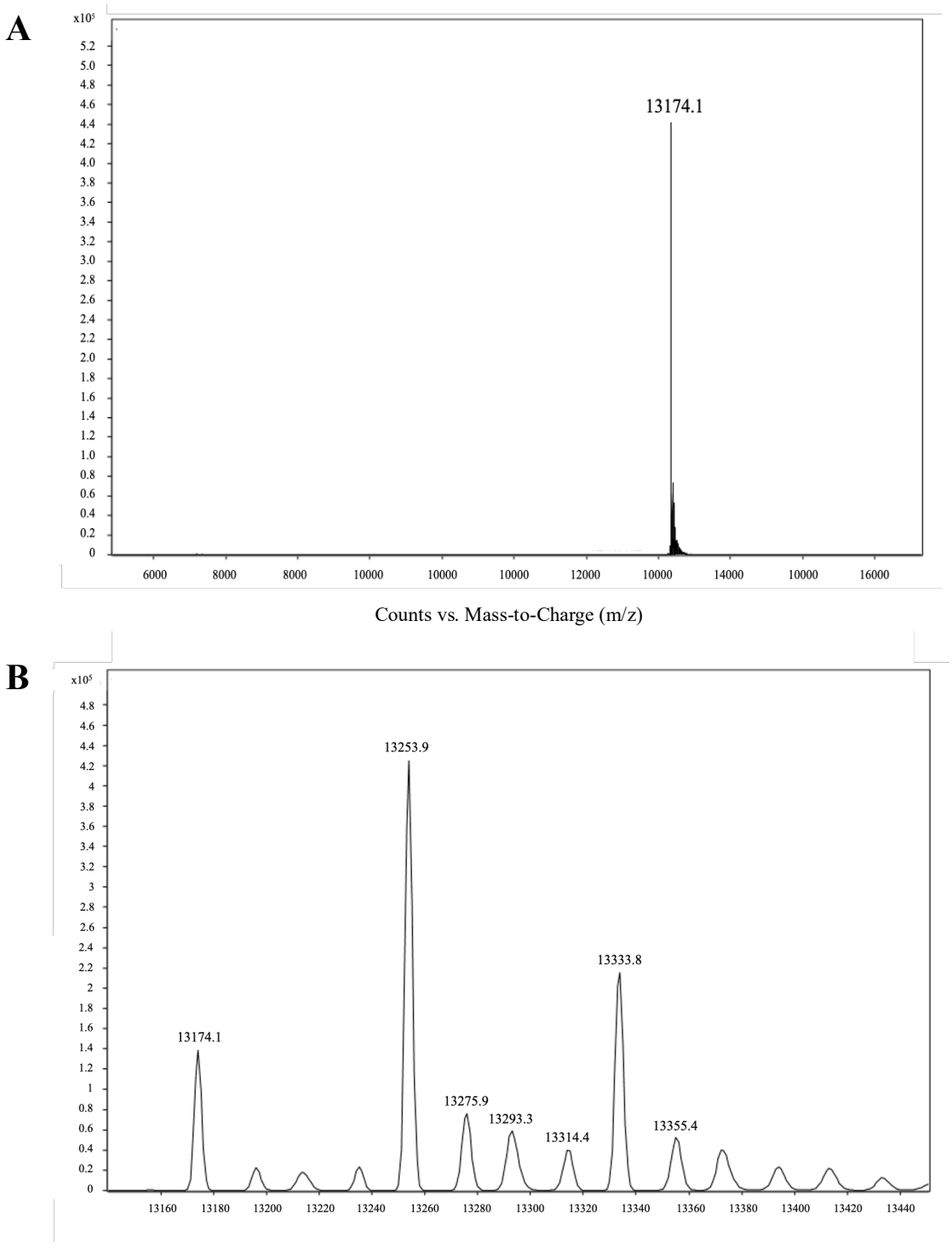

Figure 4.15: Mass-spec analysis of *Sa*GpsB$_{FL}$ A) before and B) after incubation with Stk1$_{1-291}$. Accurate mass measurements of *Sa*GpsB$_{FL}$ were taken before and after phosphorylation. Increases in mass of 79.8 Da and 159.7 Da were observed, corresponding to one and two phosphoryl groups, respectively. Some less-abundant increases in mass, with an average mass difference of 21 Da, were observed between the major peaks, and these are likely to represent $[M+Na]^-$ adducts formed in the mass spectrometer.

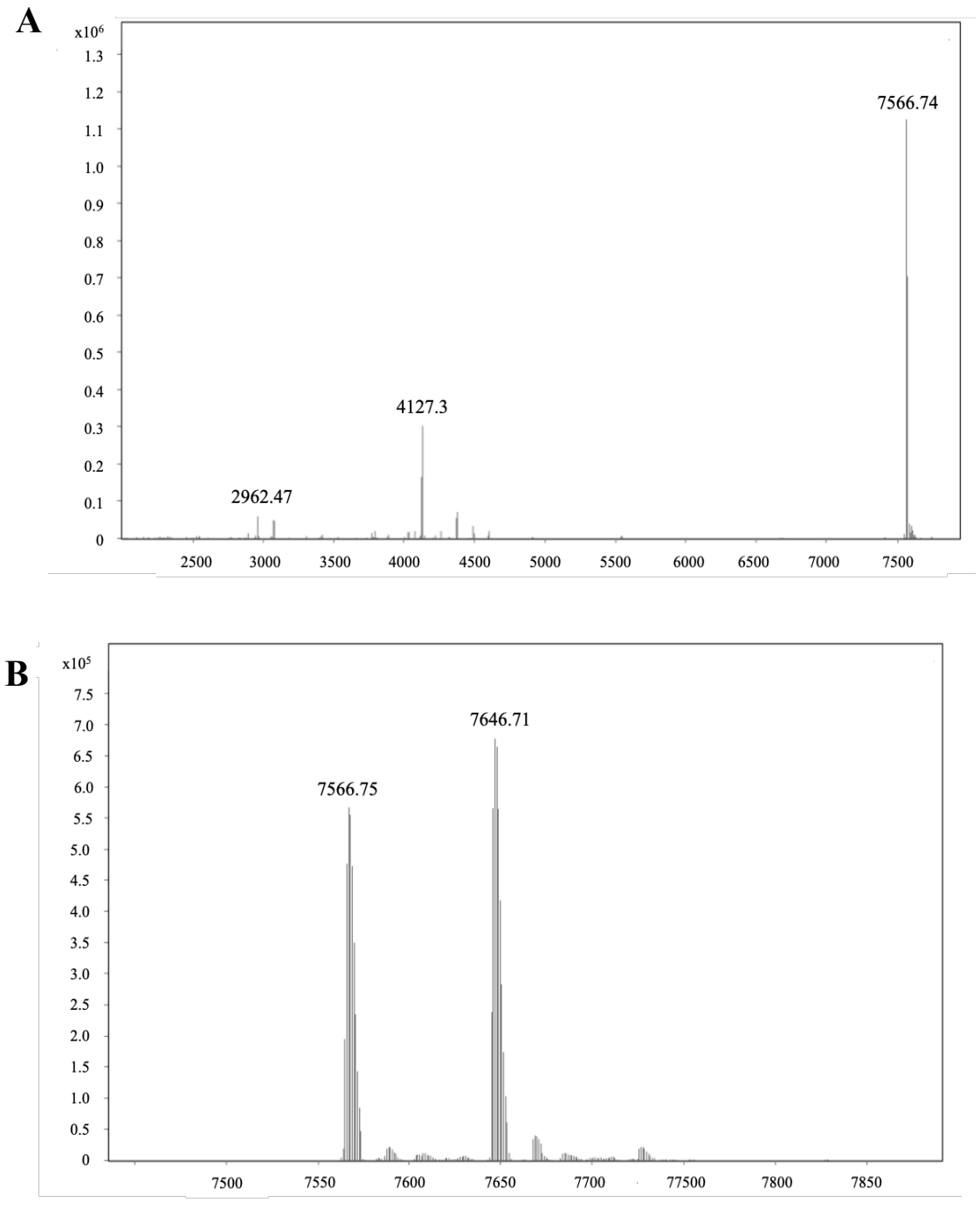

Figure 4.16: Mass-spec analysis of *Sa*GpsB$_{1-64}$ A) before and B) after incubation with Stk1. Accurate mass measurement of *Sa*GpsB$_{1-64}$ revealed the presence of a single increase in mass of 79.96 Da, consistent with the addition of a single phosphoryl group to *Sa*GpsB$_{1-64}$. Some lower molecular weight species are seen in the unphosphorylated sample, likely a result of the presence of some impurities in the sample.

4.3.3 Peptide-mass fingerprinting analysis

In order to pinpoint the residues subject to phosphorylation, peptide mass fingerprinting (PMF) analysis was employed, using the same phosphorylated *Sa*GpsB$_{FL}$ sample described above (Claire Jennings, Newcastle University). Seven serine and threonine residues in total were found to be phosphorylated on *Sa*GpsB$_{FL}$, with two phosphorylation sites on the N-terminal domain of *Sa*GpsB$_{FL}$ described by the residue boundaries 1-64 (Ser5 and Thr21) and the remaining five in the C-terminal domain, residues 65-114 (Thr89, Thr90, Thr91 and Thr93, as well as Ser105) (Figure 4.17). Interestingly, Ser5 was identified as being phosphorylated despite a lack of any obvious sequence conservation across GpsB orthologues, in contrast to Ser9, a conserved residue, which was not found to be phosphorylated by PMF analysis. Based on the structure of *Sa*GpsB$_{1-64}$, Ser5 and Thr21 would both be accessible to a protein kinase (Figure 4.8), rationalising the presence of phosphoryl groups on these residues. The cluster of phosphorylated residues at the C-terminus of *Sa*GpsB are all in close proximity (between residues 89 and 93) and are surrounded by clusters of two or three serine residues. Unfortunately, no structural data exists for this domain of GpsB, so although the presence of phosphoryl groups would suggest that these residues are solvent-accessible, there are no structural models to confirm this hypothesis. It may be the case that phosphorylation of just one of these C-terminal threonines inhibits any further phosphorylation of proximal threonines, which may explain why just one phosphorylation event is observed to rationalise the discrepancy between the intact mass measurement data and the PMF data. The phosphorylation of threonine residues in the linker between the two domains of *Sa*GpsB and the lack of any serine phosphorylation events, in spite of a wealth of potentially-available serine residues, may suggest that there is a preference for threonine as a substrate for Stk1. The preponderance of threonine phosphorylation (five) versus serine (two) sites also suggests a threonine preference for Stk1. The serine phosphorylation sites identified during peptide mass fingerprinting analysis may represent non-specific phosphorylation sites below the limit of detection by the comparatively lower resolution intact mass analysis, rationalising the lack of any phosphorylation of Ser9, as well as the discrepancy between intact mass measurement and peptide mass fingerprinting.

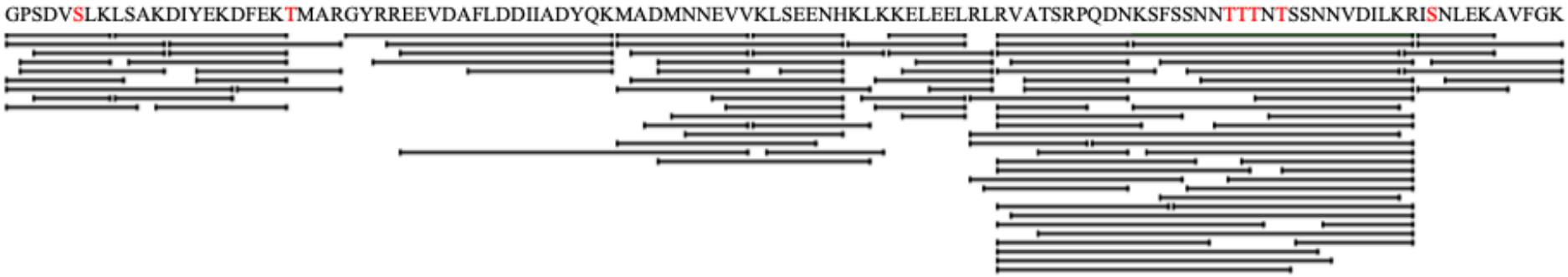

Figure 4.17: Peptide mass fingerprinting of *Sa*GpsB$_{FL}$ following phosphorylation by Stk1$_{1-291}$. The sequence of *Sa*GpsB$_{FL}$ is shown above the peptide fragments recognised as *Sa*GpsB by ProteinScape and used to identify phosphorylated residues. Seven phosphorylated residues were identified and are shown in red. Interestingly, the phosphorylation sites are grouped somewhat towards the N- and C-termini, with a long section of the middle of the protein left untouched by phosphorylation.

4.4 Discussion

Time constraints, and the absence of diffracting crystals of the *Sa*GpsB:PBP4 complex, meant that it was not possible to experimentally confirm the model of binding proposed in this Chapter, however, the data presented in this study would suggest a parallel function for GpsB in *S. aureus* as in *B. subtilis*, *L. monocytogenes*, and *S. pneumoniae* as a coordinator of PBPs. In order to thoroughly conclude *Sa*GpsBs role as a PBP coordinator, future work should concern the acquisition of an experimentally-derived model of the interaction between *Sa*GpsB and *Sa*PBP4, as well as an exploration of the effect of structure-guided mutants to key residues on *Sa*PBP4. The interaction between *Sa*GpsB and the other four PBPs present in *S. aureus* is an area that also requires more thorough exploration, and may confirm the necessity for a conserved arginine-motif for binding in *S. aureus*, as is the case in GpsB homologues. Concerning the *Sa*GpsB:*Sa*FtsZ interaction proposed by Eswara et al., 2018, future work could involve purification of *Sa*FtsZ, and its use in biochemical assays such as FP or ITC in order to characterise any interactions, or lack thereof, between the two proteins. A more thorough biophysical investigation of *Sa*GpsB^{Leu35Ser} by SAXS or CD is also necessary in order to address the concerns raised above about the folding of this mutant. Sufficient quantities of *Sa*GpsB$_{FL}$ were not producible in the time available for this study; prior work on full-length GpsB from *Listeria monocytogenes* characterised *Lm*GpsB as a hexamer, as well as establishing that the hexameric state of *Lm*GpsB was essential for proper function in this organism (Cleverley et al., 2016). Based on SEC work on *Sa*GpsB$_{FL}$ shown here (Figure 4.1), it may be that *Sa*GpsB also forms a similar oligomer to its *L. monocytogenes* homologue, however, the retention volume of *Sa*GpsB$_{FL}$ overlaps with the void volume of the column used and in any event the non-globular overall shape of *Lm*GpsB$_{FL}$, if recapitulated in *Sa*GpsB$_{FL,}$ is unlikely to lend itself to accurate estimates of oligomericity by SEC. Whether the large apparent size of *Sa*GpsB$_{FL}$ seen in Figure 4.1 is due to hexamer formation or some protein folding artefact is a shortcoming of this study that could be addressed by CD analysis of *Sa*GpsB$_{FL}$. Further work should concern the development of a robust protocol for the production and purification of sufficient *Sa*GpsB$_{FL}$ to allow for structural work such as SAXS, or SEC-MALS, and a comparison of these data to that known for *Lm*GpsB.

*Sa*DivIVA was not found to be phosphorylated by Stk1$_{1-291}$ under the experimental conditions employed herein. If *Sa*DivIVA is phosphorylated, as it has been suggested to be based on proteomic analysis and some *in vitro* experiments in other organisms (Hempel et al., 2012; Fleurie et al., 2014; Saalbach et al., 2013), it may be through a different kinase and/or a kinase

with a different substrate preference, for example, *B. subtilis* DivIVA is reported to be phosphorylated on Arg102 (Elsholz et al., 2012). Future work on *Sa*DivIVA should concern use of another eSTK encoded by *S. aureus*, such as PfkA, to determine the specificity of the phosphorylation activity of Stk1. In contrast to *Sa*DivIVA, *Sa*GpsB was found to be phosphorylated by $Stk1_{1\text{-}291}$. Whilst this work proves through several means that *Sa*GpsB is indeed phosphorylated by $Stk1_{1\text{-}291}$, it has not been possible to determine any consequences of phosphorylation on cell division regulation by *Sa*GpsB. Future work on phosphorylation of *Sa*GpsB by $Stk1_{1\text{-}291}$ could include screening of a wider range of reaction times for phosphorylation efficiency, and attempts to purify the differentially-phosphorylated species of *Sa*GpsB for further structural/biochemical study. Phospho-ablative alanine and phospho-mimetic aspartate/glutamate substitutions to the phosphorylatable residues identified here may also be generated and studied structurally/biochemically. Whether phosphorylation has any effect on binding kinetics between *Sa*GpsB and *Sa*PBP4 may be an interesting avenue worth exploring. Unfortunately, as with the interaction of *Sa*GpsB and *Sa*PBP4, the lack of any phenotype for *Sa*GpsB deletion renders *in vivo* analysis of *Sa*GpsB phosphorylation difficult until a synthetic-lethal coupling is identified, should a synthetic-lethal coupling become available, mutations to the phosphorylated residues described here may provide insight into the impact of phosphorylation on *Sa*GpsB function.

As phosphorylation is a ubiquitous tool used in cell signalling throughout nature (Johnson & Lewis, 2001), a scenario in which phosphorylation of *Sa*GpsB acts as an on/off switch for binding to its partner proteins, or the cell membrane based on phosphorylation of Thr21, could be envisaged. Thr21 equivalents are on the periphery of the PBP-binding sites in the GpsB studies published previously by others in the Lewis lab (Cleverley et al., 2019; Rismondo et al., 2016; Halbedel & Lewis, 2019b) and therefore is located in a position to influence PBP-binding, perhaps allosterically rather than directly. Furthermore, Thr21 is located in a position close to the 'crossed-loops' feature of DivIVA proteins that appears to be important in mediating the interaction with the membrane (Lenarcic et al., 2009; Oliva et al., 2010) that is also likely to contribute to membrane localisation when GpsB is bound to its membrane-embedded PBP4 target. High-resolution structure determination of full-length GpsB from any organism has yet to be achieved, perhaps if any structural changes were to be induced by phosphorylation they might assist in the production of diffraction-quality crystals of *Sa*GpsB. Clearly there is much more work to be done on *Sa*GpsB within and without the subject of phosphorylation, but the work here highlights the great potential for *Sa*GpsB to teach us about

the evolutional nuances of cell division regulation in this Gram-positive coccus. Major developments in less restrictive structural techniques such as cryo-electron microscopy (Cryo-EM) may soon enable the study of more complicated structural biology targets, indeed, recent advancements in this technique have allowed for the structure of haemoglobin to be solved using this technique (Khoshouei et al., 2017), therefore, a relatively small protein such as GpsB may become amenable to study by cryo-EM in the not too distant future. Finally, the power of artificial intelligence is being applied successfully to the routine and accurate prediction of protein structure prediction (Baek et al., 2021), and surely it will not be long before these methods will be developed further to investigate the formation of homo- and hetero-protein complexes.

Part II.

Structural and mutational studies on biofilm proteins from *Bacillus subtilis*

Chapter 5.

Introduction to biofilms and endonucleases

5.1 An overview of biofilms

In addition to their perhaps more traditionally studied free-floating planktonic state, bacteria grow in aggregated communities affixed to a wide variety of surfaces. These sessile communities of bacteria are known as biofilms, and biofilms are the form in which the majority of microorganisms exist in nature (Costerton et al., 1987) (Figure 5.1). In contrast to those in a planktonic mode of growth, bacteria in biofilms are more resistant to most environmental stresses such as extremes in temperature, pH, nutrient availability, antibiotics, and ultra-violet radiation (Hall & Mah, 2017; Yin et al., 2019; Yan & Bassler, 2019; Córdova-Alcántara et al., 2019; Çam & Brinkmeyer, 2020). Although biofilms have beneficial applications in some fields such as agriculture (Bogino et al., 2013), as biofertilizers (Timmusk et al., 2017), and in wastewater treatment (Ali et al., 2018), studies on biofilms have typically focussed on their detrimental effects on human health. A biofilm's ability to persist where free-floating/single cells would perish renders their unwanted presence on medical or industrial equipment of grave concern (Kaplan, 2010; Alvarez-Ordóñez et al., 2019).

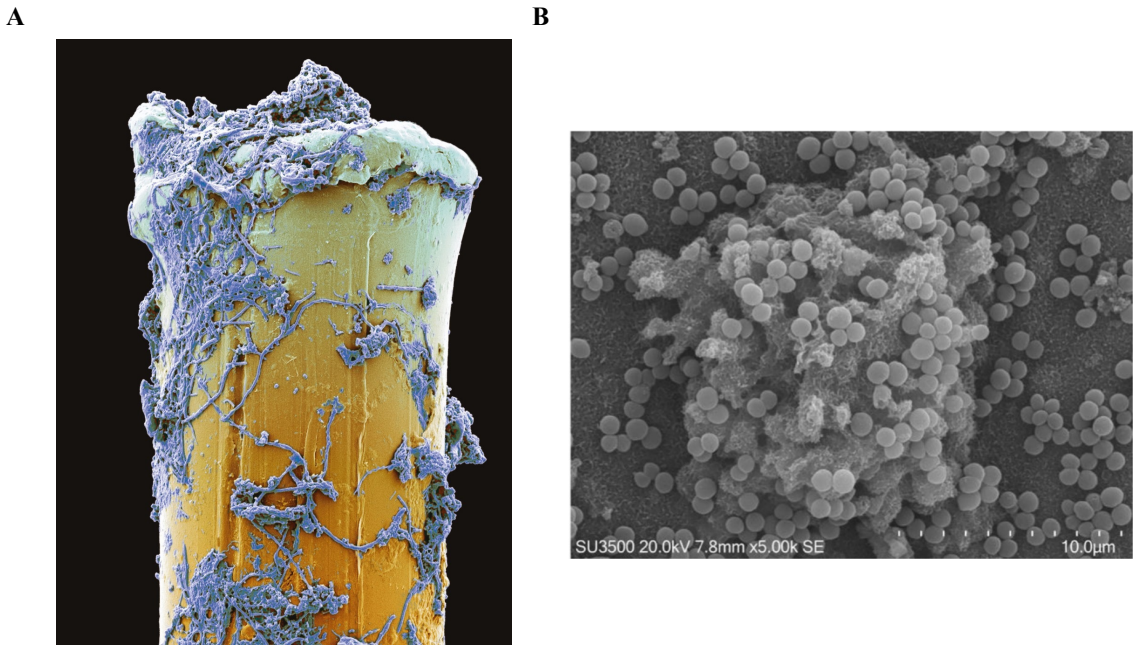

Figure 5.1: Examples of biofilms. A) Scanning-electron micrograph of a biofilm on a toothbrush bristle (taken from Dopheide, 2009). **B)** A scanning electron micrograph of a *S. aureus* biofilm (taken from Relucenti et al., 2021).

In addition to dense aggregates of bacteria, biofilms consist of a complex extracellular matrix (ECM), which plays a critical role in adhesion and integrity (Yin et al., 2019; Di Martino, 2018; Flemming & Wingender, 2010). The constituents of the ECM vary depending on the species

of bacteria present in the biofilm but, generally speaking, the ECM is a mixture of proteins, polysaccharides, lipids, and extracellular DNA (eDNA) (Cugini et al., 2019; Alim et al., 2018; Jakubovics et al., 2013; Stienberger & Holden, 2005). The ECM is therefore made up of predominantly organic polymers, and for this reason it is also commonly referred to as extracellular polymeric substances, or exopolymeric substances (EPS) (Marvasi et al., 2010; Di Martino, 2018), however, for the sake of this thesis it will be referred to as the ECM (Figure 5.2).

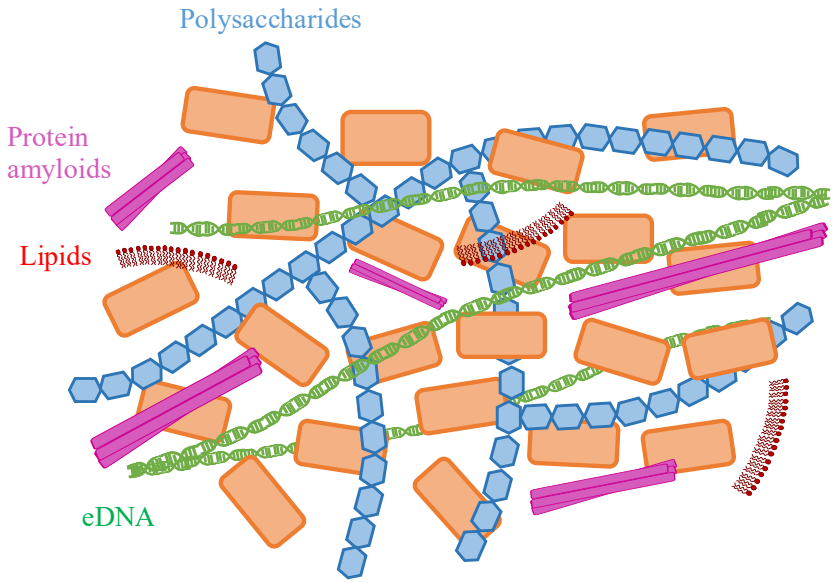

Figure 5.2: General components of the extracellular matrix. The molecular components common to the structure of many biofilms are shown as a cartoon. Polysaccharide chains are represented as chains of blue hexagons, amyloid fibres are represented as clusters of pink rectangles, eDNA is represented as green DNA chains, lipids are represented by red phospholipid-like molecules. Bacterial cells are represented as orange rods.

5.2 The extracellular matrix

The ECM is an essential component of the biofilm that can comprise up to 90 % of its dry mass (Flemming & Wingender, 2010), and its structure is responsible for the resistance of biofilms to many environmental stressors. Many clinically- and industrially-relevant dispersal mechanisms against biofilms cause the breakdown of the constituents of the ECM (Kaplan, 2010). The proportions of each component of the ECM, as well as their specific chemical nuances, varies depending not only on the species of bacteria present within it, but also the environment of the biofilm in question (Flemming & Wingender, 2010; Di Martino, 2018). It is outside the scope of this thesis to discuss the nuances in ECM constituents between all species of bacteria, but some general features applicable to most biofilms will be discussed,

and specific nuances in ECM composition applicable to a small selection of relevant species will be discussed.

5.2.1 Secreted proteins

Proteins typically represent the major fraction of the ECM and can be categorised into two populations, enzymes, and structural proteins. Enzymes within the ECM play a wide variety of roles within the biofilm, such as breaking ECM polymers down for use as nutrients, or modulating the ECM to assist with biofilm dispersal/reorganisation (Yin et al., 2019; Taglialegna et al., 2016a; Flemming & Wingender, 2010). The extracellular DNAse NucB, discussed in detail later in this Chapter (Section 5.12), is such an example of a secreted enzyme that plays a role in both biofilm modulation and in nutrient availability (Sinderen et al., 1995; Kiedrowski et al., 2011). PslG from *P. aeruginosa* is an example of a hydrolase responsible for the breakdown of the polysaccharide component of the ECM and has been implicated in self-dispersal of *P. aeruginosa* biofilms (Yu et al., 2015). Enzymes present in the ECM may also contribute to resistance of biofilms to antibiotics; secreted beta-lactamases in the ECM act as a line of defence for the inner layers of the biofilm against beta-lactam antibiotics (Heydari & Eftekhar, 2015).

In *P. aeruginosa*, surface-attached carbohydrate-binding proteins known as lectins form a structural role within the ECM, directly connecting the bacteria within the biofilm to the ECM (Passos da Silva et al., 2019). A well-studied family of structural ECM proteins are biofilm-associated surface proteins (Bap), or Bap-like proteins. First identified in *S. aureus*, Bap proteins are high-molecular weight (238 kDa in *S. aureus*) proteins attached to the cell surface of bacteria (Taglialegna et al., 2016b; Lasa & Penadés, 2006). It is known that Bap and Bap-like proteins are essential for biofilm formation, and their targeting has shown some promise as a mechanism of biofilm dispersal (Kumar Shukla & Rao, 2013). Despite their potential clinical relevance, the mechanism of action of Bap and Bap-like proteins within the ECM is still unclear (Cucarella et al., 2004; Schiffer et al., 2019): Bap and Bap-like proteins may switch between amyloid and non-amyloid like structures (based on the pH and calcium concentration of their immediate environment), representing an example of a molecular sensor underpinning the reactivity of biofilms to their environment (Taglialegna, Navarro, et al., 2016). A common theme in the secreted ECM proteins that play structural roles is a tendency to form amyloid-like structures and, by extension, amyloid fibres. Amyloid fibres self-assemble from their monomeric precursors into comparatively vast and incredibly stable structures, and amyloid-

like proteins can thus serve as a convenient and robust mechanism for inter-cell connectivity within biofilms (Taglialegna et al., 2016a).

5.2.2 Polysaccharides

Second in proportion only to proteins, polysaccharides represent another major fraction of the ECM. The polysaccharides present in the ECM constitute long, and often branched, carbohydrate chains (Schmid et al., 2015; Flemming & Wingender, 2010; Christensen, 1989). Polysaccharides form complex meshes within biofilms, large enough to be visualised by electron microscopy techniques (Reese & Guggenheim, 2007; Hassan et al., 2003). The role of polysaccharides within the ECM is primarily structural, acting as a scaffold for carbohydrate-binding proteins present on the surfaces of bacteria to attach to. Not only do polysaccharides play a primary structural role but they also contribute to the initial adhesion of biofilm progenitors to their surface, protecting the biofilm from environmental stressors, and trapping of nutrients (Limoli et al., 2015). A polysaccharide commonly found in many biofilms in large quantities is alginate, an anionic polysaccharide composed of α-*D*-mannuronic acid and α-*L*-gluronic acid. Alginate is a viscous polymer, responsible for adhesion and integrity in many biofilms (Boyd & Chakrabarty, 1995; Moradali & Rehm, 2019), and alginate lyases show potential as biofilm-dispersing agents (Blanco-Cabra et al., 2020).

5.2.3 Extracellular DNA

Initially thought a by-product of cell lysis within biofilms, eDNA is now known to play an important functional role in biofilm adhesion and structure (Stienberger & Holden, 2005; Devaraj et al., 2019; Di Martino, 2018; Whitchurch, 2002; Jakubovics et al., 2013). Many biofilms can be completely dispersed when treated with DNAses such as NucB (Shields et al., 2013; Shakir et al., 2012; Nijland et al., 2010). eDNA plays a major role in protecting biofilms of pathogenic bacteria from the host immune system (Taglialegna et al., 2016a). The eDNA present in biofilms of *Haemophilus influenzae* and *Pseudomonas aeruginosa* has been shown to have a lattice-like structure, enhancing the structural rigidity of the biofilm (Jurcisek & Bakaletz, 2007; Jurcisek et al., 2017). The eDNA lattice is chained together by Holliday junction intermediates, resulting in a connecting of the different eDNA chains (Devaraj et al., 2019). A family of DNA-binding proteins called DNABII has been shown to bind to and stabilise the eDNA lattice within the biofilm by binding at the Holliday junctions present at the intersections of the lattice (Devaraj et al., 2019). eDNA is also a source of genetic diversity for

the biofilm that has important implications for the passing of antibiotic resistance genes between bacteria within biofilms (Hall & Mah, 2017).

5.2.4 Lipids

Lipids are perhaps the least functional class of polymer present within the ECM, and certainly the least well-studied. Lipids have not been a major focus of biofilm research outside of a few bacterial and fungal strains, therefore, the significance of lipids within the ECM is unclear. There appears to be a role for lipids in cell-cell signalling of *C. albicans*, where the lipid farnesol has been implicated in preventing mycelial development (Hornby et al., 2001). A family of lipopeptides known as the serawettins are important for biofilm formation in *Serratia marcesans* (Matsuyama, 1989). Serawettins appear to function as biosurfactants, dispersing hydrophobic molecules to make them bioavailable (Matsuyama & Nakagawa, 1996). A greater understanding of the essentiality of lipids within biofilms may lead to more tools in the workbench of biofilm-dispersing agents and clearly there is much still to be done on the functions and prevalence of lipids in bacterial biofilms.

5.3 The biofilm lifecycle

The precise number and definition of stages involved in the lifecycle of a biofilm is a matter of some dispute, but it is generally accepted to involve at least an attachment phase, a colonisation/maturation phase, and a dispersal phase (Tolker-Nielsen, 2015; Yin et al., 2019; Kumar et al., 2017) (Figure 5.3). During the attachment phase, weak and reversible interactions are made between a bacterium and its destined surface, a process that is potentially aided by pili or by surface-exposed/secreted proteins/polysaccharides/lipids (Garrett et al., 2008; Steinberg et al., 2020; Okshevsky & Meyer, 2015; Donlan, 2002). Bacteria may dissociate from the surface and return to a planktonic lifecycle during this reversible attachment phase. Different species of bacteria attach to surfaces using distinct mechanisms, for instance, antigen 43 in *E. coli* is responsible for surface attachment (Ulett et al., 2007); type IV surface pili in *P. aeruginosa* aid adherence (Klausen et al., 2003), and surface proteins of pathogenic strains of *S. epidermis* and *S. aureus* attach to human proteins such as fibrinogen (Fey & Olson, 2010). Following attachment by a bacterium to a surface, interactions between it and neighbouring bacteria result in the formation of a microcolony. In parallel to the formation of microcolonies, gene regulation of individual bacteria within the nascent biofilm is altered such that genes responsible for production of ECM components (such as those responsible for production of

polysaccharides and amyloid-like proteins) are upregulated, and genes relevant to planktonic modes of growth (such as those encoding pili/flagella) are downregulated (Kumar et al., 2017). Once microcolonies have formed, and production of the ECM has been initiated, the biofilm is in its colonisation phase; at this phase the bacteria are irreversibly attached to the surface.

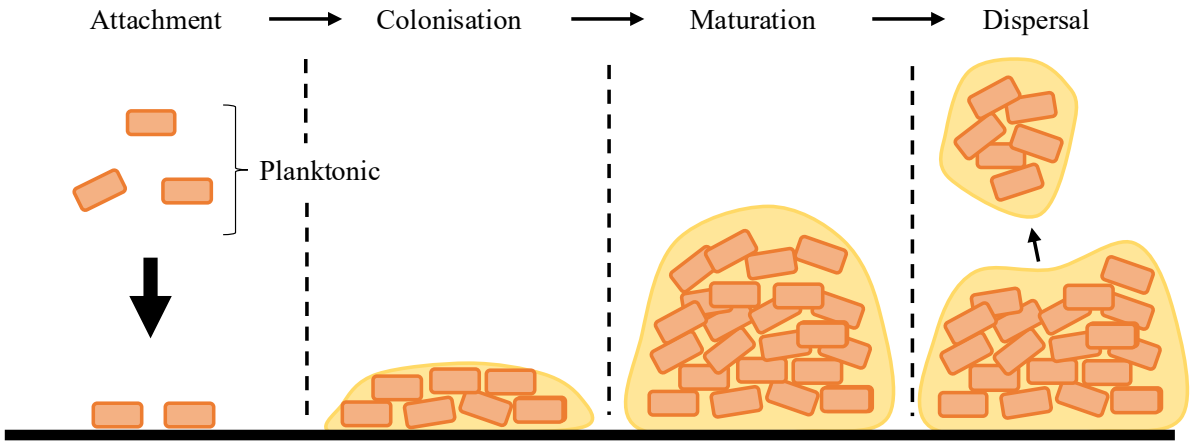

Figure 5.3: Stages of the biofilm lifecycle. The biofilm lifecycle is shown here in four stages, attachment, colonisation, maturation, and dispersal. Bacterial cells are represented by orange rectangles, and the ECM is represented in yellow.

Colonisation of the biofilm involves proliferation of the bacteria within it such that multiple layers of cells are produced. Cell proliferation in the colonisation stage is aided by nutrient trapping within the biofilm by secreted exopolysaccharides, and coordination of cell growth through quorum sensing, discussed in detail later in this Chapter, is a mechanism of intra-biofilm cell-cell communication. Polysaccharide and eDNA-based channels and lattices are formed during colonisation of a surface by a biofilm that allow for the passing of genetic information and signalling molecules between bacteria within the biofilm (Okshevsky & Meyer, 2015; Tolker-Nielsen, 2015). The biofilm is considered mature once a stable multi-layered community with nutrient and gene transfer distribution channels is established.

The final phase of the biofilm lifecycle is biofilm dispersal, which occurs once the biofilm is no longer viable due to a lack of nutrient availability, persistence of a lethal dose of antibiotic, or breakdown of the ECM by an external factor (Kaplan, 2010). Biofilm dispersal describes the process of detachment of bacteria from the biofilm, either as single cells or as clusters. Biofilm dispersal is made up of passive and active processes, such as separation of large sections of biofilm due to fluid shear/abrasion, or enzymatic dispersal by the biofilm community, respectively (Guilhen et al., 2017). Active dispersal in biofilms is a result of the secretion of ECM-dispersing enzymes by the bacteria within. A diverse set of enzymes capable

of digesting each of the structurally essential ECM components is secreted; for instance, the proteases aureolysin and Spl, (Lister & Horswill, 2014) and the DNAse, thermonuclease (Mann et al., 2009), are secreted such in *S. aureus*. As the structural rigidity of biofilms is likely a result of the combined contributions of each structural ECM constituent, it stands to reason that simultaneous degradation of multiple ECM components would result in the most efficient breakdown of the biofilm. Lysis of the inner layer of cells within the biofilm of *P.* aeruginosa appears to release signalling molecules to the cells in the outer layers (Yu et al., 2015), resulting in the downregulation of biofilm-specific genes involved in ECM production/signal transduction, and a concomitant upregulation in genes such as those encoding flagella/chemotaxis proteins (Rollet et al., 2008). Planktonic cells released from the biofilm can form further interactions with other surfaces and may become progenitor cells for further biofilms (Rumbaugh & Sauer, 2020). Dispersal of single cells or clusters of cells is a continual process that occurs throughout the biofilm lifecycle, allowing for the colonisation of multiple surfaces in any given environment (Guilhen et al., 2017).

5.4 Communication within biofilms

An interesting modern discovery in biofilm research is that bacteria within biofilms can communicate with one another. Quorum sensing describes the regulation of genes within bacterial communities in response to changes in population density and environmental stressors (Rutherford & Bassler, 2012; Miller & Bassler, 2001). Quorum sensing regulates cell density during biofilm development so that an optimum cell density for efficient biofilm expansion is maintained (Miller & Bassler, 2001). Quorum sensing allows bacterial communities within biofilms to regulate their speed of growth based on nutrient availability, alter gene expression based on the presence/absence of antibiotics, and activate mechanisms of competence for the passing of genetic information between cells (Hahn et al., 1998; Miller & Bassler, 2001). Many pathogenic bacteria, including *S. aureus*, coordinate the production of virulence factors by quorum sensing (Rutherford & Bassler, 2012). Bacteria communicate within the biofilm by use of small molecules that are often passed between cells using channels within the biofilm. Recent advancements in microscopy instrumentation have allowed for the direct visualisation of channels within an *E. coli* biofilm (Rooney et al., 2020). Gram-positive and Gram-negative bacteria utilise different quorum sensing mechanisms; Gram-positive bacteria typically utilise autoinducing peptides (AIPs) as their signalling molecules of choice (Monnet & Gardan, 2015),

whereas Gram-negative bacteria instead use small molecule autoinducers, such as acyl-homoserine lactones (AHLs) (Papenfort & Bassler, 2016).

Gram-positive bacteria have two main methods of quorum sensing through AIPs, a two-component pathway, and a self-signalling pathway (Bhatt, 2019) (Figure 5.4). AIPs are continually secreted into the ECM by ABC transporters at a constant rate (Bhatt, 2019), therefore, a concomitant increase in the concentration of AIPs is observed at high cell densities. In the two-component quorum sensing pathway of Gram-positive bacteria, secreted AIPs activate membrane-associated histidine kinases, which results in the phosphorylation of intracellular response regulators (Monnet & Gardan, 2015). The activated phosphorylated response regulators stimulate the transcription of genes in the quorum sensing regulon. The AIPs act as positive regulators for transcription factors in the self-signalling pathway, thereby regulating gene expression directly. The specific genes regulated by these pathways varies between species of bacteria, however, genes responsible for competence in *B. subtilis* and *S. pneumoniae* are upregulated through these mechanisms (Hahn et al., 1998; Shanker & Federle, 2017), and genes responsible for virulence in *S. aureus* are similarly upregulated (Yarwood & Schlievert, 2003).

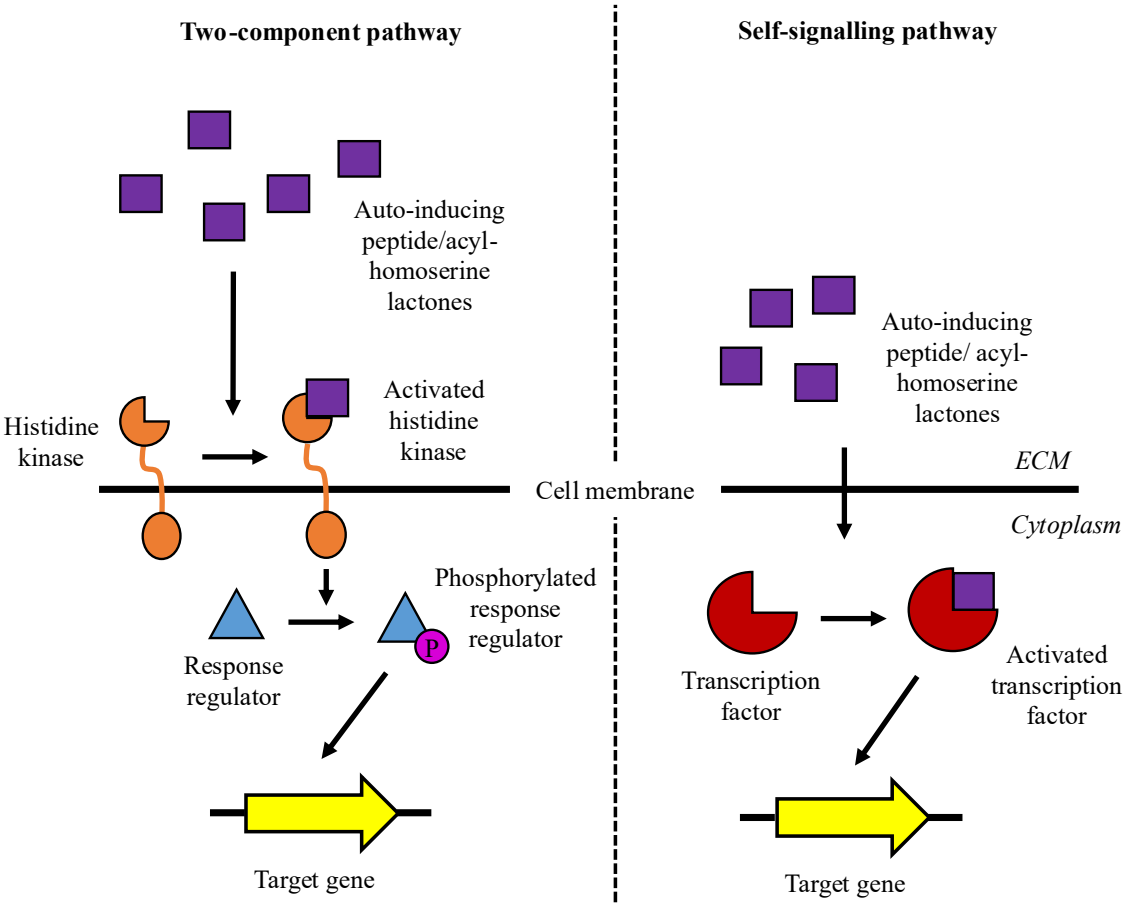

Figure 5.4: General mechanism for gene regulation by quorum sensing in Gram-negative and Gram-positive bacteria. A cartoon representing the general mechanism underpinning the two major pathways through which bacteria within biofilms regulate gene expression by quorum sensing.

Quorum sensing in Gram-negative bacteria functions similarly to that in Gram-positive bacteria, but with a key difference in that autoinducer molecules typically passively diffuse out of the cell, rather than by active secretion (Papenfort & Bassler, 2016). The AHLs of Gram-negative bacteria consist of a core *N*-acylated homoserine-lactone ring with a 4-18 carbon acyl chain (Galloway et al., 2011). The mechanisms of gene regulation by AHLs are broadly the same as for Gram-positives, in that AHLs either activate histidine kinases or directly activate intracellular transcription factors (Papenfort & Bassler, 2016).

5.5 Antibiotics and biofilms

Bacteria within biofilms are typically more tolerant to antibiotics than their free-floating planktonic counterparts; indeed, bacteria within biofilms can be 10 – 10,000 times more tolerant of certain antibiotics (Tetz et al., 2009; Yan & Bassler, 2019). In addition to antibiotic

tolerance, biofilms are also thought to promote the formation of persister cells, a sub-population of cells within the biofilm that can withstand temporary antibiotic treatment, but that re-colonise following removal of antibiotic (Brauner et al., 2016). The molecular mechanisms of antibiotic tolerance and resistance within biofilms is a result of a combination of the inert physical barrier of the ECM and rapid adaptations of the bacteria within the biofilm. The ECM of the biofilm constitutes a physical barrier against antibiotics, slowing the diffusion of antibiotic molecules into the biofilm and, by extension, the cells within (Kumar et al., 2017). The inhibition of antibiotic diffusion into the biofilm results in the generation of a concentration gradient within the biofilm in which high concentrations of antibiotic are present on the surface of the biofilm, but lower concentrations are present in the core layers (Hall & Mah, 2017). Generation of persister cells within biofilms is related to the mechanism of action of several popular families of antibiotics; common antibiotics such as beta-lactams, or RNA polymerase-targeting antibiotics are less active on slow growing bacteria than rapidly growing bacteria (Yan & Bassler, 2019). Although the outer layer of the bacteria in biofilms are likely to have high growth rates, the inner layers of bacteria within biofilms have low growth rates and as such, these growth-dependent antibiotics are less active on these cells (Kumar et al., 2017). As a result of the disparity in effectiveness of these classes of antibiotics on the cells within the biofilm, brief exposure to antibiotics results in the destruction of the outer, faster growing layer of the biofilm, but leaves intact the inner, slower growing layer of cells (Figure 5.5). This sub-population of slower growing cells are fully able to form the seeds for a new biofilm once the antibiotic is no longer present (Yan & Bassler, 2019).

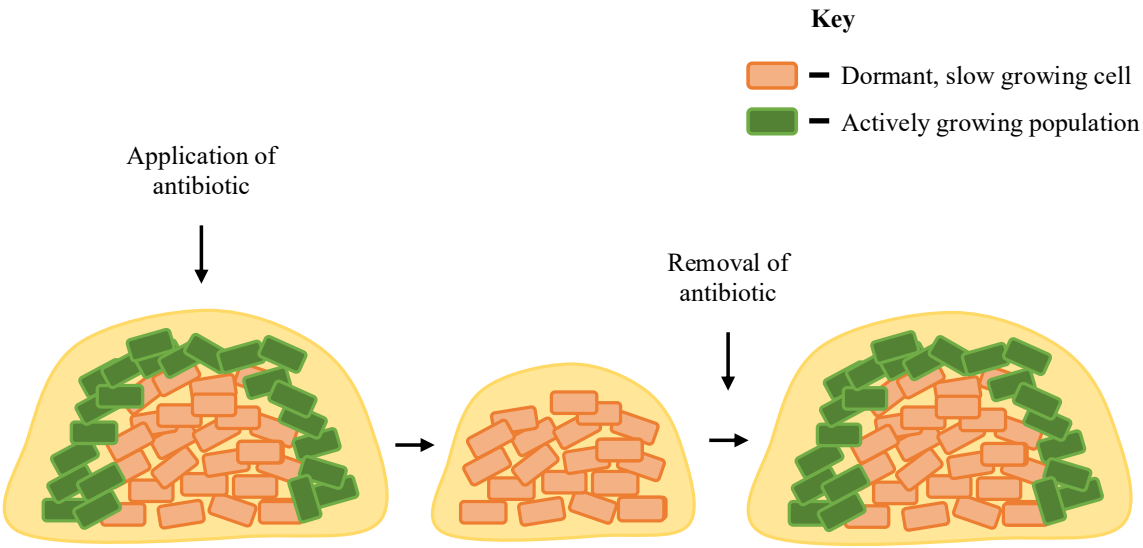

Figure 5.5: Mechanism of generation of persister cells in biofilms. The general mechanism of persistence/tolerance to antibiotics is shown in three stages. Upon application of antibiotics such as beta-lactams, the actively growing population of cells (represented as green rectangles) are lysed. The slower growing, dormant inner layer of cells within the biofilm, however, are less affected on removal of antibiotic, the dormant cells continue to grow, leading to a new population of actively growing cells on the outer layers of the biofilm.

In addition to greater tolerance to antibiotics than planktonic cells, bacterial communities within biofilms are also capable of becoming resistant to specific antibiotics at a far faster rate. Horizontal gene transfer is a more rapid process in biofilms thanks to the proximity of the cells within the biofilm, as well as because of the channels available to the cells within a biofilm as discussed above. Thanks to this increased rate of gene transfer, bacteria within biofilms rapidly take up new genetic information and alterations to genes encoding antibiotic targets (Foster, 2017; Singh et al., 2006). Outside horizontal gene transfer, the presence of eDNA in the ECM provides a large source of genetic material, enhancing genetic diversity for the entire biofilm. This generalised distribution of genes from lysed cells across the entire biofilm results in the sporadic acquisition of antibiotic resistance genes (Hannan et al., 2010). eDNA may also play a direct role in diffusion limitation within the biofilm, chelating certain antibiotics and preventing them from being able to penetrate the cell membrane (Hall & Mah, 2017). Bacteria that have taken up antibiotic resistance genes, such as beta-lactamases, may also secrete these proteins into the biofilm matrix where they form a pool of antibiotic-destroying enzymes in the ECM. This pool of antibiotic-destroying enzymes is beneficial to the entire biofilm and even protects cells that have yet to acquire antibiotic resistance genes (Amanatidou et al., 2019).

5.6 The *B. subtilis* biofilm

B. subtilis has served, as it has for many other microbiological subdisciplines, as a model organism for the study of biofilms (Figure 5.6). *B. subtilis* forms a wrinkled biofilm structure in laboratory conditions, similarly to many other species of bacteria (Vlamakis et al., 2013). The major constituent of the *B. subtilis* ECM is a large molecular weight polysaccharide whose chemical structure has yet to be determined completely. The secreted polysaccharide of *B. subtilis* is also sometimes confusingly referred to as EPS, after exopolysaccharide (Schmid et al., 2015), because of legacy studies of ECM polysaccharides. Interactions between EPS and eDNA are essential for initial adhesion of the *B. subtilis* biofilm (Peng et al., 2020). Some work has unravelled the synthesis pathways of ECM polysaccharides from *B. subtilis*: a 15-gene operon is responsible for exopolysaccharide production in *B. subtilis*, comprising genes *epsA-O* (Marvasi et al., 2010). Exopolysaccharides are produced on the edges of an expanding *B. subtilis* biofilm, coordinated by *epsA* and *epsB*, which encode the tyrosine kinases EpsA and EpsB. Together these kinases are responsible for regulating the production of exopolysaccharides by phosphorylating downstream *eps* genes as a means of positive regulation (Elsholz et al., 2014).

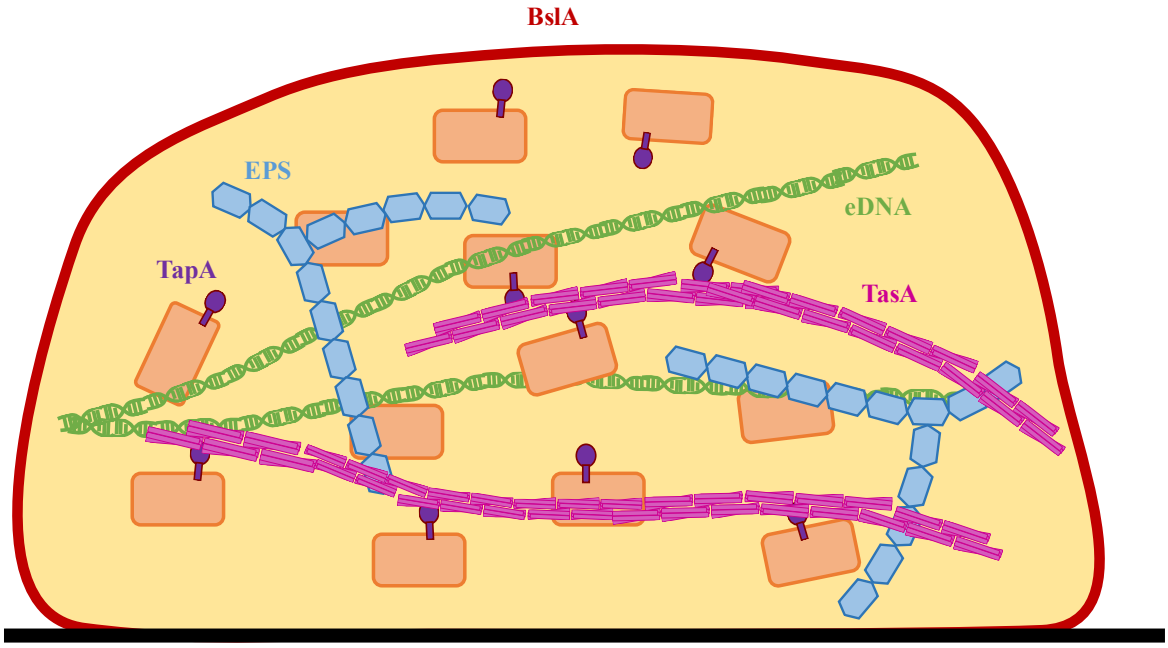

Figure 5.6: Molecular features of the *B. subtilis* biofilm. Here a typical biofilm structure of *B. subtilis* cells (orange rods) is represented as a cartoon. The hydrophobic coat protein BslA is represented as a thick red line around the ECM, the membrane-associated TasA-binding protein TapA is represented in purple, eDNA is represented as green cartoons of DNA, the EPS is represented as blue hexagons, and amyloid fibres of TasA are represented as clusters of purple rectangles.

Of the proteins that *B. subtilis* is known to secrete into its ECM, TasA, BslA, and TapA are the best-studied. TasA is the most abundant of the ECM proteins in *B. subtilis*; TasA assembles into long amyloid fibres and binds to the membrane-attached TapA. The interaction between TasA fibres and TapA is a major contributor to the structural integrity of the *B. subtilis* biofilm (Steinberg et al., 2020). Thorough integrative structural studies on TasA have monitored the structural transition of TasA during biofilm formation in *B. subtilis*, observing a switch of TasA from a globular structure to that of a protease-resistant β-sheet rich structure (Diehl et al., 2018). The biofilm surface layer protein BslA is essential for surface hydrophobicity and colony morphology by self-assembling into a hydrophobic layer atop the surface of the *B. subtilis* biofilm (Hobley et al., 2013).

5.7 Biofilm removal in clinical and industrial settings

Three primary mechanisms exist for the removal of clinically/industrially malicious biofilms, mechanical dispersal, chemical dispersal, and enzymatic dispersal. In industry, mechanical and chemical dispersal are the major methods of biofilm dispersal, where scrubbing of industrial equipment and use of concentrated biocides are the prevalent biofilm dispersal mechanisms (Vishwakarma, 2020). Based on the essentiality of the ECM for biofilm adhesion and integrity, it is perhaps unsurprising that the most successful enzymatic biofilm dispersal agents target the constituents of the ECM. As mentioned above, nucleases such as NucB have shown promise as potential biofilm-dispersing agents (Shields et al., 2013; Shakir et al., 2012; Nijland et al., 2010). Indeed, combinations of DNAses and antibiotics have been explored as biofilm-dispersal agents (Tetz et al., 2009). For the polysaccharide component of the ECM, glycoside hydrolases have shown promise in removal of biofilms in wounds (Fleming et al., 2017), as well as removing biofilms composed of heterogenous species (Snarr et al., 2017). There is clearly a gap in the market for developing recombinant enzymes active on the constituents of the ECM into robust and safe biofilm dispersal agents.

Clearly biofilms present a unique challenge in several clinically and industrially-relevant settings, therefore, the development of a novel and wide-reaching mechanism for their disruption is an area of research with potentially lucrative outcomes. Recent studies on nucleases have shown some promise in the field of biofilm-dispersing enzymes, particularly those on a secreted endonuclease from *Bacillus licheniformis*, NucB (Shields et al., 2013; Nijland et al., 2010; Shakir et al., 2012).

5.8 An overview of nucleases

Nucleases are biologically important enzymes and are found ubiquitously throughout nature, defined by their function of cleaving the sugar-phosphate backbone of DNA or RNA (Horton, 2008; Yang, 2011). In bacteria, nucleases play roles in processes including nutrient scavenging in biofilms, defence against foreign viruses/bacteria, as part of regulated cell death, and in DNA replication (Yang, 2011). Nucleases are diverse enzymes and fall into many classes, including those that break single-strands of DNA versus double-strands, those that cleave successive nucleotides from one end of a DNA molecule (exonucleases) versus those that cleave at a non-terminal location (endonucleases), those that are sequence-specific versus those which are not, and those that target RNA versus those that target DNA. A common feature of nucleases is a positively charged surface surrounding the active site of the enzyme, such that the negatively charged sugar-phosphate backbone of DNA is electrostatically attracted to the nuclease (Horton, 2008) (Figure 5.7). Many nucleases are metal-dependent and utilise a divalent metal cation as part of their mechanism of action. Some well-studied examples of nucleases will be discussed below, including their mechanisms of action.

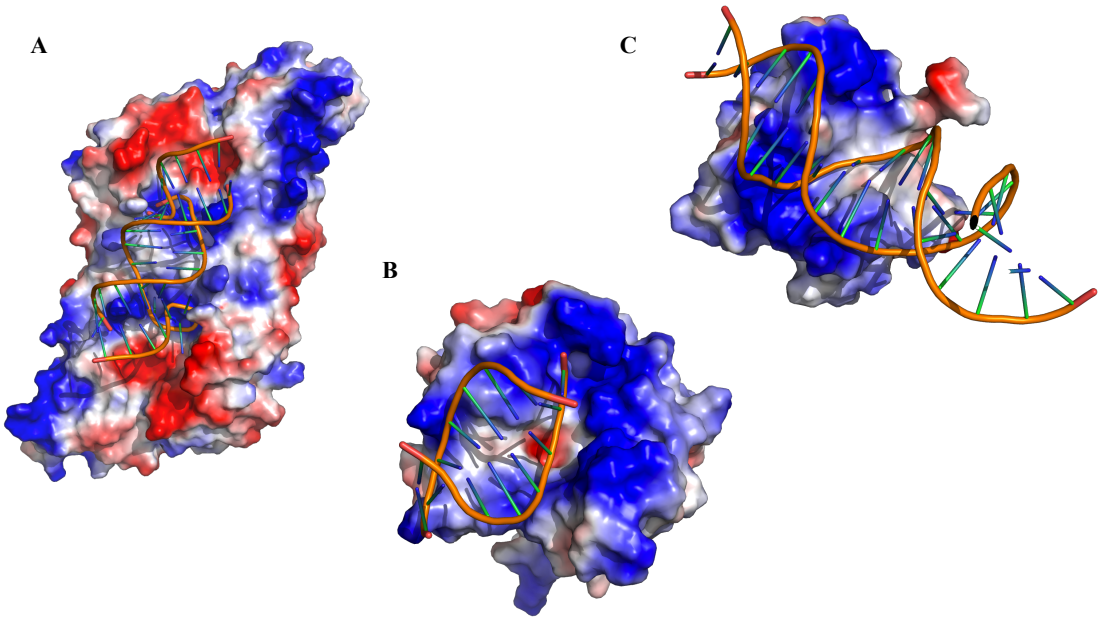

Figure 5.7: The importance of surface charge for DNA recognition by nucleases. The structures of three nuclease:DNA complexes, **A)** *Archaeoglobus fulgidus* RNAse (PDB code 2GJW; Xue et al., 2006) **B)** *Vibrio vunlificus* Vvn (PDB code 1OUP; Li et al., 2003) and **C)** *E. coli* Colicin E7 (PDB code 1PT3; Hsia et al., 2004) are shown. DNA/RNA is rendered as sticks, and the electrostatic surfaces of the nucleases are rendered with blue representing positively charged surfaces, and red representing negatively charged surfaces. In each case, the interface between DNA/RNA and the nuclease occurs at positively charged surfaces.

5.9 His-Me finger endonucleases

Another well-studied family of nucleases are the histidine-metal finger (His-Me finger) endonucleases, named as they typically contain at least one active site histidine, and require a divalent metal cation for their function. His-Me finger endonucleases are also often referred to as ββα endonucleases, named after the structural motif in which the active site of the endonuclease is housed (Figure 5.8). The mechanism of action of His-Me finger endonucleases generally involves the use of a divalent cation as a Lewis acid, and a typically invariant histidine residue as a general base to cleave the phosphodiester bond of DNA; a few exceptions to this general rule include NucB from *B. licheniformis*, which utilises glutamate for catalysis instead. Most His-Me endonucleases function as monomers and do not have a sequence specificity. His-Me endonucleases are typically involved in bacterial cell defence, DNA recombination, cell death, and for nutrient scavenging of eDNA (Wu et al., 2020).

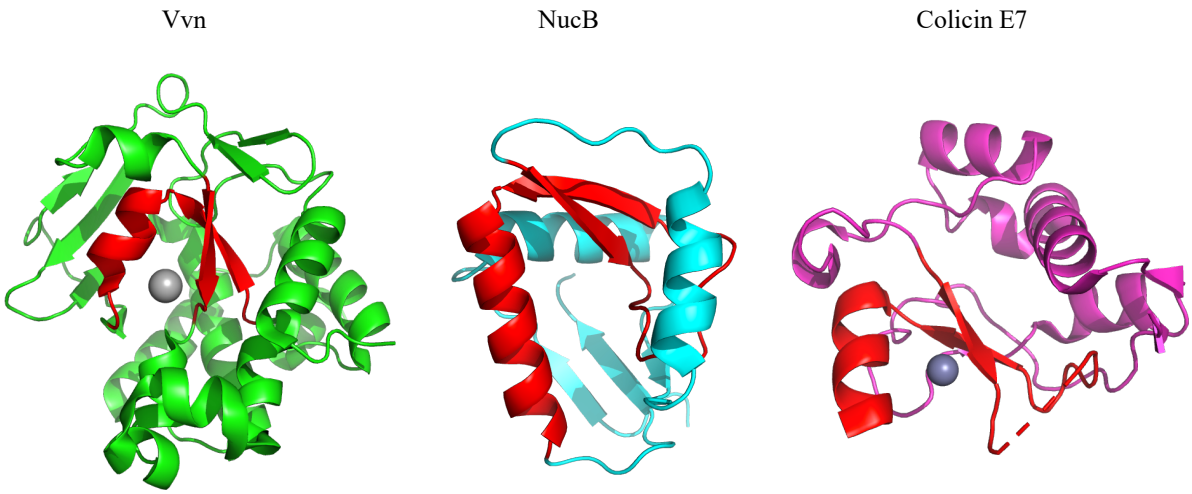

Figure 5.8: ββα motifs present in a selection of His-Me endonucleases. The structures of three His-Me finger endonucleases, Vvn (PDB code 1OUP; Li et al., 2003), NucB (PDB code 5OMT; Baslé et al., 2018), and Colicin E7 (PDB code 1PT3; Hsia et al., 2004) are rendered as cartoons, with the ββα motifs housing the active sites of each protein coloured in red.

5.10 Nuclease-inhibitor interactions

Uncontrolled nuclease activity within the cell would clearly come at a detriment to the cell's longevity. Consequently, nucleases are often expressed alongside cognate inhibitors as a means of keeping their activity in check. Some secreted nucleases function as toxins, and nuclease inhibitors protect the host cell from self-induced toxicity, much like in classical toxin-antitoxin systems (Cao et al., 2017). The interactions between nucleases and cognate inhibitors must be

incredibly tight (sub-nM dissociation constants), such that all nucleases in the cell with potential to destroy the cell's own genetic information are sufficiently impeded. As such, the interactions between some nucleases and their cognate inhibitors are sufficiently tight that many have become models of tight protein-protein interactions and have been used to predict structural features of protein-protein interactions necessary for tight binding (Buckle et al., 1994).

A well-characterised example of a nuclease-nuclease inhibitor interaction is that between Barnase and Barstar from *B. amyloliquefaciens*. Barnase (bacterial ribonuclease) is an RNAse secreted by *B. amyloliquefaciens* that plays an important role in nutrient scavenging (Yanagawa et al., 1993). Expression of Barnase is activated by Spo0A in response to phosphate starvation, although the molecular mechanisms of this trigger remain unclear (Ulyanova et al., 2011; Ulyanova et al., 2015). Barstar is an intracellular inhibitor of Barnase which binds to Barnase with a K_D in the femtomolar range measured by titration of Barnase with Barstar and measurement of Barnase activity (Buckle et al., 1994; Hartley, 1993). The structure of Barnase in complex with substrate has been solved (Buckle & Fersht, 1994), as well as the structure of Barnase in complex with Barstar (Buckle et al., 1994). Barstar binds in the active site pocket of Barnase, preventing substrate access (Figure 5.9). The interaction between Barnase and Barstar is mediated by the presence of 14 hydrogen bonds between the two proteins, 6 of which form salt bridges at their interface.

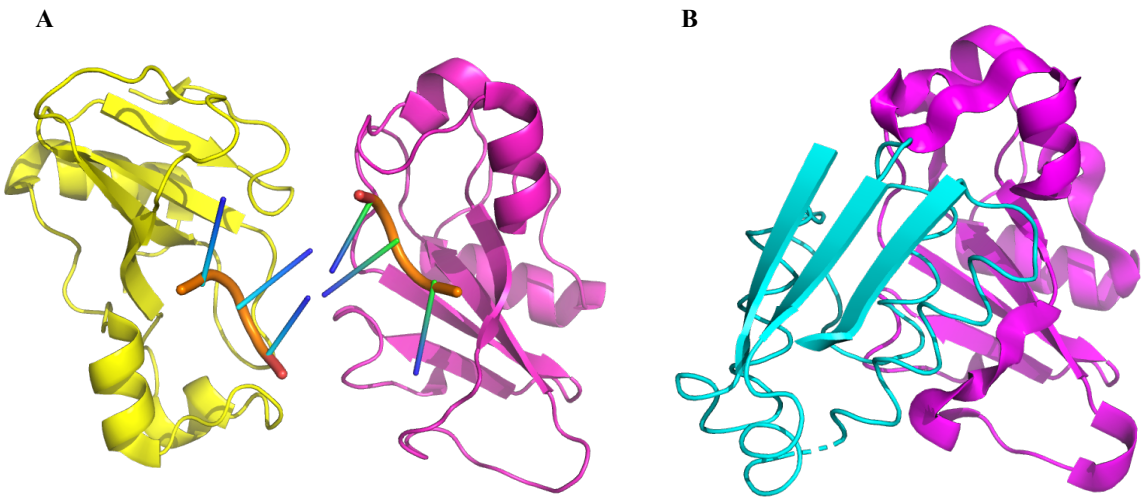

Figure 5.9: Mechanism of inhibition of Barnase by Barstar. A) The structure of Barnase in complex with DNA is shown with Barnase monomers rendered as cartoons, and DNA rendered as sticks, with each monomer of Barnase coloured in yellow and magenta (Buckle & Fersht, 1994). **B)** The structure of the Barnase-Barstar complex is shown, with Barnase rendered as a magenta cartoon, and Barstar rendered in cyan (Buckle et al., 1994). Barstar prevents access of DNA into the active site of Barnase, preventing its hydrolysis.

Another example of a well-studied nuclease-inhibitor interaction is of a subset of the Colicin family of toxins. Colicin E2, E7, E8, and E9 are all His-Me endonucleases, utilised by *E. coli* to kill competitors as part of its SOS response (Cascales et al., 2007). As with Barnase, *E. coli*'s own genome is protected from its own Colicin endonucleases by immunity proteins (Kleanthous et al., 1998). The structures of Colicin E7 and E9 have been solved in complex with their substrates, as well as with their cognate immunity proteins, Im7 and Im9, respectively (Kleanthous et al., 1998; Kühlmann et al., 2000). Interestingly, the structures of Colicin E7 and E9 with Im7 and Im9 reveal an alternative mechanism of inhibition than for Barnase. Im7 and Im9 bind away from the active sites of Colicin E7 and E9 and therefore act either by sterically preventing access of substrate to the active site or by locking Colicin E7/E9 into an inactive state (Figure 5.10). The interactions of Colicin E7 and E9 with Im7 and Im9 are further examples of high-affinity protein-protein interactions, with their K_D calculated to be in the femtomolar/sub-femtomolar range by stopped-flow fluorescent experiments (Li et al., 1997). Similarly to the Barnase:Barstar complex, there are a significant number of hydrogen bonds and salt bridges at the interface between the Colicin endonucleases described here and their immunity proteins. Colicin E7 forms 16 hydrogen bonds with Im7 at their interface, 6 of which constitute salt bridges (Ko et al., 1999; Chak et al., 1996). Colicin E9 forms a lesser number of these interactions, with 12 hydrogen bonds, 2 of which constitute salt bridges (Kleanthous et al., 1999).

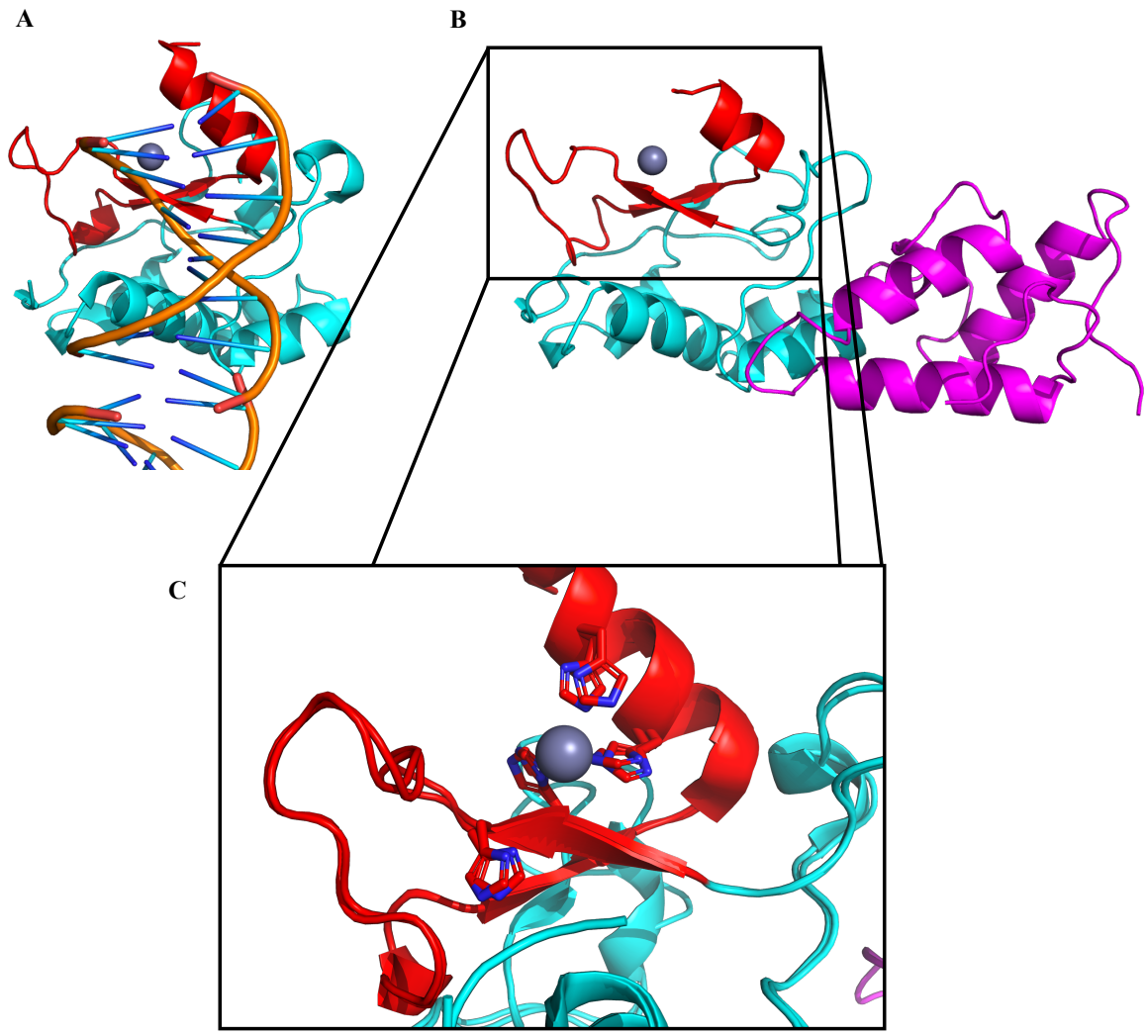

Figure 5.10: Inhibition of Colicin E7 by the immunity protein Im7. A) The structure of Colicin E7 in complex with DNA is shown, with Colicin E7 rendered as a cartoon and DNA rendered as sticks (Hsia et al., 2004). The ββα domain of Colicin E7 is coloured red. **B)** The structure of Colicin E7 in complex with the inhibitor Im7 is shown, with Im7 coloured magenta (Ko et al., 1999). As can be seen in this structure, Im7 binds away from the active site ββα, preventing access of DNA by blocking a proximal region of the protein to which DNA binds. **C)** Close-up of the superpositions of the active site of Colicin E7 in its DNA and Im7 bound form. No major structural rearrangement of the active site histidines appears to occur upon Im7 binding, suggesting that it a steric blockage of DNA remote from the active site, rather than a structural rearrangement that prevents nuclease activity upon Im7 binding.

5.11 NucA and NucB

NucA and NucB are differentially expressed endonucleases present in the genomes of several members of the firmicute phylum (Sinderen et al., 1995). Early studies on NucA from *B. subtilis* revealed that it was required for DNA cleavage during DNA uptake into *B. subtilis* for transformation (Provvedi et al., 2001; Vosman et al., 1987, 1988), however, no studies on NucA from *Bacillus* strains have been published since. NucA is required for virulence in *Streptococcus agalactiae*, and is also required for the pathogen's evasion from the host immune

system (Moon et al., 2014a). Biochemical characterisation of NucA from the cyanobacterium *Anabaena* has revealed it to be a non-specific extracellular endonuclease (Muro-Pastor et al., 1992). The first structural studies on NucA came from *Serratia marcescens*, where the structure of NucA was solved in isolation, and the mechanism of its metal-dependent activity was established (Miller et al., 1999). More recent structural investigation has come from the *Anabaena* homologue of NucA, where the structure has been solved in isolation as well as in complex with a cognate inhibitor, NuiA (Muro-Pastor et al., 1997; Ghosh et al., 2007). The structure of NucA from *S. agalactiae* has also been solved, revealing key structural features responsible for catalysis (Moon et al., 2014b). The structural studies of the NucA homologues discussed here have allowed for classification of NucA into the His-Me/ββα family of endonucleases (Ghosh et al., 2005). NucA appears to be anchored to the cell membrane by a transmembrane helix present at its N-terminus, with most of the protein, including the nuclease domain, present on the outside of the cell. As NucA is implicated in DNA uptake during transformation, it is understandable that the protein would be functional at the *trans* side of the cell membrane, across which DNA fragments would be translocated by a Type IV pilus-like uptake system. The presence of a transmembrane domain rather than a signal peptide at the N-terminus of the protein suggests that it is likely to be recognised by the Signal Recognition Particle and transported by the SRP-mediated Sec pathway (Schneewind and Missiakas, 2014b).

In contrast to the variety of NucA proteins studied, NucB has been studied predominantly in *Bacillus* strains, particularly *B. subtilis* and *B. licheniformis*. Unlike the membrane anchored NucA, NucB is secreted from the cell into the extracellular medium (Al-Wahaibi et al., 2019), mediated by an N-terminal signal peptide. NucB is implicated in degradation of the mother cell genomic DNA during sporulation in *Bacillus* (Hosoya et al., 2007). Work in *S. aureus* has implicated NucB in biofilm modulation through the non-specific cleavage of eDNA in the ECM (Kiedrowski et al., 2011). NucB may act as a biofilm dispersing agent, preventing the formation of biofilms consisting of competing bacteria (Nijland et al., 2010). Recent work on NucB has been focussed towards its potential as a biofilm-dispersing agent for use in clinical scenarios (Shakir et al., 2012; Nijland et al., 2010; Shields et al., 2013). Clinical interest in NucB has led to the protein becoming relatively well-characterised biochemically and structurally, with recent structural studies on NucB from *B. licheniformis* identifying it as a member of a novel sub-family of ββα endonuclease (Baslé et al., 2018). Unlike all other ββα endonucleases studied to-date, NucB does not rely on an invariant histidine in the active site,

but instead utilises glutamate for catalysis, therefore representing a novel mechanism of action for this family of endonucleases (Figure 5.11). The mechanism of NucB secretion is currently unknown, however, there is a body of work that may suggest that secretion is mediated by the Sec pathway (Nouaille et al., 2006). Indeed, analysis of NucB from the two *Bacillus* strains in SignalP (Nielsen et al., 2019) reveals the presence of signal peptides on both *Bs*NucB and *Bl*NucB, likely indicating that NucB in both species is secreted by the SecA-mediated Sec pathway.

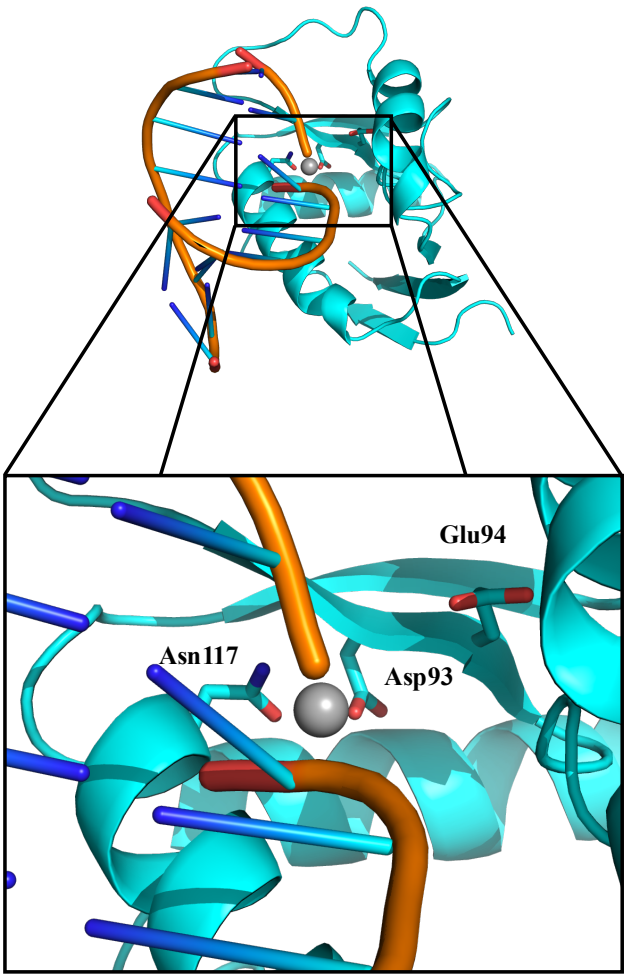

Figure 5.11: The model of *B. licheniformis* NucB DNA binding. The model of DNA binding by *B. licheniformis* NucB presented in Baslé et al., 2018 is shown, with a close-up on the active site. Unlike in the majority of His-Me finger endonucleases, a glutamate, Glu94, is proposed to act as a general base, in lieu of a histidine residue.

5.12 Nin

The operon housing NucA also contains a gene for an intracellular nuclease inhibitor, Nin (Sinderen et al., 1995; Smith et al., 1985). Despite knowledge of the existence and activity of Nin for over 25 years, functional studies on Nin to-date are limited to gene knockout experiments in which *B. subtilis* cells with *nin* knockouts were observed to have decreased competency (Provvedi et al., 2001). An effort from a structural genomics group has resulted in a structure of Nin from *B. subtilis* deposited in the PDB (PDB code 4MQD), however, there is no associated publication from this work. Nin is present as a homodimer in the aforementioned crystal structure, however, no work has been undertaken on the biological significance of this. As stated above, NucA from *Anabaena* is co-expressed with an inhibitor, NuiA, and a structure of the NucA:NuiA complex has been solved and published (Figure 5.12). The interaction between NucA and NuiA in *Anabaena* is facilitated by a metal-ion bridge between the active-site metal ion and NuiA (Ghosh et al., 2007). Nin does not share any sequence or structural similarity to NuiA, and therefore any inferences made on the mechanism of binding of Nin to NucA/B based upon NucA:NuiA are unlikely to be correct. Indeed, PDBeFold analysis (Krissinel & Henrick, 2004) of the PDB reveals that Nin shares no structural homology with any other nuclease inhibitor deposited in the PDB, therefore, the mechanism of inhibition of NucA by Nin is currently a mystery.

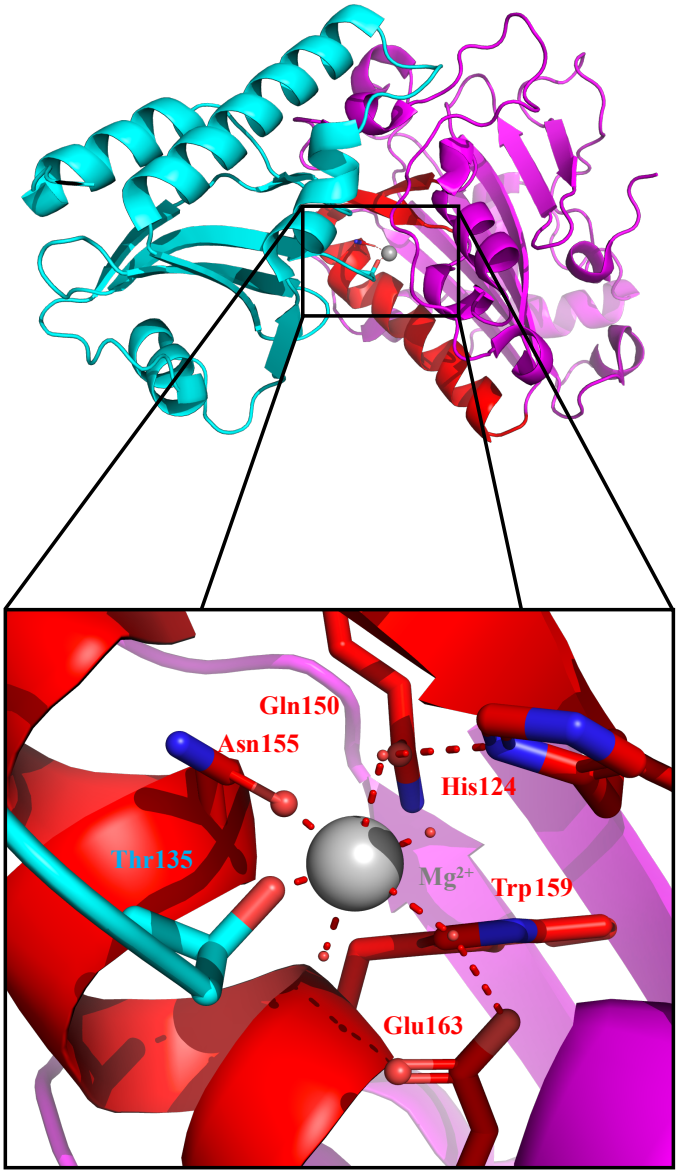

Figure 5.12: Binding of NuiA to NucA in *Anabaena* is characterised by a metal-ion bridge. The structure of the NuiA-NucA complex from *Anabaena* is shown rendered as a cartoon, with NucA coloured magenta, and NuiA coloured cyan (Ghosh et al., 2005). The ββα domain of NucA is coloured red. Residues in NucA involved in the hydrogen-bonding network surrounding the active-site Mg^{2+} are rendered as sticks and labelled. Oxygen atoms from water molecules in the coordination sphere surrounding the active-site Mg^{2+} are rendered as small red spheres Thr135 of NuiA coordinates the metal-ion (here represented by Mg^{2+}), forming a metal ion bridge with NucA, binding in the active site and preventing DNA entry.

5.13 Aims of this study

As discussed above, there is much to be discovered about NucA and NucB, and Nin in *Bacillus* strains; no biochemical studies have been reported on the *Bacillus* homologues of NucA since their discovery some ~30 years ago, nor has the interaction between NucA and Nin been probed on a molecular level. By contrast, the foundations have been laid for further study of NucB based on the structure of the *B. licheniformis* homologue of this protein (Basle et al., 2018), however, most of the work to-date has focussed on use of NucB as a biofilm-dispersing tool (Shields et al., 2013; Nijland et al., 2010; Shakir et al., 2012), rather than on its biological function. As Nin serves as a protective mechanism for several bacteria against their own endonucleases, disruption of the NucA/B:Nin interaction is likely to result in cell-death. A comprehensive understanding of the molecular basis of the interaction between these proteins is likely to facilitate the development of molecules capable of breaking up the interaction and could lead to a new class of antibiotics. In the subsequent Chapter, the interactions between NucA and NucB with Nin from *B. subtilis* are examined by a variety of biochemical techniques. A production and purification strategy is devised that circumvents cell death through genomic degradation upon expression of NucA and NucB using standard expression techniques in *E. coli*, allowing for their *in vitro* study. The structures of NucA and NucB with Nin is presented, allowing for the calculated dismantling of the protein complexes by structure-guided mutagenesis. This work builds upon much of the work described in this Section, providing further insight into key structural features required for nuclease-nuclease inhibitor interactions with sub-nM dissociation constants.

Chapter 6.

The molecular basis of the Nin-mediated inhibition of NucA and NucB endonuclease activity

6.1 Background and aims

As discussed in Section 5.11, recent work on NucB from a marine isolate of *Bacillus licheniformis* has been directed towards its potential as a biofilm dispersal agent, rather than towards its function or regulation (Baslé et al., 2018; Shields et al., 2013; Nijland et al., 2010; Shakir et al., 2012). The structures of NucA, NucB, and the Nuclease inhibitor, Nin, from the bacterial genera *Anabaena*, *Serratia, Bacillus,* and *Streptococcus* have been solved (Baslé et al., 2018; Ghosh et al., 2005; Moon et al., 2014; Shlyapnikov et al., 2000), and structural work on NucA from the marine cyanobacterium *Anabaena* has shed some light on the molecular intricacies of the interaction between NucA and NuiA, a functional, but not structural, homologue of Nin (Ghosh et al., 2007). The structure of Nin from *B. subtilis* has been solved in isolation, 4MQD, an unpublished output from a structural genomics group. To date, no structural or in-depth functional information has been published concerning the interactions between NucA and NucB with Nin from any *Bacillus* strain. This chapter describes the development and validation of a novel expression/purification strategy for NucA and NucB from *B. subtilis*, the structural basis of NucA and NucB inhibition by Nin, the determination of an upper limit of their affinities, and finally the calculated dismantling of the two protein complexes by structure-guided mutagenesis. The data generated in this chapter provide insight into the essential structural features required for the interaction between NucA/B and Nin, and may act as a basis for any structure-based bactericidal/bacteriostatic drug design targeted towards this interaction. The work discussed in this chapter also provides insight into essential molecular features of sub-nM affinity protein-protein interactions (PPIs), which may be applied generally to the study of PPIs in other organisms.

6.2 Recombinant expression and purification of NucA, NucB, and Nin in *E. coli*

Prior attempts to express NucA/B proteins using *E. coli* expression systems were unsuccessful (unpublished), likely a result of host genome degradation by NucA/B upon their expression. As a result of the difficulties associated with the production of active NucA/B in *E. coli*, all prior work concerning NucB in the Lewis lab had stemmed from a *B. subtilis* expression system that secreted *Bacillus licheniformis* NucB into the medium, and highly purified protein samples had been gifted to the lab for structural and biochemical studies. To ensure a readily-available supply of endonuclease for this work, render production of NucA/B more accessible, and develop an in-house genetic system for ease of producing site-directed mutants, a methodology

for producing NucA and NucB in *E. coli* was developed, eliminating the need for external production of Nuc proteins from *Bacillus* strains.

pET-22b(+) (Novagen) is an *E. coli* expression vector with a *pelB* signal sequence immediately upstream of its multiple-cloning site, and a hexahistidine tag immediately downstream. The PelB signal sequence is derived from the N-terminal signal sequence of pectate lyase B from *Erwinia carotovora* CE (Lei et al., 1987). Genetic attachment of the PelB signal sequence to a recombinant protein results in its localisation to the periplasm of *E. coli* through the Sec protein secretion pathway (Sockolosky & Szoka, 2013), which translocates proteins through the cytoplasmic membrane in an unfolded state. Use of the Sec pathway for translocation renders PelB-based expression a useful tool for NucA and NucB production as the endonucleases are not functional within the cell upon expression, rendering any self-induced genomic degradation highly unlikely.

NucA and NucB were amplified from *Bacillus subtilis* gDNA, such that their N-terminal transmembrane domain/signal peptide, respectively. The N-terminally truncated sequences of NucA and NucB were cloned into the multiple-cloning site of pET-22b(+) using restriction-based cloning techniques (Section 2.2.6), placing them in frame with the *pelB* signal sequence, replacing their native transmembrane domains/signal peptides with the *pelB* signal sequence (Figure 6.1). pET-22b(+) constructs harbouring NucA or NucB were transformed into competent *E. coli* C43(DE3) cells (Lucigen), a cell-line effective at expressing toxic proteins (Dumon-Seignovert et al., 2004). Expression of NucA and NucB was successful, and the two endonucleases were purified using successive steps of IMAC, ion-exchange chromatography, and gel filtration (Sections 2.); a representative polishing of NucA by gel filtration is shown in Figure 6.2.

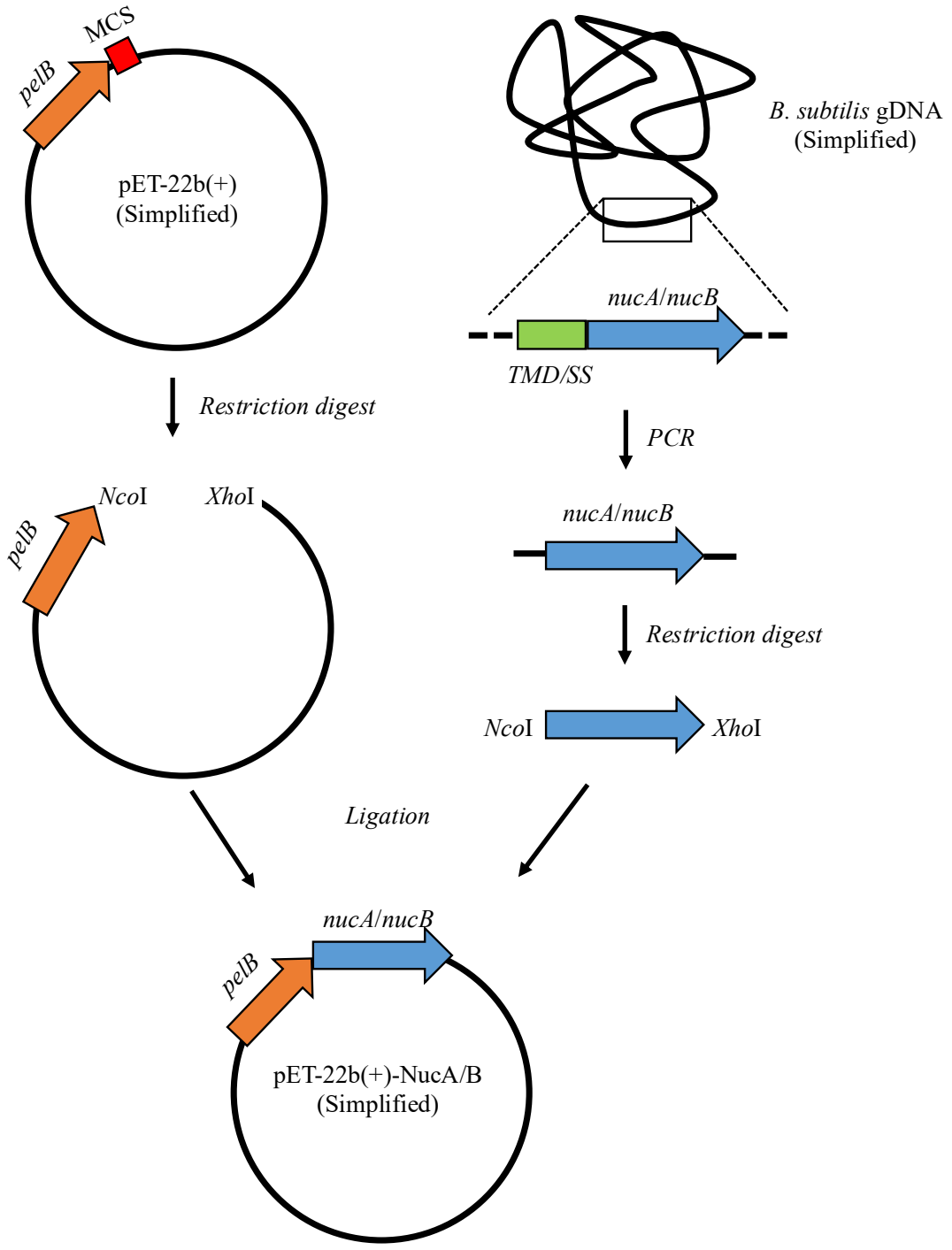

Figure 6.1. Strategy for construction of an expression vector for the endonucleases NucA and NucB. *nucA* and *nucB* were amplified by PCR from *B. subtilis* gDNA, restriction-digested, and ligated into the multiple-cloning site (MCS) of pET-22b(+). The transmembrane domain (TMD), or signal sequence (SS), from *nucA* and *nucB*, respectively, were removed from the sequences during the PCR reaction.

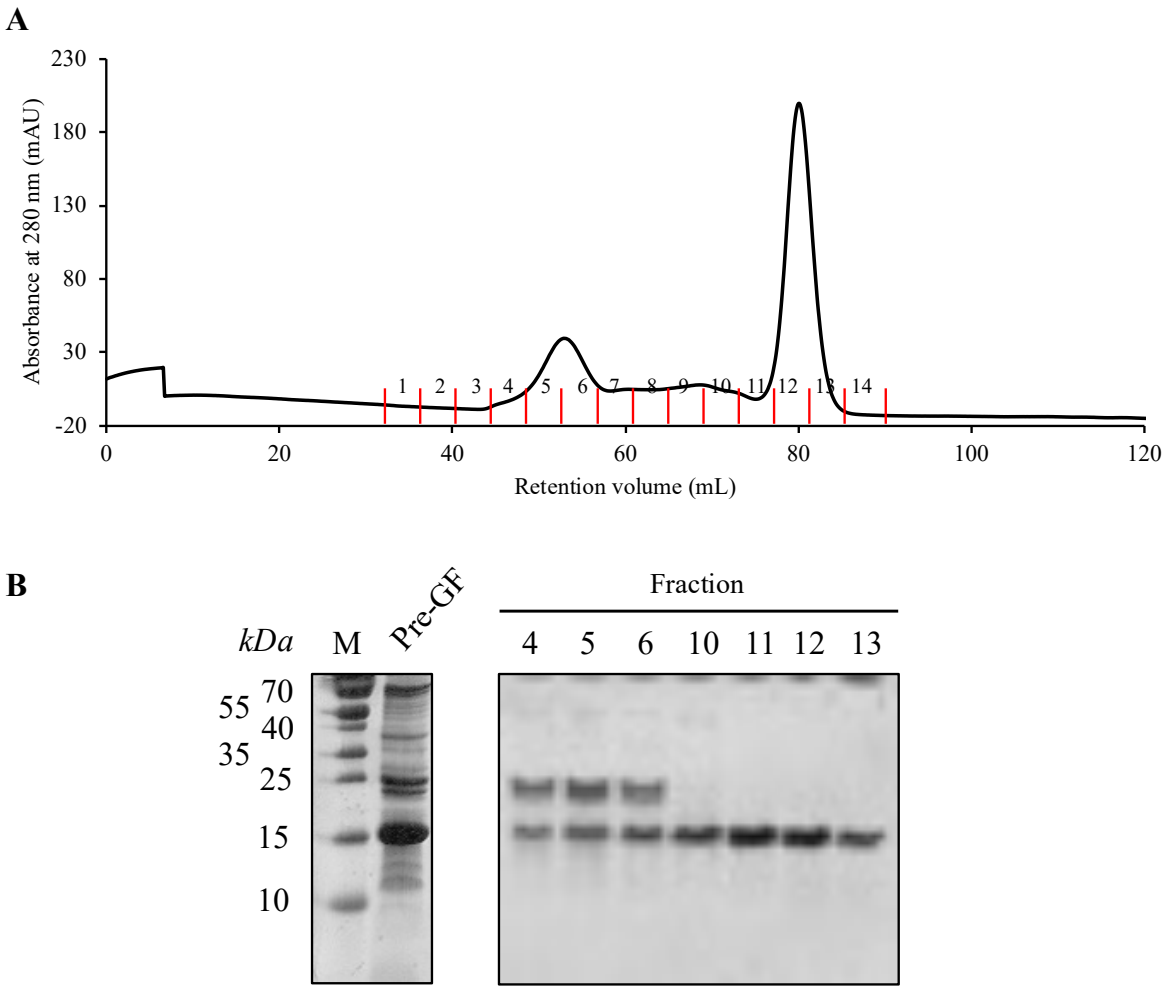

Figure 6.2. Representative polishing of *Bs*NucA by gel filtration chromatography. A) A typical gel filtration chromatogram of *Bs*NucA loaded onto a HiLoad Superdex 75 16/60 pg. **B)** A representative SDS-PAGE of *Bs*NucA. The major band running at about the 15 kDa molecular weight marker corresponds to *Bs*NucA (monomeric MW = 14.9 kDa). Based on these data, fractions 11-13 were pooled and concentrated for further analysis.

Production of *B. subtilis* Nin proved to be far more straightforward, perhaps unsurprisingly as Nin is presumably a cytoplasmic, globular protein, biochemically inert except for the inhibition of the nuclease function of Nuc proteins. Nin was cloned from *B. subtilis* gDNA into the multiple cloning site of pETM-11 (Dümmler et al., 2005), such that the hexahistidine tag and TEV protease cleavage site present in pETM-11 were fused to the N-terminus of Nin. Nin was expressed in *E. coli* BL21(DE3) cells and purified by successive steps of IMAC, reverse-IMAC, and gel filtration (Section 2.3.3-2.3.6). A representative purification of Nin is shown in Figure 6.3, all mutants of Nin described in this chapter were expressed and purified in the same fashion.

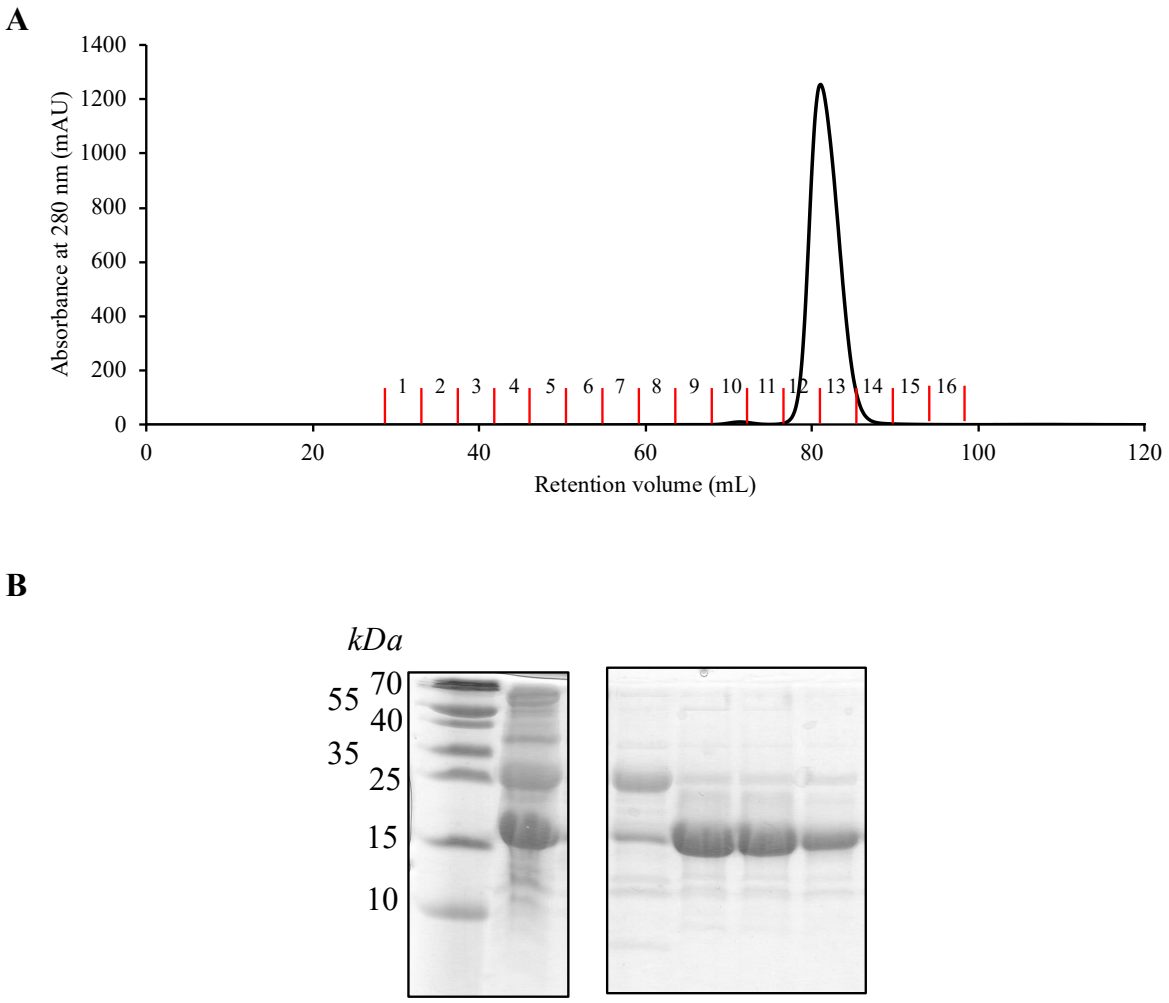

Figure 6.3. Representative polishing of *Bs*Nin by gel filtration chromatography. A) A typical gel filtration chromatogram of *Bs*Nin loaded onto a HiLoad Superdex 75 16/60 pg. **B)** A representative SDS-PAGE of *Bs*Nin. The major band running at about the 15 kDa molecular weight marker corresponds to *Bs*Nin (MW = 15.3 kDa). Based on these data, fractions 12-14 were pooled and concentrated for further analysis.

Polycistronic expression vectors were also constructed using pETM-11-Nin in which open reading frames encoding NucA or NucB were placed between the T7 promoter and the gene for Nin. Expression of NucA:Nin and NucB:Nin complexes using these vectors proved successful, however, yields of the complex were far lower than when purified in isolation (data not shown), therefore, this methodology for complex production was abandoned in favour of the construction of complexes *in vitro*. The reconstitution of complexes from individual components also enables thermodynamic and kinetic parameters of Nuc and Nin complexes to be measured.

To confirm that the purification strategy applied here to NucA and NucB had no adverse effect on their structure, NucA and NucB were analysed by circular dichroism (Section 2.4.2). The CD spectra of NucA and NucB match that of the predicted CD spectrum of NucB calculated

by the PDB2CD webserver (Mavridis & Janes, 2017) using the published structure of *Bl*NucB (PDB code 5OMT) as the input (Figure 6.4). Based on these data, it was concluded that the expression and purification strategy adopted here for NucA and NucB was appropriate for study of these proteins, and any concerns of aberrant protein folding was addressed successfully.

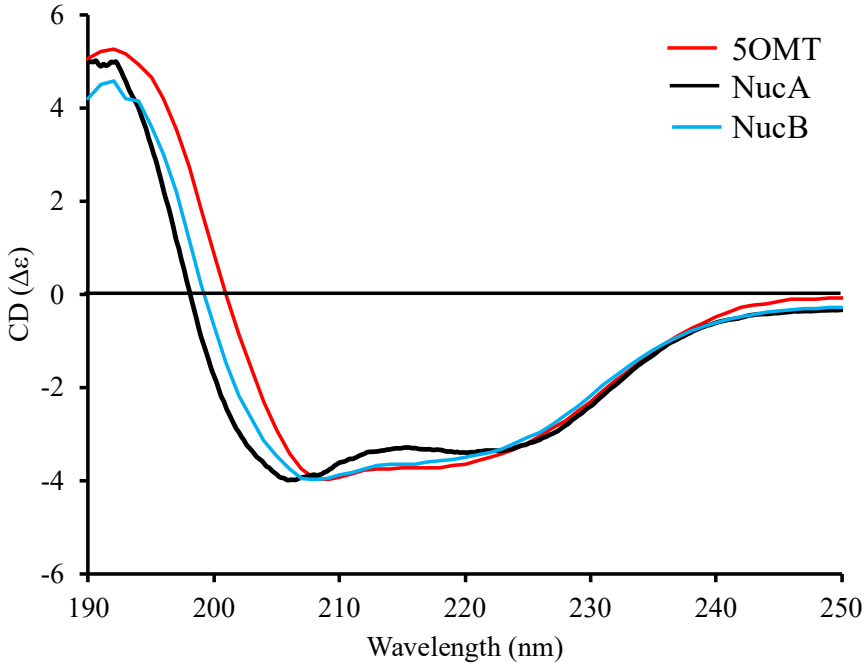

Figure 6.4. Circular dichroism of NucA and NucB compared against the structure of *Bl*NucB (PDB code 5OMT). The CD spectra for NucA and NucB were compared against the theoretical CD spectrum of *Bl*NucB generated from the crystal structure in PDB2CD. NucA and NucB are both similar enough to the theoretical spectrum of NucB that they were assumed to be properly folded.

Although this chapter focusses on work performed on *B. subtilis* NucA, NucB, and Nin, the same expression strategies were applied to the production of *B. licheniformis* NucA, NucB, and Nin. Work on the *B. licheniformis* proteins was undertaken by Lois Norton, a Master's student under my tutelage in the lab, and our results were highly consistent (see Discussion).

6.3 Interaction studies of NucA/B with Nin

6.3.1 Nuclease inhibition assays

In order to assess whether the NucA/B proteins purified in this study were biochemically functional, as well as whether Nin acted as a functional nuclease inhibitor *in vitro* or not, endonuclease reactions using NucA/B in the presence or absence of Nin were prepared and the

results of these reactions analysed by agarose gel-electrophoresis (Section 2.2.6). NucB and NucA are both known to be dependent on divalent cations for their function (Ghosh et al., 2005; Baslé et al., 2018), therefore, magnesium chloride was included in the reaction mix to ensure a sufficient supply of Mg^{2+} ions for nuclease function. Under these conditions, both NucA and NucB were capable of digesting plasmid DNA *in vitro*, and both were inhibited by the presence of Nin (Figure 6.5), suggesting that Nin could indeed inhibit the nuclease action of both NucA and NucB *in vitro*. Interestingly, the electrophoretic profile of the Nin-induced inhibition of NucA and NucB were highly comparable in this experiment, suggesting that the nature of inhibition may be similar for both complexes. In order to better characterise the NucA/B:Nin interaction proposed by the nuclease inhibition assays performed here, SPR and ITC were used to characterise the interactions.

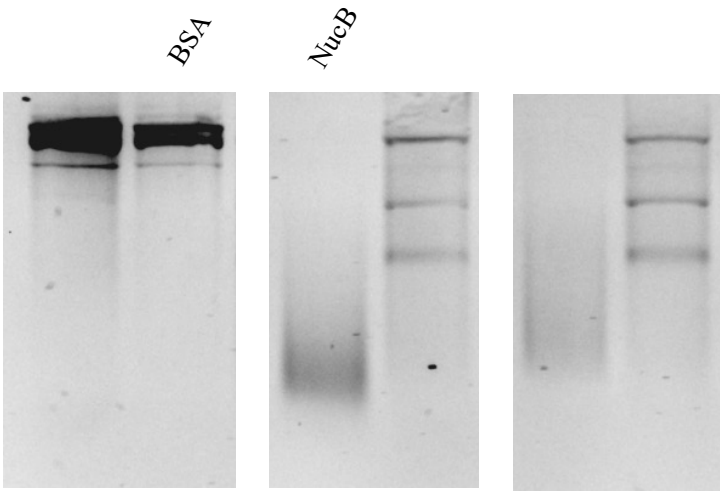

Figure 6.5. Nuclease interference assay of NucA/B with Nin. NucA and NucB were incubated with plasmid DNA in the presence and absence of Nin and the products of the reaction analysed by agarose gel electrophoresis. In comparison to the negative controls shown here (Plasmid alone and BSA), NucB and NucA both show nuclease activity, evidenced by the loss of the longer DNA bands seen in the negative controls. In the presence of Nin, the activity of NucA and NucB is reduced, and the longer DNA bands are seen in these lanes.

6.3.2 Surface plasmon resonance studies of NucA/B against Nin

For all of the SPR experiments shown here, NucA and NucB were immobilised onto a Ni-NTA sensor chip via the non-cleavable His_6-tag present at their respective C-termini. Nin was passed over the immobilised NucA or NucB and the interaction between the complexes measured (Section 2.5.2). For both NucA and NucB, binding was observed by SPR and the kinetic parameters for the NucA/B:Nin complex were assessed by a 1:1 binding model (Figure 6.6). The SPR data shown here are in agreement with the nuclease interference assay shown above,

and confirm that inhibition of NucA and NucB by Nin comes from a direct binding event between NucA/B and Nin. The K_D calculated by SPR is in the low nanomolar range, 6.5 ± 1.2 nM for NucA:Nin and 5.7 ± 3.5 nM for NucB:Nin.

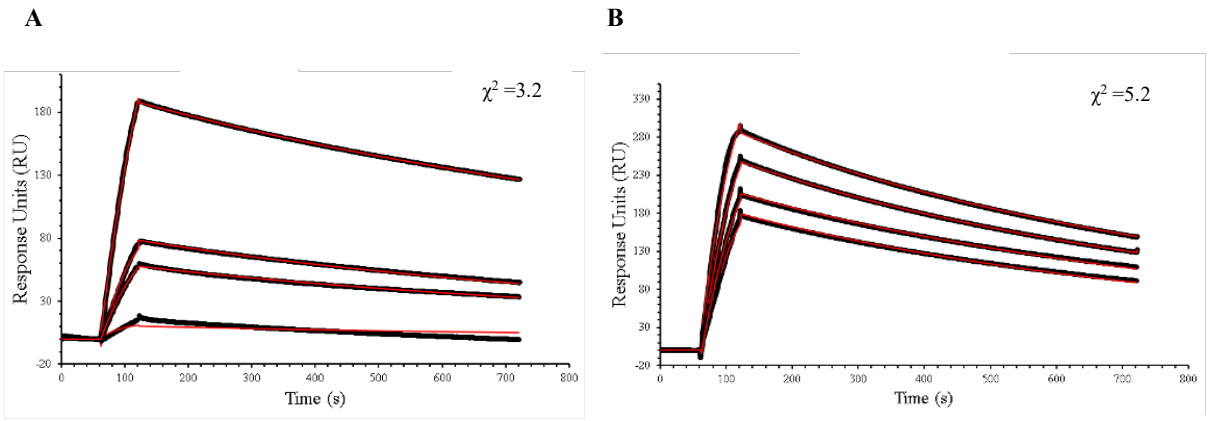

k_a	k_d	K_D
($M^{-1}s^{-1}$)	(s^{-1})	(M)
1.8 ± 0.1 x10^5	1.2 ± 0.007 x10^{-3}	6.5 x10^{-9} ± 1.2 x10^{-9}

k_a	k_d	K_D
($M^{-1}s^{-1}$)	(s^{-1})	(M)
2.6 ± 0.04 x10^5	1.5 ± 0.007 x10^{-3}	5.8 x10^{-9} ± 3.5 x10^{-9}

Figure 6.6. Surface plasmon resonance studies of A) NucA and B) NucB with Nin. NucA or NucB were immobilised onto the Ni-NTA sensor chip, and Nin was passed over in a concentration series. The binding of NucA or NucB with Nin was assessed using a 1:1 binding model in the Biacore Evaluation Software (GE Healthcare). The experimental data are plotted as a black line, the models used to determine the kinetic parameters of the reaction are plotted as red lines.

6.3.3 Isothermal titration calorimetry of NucA and NucB with Nin

In order to supplement the binding data shown above with a parallel technique that does not rely on the immobilisation of a binding partner onto a surface, the interaction between NucA and NucB with Nin was also assessed by ITC. NucA and NucB were taken up into the syringe of the ITC instrument each at 200 µM, and 200 µl of Nin was aliquoted into the cell of the ITC instrument at 20 µM (Section 2.5.1). A series of 20 injections of 2 µl of NucA or NucB into Nin followed. Using this experimental setup, both NucA and NucB were found to interact strongly with Nin (Figure 6.7). Fitting of a binding isotherm model to the data suggests a low-nanomolar K_D of 4.4 nM for NucA and 7.1 nM for NucB. Although these calculated K_D values appear to agree with those generated from the SPR data presented here, closer inspection of the ITC data suggest that the interaction between NucA/B and Nin is likely beyond the limits of detection for this methodology: as a result of the rapid saturation of all available Nin by NucA/B, very few data points are available in the interval between unsaturated and saturated states of Nin, 2 or 3 in each case, resulting in a C value outside the required range to calculate K_D accurately (Section 2.5.1). In an attempt to address this concern, and acquire an accurate

K_D, the concentration of NucA/B in the syringe was lowered, however, lowering the concentration of the protein in the syringe and increasing the concentration of protein in the cell resulted in less measurable heat energy being produced per injection (data not shown), and it was not possible to lower the concentration in the syringe sufficiently to measure the kinetics of the interaction accurately. The concentration of protein in the cell of the instrument was also increased, however, this only resulted in a right-shifting of the binding isotherm, but did not lower the C value of the isotherm (data not shown). It was concluded based on these experiments that the K_D of the NucA/B:Nin interaction is likely to be sub-nanomolar.

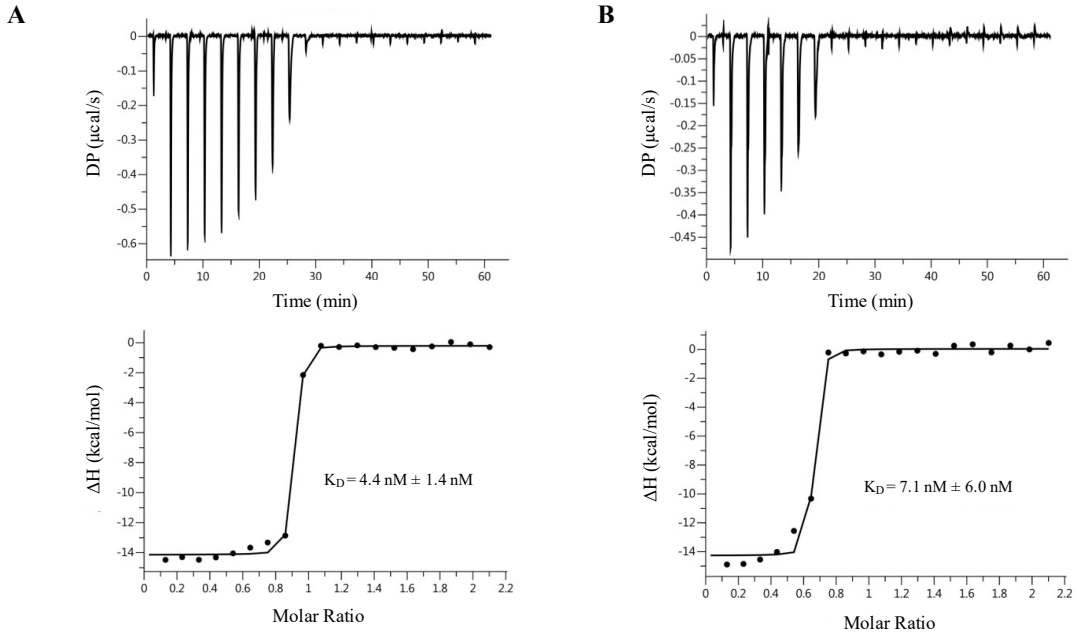

Figure 6.7. Isothermal titration calorimetry studies of A) NucA and B) NucB with Nin. NucA or NucB were injected into Nin in the ITC instrument. The interchange between unsaturated and saturated Nin is sufficiently rapid that the kinetics of the interaction between NucA and NucB with Nin are unable to be accurately determined. Therefore the K_D values shown here calculated by the MicroCal Evaluation software (Malvern Panalytical) are likely to represent an upper-limit for this interaction.

6.4 The crystal structure of NucA and NucB in complex with Nin

Based on the wealth of positive binding data acquired for NucA/B:Nin, crystallisation trials were attempted on the protein complexes. Initially, purified NucA, NucB and Nin were subjected to crystallisation trials in isolation (Section 2.4.9). Crystals appeared for Nin within one week and were subjected to in-house X-ray diffraction experiments (Section 2.4.9) as a means by which to become familiar with the structure solution pipeline. The structure of Nin was solved by molecular replacement in PHASER (McCoy et al., 2007) using the structure of *B. subtilis* Nin already in the PDB (PDB code 4MQD), before their refinement to convergence using Coot, REFMAC5, PDB-REDO and MolProbity (Murshudov et al., 2011; Joosten et al.,

2014; Williams et al., 2018; Emsley & Cowtan, 2004). The structure of Nin presented here confirms the structure of Nin in the PDB, and provides a basis for any comparisons between the structure of Nin in isolation with that of the complex (Figure 6.8). Nin's secondary structure is predominantly made up of β-sheets, with 48 % of the structure comprising β-sheet, 4.8 % comprising α-helices, and 47.2 % comprising loops/turns/disordered regions. The structure of Nin is that of a β-sandwich (Figure 6.8a), the two regions of β-sheet responsible for the formation of this β-sandwich arrangement are clearly laid out in the topology diagram for Nin (Figure 6.8b).

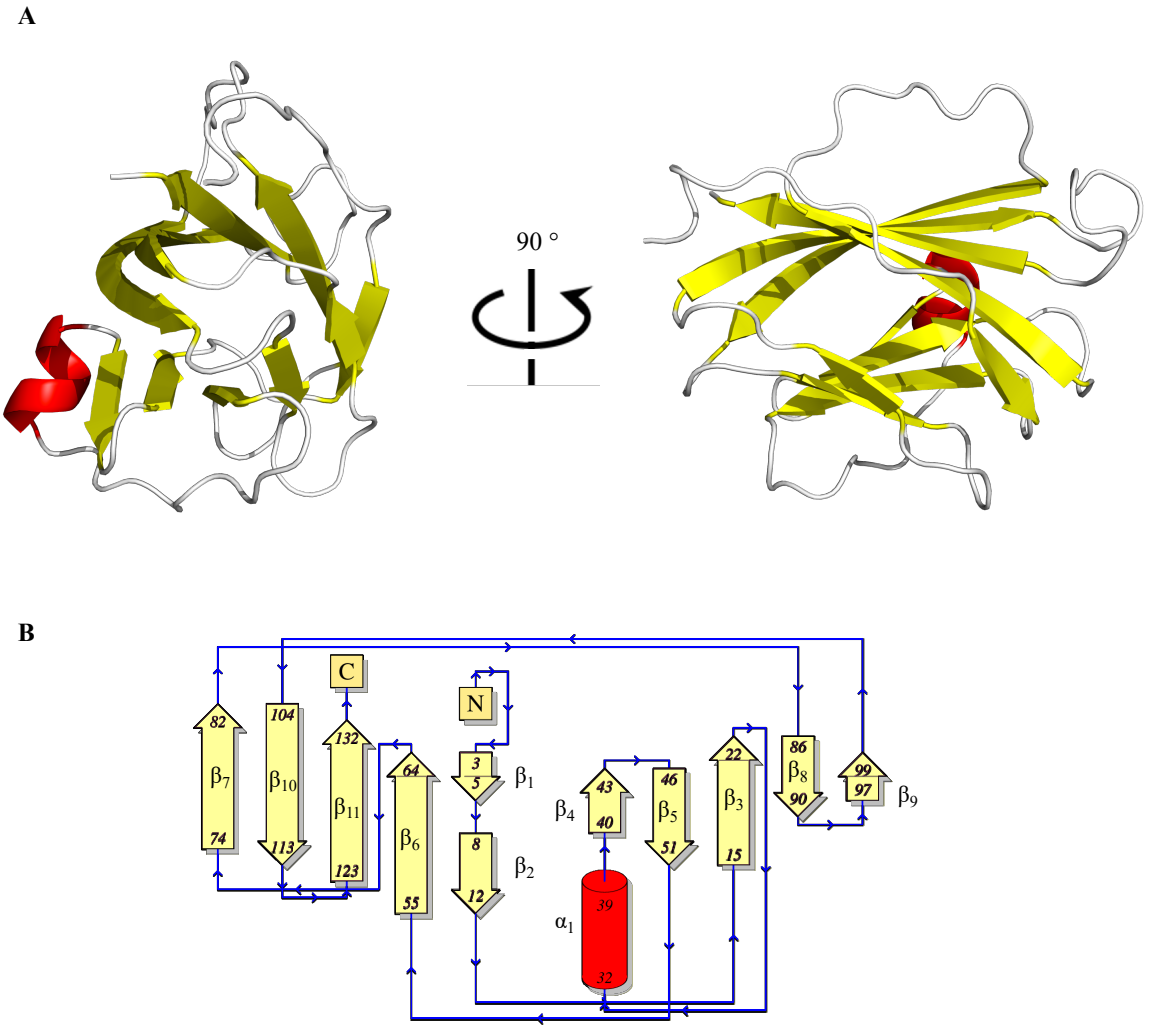

Figure 6.8. The A) structure and B) topology of Nin. Nin is rendered as a cartoon with beta-sheets coloured yellow and alpha-helices coloured in red. Nin is composed primarily of beta-sheets, comprising 48 % of the overall structure.

By contrast, no crystals of *B. subtilis* NucA or NucB appeared during the course of these experiments, although no further attempts to crystallise these proteins in isolation were made as they quickly became redundant, partly because the Lewis lab had already solved the structure of isolated *B. licheniformis* NucB (Baslé et al., 2018) and partly because of progress with the structural analysis of the Nuc:Nin complexes (see below). Purified NucA or NucB proteins were incubated separately with Nin at a 1:1 molar ratio immediately prior to setting up crystallisation trials; an alternative strategy was to purify the protein complexes from the mixture by SEC immediately prior to crystallisation, ultimately this approach was not required. Crystals for both NucA:Nin and NucB:Nin complexes from *B. subtilis* appeared after one week (Figure 6.9) and were subjected to X-ray diffraction experiments at Diamond Light Source (Section 2.4.9) with the help and guidance of Arnaud Baslé (Structural Biology Laboratory, Newcastle University).

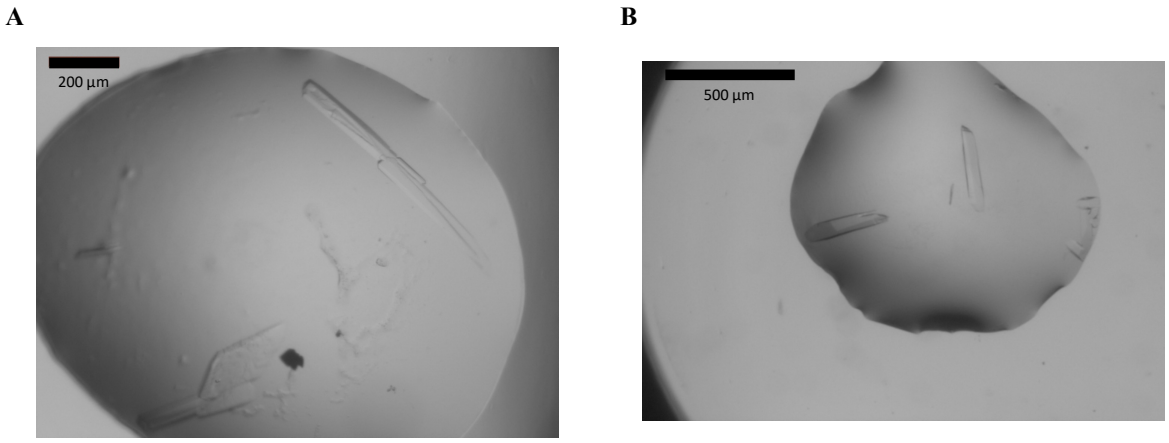

Figure 6.9. Crystallisation of A) NucA and B) NucB with Nin. NucA and NucB were incubated at an equimolar ratio and subjected to crysallisation trials. The crystals shown here appeared after one week.

The structures of NucA:Nin and NucB:Nin were solved by molecular replacement in PHASER (McCoy et al., 2007) using the structures of *B. licheniformis* NucB and *B. subtilis* Nin (PDB codes 5OMT and 4MQD, respectively) simultaneously as search models. Sequence mismatches between molecular replacement solutions and *B. subtilis* NucA/B and Nin were automatically fixed using CCP4Build before refinement to convergence using Coot, REFMAC5, PDB-REDO and MolProbity (Murshudov et al., 2011; Joosten et al., 2014; Williams et al., 2018; Emsley & Cowtan, 2004). The structure of NucA/B in complex with Nin is shown in Figure 6.10. Data collection parameters and refinement statistics for NucA:Nin and NucB:Nin are shown in Table 6.1.

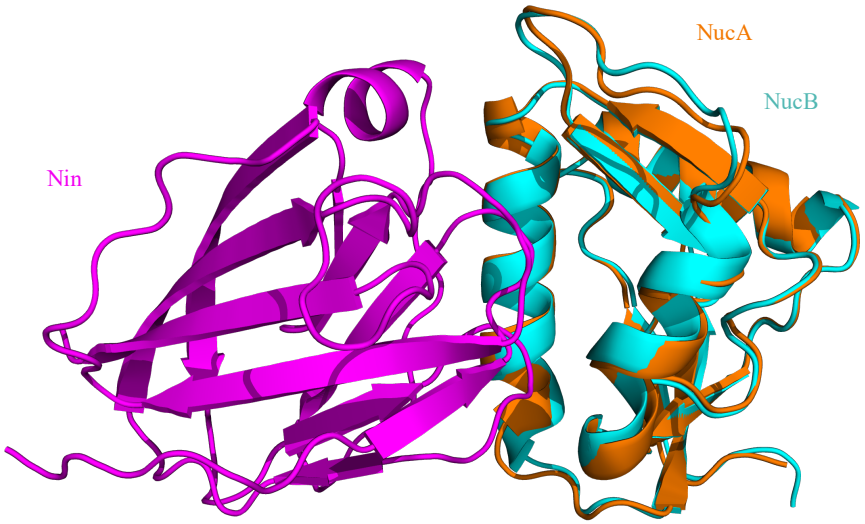

Figure 6.10. The crystal structures of *Bs*NucA and *Bs*NucB in complex with *Bs*Nin. *Bs*Nin, *Bs*NucA, and *Bs*NucB are rendered as cartoons, with *Bs*Nin coloured magenta, *Bs*NucB coloured cyan, and *Bs*NucA coloured orange. The structure of *Bs*Nin rendered here is that of the *Bs*NucB:*Bs*Nin complex.

Table 6.1. Data collection and refinement statistics for NucA:Nin and NucB:Nin

	NucA:Nin	NucB:Nin
Wavelength (Å)	0.96861	0.96861
Resolution range (Å)[a]	47.6 - 1.9 (2.0 - 1.9)	95.1 – 2.9 (3.1 – 2.9)
Space group	$P\,1\,2_1\,1$	$C\,1\,2\,1$
Unit cell dimensions		
***a*, *b*, *c* (Å)**	50.8, 49.3, 51.4	138.1, 76.0, 95.1
***α*, *β*, *γ* (°)**	90, 100.4, 90	90, 91.2, 90
Total reflections[a]	61744 (2720)	72696 (12073)
Unique reflections[a]	19805 (1185)	20766 (3443)
Multiplicity[a]	3.1 (2.3)	3.5 (3.5)
Completeness (%)[a]	99.1 (94.0)	94.6 (98.7)
Mean I/σI[a]	10.1 (2.8)	3.0 (1.4)
Wilson B-factor (Å²)	16.71	58.4
R_{merge}[a]	0.06 (0.29)	0.213 (0.493)
$R_{p.i.m.}$[a]	0.05 (0.27)	0.200 (0.464)
$CC_{1/2}$[a]	0.98 (0.56)	0.932 (0.691)
R_{work} (%)	0.20	0.24
R_{free} (%)[b]	0.24	0.29
Number of non-hydrogen atoms	2057	6119
macromolecules	1930	5841
solvent	127	278
Protein residues	241	742
RMS(bonds)	0.016	0.019
RMS(angles)	2.12	2.68
Ramachandran favored (%)	96.62	92.13
Ramachandran allowed (%)	3.38	6.08
Ramachandran outliers (%)	0.00	1.80
Clashscore	7.70	8.8
Average B-factor	29.08	66.99
macromolecules	28.89	67.34
solvent	31.90	59.65

[a]Values in parentheses denote highest resolution shell.

[b]5% of reflections were selected randomly for determination of R_{free}

The overall folds of NucA and NucB are in essence indistinguishable from each other, as well as from their non-complexed counterparts (Figure 6.11b), with pairwise r.m.s.d. values in the 0.50 Å to 0.67 Å range over 104 matched Cα atoms (out of 114 total amino acids visible) (RMSD values were calculated in PyMol (Schrödinger)). It follows from their structural similarity to *B. licheniformis* NucB that *B. subtilis* NucA and NucB are also members of the ββα family of metal-dependent endonucleases and share an identical topology to *Bl*NucB. *Bs*NucA and *Bs*NucB are single-domain globular proteins with five β-strands and three α-helices. Nin was also found to be superimposable with its non-complexed counterpart, with an r.m.s.d. of 0.52 Å (out of 97.7% of total Cα atoms) (RMSD values were calculated in PyMol (Schrödinger)), suggesting that no substantial structural re-arrangement appears to occur upon binding of any of the proteins to one another (Figure 6.11a). Key active site residues known to be essential for *Bl*NucB activity (Baslé et al., 2018) are maintained in *Bs*NucA and *Bs*NucB, and are structurally superimposable, supporting the likely importance of these residues for nuclease function (Figure 6.12).

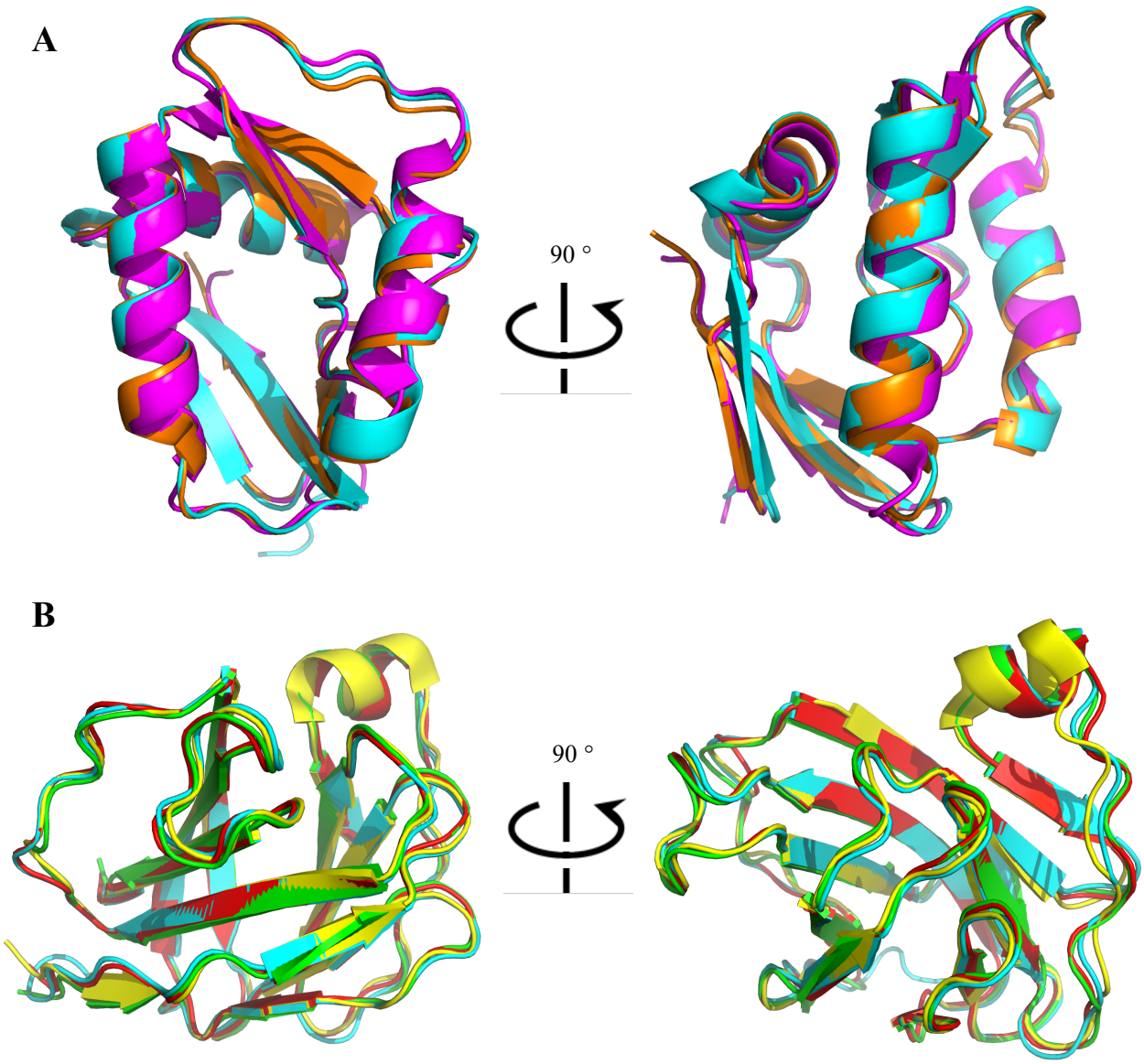

Figure 6.11. Superposition of all solved structures of NucB, NucA and Nin. A) *Bl*NucB (PDB code 5OMT), *Bs*NucB**,** and *Bs*NucA are rendered as cartoons and coloured in magenta, cyan, and orange, respectively. The structure of all three proteins is identical, suggesting no major structural rearrangement occurs upon Nin binding. **B)** *Bs*Nin from the PDB structure (PDB code 4MQD, yellow), the unbound structure presented in this study (green), and both the NucA (cyan) and NucB-bound (red) structures are overlaid. As is the case for NucA/B, each structure of Nin is superimposable, therefore no major structural rearrangement occurs for Nin upon binding to NucA/B. (RMSD values were calculated in PyMol (Schrödinger))

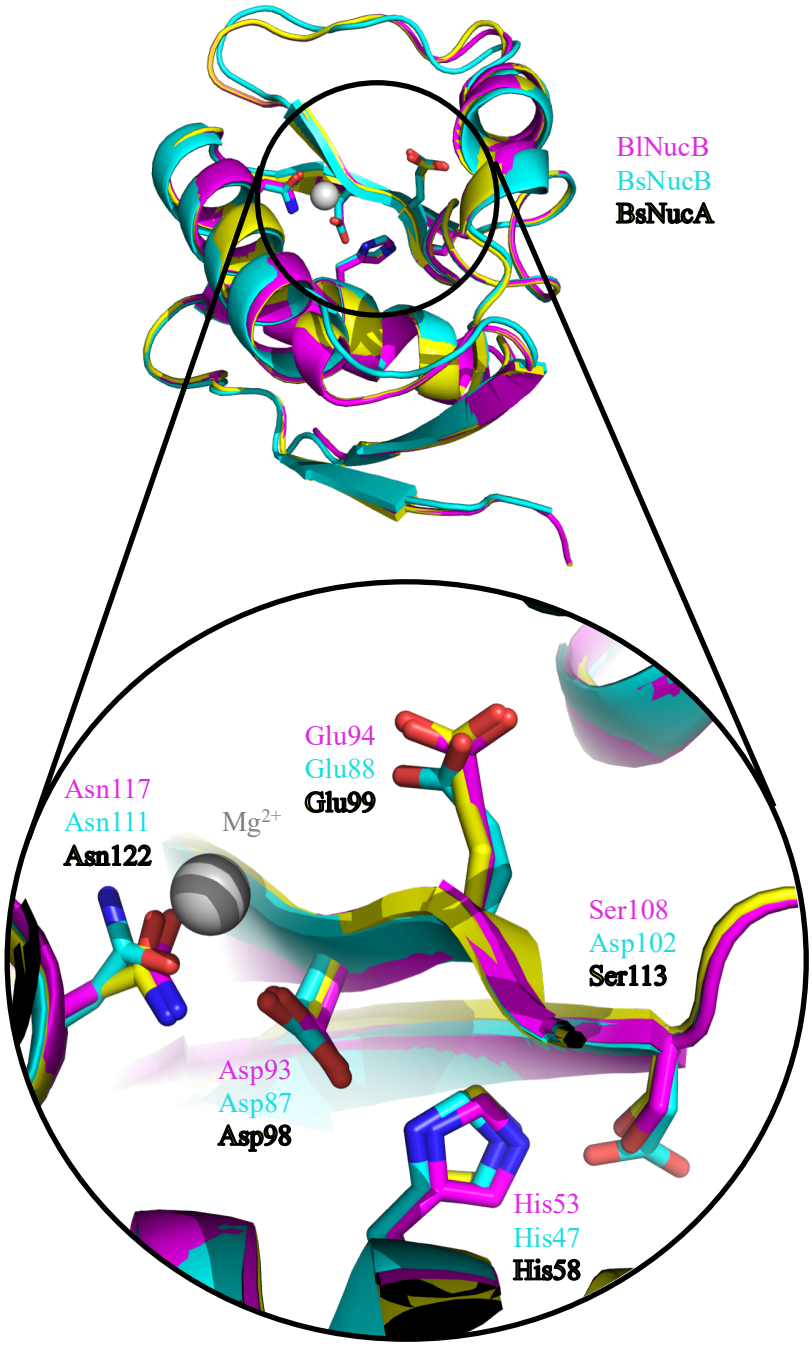

Figure 6.12. Superposition of active site residues in all solved structures of NucA/B. The residues known to be essential for nuclease activity in *Bl*NucB and *Bs*NucB are rendered as sticks and overlaid with their counterparts in *Bs*NucA. Apart from Asp102 in *Bs*NucB, each residue shown is structurally conserved between all currently solved structures, providing further evidence of the essentiality of these residues for nuclease activity. Asp102 forms a hydrogen bond with His47 in *Bs*NucB, serving the same purpose as Ser108, which forms a hydrogen bond with His53 in *Bl*NucB. (RMSD values were calculated in PyMol (Schrödinger))

Based on the model of DNA-binding proposed for *Bl*NucB and *Bs*NucB (Baslé et al., 2018), it is immediately obvious from the structure of the NucA/B:Nin complex that the mechanism of inhibition of NucA and NucB by Nin is competitive. Nin fits directly into the DNA-binding active site of NucA and NucB, rendering it impossible for DNA to access the residues responsible for cleavage of the sugar phosphate backbone at the same time that Nin is bound (Figure 6.13). Many conserved residues on NucA, NucB, and Nin sit at the interface between the proteins (Figure 6.14), in particular Tyr14, which is situated in a position that is likely to sterically occlude DNA-binding as well as displacing the catalytic divalent cation required for catalysis, is invariant in Nin orthologues. As the region of interaction on NucA/B is the endonuclease active site, the degree of conservation seen in this region of the protein is likely a result of the essentiality of residues in this region of the protein for its nuclease activity. Indeed, prior structure-guided mutagenesis work in the Lewis lab has already confirmed the essentiality of the active site residues His47, Asp87, Glu88, and Asn111 for *Bs*NucB function (Baslé et al., 2018). As Nin has no proposed roles in the cell outside of nuclease inhibition, the degree of conservation seen at the interaction site of Nin likely points to these residues as essential for the interaction between NucA/B and Nin. The structure of *Anabaena* NucA in complex with NuiA is made possible by a metal-ion bridge (Ghosh et al., 2007); no such metal-dependent interaction is seen for NucA:Nin or NucB:Nin. Instead, Nin residue Tyr14 appears to sit in the place of the metal ion in the active-site of NucA/B.

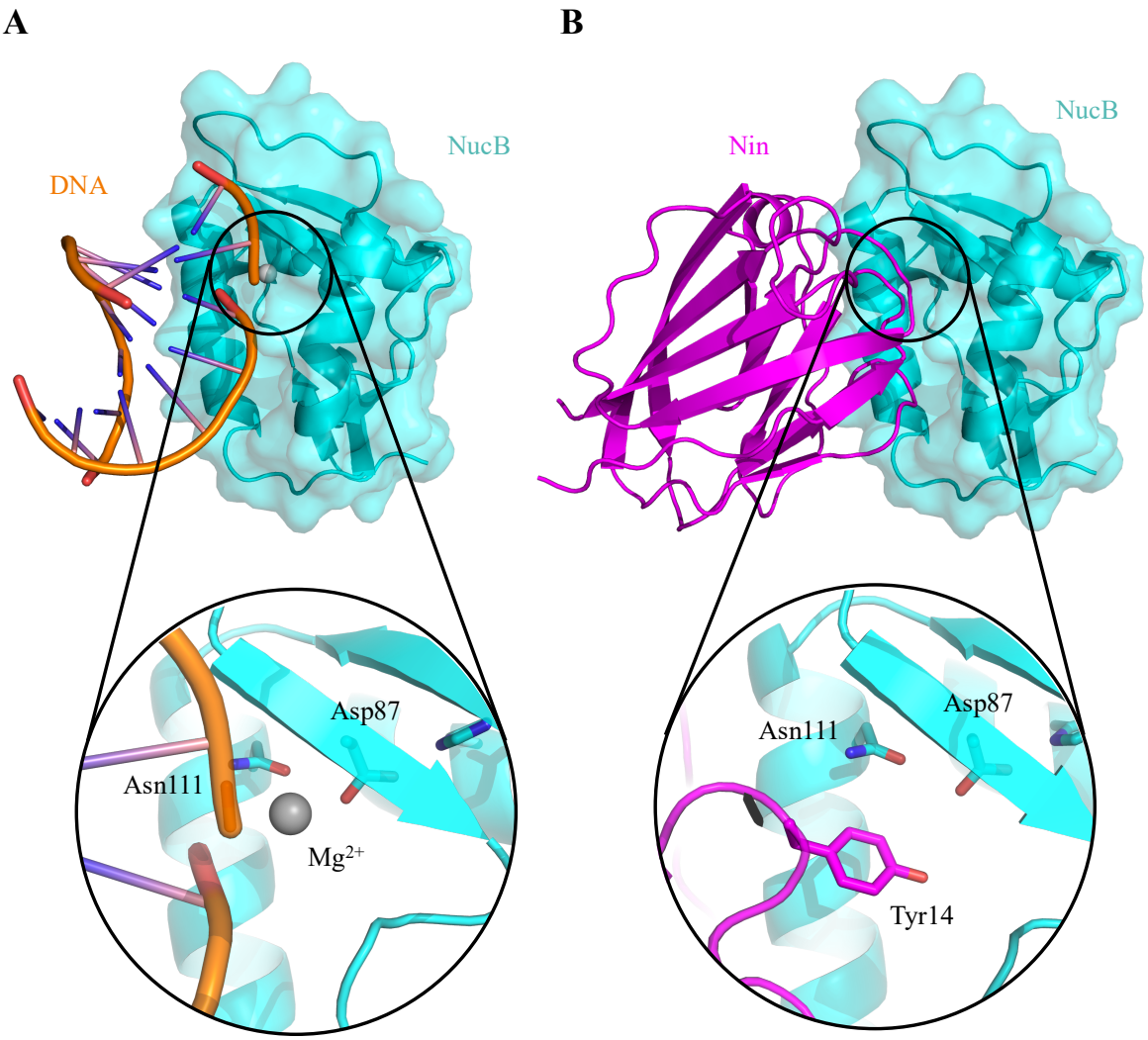

Figure 6.13. Mechanism of inhibition of nuclease activity by Nin. A) The model of DNA-binding by NucB, here modelled using the structure of *Bs*NucB from the NucB:Nin complex structure presented in this study. A close-up of the active-site is shown highlighting the putative position of the divalent cation essential for catalysis, as well as some of the residues implicated in catalysis. **B)** The structure of NucB in complex with Nin, with a close-up on the active site, where Tyr14 on Nin is buried.

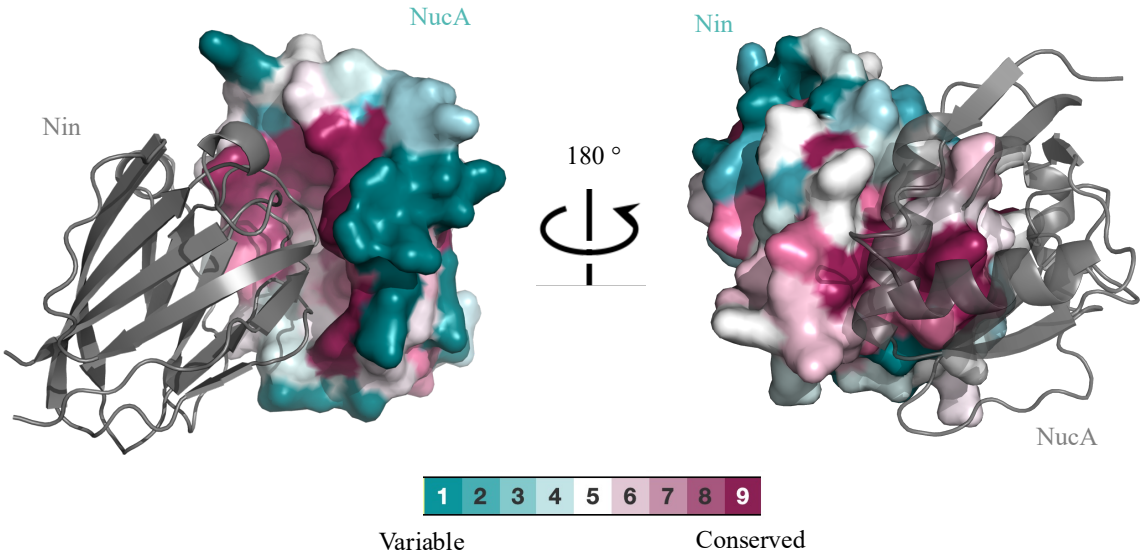

Figure 6.14. Conservation of interfacial residues between NucA and Nin. Nin or NucA are represented as a molecular surface and coloured according to degree of residue conservation. The greatest degree of conservation in the two proteins is at the interface between the two proteins. Whilst for NucA this is likely due to the essentiality of these residues for nuclease activity, for Nin, this is likely a result of interfacial residues being essential to its activity as a nuclease inhibitor.

6.5 Structure-guided dismantling of the NucA/B:Nin complex by site-directed mutagenesis

With the structure of the protein complexes in hand, attempts were made to disrupt the interaction between NucA/B and Nin. Initially, single residue point-mutations were made to Nin such that easy comparisons could be made between any features found to be important for the interaction on both the NucA and NucB complex. Residues to be mutated were chosen based on a combination of their conservation and their bonding interactions with NucA/B. Of the 22 residues on Nin involved in interactions with NucA/B, eight were chosen to be mutated, Ser11 (conservation score (CS) of 6 calculated by the ConSurf webserver, where 9 = conserved and 1 = variable), Tyr14 (CS 9), His15 (CS 8), Gln16 (CS 9), Glu50 (CS 8), Glu90 (CS 5), Met93 (CS 6) and Arg96 (CS 4), each of which sit in the binding interface between Nin and NucA/B (Figure 6.15). Arg96, Glu50, and His15 each form salt bridges with NucA/B residues Asp135/Asp130, Arg123/Arg118 and Asp96/Asp91, respectively, and as such were expected to confer some degree of essentiality for the NucA/B:Nin interaction. Gln16 and Glu90 form hydrogen bonds with NucA/B residues Arg123/Arg118 and His131/His126, respectively, rendering these residues likely to contribute significantly to the interaction between the two proteins. Ser11, His15, Met93, and Tyr14, whilst only involved in non-bonding contacts with

residues in NucA/B, are all buried within the NucA/B active-site in the complex structure, suggesting that they might contribute in part to complex formation.

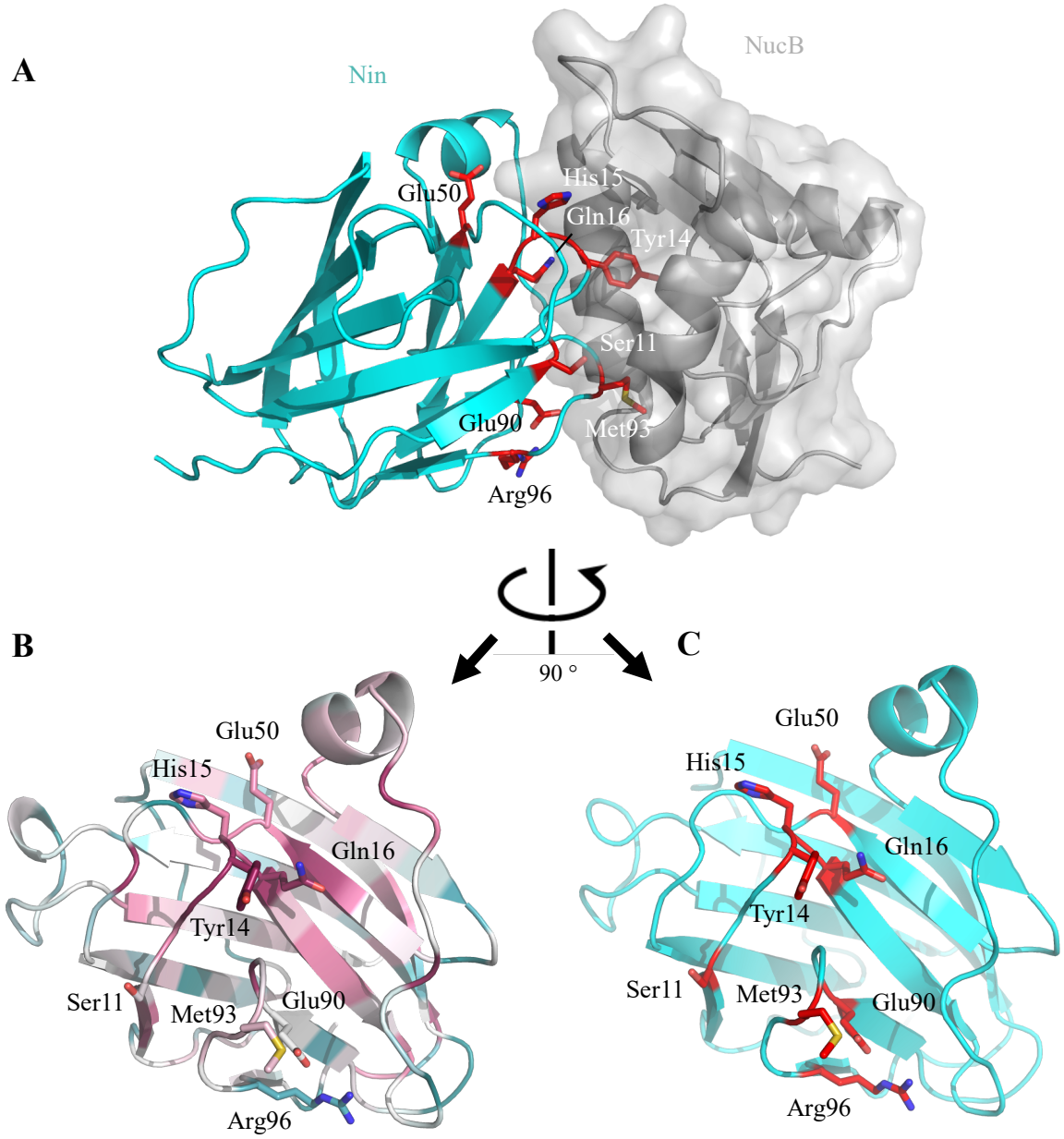

Figure 6.15. The selection of residues chosen for mutation in Nin. A) Nin is rendered as a cyan cartoon, and NucB rendered as a transparent grey surface plot and cartoon. The residues chosen for mutation are rendered as sticks and are coloured red. All of the mutations chosen in this study sit directly in the binding interface between Nin and NucA/B. **B)** Nin is rendered as a cartoon with the residues chosen for mutation rendered as sticks. Nin is coloured according to residue conservation. With the exception of Arg96, each mutation chosen in this study is well conserved. **C)** Nin is rendered as a cyan cartoon with the residues chosen for mutation rendered as red sticks.

Initially, each of the described residues were mutated to alanine, apart from Tyr14 and His15, which were both mutated to phenylalanine as well as alanine, resulting in 10 mutants overall. The plasmids for each mutant were generated by Hannah Gaimster in Heath Murray's lab (Centre for Bacterial Cell Biology, Newcastle University), and the resulting mutant plasmid DNA verified by sequencing before use. Each mutant was expressed in and purified from *E. coli*, following the same expression and purification protocol as described for wild-type Nin (Section 6.2). One mutant out of the initial 10, $Nin^{Glu90Ala}$, did not purify as expected, and the mutant protein was found in the insoluble fraction following cell lysis. It was assumed based on this observation that mutation of this residue has an aberrant effect on protein folding, and any further work on Glu90 was abandoned. Glu90 is also one of the least conserved amino acids chosen for analysis and therefore is unlikely to play a critical role in driving molecular recognition events involving Nin. Inspection of the structure of Nin suggests that the intramolecular interaction of Glu90 with Arg96 has been lost with the truncation of the former's side chain to the neutral amino acid alanine, and this interaction would thus seem to be critical to either protein folding or protein stability. The remaining nine Nin mutants were expressed and purified successfully, and their interactions with NucA and NucB were measured by ITC. Of the nine mutants tested, and the 18 experiments performed, no appreciable change in binding affinity was observed between any of the mutant Nin proteins and NucA/B by ITC and the results are summarised in Table 6.2. It is possible that the mutations tested here did have subtle impacts on the interaction between Nin and NucA/B, but because of the limits of detection of the methodology, subtle changes in binding affinity between the proteins were not detected; furthermore, it was outside the timescale of this project to develop an assay (e.g. FRET or other fluorescence-based methods) capable of measuring the sub-nanomolar K_D of the wild-type proteins, such that any subtle changes arising from the mutations tested here could be measured.

Table 6.2. K_D values measured between Nin mutants and NucA or NucB by ITC.

Mutant	NucA K_D (nM)	NucB K_D (nM)
wt	4.4 nM ± 1.4 nM	7.1 nM ± 6.0 nM
S11A	5.0 nM ± 1.2 nM	5.2 nM ± 1.8 nM
Y14F	4.8 nM ± 3.1 nM	4.6 nM ± 2.4 nM
Y14A	5.3 nM ± 4.2 nM	5.8 nM ± 3.2 nM
H15F	6.2 nM ± 4.8 nM	3.9 nM ± 5.8 nM
H15A	7.1 nM ± 2.8 nM	7.8 nM ± 5.2 nM
Q16A	3.1 nM ± 2.4 nM	5.7 nM ± 3.7 nM
E50A	8.3 nM ± 3.3 nM	8.9 nM ± 5.4 nM
E90A	N/A	N/A
M93A	3.8 nM ± 2.6 nM	6.9 nM ± 6.4 nM
R96A	6.9 nM ± 3.1 nM	9.2 nM ± 6.2 nM

Following on from the failure of the Nin mutants to elicit any measurable change in binding affinity, two charge-flip mutations were constructed in an attempt to increase the magnitude of the disruption of the complex. Since Glu50 and Arg96 in Nin form salt bridges with their binding partners in NucA and NucB, a charge-flip mutation could repel mutated Nin from NucA/B (Figure 6.16). Two charge-flip mutations, $Nin^{Glu50Arg,Tyr14Ala}$, and $Nin^{Arg96Glu,Tyr14Ala}$ were made, both mutations were made in the $Nin^{Tyr14Ala}$ background in order to increase the likelihood of success in these mutants. As with the first round of Nin mutations, plasmids for $Nin^{Arg96Glu,Tyr14Ala}$ and $Nin^{Glu50Arg,Tyr14Ala}$ were generated by Hannah Gaimster, and both mutants were expressed and purified as described for wild-type Nin (Section 6.2).

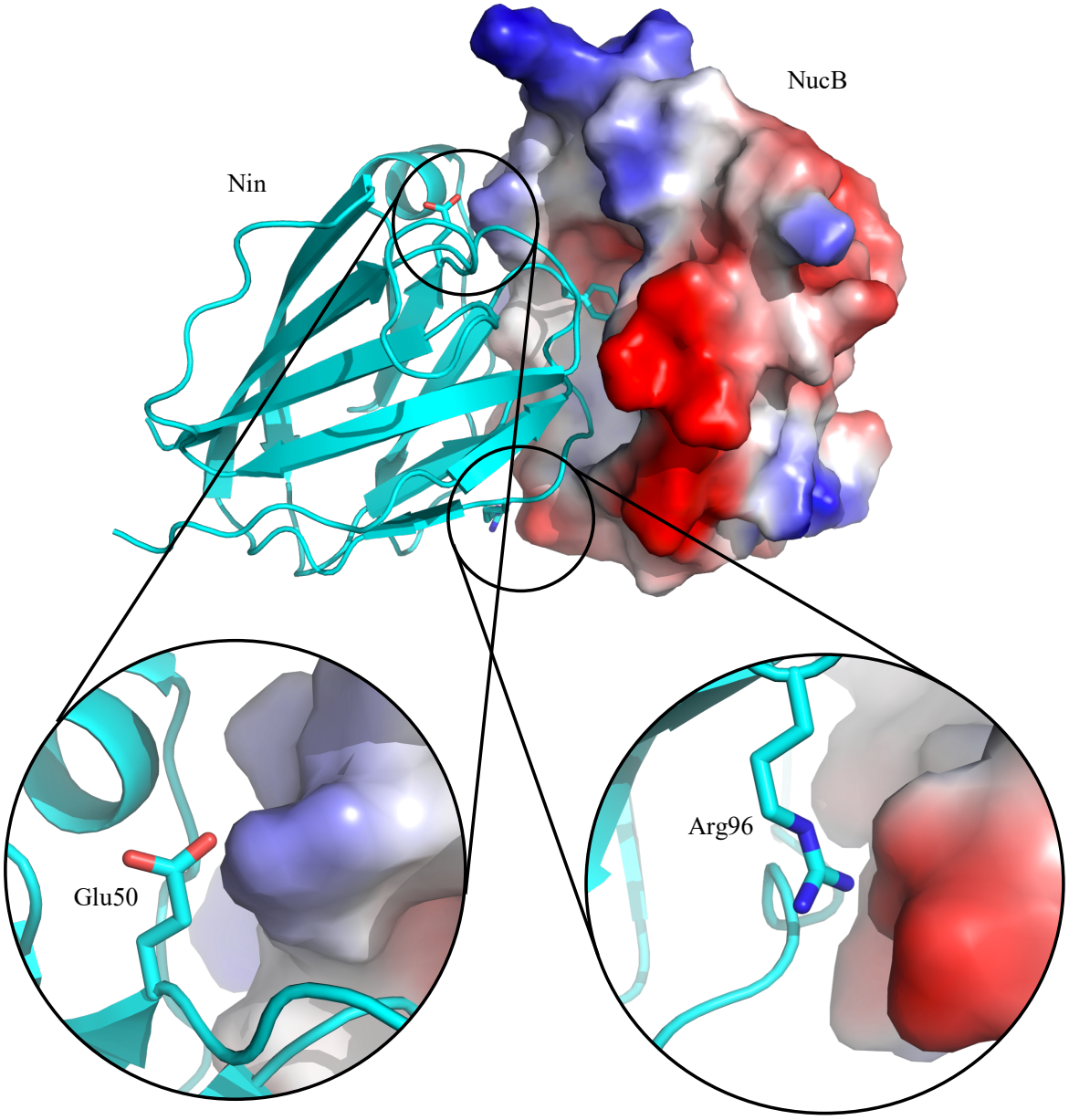

Figure 6.16. Charge-flipping mutations made to Nin. Nin is rendered as a cyan cartoon with Glu50, Arg96, and Tyr14 rendered as sticks. NucB is rendered as an electrostatic surface, where red constitutes a negatively charged region of the structure, and blue represents a positively charged region of the structure. Glu50 and Arg96 form charge-based interactions with their binding partners on NucA/B, therefore flipping the charges on these residues should result in repulsion at these sites, weakening the interaction between Nin and NucA/B.

The interaction between $Nin^{Arg96Glu,Tyr14Ala}$ and $Nin^{Glu50Arg,Tyr14Ala}$ against NucA and NucB was measured by ITC and a decrease in affinity was observed (Figure 6.17). The decrease in affinity seen between these mutant Nin proteins and NucA/B brings the K_D of the protein complexes into a measurable range for this methodology, allowing for a more accurate determination of K_D for these proteins, with at least 6 data points between the two plateaus in the thermograms in all cases, enabling a sensible C value to be calculated. $Nin^{Arg96Glu,Tyr14Ala}$ was found to have a K_D of 268 ± 57 nM, and 45.2 ± 14 nM for NucA and NucB, respectively, whilst $Nin^{Glu50Arg,Tyr14Ala}$ was found to have a K_D of 812 ± 109 nM, and 121 ± 17 nM for NucA and NucB, respectively. Following the success of both charge-flipping mutants in disrupting the NucA/B:Nin interaction, a triple mutant of Nin was generated, incorporating all of the aforementioned mutations into one Nin mutant, $Nin^{Arg96Glu,Tyr14Ala,Glu50Arg}$. Plasmid DNA for $Nin^{Arg96Glu,Tyr14Ala,Glu50Arg}$ was generated by Hannah Gaimster and expressed and purified as described for all other Nin constructs described in this study. Purified $Nin^{Arg96Glu,Tyr14Ala,Glu50Arg}$ was subjected to ITC experiments against NucA and NucB as described above, and a complete abolition of binding between the two proteins was observed (Figure 6.18).

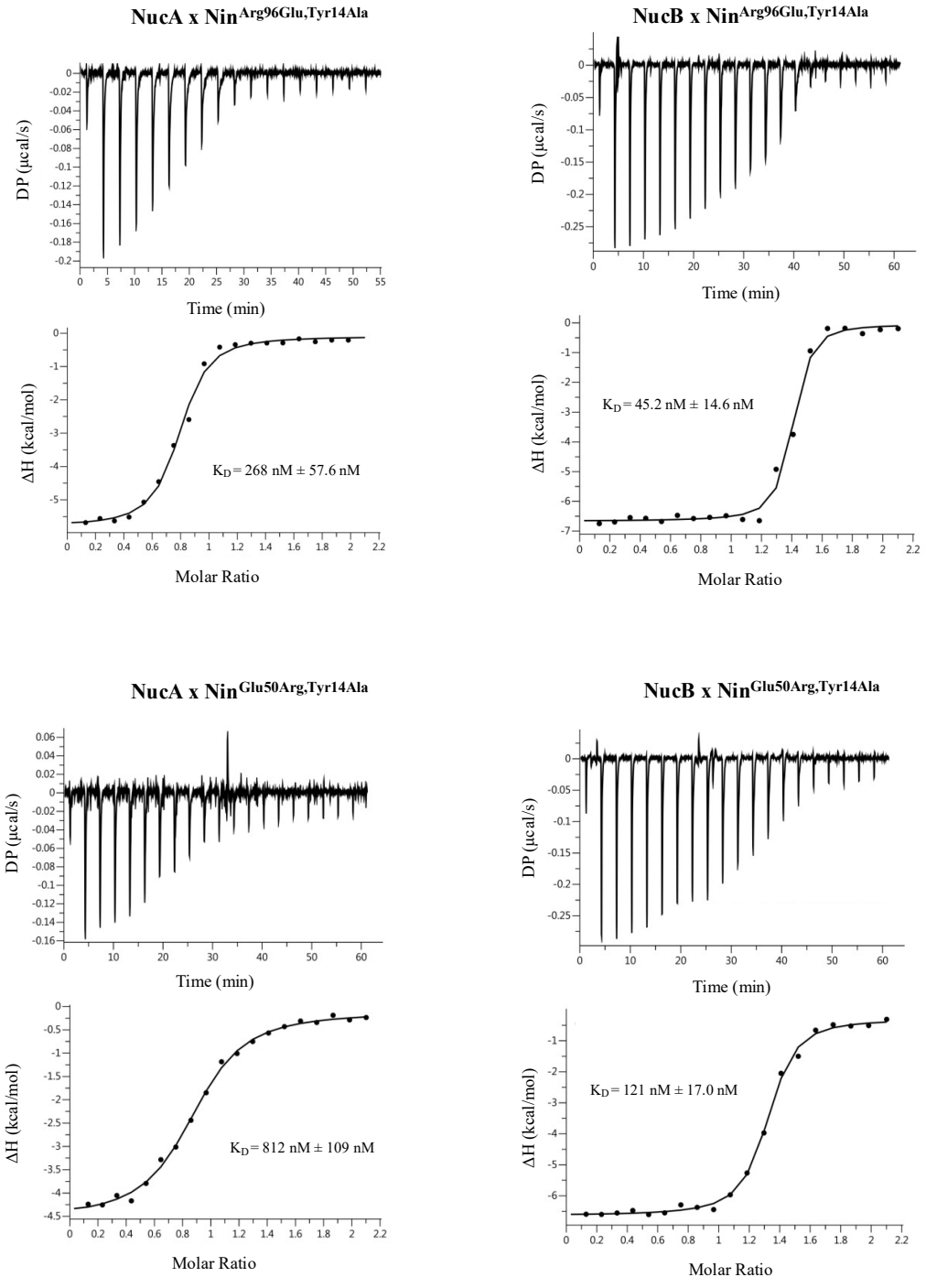

Figure 6.17. Effect of charge-flipping mutations to Nin on the NucA/B:Nin interaction. A) Introduction of either charge-flipping double mutant to Nin results in a decrease in binding affinity between NucA/B and Nin, such that an accurate K_D is measurable using this methodology. Glu50Arg, Tyr14Ala appears to have a greater effect on binding between the two proteins, and in both cases, the effect on binding to NucA is greater than for NucB.

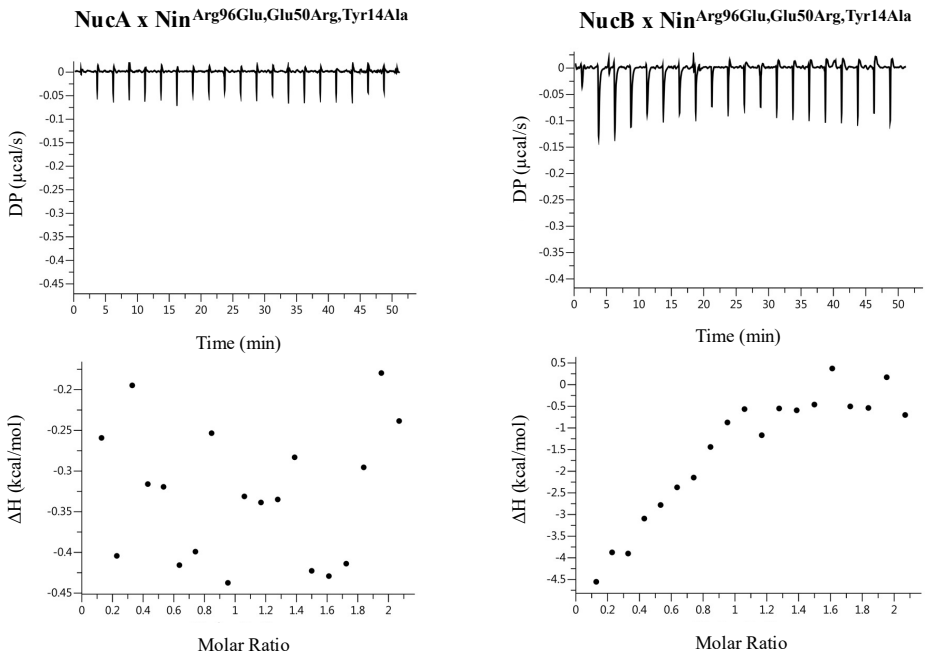

Figure 6.18. Effect of the triple mutant of Nin on binding to NucA/B. The triple Nin mutant described in this study abolishes binding of Nin to NucA and NucB, resulting in an inability to fit a binding isotherm to the data.

In order to test whether the successful complex-disruptive mutants identified in this study had any effect on nuclease inhibition *in vitro*, nuclease activity assays were carried out in which NucA was incubated with wild-type and mutant forms of Nin, and the ability of NucA to degrade plasmid DNA assessed by agarose gel electrophoresis (Figure 6.19).

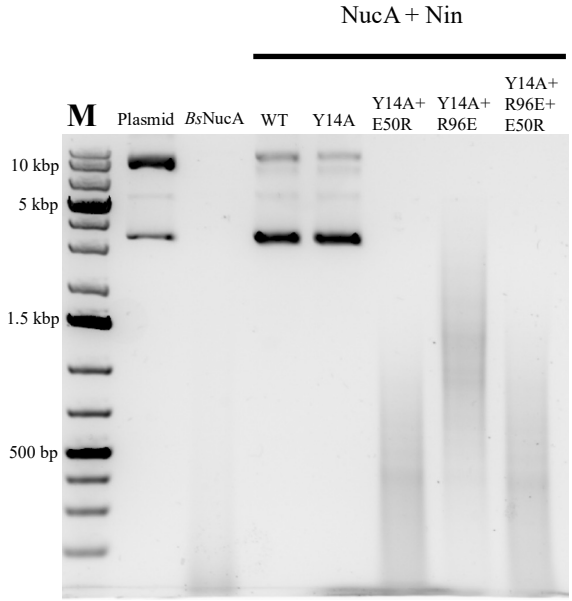

Figure 6.19. Nuclease activity assays performed with Nin mutants. NucA was incubated with plasmid DNA in the presence and absence of Nin, and a selection of the Nin mutants described in this study. WT Nin, as well as the Tyr14Ala mutant, render NucA incapable of digesting plasmid DNA. In the presence of the three charge-flipping mutants described in this study, NucA is able to digest plasmid DNA, as the interaction between the proteins is sufficiently disrupted.

Unsurprisingly, the mutations shown in this study to disrupt binding of Nin to NucA/B were less inhibitive to NucA, whilst wild-type Nin and the Tyr14Ala mutant were still able to inhibit NucA activity completely. Interestingly, the $Nin^{Tyr14Ala,Glu50Arg}$ double mutant, which still retained some binding to the two Nuc proteins, is comparable to the triple mutant of $Nin^{Tyr14Ala,Glu50Arg,Arg96Glu}$, which completely abolished binding between NucA/B and Nin, suggesting that the incredibly tight binding seen between the wild-type proteins is likely essential for the proper function of Nin as a genomic defender. In order to rule out protein misfolding as the cause of any loss of function to Nin, each complex-disruptive Nin mutant was subjected to CD analysis and compared against the spectrum for the wild-type protein, as well as the predicted spectrum of Nin generated using the PDB2CD webserver using the deposited structure of Nin (PDB code 4MQD) (Figure 6.20). The CD spectrum of each Nin mutant used in this study is comparable to that of the wild-type protein and the predicted CD spectrum, confirming that the effects on binding presented in this study are the result of genuine residue-level interaction disruption, rather than protein misfolding.

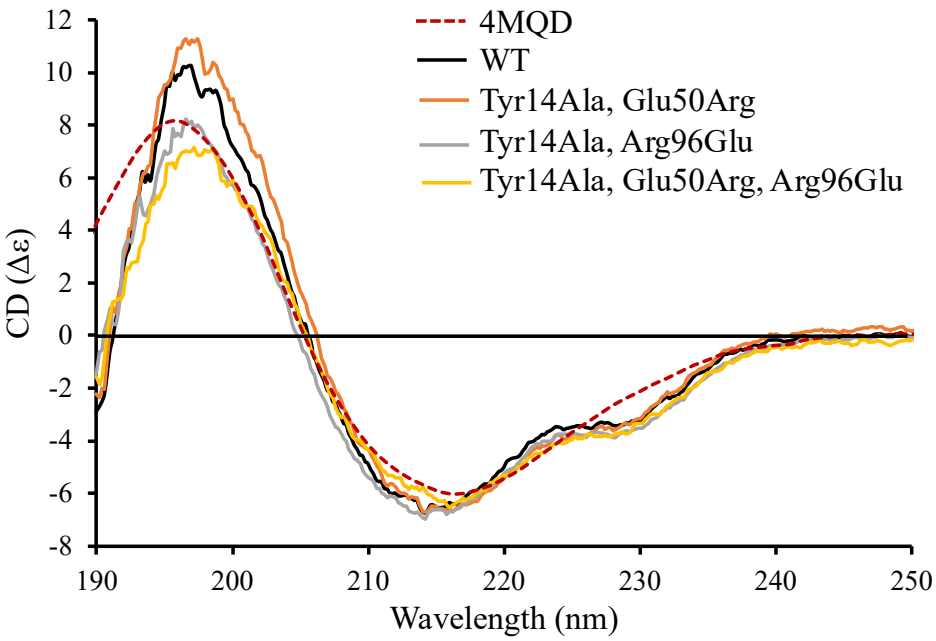

Figure 6.20. Comparison of the CD spectra of Nin mutants with wild-type Nin. The CD spectra of each mutant found to disrupt the NucA/B:Nin interaction in this study is shown compared with wild-type Nin. Also shown is the predicted spectrum of Nin based on the structure of Nin deposited in the PDB (PDB code 4MQD). The CD spectra of each Nin mutant tested are comparable with the spectrum of the wild-type protein, confirming that the reduction in binding affinity seen in the experiments in this chapter is not a result of the misfolding of Nin mutants.

6.6 Discussion

Unfortunately, time constraints did not allow for the study of the effects of complex-ablative Nin mutants on cell growth, however, the work presented here form the basis for further experiments testing the effect of the complex-ablative mutants identified here on cell viability *in vivo*. Should any of the mutations presented here convey a lethal phenotype to the host cell, future work in this area could focus on the development of a small-molecule inhibitor capable of disrupting the NucA/B:Nin interaction, as this may potentially present new avenues for bactericidal/bacteriostatic drug design. A small-molecule compound capable of disrupting the interaction between NucA/B and Nin may as a result be capable of causing self-induced genome degradation by NucA/B. It was not possible to determine an accurate binding affinity for wild-type NucA/B with Nin in this study. Few techniques are capable of accurately measuring sub-nM protein-protein interactions in any event, however, future work could concern the acquisition of an accurate K_D value for the wild-type NucA/B:Nin interaction through a technique such as Förster Resonance Energy Transfer (FRET), or stopped-flow fluorescence spectroscopy. Accurate measurement of a wild-type K_D would mean that the single-residue alanine mutations described here may be re-tested, and any subtle changes in binding affinity in these mutants may become discernible. The NucA/B:Nin interaction could provide a new system amenable to genetics, biochemistry and biophysics, and the structural biology may enable wider lessons about ultra-tight PPIs to be learned.

The molecular mechanisms underpinning NucA and NucB secretion in *Bacillus* strains are not yet understood, by extension, whether secretion of NucA/B occurs in a folded or an unfolded state is not known. Should NucA or NucB be transported in a folded state, Nin may act as a chaperone for NucA and NucB, protecting the genome from degradation during nuclease export. The sub-nM binding affinity observed in this study would pose an interesting dilemma regarding the mechanism through which the nuclease-inhibitor complex is dismantled at the cell membrane to allow for nuclease export. It is also possible that *Bacillus* NucA and NucB are translocated in an unfolded state, like their counterparts in *Serratia marcesans* (Suh et al., 1996), and a pool of Nin is present in the cytoplasm in order to "mop-up" any spontaneous nuclease folding events prior to export. The mechanism of secretion of NucA/B in *Bacillus*, as well as the exploration of Nin's potential role as a chaperone to NucA/B is a potentially fruitful avenue to explore in the future.

The absence of a divalent cation in the active site of NucA or NucB in the complex structures presented here suggest that, if present upon Nin binding, the active-site cation is ejected from

NucA/B prior to or during Nin binding. Analysis of the structures of NucA and NucB using CAVER (Chovancova et al., 2012) reveals a channel within NucA and NucB connecting the active site of the nucleases, to an exit point on the opposite face of the proteins (Figure 6.21). Future modelling of cation exit by molecular dynamics may reveal the molecular intricacies of cation exit during Nin binding.

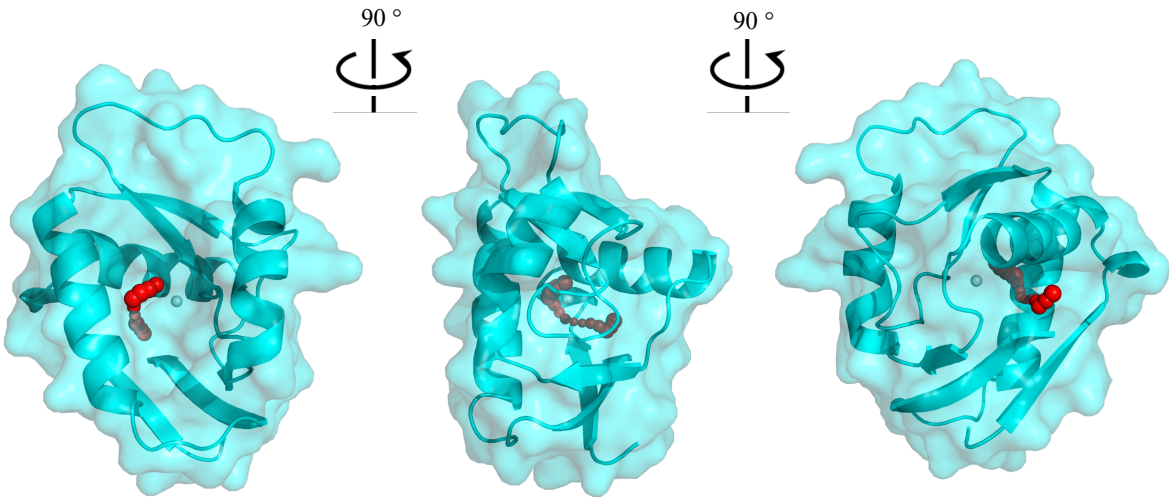

Figure 6.21. A potential mechanism for cation exit in NucB. Calculation of channels in NucB using CAVER (Chovancova et al., 2012) reveals a channel though the protein (rendered in red spheres) through which the active-site divalent cation may be ejected during a Nin binding event.

The work presented here provides structural and biochemical insight into structural features essential for high affinity protein-protein interactions, and provides a springboard for future work regarding the mechanism of NucA and NucB secretion by *Bacillus* strains, and the importance of Nin for this process. Under my supervision, a Master's student in the lab began work on *B. licheniformis* NucA, NucB, and Nin, however this work was only taken as far as protein expression, and the *B. subtilis* versions of these proteins were chosen for this study.

References

Aarsman, M.E.G., Piette, A., Fraipont, C., Vinkenvleugel, T.M.F., Nguyen-Distèche, M. & Den Blaauwen, T. (2005) Maturation of the *Escherichia coli* divisome occurs in two steps. *Molecular Microbiology*. 55 (6), 1631–1645.

Abraham, E.P. & Chain, E. (1940) An enzyme from bacteria able to destroy penicillin. *Nature*. 146 (3713), 837–837.

Achouak, W. (2001) Multiple facets of bacterial porins. *FEMS Microbiology Letters*. 199 (1), 1–7.

Adams, D.W., Wu, L.J. & Errington, J. (2014) Cell cycle regulation by the bacterial nucleoid. *Current Opinion in Microbiology*. 2294–101.

Al-Wahaibi, A.S.M., Lapinska, E., Rajarajan, N., Dobretsov, S., Upstill-Goddard, R. & Burgess, J.G. (2019) Secretion of DNases by marine bacteria: A culture based and bioinformatics approach. *Frontiers in Microbiology*. 10 (5), 1–12.

Ali, J., Sohail, A., Wang, L., Haider, M.R., Mulk, S. & Pan, G. (2018) Electro-microbiology as a promising approach towards renewable energy and environmental sustainability. *Energies*. 11 (7), 1–30.

Alim, D., Sircaik, S. & Panwar, S. (2018) The significance of lipids to biofilm formation in *Candida albicans*: an emerging perspective. *Journal of Fungi*. 4 (4), 140.

Alvarez-Ordóñez, A., Coughlan, L.M., Briandet, R. & Cotter, P.D. (2019) Biofilms in food processing environments: challenges and opportunities. *Annual Review of Food Science and Technology*. 10 (1), 173–195.

Amanatidou, E., Matthews, A.C., Kuhlicke, U., Neu, T.R., McEvoy, J.P. & Raymond, B. (2019) Biofilms facilitate cheating and social exploitation of β-lactam resistance in *Escherichia coli*. *Biofilms and Microbiomes*. 5 (1), 36.

Andreu, J.M., Schaffner-Barbero, C., Huecas, S., Alonso, D., Lopez-Rodriguez, M.L., Ruiz-Avila, L.B., Núñez-Ramírez, R., Llorca, O. & Martín-Galiano, A.J. (2010) The antibacterial cell division inhibitor PC190723 is an FtsZ polymer-stabilizing agent that induces filament assembly and condensation. *Journal of Biological Chemistry*. 285 (19), 14239–14246.

Angeles, D.M., Macia-Valero, A., Bohorquez, L.C. & Scheffers, D.-J. (2020) The PASTA domains of *Bacillus subtilis* PBP2B strengthen the interaction of PBP2B with DivIB. *Microbiology*. 166 (9), 826–836.

Badurina, D.S., Zolli-Juran, M. & Brown, E.D. (2003) CTP:glycerol 3-phosphate cytidylyltransferase (TarD) from *Staphylococcus aureus* catalyzes the cytidylyl transfer via an ordered Bi–Bi reaction mechanism with micromolar K_m values. *Biochimica et Biophysica Acta (BBA) - Proteins and Proteomics*. 1646 (1–2), 196–206.

Baek, M., Dimaio, F., Anishchenko, I., Dauparas, J., Ovchinnikov, S., Lee, G.R., Wang, J., Cong, Q., Kinch, L.N., Schaeffer, R.D., Millán, C., Park, H., Adams, C., Glassman, C.R., Degiovanni, A., Pereira, J.H., Rodrigues, A. V, Van Dijk, A.A., Ebrecht, A.C., et al. (2021) Accurate prediction of protein structures and interactions using a 3-track network. *bioRxiv*. 2021.06.14.448402.

Bartholomew, J.W. & Mittwer, T. (1952) The Gram stain. *Bacteriological Reviews*. 16 (1), 1–29.

Baslé, A., Hewitt, L., Koh, A., Lamb, H.K., Thompson, P., Burgess, J.G., Hall, M.J., Hawkins, A.R., Murray, H. & Lewis, R.J. (2018) Crystal structure of NucB, a biofilm-degrading endonuclease. *Nucleic Acids Research*. 46 (1), 473–484.

Baur, S., Marles-Wright, J., Buckenmaier, S., Lewis, R.J. & Vollmer, W. (2009) Synthesis of CDP-activated tibitol for teichoic acid precursors in *Streptococcus pneumoniae*. *Journal of Bacteriology*. 191 (4), 1200–1210.

Beilsten-Edmands, J., Winter, G., Gildea, R., Parkhurst, J., Waterman, D. & Evans, G. (2020) Scaling diffraction data in the DIALS software package: algorithms and new approaches for multi-crystal scaling. *Acta Crystallographica Section D Structural Biology*. 76 (4), 385–399.

A.Bertrand, J., Genevieve, A., Fanchon, E., Martin, L., Blanot, D., van Heijenoort, J. & Dideberg, O. (1997) Crystal structure of UDP-N-acetylmuramoyl-L-alanine:D-glutamate ligase from *Escherichia coli*. *The EMBO Journal*. 16 (12), 3416–3425.

Bhatt, V.S. (2019) Quorum sensing mechanisms in gram positive bacteria. *Implication of Quorum Sensing System in Biofilm Formation and Virulence*. 297–311.

Bhavsar, A.P., Truant, R. & Brown, E.D. (2005) The TagB protein in *Bacillus subtilis* 168 is an intracellular peripheral membrane protein that can incorporate glycerol phosphate onto a membrane-bound acceptor *in vitro*. *Journal of Biological Chemistry*. 280 (44), 36691–36700.

Bisson-Filho, A.W., Hsu, Y.-P., Squyres, G.R., Kuru, E., Wu, F., Jukes, C., Sun, Y., Dekker, C., Holden, S., VanNieuwenhze, M.S., Brun, Y. V. & Garner, E.C. (2017) Treadmilling by FtsZ filaments drives peptidoglycan synthesis and bacterial cell division. *Science*. 355 (6326), 739–743.

Blaauwen, T. Den, Hamoen, L.W. & Levin, P.A. (2017) The divisome at 25 : the road ahead. *Current Opinion in Microbiology*. (36) 85–94.

Blanco-Cabra, N., Paetzold, B., Ferrar, T., Mazzolini, R., Torrents, E., Serrano, L. & LLuch-Senar, M. (2020) Characterization of different alginate lyases for dissolving *Pseudomonas aeruginosa* biofilms. *Scientific Reports*. 10 (1), 9390.

Bloch, H. (1953) Acid-fast bacteria. *Annual Review of Microbiology*. 7 (1), 19–46.

Boes, A., Olatunji, S., Breukink, E. & Terrak, M. (2019) Regulation of the peptidoglycan polymerase activity of PBP1b by antagonist actions of the core divisome proteins FtsBLQ and FtsN. *mBio*. 10 (1), 1–16.

Bogino, P.C., Oliva, M. de las M., Sorroche, F.G. & Giordano, W. (2013) The role of bacterial biofilms and surface components in plant-bacterial associations. *International Journal of Molecular Sciences*. 14 (8), 15838–15859.

Bonomo, R.A. (2017) β-Lactamases: a focus on current challenges. *Cold Spring Harbor Perspectives in Medicine*. 7 (1), a025239.

Booth, S. & Lewis, R.J. (2019) Structural basis for the coordination of cell division with the synthesis of the bacterial cell envelope. *Protein Science*. 28 (12), 2042-2054.

Bottomley, A.L., Kabli, A.F., Hurd, A.F., Turner, R.D., Garcia-Lara, J. & Foster, S.J. (2014) *Staphylococcus aureus* DivIB is a peptidoglycan-binding protein that is required for a morphological checkpoint in cell division. *Molecular Microbiology*. 94 (5), 1041–1064.

Boyd, A. & Chakrabarty, A.M. (1995) *Pseudomonas aeruginosa* biofilms: role of the alginate exopolysaccharide. *Journal of Industrial Microbiology*. 15 (3), 162–168.

Boyle, D.S., Khattar, M.M., Addinall, S.G., Lutkenhaus, J. & Donachie, W.D. (1997) *ftsW* is an essential cell-division gene in *Escherichia coli*. *Molecular Microbiology*. 24 (6), 1263–1273.

Brauner, A., Fridman, O., Gefen, O. & Balaban, N.Q. (2016) Distinguishing between resistance, tolerance and persistence to antibiotic treatment. *Nature Reviews Microbiology*. 14 (5), 320–330.

Brown, E.D., Vivas, E.I., Walsh, C.T. & Kolter, R. (1995) MurA (MurZ), the enzyme that catalyzes the first committed step in peptidoglycan biosynthesis, is essential in *Escherichia coli*. *Journal of Bacteriology*. 177 (14), 4194–4197.

Brown, S., Meredith, T., Swoboda, J. & Walker, S. (2010) *Staphylococcus aureus* and *Bacillus subtilis* W23 make polyribitol wall teichoic acids using different enzymatic pathways. *Chemistry & Biology*. 17 (10), 1101–1110.

Brown, S., Santa Maria, J.P. & Walker, S. (2013) Wall teichoic acids of Gram-positive bacteria. *Annual Review of Microbiology*. 67 (1), 313–336.

Buckle, A.M. & Fersht, A.R. (1994) Subsite binding in an RNase: structure of a Barnase-tetranucleotide complex at 1.76-Å resolution. *Biochemistry*. 33 (7), 1644–1653.

Buckle, A.M., Schreiber, G. & Fersht, A.R. (1994) Protein-protein recognition: Crystal structural analysis of a barnase-barstar complex at 2.0-Å resolution. *Biochemistry*. 33 (30), 8878–8889.

Buddelmeijer, N. & Beckwith, J. (2004) A complex of the *Escherichia coli* cell division proteins FtsL, FtsB and FtsQ forms independently of its localization to the septal region. *Molecular Microbiology*. 52 (5), 1315–1327.

Buss, J.A., Peters, N.T., Xiao, J. & Bernhardt, T.G. (2017) ZapA and ZapB form an FtsZ-independent structure at midcell. *Molecular Microbiology*. 104 (4), 652–663.

Caffrey, M. (2011) Crystallizing membrane proteins for structure-function studies using lipidic mesophases. *Biochemical Society Transactions*. 39 (3), 725–32.

Çam, S. & Brinkmeyer, R. (2020) The effects of temperature, pH, and iron on biofilm formation by clinical versus environmental strains of *Vibrio vulnificus*. *Folia Microbiologica*. 65 (3), 557–566.

Cao, Z., Casabona, M.G., Kneuper, H., Chalmers, J.D. & Palmer, T. (2017) The type VII

secretion system of *Staphylococcus aureus* secretes a nuclease toxin that targets competitor bacteria. *Nature Microbiology*. 2 (1), 16183.

Cascales, E., Buchanan, S.K., Duché, D., Kleanthous, C., Lloubès, R., Postle, K., Riley, M., Slatin, S. & Cavard, D. (2007) Colicin biology. *Microbiology and Molecular Biology Reviews*. 71 (1), 158–229.

Chak, K.F., Safo, M.K., Ku, W.Y., Hsieh, S.Y. & Yuan, H.S. (1996) The crystal structure of the immunity protein of colicin E7 suggests a possible colicin-interacting surface. *Proceedings of the National Academy of Sciences of the United States of America*. 93 (13), 6437–6442.

Chan, Y.G.Y., Kim, H.K., Schneewind, O. & Missiakas, D. (2014) The capsular polysaccharide of *Staphylococcus aureus* is attached to peptidoglycan by the LytR-CpsA-Psr (LCP) family of enzymes. *Journal of Biological Chemistry*. 289 (22), 15680-15690

Chen, Y., Huang, H., Osawa, M. & Erickson, H.P. (2017) ZipA and FtsA* stabilize FtsZ-GDP miniring structures. *Scientific Reports*. 7 (1), 3650.

Li, C.-L., Hor, L.-I., Chang, Z.-F., Tsai, L.-C., Yang, W.-Z. & S.Yuan, H. (2003) DNA binding and cleavage by the periplasmic nuclease Vvn: a novel structure with a known active site. *The EMBO Journal*. 22 (15), 4014–4025.

Cho, H., McManus, H.R., Dove, S.L. & Bernhardt, T.G. (2011) Nucleoid occlusion factor SlmA is a DNA-activated FtsZ polymerization antagonist. *Proceedings of the National Academy of Sciences of the United States of America*. 108 (6), 3773-3778

Cho, H., Uehara, T. & Bernhardt, T.G. (2014) Beta-lactam antibiotics induce a lethal malfunctioning of the bacterial cell wall synthesis machinery. *Cell*. 159 (6), 1300-1311.

Chovancova, E., Pavelka, A., Benes, P., Strnad, O., Brezovsky, J., Kozlikova, B., Gora, A., Sustr, V., Klvana, M., Medek, P., Biedermannova, L., Sochor, J. & Damborsky, J. (2012) CAVER 3.0: A tool for the analysis of transport pathways in dynamic protein structures Andreas Prlic (ed.). *PLoS Computational Biology*. 8 (10), e1002708.

Christensen, B.E. (1989) The role of extracellular polysaccharides in biofilms. *Journal of Biotechnology*. 10 (3–4), 181–202.

Chung, B.C., Zhao, J., Gillespie, R.A., Kwon, D.-Y., Guan, Z., Hong, J., Zhou, P. & Lee, S.-Y. (2013) Crystal Structure of MraY, an Essential Membrane Enzyme for Bacterial Cell Wall Synthesis. *Science*. 341 (6149), 1012–1016.

Claessen, D., Emmins, R., Hamoen, L.W., Daniel, R.A., Errington, J. & Edwards, D.H. (2008) Control of the cell elongation–division cycle by shuttling of PBP1 protein in *Bacillus subtilis*. *Molecular Microbiology*. 68 (4), 1029–1046.

Cleverley, R.M., Barrett, J.R., Baslé, A., Bui, N.K., Hewitt, L., Solovyova, A., Xu, Z.-Q., Daniel, R.A., Dixon, N.E., Harry, E.J., Oakley, A.J., Vollmer, W. & Lewis, R.J. (2014) Structure and function of a spectrin-like regulator of bacterial cytokinesis. *Nature Communications*. 5 (1), 5421.

Cleverley, R.M., Rismondo, J., Lockhart-Cairns, M.P., Van Bentum, P.T., Egan, A.J.F., Vollmer, W., Halbedel, S., Baldock, C., Breukink, E. & Lewis, R.J. (2016) Subunit arrangement in GpsB, a regulator of cell wall biosynthesis. *Microbial Drug Resistance*. 22 (6), 446–460.

Cleverley, R.M., Rutter, Z.J., Rismondo, J., Corona, F., Tsui, H.C.T., Alatawi, F.A., Daniel, R.A., Halbedel, S., Massidda, O., Winkler, M.E. & Lewis, R.J. (2019) The cell cycle regulator GpsB functions as cytosolic adaptor for multiple cell wall enzymes. *Nature Communications*. 10 (1), 1–17.

Condon, S.G.F., Mahbuba, D.-A., Armstrong, C.R., Díaz-Vázquez, G., Craven, S.J., LaPointe, L.M., Khadria, A.S., Chadda, R., Crooks, J.A., Rangarajan, N., Weibel, D.B., Hoskins, A.A., Robertson, J.L., Cui, Q. & Senes, A. (2017) The FtsLB sub-complex of the bacterial divisome is tetramer with an uninterrupted FtsL helix linking the transmembrane and periplasmic regions. *Journal of Biological Chemistry*. 293 (5), 1623-1641.

Conti, J., Viola, M.G. & Camberg, J.L. (2018) FtsA reshapes membrane architecture and remodels the Z-ring in *Escherichia coli*. *Molecular Microbiology*. 107 (4), 558-576.

Córdova-Alcántara, I.M., Venegas-Cortés, D.L., Martínez-Rivera, M.Á., Pérez, N.O. & Rodriguez-Tovar, A.V. (2019) Biofilm characterization of *Fusarium solani* keratitis isolate: increased resistance to antifungals and UV light. *Journal of Microbiology*. 57 (6), 485–497.

Contreras-Martel, C., Dahout-Gonzalez, C., Martins, A.D.S., Kotnik, M. & Dessen, A. (2009) PBP active site flexibility as the key mechanism for β-lactam resistance in *Pneumococci*. *Journal of Molecular Biology*. 387 (4), 899–909.

Costerton, J.W., Cheng, K.J., Geesey, G.G., Ladd, T.I., Nickel, J.C., Dasgupta, M. & Marrie, T.J. (1987) Bacterial biofilms in nature and disease. *Annual Review of Microbiology*. 41 (1), 435–464.

Cowan, S., Garavito, R., Jansonius, J., Jenkins, J., Karlsson, R., König, N., Pai, E., Pauptit, R., Rizkallah, P., Rosenbusch, J., Rummel, G. & Schirmer, T. (1995) The structure of OmpF porin in a tetragonal crystal form. *Structure*. 3 (10), 1041–1050.

Cowtan, K. (2006) The Buccaneer software for automated model building. 1. Tracing protein chains. *Acta Crystallographica Section D Biological Crystallography*. 62 (9), 1002–1011.

Cucarella, C., Tormo, M.A., Úbeda, C., Trotonda, M.P., Monzón, M., Peris, C., Amorena, B., Lasa, I. & Penadés, J.R. (2004) Role of biofilm-associated protein Bap in the pathogenesis of bovine *Staphylococcus aureus*. *Infection and Immunity*. 72 (4), 2177–2185.

Cugini, C., Shanmugam, M., Landge, N. & Ramasubbu, N. (2019) The role of exopolysaccharides in oral biofilms. *Journal of Dental Research*. 98 (7), 739–745.

D'Elia, M.A., Henderson, J.A., Beveridge, T.J., Heinrichs, D.E. & Brown, E.D. (2009) The N-acetylmannosamine transferase catalyzes the first committed step of teichoic acid assembly in *Bacillus subtilis* and *Staphylococcus aureus*. *Journal of Bacteriology*. 191 (12), 4030–4034.

Davies, J. & Davies, D. (2010) Origins and evolution of antibiotic resistance. *Microbiology and Molecular Biology Reviews*. 74 (3), 417–433.

Débarbouillé, M., Dramsi, S., Dussurget, O., Nahori, M.A., Vaganay, E., Jouvion, G., Cozzone, A., Msadek, T. & Duclos, B. (2009) Characterization of a serine/threonine kinase involved in virulence of *Staphylococcus aureus*. *Journal of Bacteriology*. 191 (13), 4070-4081.

Dengler, V., Meier, P.S., Heusser, R., Kupferschmied, P., Fazekas, J., Friebe, S., Staufer, S.B., Majcherczyk, P.A., Moreillon, P., Berger-Bächi, B. & Mccallum, N. (2012) Deletion of hypothetical wall teichoic acid ligases in *Staphylococcus aureus* activates

the cell wall stress response. *FEMS Microbiology Letters*. 333 (2), 109-120.

Deva, T., Baker, E.N., Squire, C.J. & Smith, C.A. (2006) Structure of *Escherichia coli* UDP-N-acetylmuramoyl:L-alanine ligase (MurC). *Acta Crystallographica Section D Biological Crystallography*. 62 (12), 1466–1474.

Devaraj, A., Buzzo, J.R., Mashburn-Warren, L., Gloag, E.S., Novotny, L.A., Stoodley, P., Bakaletz, L.O. & Goodman, S.D. (2019) The extracellular DNA lattice of bacterial biofilms is structurally related to Holliday junction recombination intermediates. *Proceedings of the National Academy of Sciences*. 116 (50), 25068–25077.

Diehl, A., Roske, Y., Ball, L., Chowdhury, A., Hiller, M., Molière, N., Kramer, R., Stöppler, D., Worth, C.L., Schlegel, B., Leidert, M., Cremer, N., Erdmann, N., Lopez, D., Stephanowitz, H., Krause, E., van Rossum, B.-J., Schmieder, P., Heinemann, U., et al. (2018) Structural changes of TasA in biofilm formation of *Bacillus subtilis*. *Proceedings of the National Academy of Sciences*. 115 (13), 3237–3242.

Donlan, R.M. (2002) Biofilms: Microbial life on surfaces. *Emerging Infectious Diseases*. 8 (9), 881–890.

Duman, R., Ishikawa, S., Celik, I., Strahl, H., Ogasawara, N., Troc, P., Löwe, J. & Hamoen, L.W. (2013) Structural and genetic analyses reveal the protein SepF as a new membrane anchor for the Z ring. *Proceedings of the National Academy of Sciences*. 110 (48), E4601–E4610.

Dümmler, A., Lawrence, A.M. & de Marco, A. (2005) Simplified screening for the detection of soluble fusion constructs expressed in *E. coli* using a modular set of vectors. *Microbial Cell Factories*. (4), 34.

Dumon-Seignovert, L., Cariot, G. & Vuillard, L. (2004) The toxicity of recombinant proteins in *Escherichia coli*: A comparison of overexpression in BL21(DE3), C41(DE3), and C43(DE3). *Protein Expression and Purification*. 37 (1), 203–206.

Duplessis, C. (2011) A new cephalosporin with activity against methicillin-resistant *Staphylococcus aureus* (MRSA). *Clin Med Rev Ther.* (3), 1-17.

Durand-Heredia, J.M., Yu, H.H., De Carlo, S., Lesser, C.F. & Janakiraman, A. (2011) Identification and characterization of ZapC, a stabilizer of the FtsZ ring in *Escherichia*

coli. *Journal of Bacteriology*. 193 (6), 1405-1413.

Egan, A.J.F. (2018) Bacterial outer membrane constriction. *Molecular Microbiology*. 107 (6), 676–687.

Egan, A.J.F., Biboy, J., van't Veer, I., Breukink, E. & Vollmer, W. (2015) Activities and regulation of peptidoglycan synthases. *Philosophical Transactions of the Royal Society B: Biological Sciences*. 370 (1679), 20150031.

Egan, A.J.F. & Vollmer, W. (2013) The physiology of bacterial cell division. *Annals of the New York Academy of Sciences*. 1277 (1), 8–28.

Elsen, N.L., Lu, J., Parthasarathy, G., Reid, J.C., Sharma, S., Soisson, S.M. & Lumb, K.J. (2012) Mechanism of action of the cell-division inhibitor PC190723: Modulation of FtsZ assembly cooperativity. *Journal of the American Chemical Society*. 134 (30), 12342–12345.

Elsholz, A.K.W., Turgay, K., Michalik, S., Hessling, B., Gronau, K., Oertel, D., Mader, U., Bernhardt, J., Becher, D., Hecker, M. & Gerth, U. (2012) Global impact of protein arginine phosphorylation on the physiology of *Bacillus subtilis*. *Proceedings of the National Academy of Sciences*. 109 (19), 7451–7456.

Elsholz, A.K.W., Wacker, S.A. & Losick, R. (2014) Self-regulation of exopolysaccharide production in *Bacillus subtilis* by a tyrosine kinase. *Genes & Development*. 28 (15), 1710–1720.

Emami, K., Guyet, A., Kawai, Y., Devi, J., Wu, L.J., Allenby, N., Daniel, R.A. & Errington, J. (2017) RodA as the missing glycosyltransferase in *Bacillus subtilis* and antibiotic discovery for the peptidoglycan polymerase pathway. *Nature Microbiology*. 2 (3), 16253.

Emsley, P. & Cowtan, K. (2004) Coot: Model-building tools for molecular graphics. *Acta Crystallographica Section D: Biological Crystallography*. 60 (12), 2126-2132.

van den Ent, F. (2000) Crystal structure of the cell division protein FtsA from *Thermotoga maritima*. *The EMBO Journal*. 19 (20), 5300-5307.

Van Den Ent, F. & Löwe, J. (2006) RF cloning: A restriction-free method for inserting target genes into plasmids. *Journal of Biochemical and Biophysical Methods*. 67 (1), 67–74.

van den Ent, F., Vinkenvleugel, T.M.F., Ind, A., West, P., Veprintsev, D., Nanninga, N., den

Blaauwen, T. & Löwe, J. (2008) Structural and mutational analysis of the cell division protein FtsQ. *Molecular Microbiology*. 68 (1), 110–123.

Erickson, H. (1997) FtsZ, a tubulin homologue in prokaryote cell division. *Trends in Cell Biology*. 7 (9), 362–367.

Eschenburg, S., Kabsch, W., Healy, M.L. & Schönbrunn, E. (2003) A new view of the mechanisms of UDP-N-acetylglucosamine enolpyruvyl transferase (MurA) and 5-enolpyruvylshikimate-3-phosphate synthase (AroA) derived from X-ray structures of their tetrahedral reaction intermediate states. *Journal of Biological Chemistry*. 278 (49), 49215–49222.

Eswara, P.J., Brzozowski, R.S., Viola, M.G., Graham, G., Spanoudis, C., Trebino, C., Jha, J., Aubee, J.I., Thompson, K.M., Camberg, J.L. & Ramamurthi, K.S. (2018) An essential *Staphylococcus aureus* cell division protein directly regulates FtsZ dynamics. *eLife*. (7), 1–24.

Evans, P.R. & Murshudov, G.N. (2013) How good are my data and what is the resolution? *Acta Crystallographica Section D Biological Crystallography*. 69 (7), 1204–1214.

Farha, M.A., Leung, A., Sewell, E.W., D'Elia, M.A., Allison, S.E., Ejim, L., Pereira, P.M., Pinho, M.G., Wright, G.D. & Brown, E.D. (2013) Inhibition of WTA synthesis blocks the cooperative action of PBPs and sensitizes MRSA to β-lactams. *ACS chemical biology*. 8 (1), 226–33.

Fernandes, R., Amador, P. & Prudêncio, C. (2013) β-Lactams: chemical structure, mode of action and mechanisms of resistance. *Reviews in Medical Microbiology*. 24 (1), 7–17.

Fey, P.D. & Olson, M.E. (2010) Current concepts in biofilm formation of *Staphylococcus epidermidis*. *Future Microbiology*. 5 (6), 917–933.

Fischer, W. & Tomasz, A. (2014) 'The Cell Wall of *Streptococcus pneumoniae*', in *Gram-Positive Pathogens, Second Edition*. [Online]. American Society of Microbiology. pp. 230–240.

Fleming, D., Chahin, L. & Rumbaugh, K. (2017) Glycoside Hydrolases Degrade Polymicrobial bacterial biofilms in wounds. *Antimicrobial Agents and Chemotherapy*. 61 (2), 1-9.

Flemming, H.-C. & Wingender, J. (2010) The biofilm matrix. *Nature Reviews Microbiology*. 8 (9), 623–633.

Fleurie, A., Manuse, S., Zhao, C., Campo, N., Cluzel, C., Lavergne, J.P., Freton, C., Combet, C., Guiral, S., Soufi, B., Macek, B., Kuru, E., VanNieuwenhze, M.S., Brun, Y. V., Di Guilmi, A.M., Claverys, J.P., Galinier, A. & Grangeasse, C. (2014) Interplay of the serine/threonine-kinase StkP and the paralogs DivIVA and GpsB in pneumococcal cell elongation and division. *PLoS Genetics*. 10 (4), e1004275.

Formstone, A., Carballido-Lopez, R., Noirot, P., Errington, J. & Scheffers, D.-J. (2008) Localization and interactions of teichoic acid synthetic enzymes in *Bacillus subtilis*. *Journal of Bacteriology*. 190 (5), 1812–1821.

Foster, T.J. (2017) Antibiotic resistance in *Staphylococcus aureus*. Current status and future prospects. *FEMS Microbiology Reviews*. 41 (3), 430–449.

Franke, D. & Svergun, D.I. (2009) DAMMIF, a program for rapid ab-initio shape determination in small-angle scattering. *Journal of Applied Crystallography*. 42 (2), 342–346.

Fu, X., Shih, Y.-L., Zhang, Y. & Rothfield, L.I. (2001) The MinE ring required for proper placement of the division site is a mobile structure that changes its cellular location during the *Escherichia coli* division cycle. *Proceedings of the National Academy of Sciences*. 98 (3), 980–985.

Fujita, J., Maeda, Y., Nagao, C., Tsuchiya, Y., Miyazaki, Y., Hirose, M., Mizohata, E., Matsumoto, Y., Inoue, T., Mizuguchi, K. & Matsumura, H. (2014) Crystal structure of FtsA from Staphylococcus aureus. *FEBS Letters*. 588 (10), 1879–1885.

Gale, R.T., Li, F.K.K., Sun, T., Strynadka, N.C.J. & Brown, E.D. (2017) *B. subtilis* LytR-CpsA-Psr enzymes transfer wall teichoic acids from authentic lipid-linked substrates to mature peptidoglycan *in vitro*. *Cell Chemical Biology*. 24 (12), 1537-1546.

Galli, E. & Gerdes, K. (2012) FtsZ-ZapA-ZapB interactome of *Escherichia coli*. *Journal of Bacteriology*. 194 (2), 292–302.

Galloway, W.R.J.D., Hodgkinson, J.T., Bowden, S.D., Welch, M. & Spring, D.R. (2011) Quorum sensing in Gram-negative bacteria: Small-molecule modulation of AHL and AI-2 quorum sensing pathways. *Chemical Reviews*. 111 (1), 28–67.

Garcia, P.S., Simorre, J.-P., Brochier-Armanet, C. & Grangeasse, C. (2016) Cell division of *Streptococcus pneumoniae*: think positive! *Current Opinion in Microbiology*. (34), 18–

23.

Garrett, T.R., Bhakoo, M. & Zhang, Z. (2008) Bacterial adhesion and biofilms on surfaces. *Progress in Natural Science*. 18 (9), 1049–1056.

Geissler, B., Elraheb, D. & Margolin, W. (2003) A gain-of-function mutation in *ftsA* bypasses the requirement for the essential cell division gene *zipA* in *Escherichia coli*. *Proceedings of the National Academy of Sciences*. 100 (7), 4197–4202.

Ghosh, M., Meiss, G., Pingoud, A., London, R.E. & Pedersen, L.C. (2005) Structural insights into the mechanism of nuclease A, a ββα metal nuclease from *Anabaena*. *Journal of Biological Chemistry*. 280 (30), 27990–27997.

Ghosh, M., Meiss, G., Pingoud, A.M., London, R.E. & Pedersen, L.C. (2007) The nuclease A-inhibitor complex is characterized by a novel metal ion bridge. *Journal of Biological Chemistry*. 282 (8), 5682–5690.

Glenwright, A.J., Pothula, K.R., Bhamidimarri, S.P., Chorev, D.S., Baslé, A., Firbank, S.J., Zheng, H., Robinson, C. V., Winterhalter, M., Kleinekathöfer, U., Bolam, D.N. & van den Berg, B. (2017) Structural basis for nutrient acquisition by dominant members of the human gut microbiota. *Nature*. 541 (7637), 407–411.

Gordon, E., Flouret, B., Chantalat, L., van Heijenoort, J., Mengin-Lecreulx, D. & Dideberg, O. (2001) Crystal structure of UDP-N-acetylmuramoyl-L-alanyl-D-glutamate:meso-diaminopimelate ligase from *Escherichia coli*. *Journal of Biological Chemistry*. 276 (14), 10999–11006.

Gorrec, F. (2009) The MORPHEUS protein crystallization screen. *Journal of Applied Crystallography*. 42 (6), 1035–1042.

Gray, A.N., Egan, A.J., van't Veer, I.L., Verheul, J., Colavin, A., Koumoutsi, A., Biboy, J., Altelaar, A.F.M., Damen, M.J., Huang, K.C., Simorre, J.-P., Breukink, E., den Blaauwen, T., Typas, A., Gross, C.A. & Vollmer, W. (2015) Coordination of peptidoglycan synthesis and outer membrane constriction during *Escherichia coli* cell division. *eLife*. 4 (5), 1-29.

Gründling, A. & Schneewind, O. (2007) Genes required for glycolipid synthesis and lipoteichoic acid anchoring in *Staphylococcus aureus*. *Journal of Bacteriology*. 189 (6), 2521-2530.

Guilhen, C., Forestier, C. & Balestrino, D. (2017) Biofilm dispersal: multiple elaborate strategies for dissemination of bacteria with unique properties. *Molecular Microbiology*. 105 (2), 188–210.

Ha, S., Walker, D., Shi, Y. & Walker, S. (2000) The 1.9 Å crystal structure of *Escherichia coli* MurG, a membrane-associated glycosyltransferase involved in peptidoglycan biosynthesis. *Protein Science*. 9 (6), 1045–1052.

Hahn, J., Burghoorn, J. & Dubnau, D. (1998) Competence in *Bacillus subtilis* is controlled by regulated proteolysis of a transcription factor. *The EMBO Journal*. 17 (22), 6730–6738.

Halbedel, S. & Lewis, R.J. (2019) Structural basis for interaction of DivIVA/GpsB proteins with their ligands. *Molecular Microbiology*. 111 (6), 1404–1415.

Hale, C.A. & de Boer, P.A.. (1997) Direct binding of FtsZ to ZipA, an essential component of the septal ring structure that mediates cell division in *E. coli*. *Cell*. 88 (2), 175–185.

Hall, B.G. & Barlow, M. (2004) Evolution of the serine β-lactamases: past, present and future. *Drug Resistance Updates*. 7 (2), 111–123.

Hall, C.W. & Mah, T.-F. (2017) Molecular mechanisms of biofilm-based antibiotic resistance and tolerance in pathogenic bacteria. *FEMS Microbiology Reviews*. 41 (3), 276–301.

Hannan, S., Ready, D., Jasni, A.S., Rogers, M., Pratten, J. & Roberts, A.P. (2010) Transfer of antibiotic resistance by transformation with eDNA within oral biofilms. *FEMS Immunology & Medical Microbiology*. 59 (3), 345–349.

Hartley, R.W. (1993) Directed mutagenesis and barnase-barstar recognition. *Biochemistry*. 32 (23), 5978–5984.

Hassan, A.N., Frank, J.F. & Elsoda, M. (2003) Observation of bacterial exopolysaccharide in dairy products using cryo-scanning electron microscopy. *International Dairy Journal*. 13 (9), 755–762.

Hayami, M, Okabe, A., Kariyama, R., Abe, M. & Kanemasa, Y. (1979) Lipid composition of *Staphylococcus aureus* and its derived L-forms. *Microbiology and Immunology*. 23 (6), 435–442.

Haydon, D.J., Stokes, N.R., Ure, R., Galbraith, G., Bennett, J.M., Brown, D.R., Baker, P.J., Barynin, V. V., Rice, D.W., Sedelnikova, S.E., Heal, J.R., Sheridan, J.M., Aiwale, S.T., Chauhan, P.K., Srivastava, A., Taneja, A., Collins, I., Errington, J. & Czaplewski, L.G.

(2008) An inhibitor of FtsZ with potent and selective anti-*Staphylococcal* activity. *Science*. 321 (5896), 1673–1675.

Hempel, A.M., Cantlay, S., Molle, V., Wang, S.B., Naldrett, M.J., Parker, J.L., Richards, D.M., Jung, Y.G., Buttner, M.J. & Flärdh, K. (2012) The Ser/Thr protein kinase AfsK regulates polar growth and hyphal branching in the filamentous bacteria *Streptomyces*. *Proceedings of the National Academy of Sciences of the United States of America*. 109 (35), 2371-2379.

Heydari, S. & Eftekhar, F. (2015) Biofilm Formation and β-Lactamase Production in Burn Isolates of Pseudomonas aeruginosa. *Jundishapur Journal of Microbiology*. 8 (3), 1-5.

Hsia, K.-C., Chak, K.-F., Liang, P.-H., Cheng, Y.-S., Ku, W.-Y. & Yuan, H.S. (2004) DNA binding and degradation by the HNH protein ColE7. *Structure*. 12 (2), 205–214.

Hirschfeld, C., Gómez-Mejia, A., Bartel, J., Hentschker, C., Rohde, M., Maaß, S., Hammerschmidt, S. & Becher, D. (2020) Proteomic investigation uncovers potential targets and target sites of *Pneumococcal* serine-threonine kinase StkP and phosphatase PhpP. *Frontiers in Microbiology*. (10), 1-20.

Hobley, L., Ostrowski, A., Rao, F. V., Bromley, K.M., Porter, M., Prescott, A.R., MacPhee, C.E., van Aalten, D.M.F. & Stanley-Wall, N.R. (2013) BslA is a self-assembling bacterial hydrophobin that coats the *Bacillus subtilis* biofilm. *Proceedings of the National Academy of Sciences*. 110 (33), 13600–13605.

Hornby, J.M., Jensen, E.C., Lisec, A.D., Tasto, J.J., Jahnke, B., Shoemaker, R., Dussault, P. & Nickerson, K.W. (2001) Quorum sensing in the dimorphic fungus *Candida albicans* is mediated by Farnesol. *Applied and Environmental Microbiology*. 67 (7), 2982–2992.

Horton, N.C. (2008) 'DNA Nucleases', in *Protein-Nucleic Acid Interactions*. pp. 339–373.

Hosoya, S., Lu, Z., Ozaki, Y., Takeuchi, M. & Sato, T. (2007) Cytological analysis of the mother cell death process during sporulation in *Bacillus subtilis*. *Journal of Bacteriology*. 189 (6), 2561–2565.

Hrast, M., Sosič, I., Šink, R. & Gobec, S. (2014) Inhibitors of the peptidoglycan biosynthesis enzymes MurA-F. *Bioorganic Chemistry*. 55, 2–15.

Hu, Z. & Lutkenhaus, J. (2000) Analysis of MinC reveals two independent domains involved in interaction with MinD and FtsZ. *Journal of Bacteriology*. 182 (14), 3965-3971.

Hu, Z., Mukherjee, A., Pichoff, S. & Lutkenhaus, J. (1999) The MinC component of the division site selection system in *Escherichia coli* interacts with FtsZ to prevent polymerization. *Proceedings of the National Academy of Sciences of the United States of America*. 96 (26), 14819-14824.

Inoue, A., Murata, Y., Takahashi, H., Tsuji, N., Fujisaki, S. & Kato, J. -i. (2008) Involvement of an essential gene, mviN, in murein synthesis in *Escherichia coli*. *Journal of Bacteriology*. 190 (21), 7298–7301.

Jackson, S.G., Zhang, F., Chindemi, P., Junop, M.S. & Berti, P.J. (2009) Evidence of kinetic control of ligand binding and staged product release in MurA (Enolpyruvyl UDP-GlcNAc synthase)-catalyzed reactions. *Biochemistry*. 48 (49), 11715–11723.

Jacques, D.A., Guss, J.M., Svergun, D.I. & Trewhella, J. (2012) Publication guidelines for structural modelling of small-angle scattering data from biomolecules in solution. *Acta Crystallographica Section D Biological Crystallography*. 68 (6), 620–626.

Jakubovics, N.S., Shields, R.C., Rajarajan, N. & Burgess, J.G. (2013) Life after death: the critical role of extracellular DNA in microbial biofilms. *Letters in Applied Microbiology*. 57 (6), 467–475.

Jamroškovič, J., Pavlendová, N., Muchová, K., Wilkinson, A.J. & Barák, I. (2012) An oscillating Min system in *Bacillus subtilis* influences asymmetrical septation during sporulation. *Microbiology*. 158 (8), 1972–1981.

Jindal, B. & Panda, D. (2013) Understanding FtsZ assembly: Cues from the behavior of its N- and C-terminal domains. *Biochemistry*. 52 (40), 7071-7081.

Johnson, L.N. & Lewis, R.J. (2001) Structural basis for control by phosphorylation. *Chemical Reviews*. 101 (8), 2209–2242.

Joosten, R.P., Long, F., Murshudov, G.N. & Perrakis, A. (2014) The PDB-REDO server for macromolecular structure model optimization. *International Union of Crystallography Journal*. 1 (4), 213-220.

Jurcisek, J.A. & Bakaletz, L.O. (2007) Biofilms formed by nontypeable *Haemophilus influenzae* in vivo contain both double-stranded DNA and type IV pilin protein. *Journal of Bacteriology*. 189 (10), 3868–3875.

Jurcisek, J.A., Brockman, K.L., Novotny, L.A., Goodman, S.D. & Bakaletz, L.O. (2017)

Nontypeable *Haemophilus influenzae* releases DNA and DNABII proteins via a T4SS-like complex and ComE of the type IV pilus machinery. *Proceedings of the National Academy of Sciences of the United States of America*. 114 (32), E6632–E6641.

Kang, C.M., Abbott, D.W., Sang, T.P., Dascher, C.C., Cantley, L.C. & Husson, R.N. (2005) The *Mycobacterium tuberculosis* serine/threonine kinases PknA and PknB: Substrate identification and regulation of cell shape. *Genes and Development*. 19 (14), 1692-1704.

Kaplan, J.B. (2010) Biofilm Dispersal: Mechanisms, Clinical Implications, and Potential Therapeutic Uses. *Journal of Dental Research*. 89 (3), 205–218.

Karamata, D., Lazarevic, V. & Soldo, B. (2002) *tagO* is involved in the synthesis of all anionic cell-wall polymers in *Bacillus subtilis* 168 a. *Microbiology*. 148 (7), 2079–2087.

Kattke, M.D., Gosschalk, J.E., Martinez, O.E., Kumar, G., Gale, R.T., Cascio, D., Sawaya, M.R., Philips, M., Brown, E.D. & Clubb, R.T. (2019) Structure and mechanism of TagA, a novel membrane-associated glycosyltransferase that produces wall teichoic acids in pathogenic bacteria. *PLOS Pathogens*. 15 (4), e1007723.

Karimova, G., Pidoux, J., Ullmann, A. & Ladant, D. (1998) A bacterial two-hybrid system based on a reconstituted signal transduction pathway. *Proceedings of the National Academy of Sciences of the United States of America*. 95 (10), 5752–5756.

Kawai, Y., Marles-Wright, J., Cleverley, R.M., Emmins, R., Ishikawa, S., Kuwano, M., Heinz, N., Bui, N.K., Hoyland, C.N., Ogasawara, N., Lewis, R.J., Vollmer, W., Daniel, R.A. & Errington, J. (2011) A widespread family of bacterial cell wall assembly proteins. *The EMBO Journal*. 30 (24), 4931–4941.

Kelly, S.M., Jess, T.J. & Price, N.C. (2005) How to study proteins by circular dichroism. *Biochimica et Biophysica Acta - Proteins and Proteomics*. 1751 (2), 119–139.

Khoshouei, M., Radjainia, M., Baumeister, W. & Danev, R. (2017) Cryo-EM structure of haemoglobin at 3.2 Å determined with the Volta phase plate. *Nature Communications*. 8 (5), 1–6.

Kiedrowski, M.R., Kavanaugh, J.S., Malone, C.L., Mootz, J.M., Voyich, J.M., Smeltzer, M.S., Bayles, K.W. & Horswill, A.R. (2011) Nuclease modulates biofilm formation in community-associated methicillin-resistant *Staphylococcus aureus*. *PLoS ONE*. 6 (11), e26714.

Kim, S.J., Chang, J. & Singh, M. (2015) Peptidoglycan architecture of Gram-positive bacteria by solid-state NMR. *Biochimica et biophysica acta*. 1848 (1 Pt B), 350–62.

Kiriukhin, M.Y., Debabov, D. V., Shinabarger, D.L. & Neuhaus, F.C. (2001) Biosynthesis of the glycolipid anchor in lipoteichoic acid of *Staphylococcus aureus* RN4220: Role of YpfP, the diglucosyldiacylglycerol synthase. *Journal of Bacteriology*. 183 (11), 3506–3514.

Klausen, M., Heydorn, A., Ragas, P., Lambertsen, L., Aaes-Jørgensen, A., Molin, S. & Tolker-Nielsen, T. (2003) Biofilm formation by *Pseudomonas aeruginosa* wild type, flagella and type IV pili mutants. *Molecular Microbiology*. 48 (6), 1511–1524.

Kleanthous, C., Hemmings, A.M., Moore, G.R. & James, R. (1998) Immunity proteins and their specificity for endonuclease colicins: telling right from wrong in protein-protein recognition. *Molecular Microbiology*. 28 (2), 227–233.

Kleanthous, C., Kühlmann, U.C., Pommer, A.J., Ferguson, N., Radford, S.E., Moore, G.R., James, R. & Hemmings, A.M. (1999) Structural and mechanistic basis of immunity toward endonuclease colicins. *Nature Structural Biology*. 6 (3), 243–252.

Ko, T.P., Liao, C.C., Ku, W.Y., Chak, K.F. & Yuan, H.S. (1999) The crystal structure of the DNase domain of colicin E7 in complex with its inhibitor Im7 protein. *Structure*. 7 (1), 91–102.

Krissinel, E. (2012) Enhanced fold recognition using efficient short fragment clustering. *Journal of Molecular Biochemistry*. 1 (2), 76-85.

Krissinel, E. & Henrick, K. (2004) Secondary-structure matching (SSM), a new tool for fast protein structure alignment in three dimensions. *Acta Crystallographica Section D Biological Crystallography*. 60 (12), 2256–2268.

de Kruijff, B., van Dam, V. & Breukink, E. (2008) Lipid II: A central component in bacterial cell wall synthesis and a target for antibiotics. *Prostaglandins, Leukotrienes and Essential Fatty Acids*. 79 (3–5), 117–121.

Krupka, M., Sobrinos-Sanguino, M., Jiménez, M., Rivas, G. & Margolin, W. (2018) *Escherichia coli* ZipA organizes FtsZ polymers into dynamic ring-like protofilament structures. *mBio*. 9 (3), 1–15.

Kühlmann, U.C., Pommer, A.J., Moore, G.R., James, R. & Kleanthous, C. (2000) Specificity in protein-protein interactions: the structural basis for dual recognition in endonuclease

colicin-immunity protein complexes. *Journal of Molecular Biology*. 301 (5), 1163–1178.

Kuk, A.C.Y., Hao, A., Guan, Z. & Lee, S.-Y. (2019) Visualizing conformation transitions of the Lipid II flippase MurJ. *Nature Communications*. 10 (1), 1736.

Kuk, A.C.Y., Mashalidis, E.H. & Lee, S.-Y. (2017) Crystal structure of the MOP flippase MurJ in an inward-facing conformation. *Nature Structural & Molecular Biology*. 24 (2), 171–176.

Kumar, A., Alam, A., Rani, M., Ehtesham, N.Z. & Hasnain, S.E. (2017) Biofilms: Survival and defense strategy for pathogens. *International Journal of Medical Microbiology*. 307 (8), 481–489.

Kumar Shukla, S. & Rao, T.S. (2013) Dispersal of Bap-mediated *Staphylococcus aureus* biofilm by proteinase K. *The Journal of Antibiotics*. 66 (2), 55–60.

Kureisaite-Ciziene, D., Varadajan, A., McLaughlin, S.H., Glas, M., Montón Silva, A., Luirink, R., Mueller, C., den Blaauwen, T., Grossmann, T.N., Luirink, J. & Löwe, J. (2018) Structural analysis of the interaction between the bacterial cell division proteins FtsQ and FtsB. *mBio*. 9 (5), 1–17.

Lan, G., Dajkovic, A., Wirtz, D. & Sun, S.X. (2008) Polymerization and bundling kinetics of FtsZ filaments. *Biophysical Journal*. 95 (8), 4045-4056.

Land, A.D., Luo, Q. & Levin, P.A. (2014) Functional domain analysis of the cell division inhibitor EzrA. *PLoS ONE*. 9 (7), e102616.

Landau, E.M. & Rosenbusch, J.P. (1996) Lipidic cubic phases: A novel concept for the crystallization of membrane proteins. *Proceedings of the National Academy of Sciences*. 93 (25), 14532–14535.

Lasa, I. & Penadés, J.R. (2006) Bap: A family of surface proteins involved in biofilm formation. *Research in Microbiology*. 157 (2), 99–107.

Lazarevic, V. & Karamata, D. (1995) The tagGH operon of *Bacillus subtilis* 168 encodes a two-component ABC transporter involved in the metabolism of two wall teichoic acids. *Molecular Microbiology*. 16 (2), 345–355.

Lees, W.J., Benson, T.E., Hogle, J.M. & Walsh, C.T. (1996) (E)-enolbutyryl-UDP-N-acetylglucosamine as a mechanistic probe of UDP-N-acetylenolpyruvylglucosamine reductase (MurB). *Biochemistry*. 35 (5), 1342–1351.

Lei, S.P., Lin, H.C., Wang, S.S., Callaway, J. & Wilcox, G. (1987) Characterization of the *Erwinia carotovora* pelB gene and its product pectate lyase. *Journal of Bacteriology*. 169 (9), 4379–4383.

Lenarcic, R., Halbedel, S., Visser, L., Shaw, M., Wu, L.J., Errington, J., Marenduzzo, D. & Hamoen, L.W. (2009) Localisation of DivIVA by targeting to negatively curved membranes. *The EMBO Journal*. 28 (15), 2272–2282.

Levin, P.A., Kurtser, I.G. & Grossman, A.D. (1999) Identification and characterization of a negative regulator of FtsZ ring formation in *Bacillus subtilis*. *Proceedings of the National Academy of Sciences*. 96 (17), 9642–9647.

Lewis, R.J. (2017) The GpsB files: the truth is out there. *Molecular Microbiology*. 103 (6), 913-918.

Li, W., Dennis, C.A., Moore, G.R., James, R. & Kleanthous, C. (1997) Protein-Protein Interaction specificity of Im9 for the endonuclease toxin Colicin E9 defined by homologue-scanning mutagenesis. *Journal of Biological Chemistry*. 272 (35), 22253–22258.

Libby, E.A., Goss, L.A. & Dworkin, J. (2015) The eukaryotic-like Ser/Thr kinase PrkC regulates the essential WalRK two-component system in *Bacillus subtilis*. *PLoS Genetics*. 11 (6), e1005275.

Lima, A., Durán, R., Schujman, G.E., Marchissio, M.J., Portela, M.M., Obal, G., Pritsch, O., de Mendoza, D. & Cerveñansky, C. (2011) Serine/threonine protein kinase PrkA of the human pathogen *Listeria monocytogenes*: Biochemical characterization and identification of interacting partners through proteomic approaches. *Journal of Proteomics*. 74 (9), 1720-1734.

Limoli, D.H., Jones, C.J. & Wozniak, D.J. (2015) Bacterial Extracellular Polysaccharides in Biofilm Formation and Function. *Microbiology Spectrum*. 3 (3), 1–19.

Lister, J.L. & Horswill, A.R. (2014) *Staphylococcus aureus* biofilms: recent developments in biofilm dispersal. *Frontiers in Cellular and Infection Microbiology*. 4 (12), 1–9.

Lobanovska, M. & Pilla, G. (2017) Penicillin's discovery and antibiotic resistance: Lessons for the future? *The Yale Journal of Biology and Medicine*. 90 (1), 135–145.

Loose, M. & Mitchison, T.J. (2014) The bacterial cell division proteins FtsA and FtsZ self-organize into dynamic cytoskeletal patterns. *Nature Cell Biology*. 16 (1), 38–46.

Lovering, A.L., Lin, L.Y.C., Sewell, E.W., Spreter, T., Brown, E.D. & Strynadka, N.C.J. (2010) Structure of the bacterial teichoic acid polymerase TagF provides insights into membrane association and catalysis. *Nature Structural & Molecular Biology*. 17 (5), 582–589.

Lovering, A.L., Gretes, M.C., Safadi, S.S., Danel, F., De Castro, L., Page, M.G.P. & Strynadka, N.C.J. (2012) Structural insights into the anti-methicillin-resistant *Staphylococcus aureus* (MRSA) activity of ceftobiprole. *Journal of Biological Chemistry*. 287 (38), 32096–32102.

Lovering, A.L, Safadi, S.S. & Strynadka, N.C.J. (2012) Structural perspective of peptidoglycan biosynthesis and assembly. *Annual Review of Biochem*. 81 (1), 451–78.

Low, H.H., Moncrieffe, M.C. & Löwe, J. (2004) The crystal structure of ZapA and its modulation of FtsZ polymerisation. *Journal of Molecular Biology*. 341 (3), 839-852.

Löwe, J. & Amos, L.A. (1998) Crystal structure of the bacterial cell-division protein FtsZ. *Nature*. 391 (6663), 203–206.

Lupas, A., Van Dyke, M. & Stock, J. (1991) Predicting coiled coils from protein sequences. *Science*. 252 (5009), 1162–1164.

Lutkenhaus, J. (2012) The ParA/MinD family puts things in their place. *Trends in Microbiology*. 20 (9), 411-418.

Lutkenhaus, J. (1998) The regulation of bacterial cell division: a time and place for it. *Current Opinion in Microbiology*. 1 (2), 210–215.

Lutkenhaus, J. & Addinall, S.G. (1997) Bacterial cell division and the Z ring. *Annual Review of Biochem*. 66, 93–116.

Malanovic, N. & Lohner, K. (2016) Gram-positive bacterial cell envelopes: The impact on the activity of antimicrobial peptides. *Biochimica et Biophysica Acta (BBA) - Biomembranes*. 1858 (5), 936–946.

Mann, E.E., Rice, K.C., Boles, B.R., Endres, J.L., Ranjit, D., Chandramohan, L., Tsang, L.H., Smeltzer, M.S., Horswill, A.R. & Bayles, K.W. (2009) Modulation of eDNA release and degradation affects *Staphylococcus aureus* biofilm maturation. *PLoS ONE*. 4 (6), e5822.

Männik, J., Wu, F., Hol, F.J.H., Bisicchia, P., Sherratt, D.J., Keymer, J.E. & Dekker, C. (2012) Robustness and accuracy of cell division in *Escherichia coli* in diverse cell shapes. *Proceedings of the National Academy of Sciences of the United States of America*. 109 (18), 6957–62.

Manuse, S., Fleurie, A., Zucchini, L., Lesterlin, C. & Grangeasse, C. (2016) Role of eukaryotic-like serine/threonine kinases in bacterial cell division and morphogenesis. *FEMS Microbiology Reviews*. 40 (1), 41–56.

Marie, A., Guilmi, D., Dessen, A., Dideberg, O. & Vernet, T. (2010) Bifunctional penicillin-binding proteins: Focus on the glycosyltransferase domain and its specific inhibitor Moenomycin. *Current Pharmaceutical Biotechnology*. 3 (33), 63–75.

Marie, A., Guilmi, D., Dideberg, O. & Vernet, T. (2003) Functional Characterization of Penicillin-Binding Protein 1b from Streptococcus pneumoniae. *Journal of Bacteriology*. 185 (5), 1650–1658.

Di Martino, P. (2018) Extracellular polymeric substances, a key element in understanding biofilm phenotype. *AIMS Microbiology*. 4 (2), 274–288.

Marvasi, M., Visscher, P.T. & Casillas Martinez, L. (2010) Exopolymeric substances (EPS) from *Bacillus subtilis*: polymers and genes encoding their synthesis. *FEMS Microbiology Letters*. 313 (1), 1–9.

Masson, S., Kern, T., Le Gouëllec, A., Giustini, C., Simorre, J.P., Callow, P., Vernet, T., Gabel, F. & Zapun, A. (2009) Central domain of DivIB caps the C-terminal regions of the FtsL/DivIC coiled-coil rod. *Journal of Biological Chemistry*. 284 (40), 27687–27700.

Matsuyama, T. (1989) Fractal spreading growth of *Serratia marcescens* which produces surface active exolipids. *FEMS Microbiology Letters*. 61 (3), 243–246.

Matsuyama, T. & Nakagawa, Y. (1996) Surface-active exolipids: analysis of absolute chemical structures and biological functions. *Journal of Microbiological Methods*. 25 (2), 165–175.

Mavridis, L. & Janes, R.W. (2017) PDB2CD: a web-based application for the generation of

circular dichroism spectra from protein atomic coordinates. *Bioinformatics*. 33 (1), 56–63.

McCoy, A.J., Grosse-Kunstleve, R.W., Adams, P.D., Winn, M.D., Storoni, L.C. & Read, R.J. (2007) Phaser crystallographic software. *Journal of Applied Crystallography*. 40 (4), 658–674.

Meeske, A.J., Riley, E.P., Robins, W.P., Uehara, T., Mekalanos, J.J., Kahne, D., Walker, S., Kruse, A.C., Bernhardt, T.G. & Rudner, D.Z. (2016) SEDS proteins are a widespread family of bacterial cell wall polymerases. *Nature*. 537 (7622), 634–638.

Micsonai, A., Wien, F., Kernya, L., Lee, Y.-H., Goto, Y., Réfrégiers, M. & Kardos, J. (2015) Accurate secondary structure prediction and fold recognition for circular dichroism spectroscopy. *Proceedings of the National Academy of Sciences*. 112 (24), E3095–E3103.

Miller, M.B. & Bassler, B.L. (2001) Quorum sensing in bacteria. *Annual Review of Microbiology*. 55 (1), 165–199.

Miller, M.D., Cai, J. & Krause, K.L. (1999) The active site of *Serratia endonuclease* contains a conserved magnesium-water cluster. *Journal of Molecular Biology*. 288 (5), 975–987.

Mohammadi, T., van Dam, V., Sijbrandi, R., Vernet, T., Zapun, A., Bouhss, A., Diepeveen-de Bruin, M., Nguyen-Distèche, M., de Kruijff, B. & Breukink, E. (2011) Identification of FtsW as a transporter of lipid-linked cell wall precursors across the membrane. *The EMBO Journal*. 30 (8), 1425–1432.

Mohammadi, T., Sijbrandi, R., Lutters, M., Verheul, J., Martin, N.I., den Blaauwen, T., de Kruijff, B. & Breukink, E. (2014) Specificity of the transport of lipid II by FtsW in *Escherichia coli*. *Journal of Biological Chemistry*. 289 (21), 14707–14718.

Monnet, V. & Gardan, R. (2015) Quorum-sensing regulators in Gram-positive bacteria: ‘cherchez le peptide ’. *Molecular Microbiology*. 97 (2), 181–184.

Moon, A.F., Gaudu, P. & Pedersen, L.C. (2014) Structural characterization of the virulence factor nuclease A from *Streptococcus agalactiae*. *Acta Crystallographica Section D Biological Crystallography*. 70 (11), 2937–2949.

Moradali, M.F. & Rehm, B.H.A. (2019) '*The Role of Alginate in Bacterial Biofilm Formation*', in *Extracellular Sugar-Based Biopolymers Matrices*. pp. 517–537.

Morlot, C., Straume, D., Peters, K., Hegnar, O.A., Simon, N., Villard, A.-M., Contreras-Martel, C., Leisico, F., Breukink, E., Gravier-Pelletier, C., Le Corre, L., Vollmer, W., Pietrancosta, N., Håvarstein, L.S. & Zapun, A. (2018) Structure of the essential peptidoglycan amidotransferase MurT/GatD complex from *Streptococcus pneumoniae*. *Nature Communications*. 9 (1), 3180.

Muro-Pastor, A.M., Flores, E., Herrero, A. & Wolk, C.P. (1992) Identification, genetic analysis and characterization of a sugar-non-specific nuclease from the cyanobacterium *Anabaena* sp. PCC 7120. *Molecular Microbiology*. 6 (20), 3021–3030.

Muro-Pastor, A.M., Herrero, A. & Flores, E. (1997) The nuiA Gene from *Anabaena* sp. encoding an inhibitor of the NucA sugar-non-specific nuclease. *Journal of Molecular Biology*. 268 (3), 589–598.

Murshudov, G.N., Skubák, P., Lebedev, A.A., Pannu, N.S., Steiner, R.A., Nicholls, R.A., Winn, M.D., Long, F. & Vagin, A.A. (2011) REFMAC5 for the refinement of macromolecular crystal structures. *Acta Crystallographica Section D: Biological Crystallography*. 67 (4), 355-367.

Nielsen, H., Tsirigos, K.D., Brunak, S. & von Heijne, G. (2019) A Brief History of Protein Sorting Prediction. *The Protein Journal.* 38 (3), 200–216.

Newman, J., Egan, D., Walter, T.S., Meged, R., Berry, I., Ben Jelloul, M., Sussman, J.L., Stuart, D.I. & Perrakis, A. (2005) Towards rationalization of crystallization screening for small- to medium-sized academic laboratories: the PACT/JCSG+ strategy. *Acta Crystallographica Section D Biological Crystallography*. 61 (10), 1426–1431.

Nicolau, D., Zmarlicka, M. & Nailor, M. (2015) Impact of the New Delhi metallo-beta-lactamase on beta-lactam antibiotics. *Infection and Drug Resistance*. 8, 297-309.

Nijland, R., Hall, M.J. & Burgess, J.G. (2010) Dispersal of biofilms by secreted, matrix degrading, bacterial DNase. *PLoS ONE*. 5 (12), e15668.

Nikaido, H. (2009) 'Outer Membrane, Gram-Negative Bacteria', in *Encyclopedia of Microbiology*. Elsevier. pp. 439–452.

Noirclerc-Savoye, M., Lantez, V., Signor, L., Philippe, J., Vernet, T. & Zapun, A. (2013) Reconstitution of membrane protein complexes involved in *Pneumococcal* septal cell wall assembly. *PLoS ONE*. 8 (9), e75522.

Nouaille, S., Morello, E., Cortez-Peres, N., Le Loir, Y., Commissaire, J., Gratadoux, J.J., Poumerol, E., Gruss, A. & Langella, P. (2006) Complementation of the *Lactococcus lactis* secretion machinery with *Bacillus subtilis* SecDF improves secretion of *Staphylococcal* nuclease. *Applied and Environmental Microbiology*. 72 (3), 2272–2279.

Nováková, L., Sasková, L., Pallová, P., Janeček, J., Novotná, J., Ulrych, A., Echenique, J., Trombe, M.C. & Branny, P. (2005) Characterization of a eukaryotic type serine/threonine protein kinase and protein phosphatase of *Streptococcus pneumoniae* and identification of kinase substrates. *FEBS Journal*. 272 (5), 1243-1254.

Okada, U., Yamashita, E., Neuberger, A., Morimoto, M., van Veen, H.W. & Murakami, S. (2017) Crystal structure of tripartite-type ABC transporter MacB from *Acinetobacter baumannii*. *Nature Communications*. 8 (1), 1336.

Okshevsky, M. & Meyer, R.L. (2015) The role of extracellular DNA in the establishment, maintenance and perpetuation of bacterial biofilms. *Critical Reviews in Microbiology*. 41 (3), 341–352.

Oliva, M.A., Halbedel, S., Freund, S.M., Dutow, P., Leonard, T.A., Veprintsev, D.B., Hamoen, L.W. & Löwe, J. (2010) Features critical for membrane binding revealed by DivIVA crystal structure. *The EMBO Journal*. 29 (12), 1988–2001.

Ortiz, C., Natale, P., Cueto, L. & Vicente, M. (2015) The keepers of the ring: Regulators of FtsZ assembly. *FEMS Microbiology Reviews*. 40 (1), 57-67.

Otero, L.H., Rojas-Altuve, A., Llarrull, L.I., Carrasco-Lopez, C., Kumarasiri, M., Lastochkin, E., Fishovitz, J., Dawley, M., Hesek, D., Lee, M., Johnson, J.W., Fisher, J.F., Chang, M., Mobashery, S. & Hermoso, J.A. (2013) How allosteric control of *Staphylococcus aureus* penicillin binding protein 2a enables methicillin resistance and physiological function. *Proceedings of the National Academy of Sciences*. 110 (42), 16808–16813.

Panjkovich, A. & Svergun, D.I. (2018) CHROMIXS: automatic and interactive analysis of chromatography-coupled small-angle X-ray scattering data. *Bioinformatics*. 34 (11), 1944–1946.

Papenfort, K. & Bassler, B.L. (2016) Quorum sensing signal–response systems in Gram-negative bacteria. *Nature Reviews Microbiology*. 14 (9), 576–588.

Park, K.T., Wu, W., Battaile, K.P., Lovell, S., Holyoak, T. & Lutkenhaus, J. (2011) The min

oscillator uses MinD-dependent conformational changes in MinE to spatially regulate cytokinesis. *Cell*. 146 (3), 396-407

Passos da Silva, D., Matwichuk, M.L., Townsend, D.O., Reichhardt, C., Lamba, D., Wozniak, D.J. & Parsek, M.R. (2019) The *Pseudomonas aeruginosa* lectin LecB binds to the exopolysaccharide Psl and stabilizes the biofilm matrix. *Nature Communications*. 10 (1), 2183.

Pazos, M., Natale, P. & Vicente, M. (2013) A specific role for the ZipA protein in cell division. *Journal of Biological Chemistry*. 288 (5), 3219–3226.

Pazos, M., Peters, K., Casanova, M., Palacios, P., VanNieuwenhze, M., Breukink, E., Vicente, M. & Vollmer, W. (2018) Z-ring membrane anchors associate with cell wall synthases to initiate bacterial cell division. *Nature Communications*. 9 (1), 5090.

Peacock, S.J. & Paterson, G.K. (2015) Mechanisms of methicillin resistance in *Staphylococcus aureus*. *Annual Review of Biochemistry*. 84 (1), 577–601.

Peng, N., Cai, P., Mortimer, M., Wu, Y., Gao, C. & Huang, Q. (2020) The exopolysaccharide–eDNA interaction modulates 3D architecture of *Bacillus subtilis* biofilm. *BMC Microbiology*. 20 (1), 115.

Percy, M.G. & Gründling, A. (2014) Lipoteichoic acid synthesis and function in Gram-positive bacteria. *Annual Review of Microbiology*. 68 (1), 81–100.

Percy, M.G., Karinou, E., Webb, A.J. & Gründling, A. (2016) Identification of a lipoteichoic acid glycosyltransferase enzyme reveals that GW-domain-containing proteins can be retained in the cell wall of *Listeria monocytogenes* in the absence of lipoteichoic acid or its modifications. *Journal of Bacteriology*. 198 (15), 2029–2042.

Peters, K., Kannan, S., Rao, V.A., Biboy, J., Vollmer, D., Erickson, S.W., Lewis, R.J., Young, K.D. & Vollmer, W. (2016) The redundancy of peptidoglycan carboxypeptidases ensures robust cell shape maintenance in *Escherichia coli*. *mBio*. 7 (3), e00819-16.

Petoukhov, M. V., Franke, D., Shkumatov, A. V., Tria, G., Kikhney, A.G., Gajda, M., Gorba, C., Mertens, H.D.T., Konarev, P. V. & Svergun, D.I. (2012) New developments in the ATSAS program package for small-angle scattering data analysis. *Journal of Applied Crystallography*. 45 (2), 342–350.

Petoukhov, M. V., Konarev, P. V., Kikhney, A.G. & Svergun, D.I. (2007) ATSAS 2.1 –

towards automated and web-supported small-angle scattering data analysis. *Journal of Applied Crystallography*. 40 (s1), s223–s228.

Pichoff, S. & Lutkenhaus, J. (2005) Tethering the Z ring to the membrane through a conserved membrane targeting sequence in FtsA. *Molecular Microbiology*. 84 (1), 577-601.

Pinho, M.G. & Errington, J. (2004) A *divIVA* null mutant of *Staphylococcus aureus* undergoes normal cell division. *FEMS Microbiology Letters*. 240 (2), 145–149.

Pompeo, F., Foulquier, E., Serrano, B., Grangeasse, C. & Galinier, A. (2015) Phosphorylation of the cell division protein GpsB regulates PrkC kinase activity through a negative feedback loop in *Bacillus subtilis*. *Molecular Microbiology*. 97 (1), 139-150.

Provvedi, R., Chen, I. & Dubnau, D. (2001) NucA is required for DNA cleavage during transformation of *Bacillus subtilis*. *Molecular Microbiology*. 40 (3), 634–644.

Raskin, D.M. & De Boer, P.A.J. (1999) Rapid pole-to-pole oscillation of a protein required for directing division to the middle of *Escherichia coli*. *Proceedings of the National Academy of Sciences of the United States of America*. 96 (9), 4971-4976.

Rausch, M., Deisinger, J.P., Ulm, H., Müller, A., Li, W., Hardt, P., Wang, X., Li, X., Sylvester, M., Engeser, M., Vollmer, W., Müller, C.E., Sahl, H.G., Lee, J.C. & Schneider, T. (2019) Coordination of capsule assembly and cell wall biosynthesis in *Staphylococcus aureus*. *Nature Communications*. 10 (1), 1404.

Reese, S. & Guggenheim, B. (2007) A novel TEM contrasting technique for extracellular polysaccharides in in vitro biofilms. *Microscopy Research and Technique*. 70 (9), 816–822.

Renner, L.D. & Weibel, D.B. (2012) MinD and MinE interact with anionic phospholipids and regulate division plane formation in *Escherichia coli*. *Journal of Biological Chemistry*. 287 (46), 38835-38844.

Reynolds, J., Moyes, R.B. & Breakwell, D.P. (2009) Differential staining of bacteria: acid fast stain. *Current Protocols in Microbiology*. 15 (1), 1–5.

Rismondo, J., Cleverley, R.M., Lane, H. V., Großhennig, S., Steglich, A., Möller, L., Mannala, G.K., Hain, T., Lewis, R.J. & Halbedel, S. (2016) Structure of the bacterial cell division determinant GpsB and its interaction with penicillin-binding proteins. *Molecular Microbiology*. 99 (5), 978–998.

Roach, E.J., Wroblewski, C., Seidel, L., Berezuk, A.M., Brewer, D., Kimber, M.S. & Khursigara, C.M. (2016) Structure and mutational analyses of *Escherichia coli* ZapD reveal charged residues involved in FtsZ filament bundling. *Journal of Bacteriology*. 198 (11), 1683-1693.

Robson, S. a & King, G.F. (2006) Domain architecture and structure of the bacterial cell division protein DivIB. *Proceedings of the National Academy of Sciences of the United States of America*. 103 (17), 6700–5.

Robson, S.A. & King, G.F. (2005) Backbone and side-chain 1H, 15N and 13C assignments for the cis conformer of the β domain of the bacterial cell division protein DivIB. *Journal of Biomolecular NMR*. 33 (2), 135.

Rollauer, S.E., Sooreshjani, M.A., Noinaj, N. & Buchanan, S.K. (2015) Outer membrane protein biogenesis in Gram-negative bacteria. *Philosophical Transactions of the Royal Society B: Biological Sciences*. 370 (1679), 1-10.

Rollet, C., Gal, L. & Guzzo, J. (2008) Biofilm-detached cells, a transition from a sessile to a planktonic phenotype: a comparative study of adhesion and physiological characteristics in *Pseudomonas aeruginosa*. *FEMS Microbiology Letters*. 290 (2), 135–142.

Rooney, L.M., Amos, W.B., Hoskisson, P.A. & McConnell, G. (2020) Intra-colony channels in *E. coli* function as a nutrient uptake system. *The ISME Journal*. 14 (10), 2461–2473.

Roseboom, W., Nazir, M.G., Meiresonne, N.Y., Mohammadi, T., Verheul, J., Buncherd, H., Bonvin, A.M.J.J., de Koning, L.J., de Koster, C.G., De Jong, L. & Den Blaauwen, T. (2018) Mapping the contact sites of the escherichia coli division-initiating proteins FtsZ and ZapA by BAMG cross-linking and site-directed mutagenesis. *International Journal of Molecular Sciences*. 19 (10), 2928.

Rowlett, V.W. & Margolin, W. (2013) The bacterial Min system. *Current Biology*. 23 (13), R553–R556.

Rowlett, V.W. & Margolin, W. (2015) The Min system and other nucleoid-independent regulators of Z ring positioning. *Frontiers in Microbiology*. 6 (478), 1-10.

Rued, B.E., Zheng, J.J., Mura, A., Tsui, H.C.T., Boersma, M.J., Mazny, J.L., Corona, F., Perez, A.J., Fadda, D., Doubravová, L., Buriánková, K., Branny, P., Massidda, O. & Winkler, M.E. (2017) Suppression and synthetic-lethal genetic relationships of Δ*gpsB* mutations indicate that GpsB mediates protein phosphorylation and penicillin-binding

protein interactions in *Streptococcus pneumoniae* D39. *Molecular Microbiology*. 103 (6), 931-957.

Ruiz, N. (2008) Bioinformatics identification of MurJ (MviN) as the peptidoglycan lipid II flippase in *Escherichia coli*. *Proceedings of the National Academy of Sciences*. 105 (40), 15553–15557.

Ruiz, N. (2016) Lipid flippases for bacterial peptidoglycan biosynthesis. *Lipid Insights*. 8 (Suppl 1), 21-31.

Ruiz, N., Kahne, D. & Silhavy, T.J. (2006) Advances in understanding bacterial outer-membrane biogenesis. *Nature Reviews Microbiology*. 4 (1), 57–66.

Rumbaugh, K.P. & Sauer, K. (2020) Biofilm dispersion. *Nature Reviews Microbiology*. 18 (10), 571–586.

Rutherford, S.T. & Bassler, B.L. (2012) Bacterial quorum sensing: its role in virulence and possibilities for its control. *Cold Spring Harbor Perspectives in Medicine*. 2 (11), a012427–a012427.

Saalbach, G., Hempel, A.M., Vigouroux, M., Flärdh, K., Buttner, M.J. & Naldrett, M.J. (2013) Determination of phosphorylation sites in the DivIVA cytoskeletal protein of *Streptomyces coelicolor* by targeted LC-MS/MS. *Journal of Proteome Research*. 12 (9), 4187-4192.

Sauvage, E., Kerff, F., Terrak, M., Ayala, J.A. & Charlier, P. (2008) The penicillin-binding proteins: structure and role in peptidoglycan biosynthesis. *FEMS microbiology reviews*. 32 (2), 234–58.

Schägger, H. (2006) Tricine–SDS-PAGE. *Nature Protocols*. 1 (1), 16–22.

Schertzer, J.W. & Brown, E.D. (2003) Purified, recombinant TagF protein from *Bacillus subtilis* 168 catalyzes the polymerization of glycerol phosphate onto a membrane ccceptor *in vitro*. *Journal of Biological Chemistry*. 278 (20), 18002–18007.

Schiffer, C., Hilgarth, M., Ehrmann, M. & Vogel, R.F. (2019) Bap and cell surface hydrophobicity are important factors in *Staphylococcus xylosus* biofilm formation. *Frontiers in Microbiology*. 10 (6), 1–10.

Schindelin, J., Arganda-Carreras, I., Frise, E., Kaynig, V., Longair, M., Pietzsch, T., Preibisch, S., Rueden, C., Saalfeld, S., Schmid, B., Tinevez, J.-Y., White, D.J.,

Hartenstein, V., Eliceiri, K., Tomancak, P. & Cardona, A. (2012) Fiji: an open-source platform for biological-image analysis. *Nature Methods*. 9 (7), 676–682.

Schmid, J., Sieber, V. & Rehm, B. (2015) Bacterial exopolysaccharides: biosynthesis pathways and engineering strategies. *Frontiers in Microbiology*. 6 (5), 1–24.

Schneewind, O. & Missiakas, D. (2014a) Lipoteichoic acids, phosphate-containing polymers in the envelope of Gram-positive bacteria. *Journal of Bacteriology*. 196 (6), 1133–1142.

Schneewind, O. & Missiakas, D. (2014b) Sec-secretion and sortase-mediated anchoring of proteins in Gram-positive bacteria. *Biochimica et Biophysica Acta (BBA) - Molecular Cell Research.* 1843 (8), 1687–1697.

Schneidman-Duhovny, D., Kim, S.J. & Sali, A. (2012) Integrative structural modelling with small angle X-ray scattering profiles. *BMC structural biology*. 12 (1), 17.

Schumacher, M.A. (2017) 'Bacterial Nucleoid Occlusion: Multiple Mechanisms for Preventing Chromosome Bisection During Cell Division', in *Sub-Cellular Biochemistry*. pp. 267–298.

Sewell, E.W.C., Pereira, M.P. & Brown, E.D. (2009) The wall teichoic acid polymerase TagF is non-processive *in vitro* and amenable to study using steady state kinetic analysis. *Journal of Biological Chemistry*. 284 (32), 21132–21138.

Shakir, A., ElBadawey, M.R., Shields, R.C., Jakubovics, N.S. & Burgess, J.G. (2012) Removal of biofilms from tracheoesophageal speech valves using a novel marine microbial deoxyribonuclease. *Otolaryngology–Head and Neck Surgery*. 147 (3), 509–514.

Sham, L.-T., Butler, E.K., Lebar, M.D., Kahne, D., Bernhardt, T.G. & Ruiz, N. (2014) MurJ is the flippase of lipid-linked precursors for peptidoglycan biogenesis. *Science*. 345 (6193), 220–222.

Shanker, E. & Federle, M.J. (2017) Quorum sensing regulation of competence and bacteriocins in *Streptococcus pneumoniae* and mutans. *Genes*. 8 (1), 1-17.

Shields, R.C., Mokhtar, N., Ford, M., Hall, M.J., Burgess, J.G., ElBadawey, M.R. & Jakubovics, N.S. (2013) Efficacy of a marine bacterial nuclease against biofilm forming microorganisms isolated from chronic rhinosinusitis. *PLoS ONE*. 8 (2), e55339.

Shlyapnikov, S. V., Lunin, V. V., Perbandt, M., Polyakov, K.M., Lunin, V.Y., Levdikov, V.M., Betzel, C. & Mikhailov, A.M. (2000) Atomic structure of the *Serratia marcescens* endonuclease at 1.1 Å resolution and the enzyme reaction mechanism. *Acta Crystallographica Section D: Biological Crystallography*. 56 (5), 567-572.

Siegel, S.D., Liu, J. & Ton-That, H. (2016) Biogenesis of the Gram-positive bacterial cell envelope. *Current Opinion in Microbiology*. 3431–37.

Sieger, B., Schubert, K., Donovan, C. & Bramkamp, M. (2013) The lipid II flippase RodA determines morphology and growth in *Corynebacterium glutamicum*. *Molecular Microbiology*. 90 (5), 966–982.

Silhavy, T.J., Kahne, D. & Walker, S. (2010) The bacterial cell envelope. *Cold Spring Harbor Perspectives in Biology*. 2 (5), 1–16.

Sinderen, D., Kiewiet, R. & Venema, G. (1995) Differential expression of two closely related deoxyribonuclease genes, nucA and nucB, in *Bacillus subtilis*. *Molecular Microbiology*. 15 (2), 213–223.

Singh, J.K., Makde, R.D., Kumar, V. & Panda, D. (2007) A membrane protein, EzrA, regulates assembly dynamics of FtsZ by interacting with the C-terminal tail of FtsZ. *Biochemistry*. 46 (38), 11013–11022.

Singh, R., Paul, D. & Jain, R.K. (2006) Biofilms: implications in bioremediation. *Trends in Microbiology*. 14 (9), 389–397.

Skarzynski, T., Mistry, A., Wonacott, A., Hutchinson, S.E., Kelly, V.A. & Duncan, K. (1996) Structure of UDP-N-acetylglucosamine enolpyruvyl transferase, an enzyme essential for the synthesis of bacterial peptidoglycan, complexed with substrate UDP-N-acetylglucosamine and the drug fosfomycin. *Structure*. 4 (12), 1465–1474.

Slabinski, L., Jaroszewski, L., Rychlewski, L., Wilson, I.A., Lesley, S.A. & Godzik, A. (2007) XtalPred: A web server for prediction of protein crystallizability. *Bioinformatics*. 23 (24), 3403–3405.

Smith, H., Wiersma, K., Venema, G. & Bron, S. (1985) Transformation in *Bacillus subtilis*: Further characterization of a 75,000-dalton protein complex involved in binding and entry of donor DNA. *Journal of Bacteriology*. 164 (1), 201–206.

Snarr, B.D., Baker, P., Bamford, N.C., Sato, Y., Liu, H., Lehoux, M., Gravelat, F.N., Ostapska, H., Baistrocchi, S.R., Cerone, R.P., Filler, E.E., Parsek, M.R., Filler, S.G.,

Howell, P.L. & Sheppard, D.C. (2017) Microbial glycoside hydrolases as antibiofilm agents with cross-kingdom activity. *Proceedings of the National Academy of Sciences*. 114 (27), 7124–7129.

Sockolosky, J.T. & Szoka, F.C. (2013) Periplasmic production via the pET expression system of soluble, bioactive human growth hormone. *Protein Expression and Purification*. 87 (2), 129–135.

Söderström, B. & Daley, D.O. (2017) The bacterial divisome: more than a ring? *Current Genetics*. 63 (2), 161–164.

Stahlberg, H., Kutejová, E., Muchová, K., Gregorini, M., Lustig, A., Müller, S.A., Olivieri, V., Engel, A., Wilkinson, A.J. & Barák, I. (2004) Oligomeric structure of the *Bacillus subtilis* cell division protien DivIVA determined by transmission microscopy. *Molecular Microbiology*. 52 (5), 1281–1290.

Steele, V.R., Bottomley, A.L., Garcia-Lara, J., Kasturiarachchi, J. & Foster, S.J. (2011) Multiple essential roles for EzrA in cell division of *Staphylococcus aureus*. *Molecular Microbiology*. 80 (2), 542–555.

Steinberg, N., Keren-Paz, A., Hou, Q., Doron, S., Yanuka-Golub, K., Olender, T., Hadar, R., Rosenberg, G., Jain, R., Cámara-Almirón, J., Romero, D., van Teeffelen, S. & Kolodkin-Gal, I. (2020) The extracellular matrix protein TasA is a developmental cue that maintains a motile subpopulation within *Bacillus subtilis* biofilms. *Science Signaling*. 13 (632), 1-15.

Stienberger, R.E. & Holden, P.A. (2005) Extracellular DNA in single- and multiple-species unsaturated biofilm. *Applied and Environmental Microbiology*. 71 (9), 5404–5410.

Strahl, H. & Hamoen, L.W. (2012) Finding the corners in a cell. *Current Opinion in Microbiology*. 15 (6), 731–736.

Suh, Y., Jin, S., Ball, T.K. & Benedik, M.J. (1996) Two-step secretion of the *Serratia marcescens* extracellular nuclease. *Journal of Bacteriology*. 178 (13), 3771–3778.

Sung, M.-T., Lai, Y.-T., Huang, C.-Y., Chou, L.-Y., Shih, H.-W., Cheng, W.-C., Wong, C.-H. & Ma, C. (2009) Crystal structure of the membrane-bound bifunctional transglycosylase PBP1b from *Escherichia coli*. *Proceedings of the National Academy of Sciences*. 106 (22), 8824–8829.

Svergun, D.I. (1999) Restoring low resolution structure of biological macromolecules from solution scattering using simulated annealing. *Biophysical Journal*. 76 (6), 2879–2886.

Swoboda, J.G., Campbell, J., Meredith, T.C. & Walker, S. (2009) Wall teichoic acid function, biosynthesis, and inhibition. *ChemBioChem*. 11 (1), 35–45.

Swoboda, J.G., Meredith, T.C., Campbell, J., Brown, S., Suzuki, T., Bollenbach, T., Malhowski, A.J., Kishony, R., Michael, S. & Walker, S. (2010) Discovery of a small molecule that blocks wall teichoic acid biosynthesis in *Staphlyococcus aureus*. *ACS Chemical Biology*. 4 (10), 875–883.

Sylvester, D.R., Alvarez, E., Patel, A., Ratnam, K., Kallender, H. & Wallis, N.G. (2001) Identification and characterization of UDP-N-acetylenolpyruvylglucosamine reductase (MurB) from the Gram-positive pathogen *Streptococcus pneumoniae*. *Biochemical Journal*. 355 (2), 431–435.

Szwedziak, P., Wang, Q., Bharat, T.A.M., Tsim, M. & Löwe, J. (2014) Architecture of the ring formed by the tubulin homologue FtsZ in bacterial cell division. *eLife*. 3, 1-22

Taglialegna, A., Lasa, I. & Valle, J. (2016a) Amyloid structures as biofilm matrix scaffolds. *Journal of Bacteriology*. 198 (19), 2579–2588.

Taglialegna, A., Navarro, S., Ventura, S., Garnett, J.A., Matthews, S., Penades, J.R., Lasa, I. & Valle, J. (2016b) *Staphylococcal* Bap proteins build amyloid scaffold biofilm matrices in response to environmental signals Matthew R. Parsek (ed.). *PLOS Pathogens*. 12 (6), e1005711.

Taguchi, A., Welsh, M.A., Marmont, L.S., Lee, W., Sjodt, M., Kruse, A.C., Kahne, D., Bernhardt, T.G. & Walker, S. (2019) FtsW is a peptidoglycan polymerase that is functional only in complex with its cognate penicillin-binding protein. *Nature Microbiology*. 4 (4), 587–594.

Tetz, G. V., Artemenko, N.K. & Tetz, V. V. (2009) Effect of DNase and antibiotics on biofilm characteristics. *Antimicrobial Agents and Chemotherapy*. 53 (3), 1204–1209.

Park, J., Throop, A.L. & LaBaer, J. (2015) Site-Specific Recombinational Cloning Using Gateway and In-Fusion Cloning Schemes. *Current Protocols in Molecular Biology*. 110 (1), 3.20.1-3.20.23.

Timmusk, S., Behers, L., Muthoni, J., Muraya, A. & Aronsson, A.-C. (2017) Perspectives and challenges of microbial application for crop improvement. *Frontiers in Plant Science*. 8 (2), 1–10.

Tolker-Nielsen, T. (2015) Biofilm development. *Microbiology Spectrum*. 3 (2), 1–12.

Tonthat, N.K., Arold, S.T., Pickering, B.F., Van Dyke, M.W., Liang, S., Lu, Y., Beuria, T.K., Margolin, W. & Schumacher, M.A. (2011) Molecular mechanism by which the nucleoid occlusion factor, SlmA, keeps cytokinesis in check. *EMBO Journal*. 30 (1), 154-164.

Turner, R.D., Ratcliffe, E.C., Wheeler, R., Golestanian, R., Hobbs, J.K. & Foster, S.J. (2010) Peptidoglycan architecture can specify division planes in *Staphylococcus aureus*. *Nature Communications*. 1 (3), 1–9.

Turner, R.D., Vollmer, W. & Foster, S.J. (2014) Different walls for rods and balls: the diversity of peptidoglycan. *Molecular Microbiology*. 91 (5), 862–874.

Ulett, G.C., Valle, J., Beloin, C., Sherlock, O., Ghigo, J.-M. & Schembri, M.A. (2007) Functional Analysis of Antigen 43 in Uropathogenic *Escherichia coli* reveals a role in long-term persistence in the urinary tract. *Infection and Immunity*. 75 (7), 3233–3244.

Ulyanova, V., Vershinina, V. & Ilinskaya, O. (2011) Barnase and binase: Twins with distinct fates. *FEBS Journal*. 278 (19), 3633–3643.

Ulyanova, V., Vershinina, V., Ilinskaya, O. & Harwood, C.R. (2015) Binase-like guanyl-preferring ribonucleases are new members of Bacillus PhoP regulon. *Microbiological Research.* 170131–138.

Vagin, A. & Teplyakov, A. (1997) MOLREP: an Automated Program for Molecular Replacement. *Journal of Applied Crystallography*. 30 (6), 1022–1025.

VanNieuwenhze, M.S., Mauldin, S.C., Zia-Ebrahimi, M., Aikins, J.A. & Blaszczak, L.C. (2001) The total synthesis of Lipid I. *Journal of the American Chemical Society*. 123 (29), 6983–6988.

Veiga, H., Jorge, A.M. & Pinho, M.G. (2011) Absence of nucleoid occlusion effector Noc impairs formation of orthogonal FtsZ rings during *Staphylococcus aureus* cell division. *Molecular Microbiology*. 80 (5), 1366-1380.

Vishwakarma, V. (2020) Impact of environmental biofilms: Industrial components and its remediation. *Journal of Basic Microbiology*. 60 (3), 198–206.

Vlamakis, H., Chai, Y., Beauregard, P., Losick, R. & Kolter, R. (2013) Sticking together: Building a biofilm the *Bacillus subtilis* way. *Nature Reviews Microbiology*. 11 (3), 157–168.

Vollmer, W. (2008) Structural variation in the glycan strands of bacterial peptidoglycan. *FEMS Microbiology Reviews*. 32 (2), 287–306.

Vollmer, W., Blanot, D. & De Pedro, M.A. (2008) Peptidoglycan structure and architecture. *FEMS Microbiology Reviews*. 32 (2), 149–167.

Vosman, B., Kooistra, J., Olijve, J. & Venema, G. (1987) Cloning in *Escherichia coli* of the gene specifying the DNA-entry nuclease of *Bacillus subtilis*. *Gene*. 52 (2–3), 175–183.

Vosman, B., Kuiken, G., Kooistra, J. & Venema, G. (1988) Transformation in *Bacillus subtilis*: involvement of the 17-kilodalton DNA-entry nuclease and the competence-specific 18-kilodalton protein. *Journal of Bacteriology*. 170 (8), 3703–3710.

Walsh, J.C., Angstmann, C.N., Bisson-Filho, A.W., Garner, E.C., Duggin, I.G. & Curmi, P.M.G. (2019) Division plane placement in pleomorphic archaea is dynamically coupled to cell shape. *Molecular Microbiology*. 112 (3), 785-799

Walter, T.S., Meier, C., Assenberg, R., Au, K.-F., Ren, J., Verma, A., Nettleship, J.E., Owens, R.J., Stuart, D.I. & Grimes, J.M. (2006) Lysine methylation as a routine rescue strategy for protein crystallization. *Structure*. 14 (11), 1617–1622.

Wanner, S., Schade, J., Keinhörster, D., Weller, N., George, S.E., Kull, L., Bauer, J., Grau, T., Winstel, V., Stoy, H., Kretschmer, D., Kolata, J., Wolz, C., Bröker, B.M. & Weidenmaier, C. (2017) Wall teichoic acids mediate increased virulence in *Staphylococcus aureus*. *Nature Microbiology*. 2 (1), 16257.

Waxman, D.J. & Strominger, J.L. (1983) Penicillin-binding proteins and the mechanism of action of beta-lactam antibiotics. *Annual Review of Biochemistry*. 52 (1), 825–869.

Weiss, M.S. & Schulz, G.E. (1992) Structure of porin refined at 1.8 Å resolution. *Journal of Molecular Biology*. 227 (2), 493–509.

Whitchurch, C.B. (2002) Extracellular DNA required for bacterial biofilm formation. *Science*. 295 (5559), 1487–1487.

Williams, C.J., Headd, J.J., Moriarty, N.W., Prisant, M.G., Videau, L.L., Deis, L.N., Verma, V., Keedy, D.A., Hintze, B.J., Chen, V.B., Jain, S., Lewis, S.M., Arendall, W.B.,

Snoeyink, J., Adams, P.D., Lovell, S.C., Richardson, J.S. & Richardson, D.C. (2018) MolProbity: More and better reference data for improved all-atom structure validation. *Protein Science*. 27 (1), 293-315.

Winn, M.D., Ballard, C.C., Cowtan, K.D., Dodson, E.J., Emsley, P., Evans, P.R., Keegan, R.M., Krissinel, E.B., Leslie, A.G.W., McCoy, A., McNicholas, S.J., Murshudov, G.N., Pannu, N.S., Potterton, E.A., Powell, H.R., Read, R.J., Vagin, A. & Wilson, K.S. (2011) Overview of the CCP4 suite and current developments. *Acta Crystallographica Section D Biological Crystallography*. 67 (4), 235–242.

Wu, C.C., Lin, J.L.J. & Yuan, H.S. (2020) Structures, mechanisms, and functions of His-Me finger nucleases. *Trends in Biochemical Sciences*. 45 (11), 935–946.

Wu, L.J. & Errington, J. (2012) Nucleoid occlusion and bacterial cell division. *Nature Reviews Microbiology*. 10 (1), 8–12.

Xia, G., Maier, L., Sanchez-Carballo, P., Li, M., Otto, M., Holst, O. & Peschel, A. (2010) Glycosylation of wall teichoic acid in *Staphylococcus aureus* by TarM. *Journal of Biological Chemistry*. 285 (18), 13405–13415.

Xue, S., Calvin, K. & Li, H. (2006) RNA recognition and cleavage by a splicing endonuclease. *Science*. 312 (5775), 906–910.

Yan, J. & Bassler, B.L. (2019) Surviving as a community: Antibiotic tolerance and persistence in bacterial biofilms. *Cell Host & Microbe*. 26 (1), 15–21.

Yan, Y., Munshi, S., Leiting, B., Anderson, M.S., Chrzas, J. & Chen, Z. (2000) Crystal structure of *Escherichia coli* UDP-MurNAc-tripeptide D-alanyl-D-alanine-adding enzyme (MurF) at 2.3 Å resolution. *Journal of Molecular Biology*. 304 (3), 435–445.

Yanagawa, H., Yoshida, K., Torigoe, C., Park, J.S., Sato, K., Shirai, T. & Go, M. (1993) Protein anatomy: functional roles of barnase module. *Journal of Biological Chemistry*. 268 (8), 5861–5865.

Yang, W. (2011) Nucleases: diversity of structure, function and mechanism. *Quarterly Reviews of Biophysics*. 44 (1), 1–93.

Yarwood, J.M. & Schlievert, P.M. (2003) Quorum sensing in *Staphylococcus* infections. *Journal of Clinical Investigation*. 112 (11), 1620–1625.

Yin, W., Wang, Y., Liu, L. & He, J. (2019) Biofilms: The microbial “protective clothing” in extreme environments. *International Journal of Molecular Sciences*. 20 (14), 3423.

Yong, D., Toleman, M.A., Giske, C.G., Cho, H.S., Sundman, K., Lee, K. & Walsh, T.R. (2009) Characterization of a new metallo-lactamase gene, blaNDM-1, and a novel erythromycin esterase gene carried on a unique genetic structure in *Klebsiella pneumoniae* sequence type 14 from India. *Antimicrobial Agents and Chemotherapy*. 53 (12), 5046–5054.

Yu, S., Su, T., Wu, H., Liu, S., Wang, D., Zhao, T., Jin, Z., Du, W., Zhu, M.-J., Chua, S.L., Yang, L., Zhu, D., Gu, L. & Ma, L.Z. (2015) PslG, a self-produced glycosyl hydrolase, triggers biofilm disassembly by disrupting exopolysaccharide matrix. *Cell Research*. 25 (12), 1352–1367.

Yu, X.C. & Margolin, W. (1999) FtsZ ring clusters in min and partition mutants: Role of both the Min system and the nucleoid in regulating FtsZ ring localization. *Molecular Microbiology*. 32 (2), 315-326.

Zapun, A., Philippe, J., Abrahams, K.A., Signor, L., Roper, D.I., Breukink, E. & Vernet, T. (2013) In vitro reconstitution of peptidoglycan assembly from the Gram-positive pathogen *Streptococcus pneumoniae*. *ACS Chemical Biology*. 8 (12), 2688–96.

Zheng, L. (2004) An efficient one-step site-directed and site-saturation mutagenesis protocol. *Nucleic Acids Research*. 32 (14), e115–e115.

Zheng, S., Sham, L.-T., Rubino, F.A., Brock, K.P., Robins, W.P., Mekalanos, J.J., Marks, D.S., Bernhardt, T.G. & Kruse, A.C. (2018) Structure and mutagenic analysis of the lipid II flippase MurJ from *Escherichia coli*. *Proceedings of the National Academy of Sciences*. 115 (26), 6709–6714.

Zheng, W., Cai, X., Li, S. & Li, Z. (2018) Autophosphorylation mechanism of the Ser/Thr Kinase Stk1 from *Staphylococcus aureus*. *Frontiers in Microbiology*. 9 (4), 1–10.

El Zoeiby, A., Sanschagrin, F. & Levesque, R.C. (2002) Structure and function of the Mur enzymes: development of novel inhibitors. *Molecular Microbiology*. 47 (1), 1–12.

Appendix I. Data published in Eswara et al., 2018

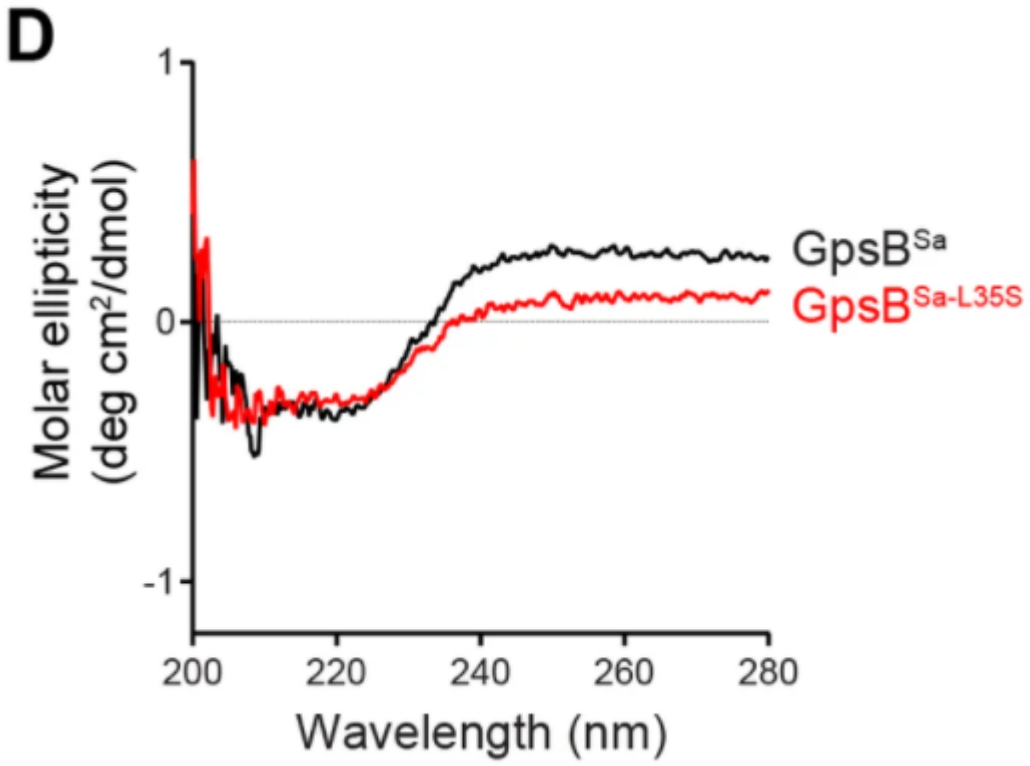

Supplementary Figure 1: CD Data presented in Eswara et al., 2018. The range used during analysis covers 200-280 nm, and is particularly noisy at the lower wavelengths.

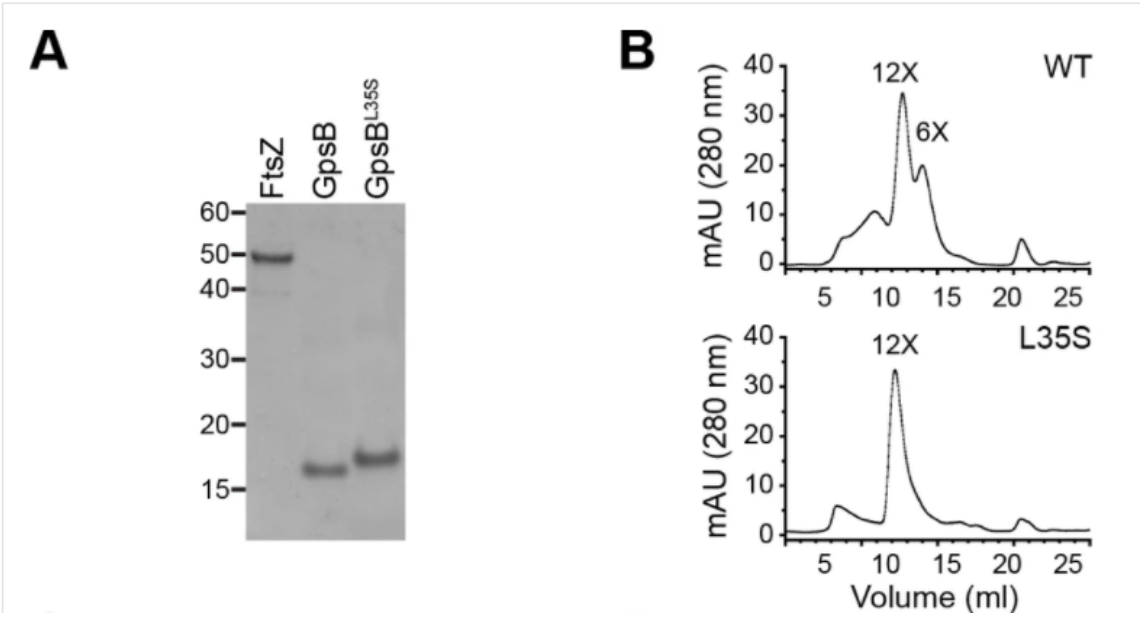

Supplementary Figure 2: A) SDS-PAGE analysis of *Sa*GpsB and *Sa*GpsB^{L35S}, a clear difference in electrophoresis is seen between the wild-type protein and the single point mutant, not rationalised by the author

Appendix II. List of primers used in this study

DivIVA_FL_NtermMBP_EcoRI	gatgagctctacaaaGGTAGCGGCAGCGGTAGCGGCatgCCGTTCACCCCGAAC
DivIVA_MBP_Rv_XhoI	ACTCGAGCTGGTCTAGAAAGCTTTATTTCTTGGTGGTTTCGCTAT
D4A_56-120_iPCR_rev	GTTGGTATCACGTTCCTCGATCACTTT
D4A_57-120_iPCR_rev	AATGTTGGTATCACGTTCCTCGATCAC
D4A_57-120_iPCR_fwd	GATATGAAGCGTCAAAGCAAAGTGTTC
D4A_57-121_iPCR_fwd	ATGAAGCGTCAAAGCAAAGTGTTCCGT
S59STOP_fwd	GAACGTGATACCAACATTAAGTAATACCAGGACGTGCACCAAAG
S59STOP_rev	CTTTGGTGCACGTCCTGGTATTACTTAATGTTGGTATCACGTTC
D4A_1-57_CtermHis_fwd	GCGGCGCTCGAGAATGTTGGTATCACGTTCCTCG
D4A_1-57_CtermHis_fwd	GCGGCGCATATGCCGTTCACCCCGAACGAGATC
DivIVA_Cterm_Asp72_fwd	GGTCTGGAAGTTCTGTTTCAGGGTCCGGATACCAACATTAAGAGCT
DivIVA_Cterm_Ala88_fwd	GGTCTGGAAGTTCTGTTTCAGGGTCCGGCGCTGATCCAGGCGCAAAAAG
DivIVA_Cterm_Ala109_fwd	GGTCTGGAAGTTCTGTTTCAGGGTCCGGCGATCATTGCGAAGGCGGA
DivIVA_Cterm_Met139_fwd	GGTCTGGAAGTTCTGTTTCAGGGTCCGATGAAGCGTCAAAGCAAAGT
DivIVA_Cterm_rev	CGCTTTCCAGTCGGGTCGACGGTTATTTCTTGGTGGTTTCGCTATCG
M139STOP_SpeI_fwd	gtcgtctggcgtttcagaccgaagactagtagcgtcaaagcaaagtgttc
M139STOP_SpeI_rev	gaacactttgctttgacgctactagtcttcggtctgaaacgccagacgac
Q157STOP_AflII_fwd	gttttcgtatgctggttgaggcttaagtggacctgctgaagaacgaagactg
Q157STOP_AflII_rev	cagtcttcgttcttcagcaggtccacttaagcctcaaccagcatacgaaaac

I184STOP_SpeI_fwd	GCAAGTGACCCTGGAAAACTAGTACCACCTGCACGAGAACGAC
I184_STOP_SpeI_rev	GTCGTTCTCGTGCAGGTGGTACTAGTTTTCCAGGGTCACTTGC
S206STOP_AflII_Fwd	CGAACGCGCAGAACAACGCTTAAGACACCCCGGACAACAACCAG
S206STOP_AflII_Rev	CTGGTTGTTGTCCGGGGTGTCTTAAGCGTTGTTCTGCGCGTTCG
nin_NcoI_fwd	GCGGCGCCATGGCGATGATCAAATCATGGAAGCCGCAA
nin_NdeI_fwd	GCGGCGCATATGATCAAATCATGGAAGCCGCAA
nin_XhoI_rev	GCGGCGCTCGAGTTACACAGAAACAGCATCAAT
nucA_NcoI_fwd	GCGGCGCCATGGGAGACTTTTTCTCAGCTGAT
nucA_XhoI_rev	GCGGCGCTCGAGCTGAATTGTGAATAAAACCTT
nucB_NcoI_fwd	GCGGCGCCATGGGCGCATCTTCGTATGACAAA
nucB_XhoI_rev	GCGGCGCTCGAGCTGCACAATAAACAGCACTCT
E83STOP_SpeI_fwd	gaGGAAAACCACAAACTGAAGAAATaactagtGGAACTGCGtctgcgtg
E83STOP_SpeI_rev	cacgcagaCGCAGTTCCactagttATTTCTTCAGTTTGTGGTTTTCCtc

Received: 15 August 2019 | Revised: 29 August 2019 | Accepted: 29 August 2019

DOI: 10.1002/pro.3722

REVIEW

THE PROTEIN SOCIETY WILEY

Structural basis for the coordination of cell division with the synthesis of the bacterial cell envelope

Simon Booth | **Richard J. Lewis**

Institute for Cell and Molecular Biosciences, Faculty of Medical Sciences, Newcastle University, Newcastle upon Tyne, UK

Correspondence
Richard J. Lewis, Institute for Cell and Molecular Biosciences, Newcastle University, Newcastle upon Tyne, NE2 4HH, UK.
Email: r.lewis@ncl.ac.uk

Funding information
Newcastle University

Abstract

Bacteria are surrounded by a complex cell envelope made up of one or two membranes supplemented with a layer of peptidoglycan (PG). The envelope is responsible for the protection of bacteria against lysis in their oft-unpredictable environments and it contributes to cell integrity, morphology, signaling, nutrient/small-molecule transport, and, in the case of pathogenic bacteria, host–pathogen interactions and virulence. The cell envelope requires considerable remodeling during cell division in order to produce genetically identical progeny. Several proteinaceous machines are responsible for the homeostasis of the cell envelope and their activities must be kept coordinated in order to ensure the remodeling of the envelope is temporally and spatially regulated correctly during multiple cycles of cell division and growth. This review aims to highlight the complexity of the components of the cell envelope, but focusses specifically on the molecular apparatuses involved in the synthesis of the PG wall, and the degree of cross talk necessary between the cell division and the cell wall remodeling machineries to coordinate PG remodeling during division. The current understanding of many of the proteins discussed here has relied on structural studies, and this review concentrates particularly on this structural work.

KEYWORDS

cell division, cell wall, divisome, peptidoglycan

1 | INTRODUCTION

Bacteria are classified into two groups, Gram-negative and Gram-positive, based on their response to the Gram stain. Gram-negative cell envelopes consist of both an inner and an outer membrane (IM and OM, respectively), which encapsulate a relatively thin peptidoglycan (PG) layer a few nanometers (nm) thick.[1] By contrast, Gram-positive bacteria have only a single membrane surrounded by a much thicker PG layer, ranging from 30 to 100 nm in thickness.[2] It is this thick, external layer of PG in Gram-positive bacteria that allows for the retention of the Gram stain. It makes sense that the Gram nomenclature for bacterial cells has remained an important classification since its development by Hans Christian Gram in 1884, as it provides important information about the gross structure of bacterial cell walls. The PG layer is a defining feature of bacteria, distinguishing them from archaea or eukaryotes. The tensile strength of PG allows bacteria to thrive in a variety of environments, indeed, targeting the proteins responsible for PG renewal in bacteria has been central to mankind's fight against infectious diseases.[3] While some chemical moieties in PG differ between species of bacteria, the general structure of PG comprises repeating disaccharides of *N*-acetylglucosamine (Glc*N*Ac) and *N*-acetylmuramic acid (Mur*N*Ac), cross-linked between Mur*N*Acs via short (four or five residues) peptide stems (Figure 1), to form a lattice-like arrangement.[4] The fifth, terminal *D*-alanine is normally lost during PG maturation.

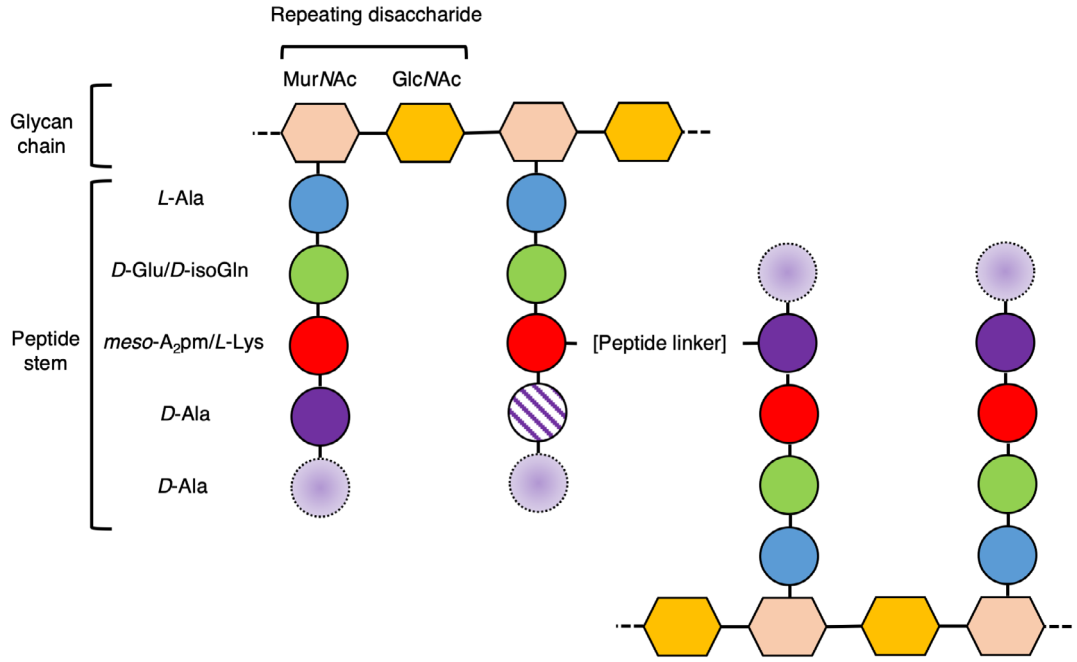

FIGURE 1 The general structure of peptidoglycan (PG). The general structure of the matrix of PG is shown as a cartoon in which sugar moieties are represented as hexagons and the amino acids that comprise the peptide stems are shown as circles. The identity of the residues present in the cartoon represent the majority of Gram-negative/Gram-positive peptide stems, respectively. Variability in the presence of the *D*-Ala residues in mature PG at positions 4 (which is sometimes lost) and 5 (which is always lost) of the peptide stem is represented by a cross-hatched fill and a dashed outline with a gradient fill, respectively. The most common peptide linker in PG is formed between positions 3 and 4 of the peptide stem (as shown here). The chemical structure of the peptide cross-link varies, and may be composed of a direct link between residues in the peptide stem, or may be comprised of a peptide link, such as the penta-glycine linker present typically in *S. aureus*

Some variations on this basic theme include additional short (one to five residue) peptide linkers between the peptide stems, which normally (but not exclusively) are cross-linked between the amino group from the sidechain of residue 3 and the carboxyl group of *D*-alanine at position 4 (a three to four cross-link). The direct cross-links typically also involve residues 3 and 4. Differences in the structure and regulation of PG and its synthesis are responsible for variations in cell integrity and morphology,[4,5] highlighting the importance of the PG layer to bacteria. The synthesis of PG is a complex multienzyme process initiated in the cytoplasm and subsequently linked to the inner (and outer) leaflet of the cell membrane. PG synthesis has been studied relatively extensively, particularly in the rod-shaped model organisms *Escherichia coli* and *Bacillus subtilis*, which are representatives of the Gram-negative and Gram-positive groups, respectively. Consequently, the anabolism of PG is fairly well understood.[6] The coupling of PG hydrolysis and resynthesis during cell division is essential for the cell to avoid an untimely death; however, the study of this synergy is a field that remains in its infancy.

In the majority of cases, bacteria undertake a process of binary fission through which two identical daughter cells are produced from a parental cell, which involves the establishment of a site of division, elongation (in some cases), chromosome replication and segregation, generation and closure of a septum, and finally separation of the two cells at the septum. Cell division is thus an exceptionally complicated cycle of events requiring a multitude of spatial and temporal backstops for it to be undertaken successfully. There is, however, insufficient scope in this review to consider the spatiotemporal coordination of chromosome replication and segregation with the later steps of cell division. While the fundamental events in this process are conserved across the entire bacterial kingdom, species-specific nuances are observed, often related to the structure of the cell envelope, variations in morphology, or the identity and nature of some of the regulators. Defining mid-cell is a critical step of division and is undertaken differently depending on the bacterial species. In rod-shaped bacteria, such as *B. subtilis* and *E. coli*, the mid-cell is defined at the mid-point of the longest edge of the cell, where the septum forms in a ring across the shortest width of the cell. In spherical bacteria (cocci), such as the *Staphylococci*, mid-cell is defined at the point at which there is the longest diameter of cross section of the spherical cell, and the septum forms around the circumference of the cell in a ring,[7–9] and subsequent division planes are placed orthogonally to the previous because the PG "pie-crust" rings are important topological markers of past sites of division in *Staphylococcus aureus*.[9]

In ovococci, like *Streptococcus pneumoniae*, both cell length and diameter considerations are important for determining mid-cell.[10] The location of septum formation is a good example of the level of control involved throughout; in many rod-shaped bacteria (such as *E. coli*) its position rarely varies in location beyond a few percent, resulting in progeny that rarely vary in volume outside of this margin (~4%).[11] Placement of the septum is aided by the Min and nucleoid occlusion systems, which both act as inhibitors of the septal ring progenitor protein, FtsZ.[12–15] Some bacteria that lack the Min system, such as *Mycobacterium tuberculosis*, seem to utilize a different, albeit less-efficient system for determining mid-cell as cell division of this species results in daughter cells of different sizes.[12] Septum formation and constriction of the cell into two daughter cells are common themes between both Gram-negative and Gram-positive bacteria; however, Gram-positive bacteria form a complete septum across the mid-cell before division occurs, whereas a Gram-negative bacterium divides while developing its septum simultaneously.[7] Whether cell elongation occurs during/prior to this process is also species specific and is not necessarily predictable by morphology and/or cell wall composition alone.

There are obviously a great number of fine details relevant to these processes suitable for review but, for the sake of brevity, we will discuss briefly the make-up of the envelope of both Gram-negative and Gram-positive bacteria, before discussing the mechanisms through which bacteria build their wall, the proteins involved in regulating cell division in context of the life cycle of the cell, and the significance of understanding these processes with regards to their potential for exploitation in the pursuit of much needed new antibiotics.

2 | THE GRAM-NEGATIVE ENVELOPE

The OM of Gram-negative bacteria is an asymmetrical bilayer (Figure 2) consisting of phospholipids and lipopolysaccharides, which assemble into the inner and outer leaflets

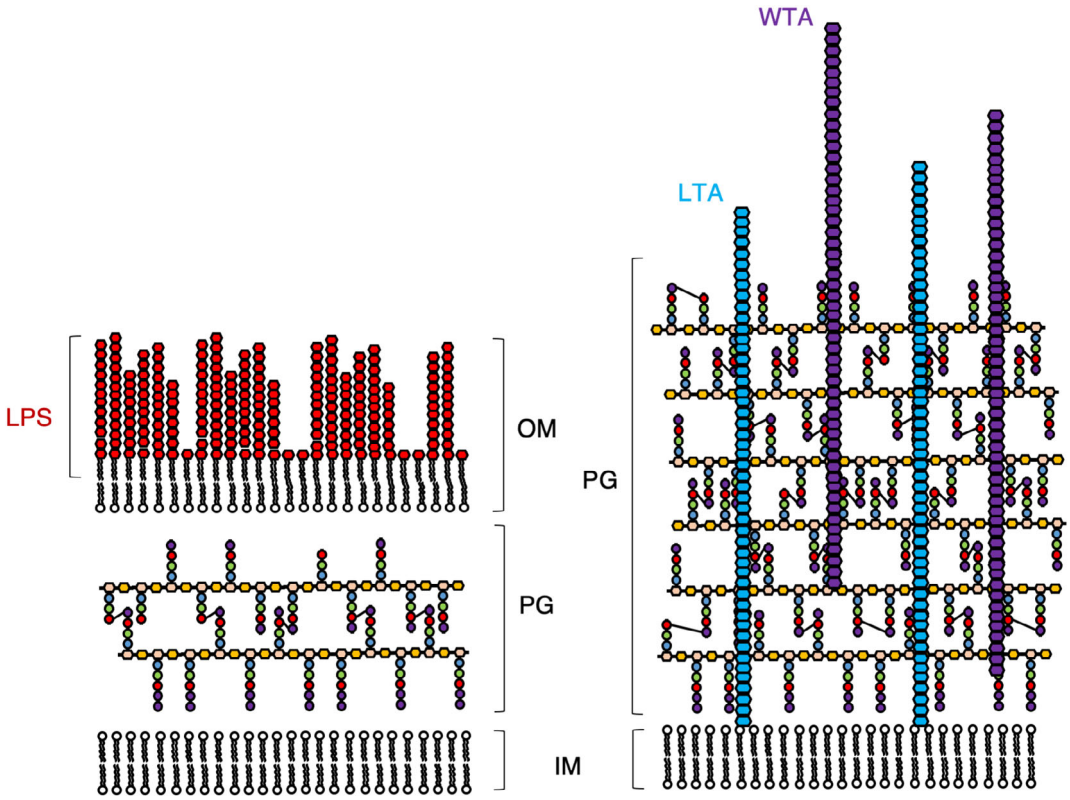

FIGURE 2 Comparison of the cell envelopes of Gram-negative (left) and Gram-positive (right) bacteria. The cell envelope of Gram-negative bacteria comprises of an inner (IM) and outer membrane (OM) decorated with lipopolysaccharide (LPS), sandwiching a relatively thin layer of peptidoglycan (PG). By contrast, the cell envelope of Gram-positive bacteria is comprised of a single cell membrane surrounded much thicker PG layer complemented with lipoteichoic acid (LTA) and wall teichoic acid (WTA). Cross-links between peptide stems are shown as three to four cross-links for the sake of simplicity. Not shown are the multitude of proteins that sit in the inner and OM of Gram-negative bacteria, nor those that reside in the membrane or the PG of Gram-positive bacteria. The components of PG are displayed using the same scheme as in Figure 1, with the nascent PG chain containing *D*-Ala at positions 4 and 5. The mature PG is represented without the *D*-Ala at position 5 and occasionally also without the *D*-Ala at position 4 to represent the natural variability of the peptide stem in the mature PG mesh

of the membrane, respectively.[1,2] The structure, function, and synthesis of the Gram-negative OM are all complex discussion points appropriate for review in their own right.[1,2,16] Broadly speaking, the OM serves as a protective layer for Gram-negative bacteria, functioning as a semi-permeable barrier to the periplasm,[17] and as an added layer of protection from environmental turgor.[2] The OM accommodates a variety of OM proteins (OMPs), which consist of porins, proteases, lipases, transporters, and various receptors embedded into the OM.[16] Unsurprisingly given their nomenclature, porins and transporters are responsible for the diffusion/transport of small molecules into the periplasm, respectively,[18] and are responsible for the semi-permeable nature of the OM. Several members of the porin family of OMPs have been amenable to structural study by crystallography[19–21] and the resulting structural models have had essential roles in the elucidation of molecular mechanisms of transport, highlighting the complexity of the OM. The OM also requires remodeling during cell division and a more complete picture of the OM and its constituents is thus key to understanding how this is regulated on a molecular level,[22,23] and an integrative approach[21] will lead to a far greater mechanistic understanding than with structure alone.

3 | THE GRAM-POSITIVE CELL ENVELOPE

Gram-positive bacteria compensate for the lack of the protective/stabilizing presence of the OM with a thicker layer of PG.[2,24] As well as the obvious difference in thickness, the PG layer of Gram-positive bacteria is distinguished from Gram-negative bacteria by its decoration with anionic glycopolymers called teichoic acids (TAs).[25,26] TAs constitute 30–60% of the Gram-positive cell wall. There are two types of TA; wall TAs (WTAs), which are covalently attached to the PG, and lipoteichoic acids (LTAs), which are attached to the cytoplasmic membrane and extend deep into the wall (Figure 2).[27,28] TAs may act as a functional substitute for the OMPs present in Gram-negative bacteria as they are also capable of affecting permeability and integrity, and are responsible for host–pathogen interactions.[29] It follows that TAs are a virulence factor for Gram-positive pathogens and for this reason are of interest for study, as their synthesis pathways are also a potential target for future antibiotics.[30–32] The TA chemical structure, similarly to PG, also varies from species to species. The general structure is a β-1 → 4 linked *N*-acetylmannosamine/Glc*N*Ac (Man*N*Ac/Glc*N*Ac) disaccharide, a glycerophosphate linker made of three phosphoglycerol molecules, followed by a long chain of glycerol- or ribitol-phosphate repeats.[33] In WTAs, the Man*N*Ac/Glc*N*Ac is linked to the Mur*N*Ac residues of the glycan chain of PG by a phosphodiester bond.[34] In LTAs, a lipid anchors the TA to the cell membrane and the lipid anchor is another example of a species-specific variable region in the molecule.[34]

The cell walls of Gram-positive bacteria, not unlike the OMs of Gram-negative bacteria, also contain surface proteins. The surface proteins present in the wall are transported out of the cell by secretory systems such as the Sec or TAT pathways.[35,36] Following secretion, surface proteins are attached either to the IM by way of lipid anchors/transmembrane domains, or to the PG/TAs that make up the cell wall.[37]

4 | PG SYNTHESIS

4.1 | Cytosolic pathway

The cytosolic reactions of PG synthesis are undertaken chiefly by a family of ligases designated "Mur" (MurA, MurB, etc.); these enzymes are involved in the production of the PG precursor, Lipid II, in the inner leaflet of the IM.[38] The first step in the cytosolic pathway of PG synthesis is undertaken by MurA, which catalyzes the production of uridine diphosphate (UDP)-Glc*N*Ac-enolpyruvate from phosphoenolpyruvate (PEP), and UDP-Glc*N*Ac.[39] The production of UDP-Glc*N*Ac-enolpyruvate is followed by its reduction into UDP-Mur*N*Ac, catalyzed by MurB.[40] Extension of UDP-Mur*N*Ac by sequential addition of the residues present in the stem peptide is taken on by the enzymes MurC-F to produce Park's nucleotide. In Gram-negative bacteria Park's nucleotide comprises UDP-Mur*N*Ac, *L*-alanine (*L*-Ala), *D*-glutamine (*D*-Gln), *meso*-diaminopimelic acid (*meso*-A_2pm), *D*-alanine (*D*-Ala), *D*-Ala. Park's nucleotide is attached to undecaprenyl (C_{55}) diphosphate by MraY, resulting in a lipid PG precursor referred to as Lipid I.[41] The final cytoplasmic enzymatic step involves the formation of the β-1 → 4 glycosidic bond of Mur*N*Ac with Glc*N*Ac via a glycosyltransferase (MurG) to produce Lipid II,[42] which is then flipped to the outside of the membrane of the cell by a flippase.[43] The structure of each of the Mur enzymes from at least one species of bacteria have now been solved,[38] a process that started with the structure of MurA in 1996.[44] The structure of MurA was solved in complex with both its substrate UDP-Glc*N*Ac and the antibiotic fosfomycin,[44] revealing both the mechanism of action[45] and the mode of inhibition of MurA. Similar studies have been carried out on the remainder of the Mur enzymes in this pathway (Figure 3), lending the entire cytoplasmic pathway of the process to rational drug design.[38,46]

4.2 | The elusive flippase

The identity of the flippase responsible for the transfer of Lipid II across the cell membrane has recently been a subject of some debate. Three major candidates for the flippase were initially proposed, FtsW, RodA, and MurJ.[47–49] All three

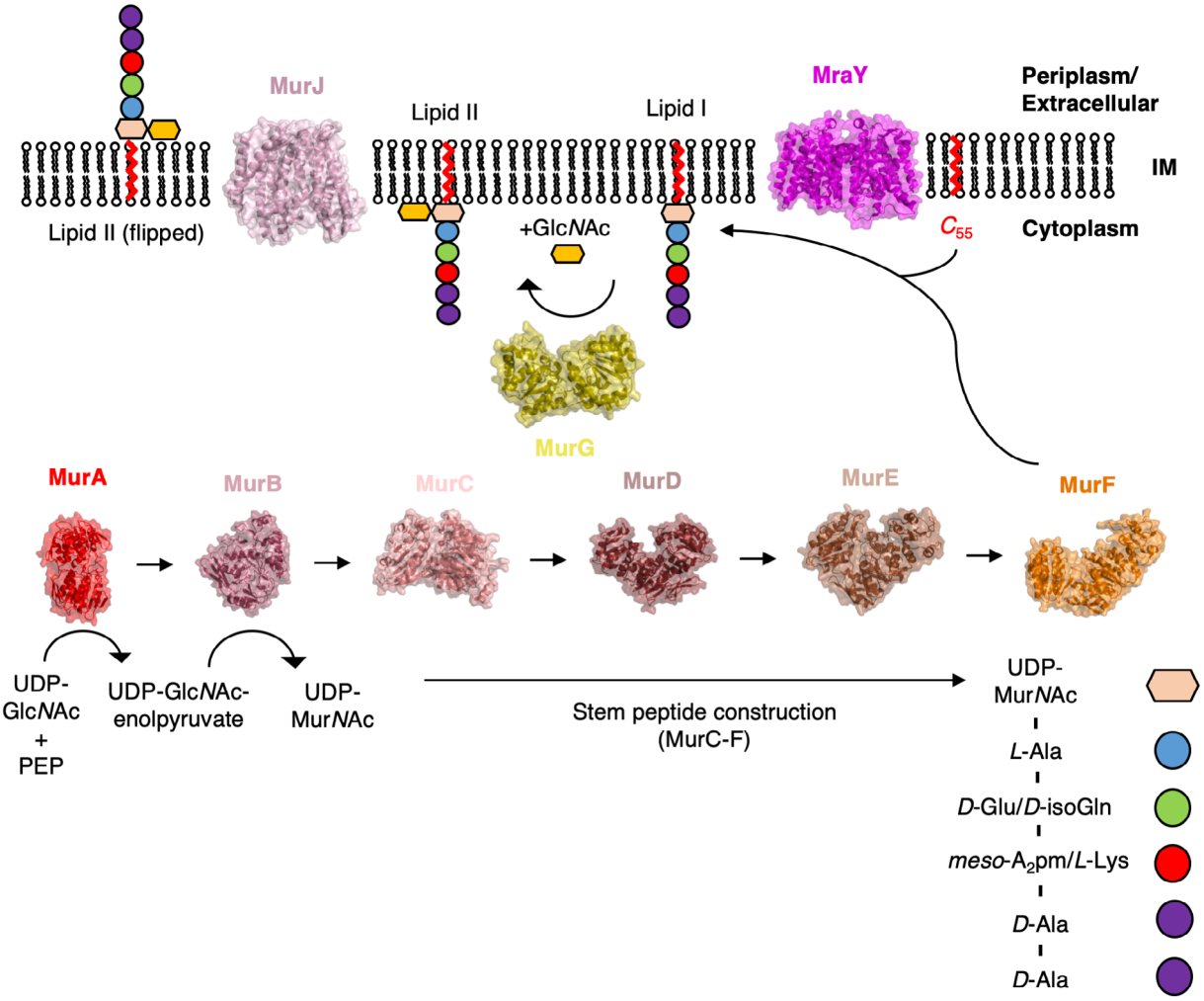

FIGURE 3 A structural overview of Lipid II construction. The structure of every enzyme involved in the cytoplasmic pathway of Lipid II synthesis has now been determined by X-ray crystallographic techniques. Here, the structures of every enzyme involved in Lipid II synthesis are displayed alongside the reaction(s) they are responsible for catalyzing on either face of the cell membrane (IM). For the sake of consistency, the structures shown here are those derived from *E. coli*

proteins are integral membrane proteins, with 10 (FtsW/RodA) and 14 (MurJ) predicted transmembrane domains. All three proteins are highly conserved and essential[50] for growth in both Gram-positive and Gram-negative bacteria, which would suggest that they do not play redundant roles in the cell. The first studies that appeared to observe FtsW as the Lipid II flippase were in vitro experiments in which the ability of *E. coli* FtsW to flip fluorescently Lipid II was measured using model membranes/liposomes.[47] These initial experiments suggested that FtsW was indeed capable of flipping Lipid II whereas, under the same conditions, MurJ was not.[47] Follow-up experiments worked to identify the region of the protein responsible for the flippase activity by removing transmembrane domains of FtsW and performing the same fluorescence-based flipping assays, with concomitant microscopy experiments on *E. coli* cells harboring the same FtsW mutants.[51] The in vitro and in vivo experiments performed in this study suggested that FtsW likely acted through a pore-like mechanism.[51] MurJ was proposed as an alternative Lipid II flippase in *E. coli* through a combination of a bioinformatics approach coupled with in vivo genetic analyses.[52] Mutational studies of *E. coli* harboring MurJ mutations revealed an accumulation of intracellular PG precursors,[53] suggesting an inability to flip Lipid II. More recent work now suggests that both FtsW and RodA function as PG polymerases,[32,54,55] swaying the flippase argument toward MurJ as the Lipid II flippase. Aided by recent advancements in membrane protein crystallographic techniques,[56] the crystal structure of MurJ from the extremophile *Thermosipho africanus* was solved in an inward conformation, allowing for the generation of an alternative access model of Lipid II flipping based on a combination of in silico docking and in vivo experiments.[57] Subsequently, the structure of MurJ in several different conformations was solved, allowing for modelling of the mechanism of Lipid II

flipping.[58] The structure of MurJ from *E. coli* has also since been solved, and high-throughput mutagenesis performed, leading to the identification of sites for potential inhibitor development.[59]

4.3 | Extracellular pathway

The extracellular members of the PG synthesis pathway are membrane-associated penicillin-binding proteins (PBPs), named for their affinity for penicillin. The PBPs are responsible for the polymerization of the growing glycan chain, and/or for linking the peptide chains extruding from the glycan backbone; these are glycosyltransferase and transpeptidase activities, respectively.[60] Some PBPs also have carboxypeptidase activity; these are responsible for the trimming of the peptide stem as a mechanism of regulating the number of cross-links formed in the cell wall and are responsible for cell shape maintenance in *E. coli*.[7,61] PBPs can be separated into two groups, those that solely have transpeptidase activity (Class B PBPs), or bifunctional PBPs that possess both activities (Class A PBPs). Some examples of bifunctional PBPs include PBP1a, b, and c in *E. coli*; PBP1, 2c, and 4 in *B. subtilis*; and PBP1a, 2a, and 1b in *S. pneumonia*.[62–64] Glycosyltransferases act early in the extracellular pathway to catalyze the polymerization of the non-lipid region of Lipid II into the nascent glycan chain,[60,64] while downstream transpeptidases are responsible for the linking of the *D*-Ala residues of the extruding peptide chain to form the strong and stable PG mesh.[60,64] The transpeptidase forms an acyl-enzyme intermediate with the *D*-Ala residue of the acceptor peptide, before being cross-linked to the donor peptide via an amino group, which in Gram-positive organisms is glycine or lysine.[4,65] Structural studies of PBPs have been performed extensively in several Gram-negative and Gram-positive species of bacteria, and their activities and inhibition by antibiotics have been reviewed excellently elsewhere.[6,60,64,66,67]

4.4 | Differences between PG from Gram-negative and Gram-positive bacteria

As well as the obvious differences in thickness of the PG layer and associated macromolecules (TAs/surface proteins) described above, there are further subtle nuances to the precise chemical make-up of the PG from Gram-positive and Gram-negative bacteria. Chemical differences of the glycan chain between Gram-negative and Gram-positive species include variations in modifications such as glycosylation, phosphorylation, and deacetylation.[68] In contrast to the lack of chemical diversity in the glycan chain, differences in the peptide stems of PG between Gram-negative and Gram-positive bacteria are far more common.[68] The majority of peptide stems in the PG of Gram-negative bacteria follows the pattern *L*-Ala, *D*-glutamate (*D*-Glu), *meso*-A_2pm, followed by two *D*-Ala residues. In Gram-positive bacteria, however, the residues present in the stem peptide vary at positions 2 and 3, at which *D-iso*glutamine (*D-iso*Gln) and *L*-lysine (*L*-Lys) are prevalent, respectively.[68] In both Gram-positive and Gram-negative bacteria, *D*-Glu is initially added to the growing peptide stem by MurD at position 2 during construction of the peptide stem.[4,6] In those Gram-positive species where *D-iso*Gln is found at Position 2, *D*-Glu is enzymatically deamidated to *D-iso*Gln by an enzyme complex of MurT/GatD.[69] The structure of the MurT/GatD complex has been solved recently, revealing the mechanism of PG amidation by MurT, and also the mechanism through which GatD produces and channels the ammonia required for PG amidation to the MurT active site.[70]

5 | COORDINATION OF CELL WALL SYNTHESIS WITH CELL DIVISION

5.1 | The divisome

The collection of ~20–30 proteins responsible for regulating cell division has come to be known as the "divisome" (Figure 4). Proteins in the divisome ensure that one round of division occurs at a time, with one copy of the chromosome present in each cell, that cell wall synthesis is undertaken appropriately to circumvent lysis during septum formation, and that cell separation occurs through the function of cell wall hydrolases (autolysins).[7] Investigation of the divisome has chiefly been undertaken in rod-shaped bacteria, yet there is still a lot to learn about divisome formation and organization in these bacteria as well as in other bacteria with different shapes, such as the spherical cocci. Some archaea with profound differences in morphology and cell division, such as the triangular *Haloferax volcanii* which divides by a process of ternary fission, also utilize some of the same proteins as in bacteria when regulating division.[71] The divisome is an attractive target for the generation of novel antimicrobials, as disruption of the machinery responsible for organizing cell division would ultimately result in a reduction and cessation of propagation. A lack of structural and functional information about lesser studied components of the divisome, and the divisome itself as a dynamic molecular machine, presents a stumbling block in the antimicrobial pipeline and is thus a potentially lucrative area of research. The function of the divisome to coordinate chromosome replication and segregation with cytokinesis is common to both Gram-negative and Gram-positive organisms, but the precise constituents of the divisome vary across species.[72]

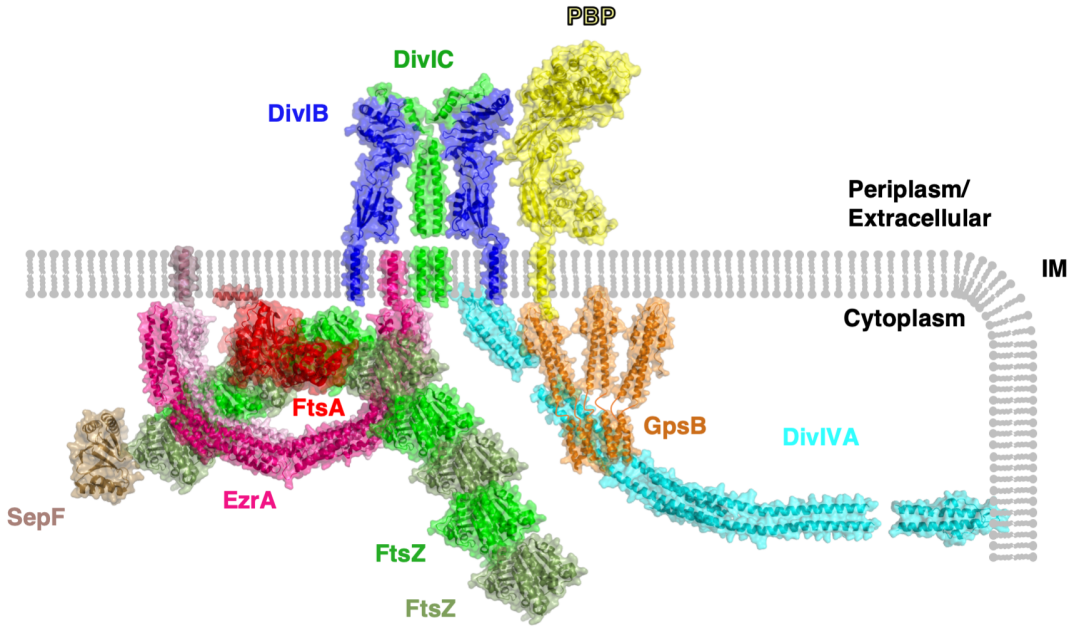

FIGURE 4 Structural model of the divisome. A selection of divisome proteins for which atomic structures have been determined are shown in context of the cell membrane (IM). Where structural data regarding protein–protein interactions are known, this figure reflects this information. Where available, structures have been taken from the model organism *B. subtilis*; however, in the cases where there is a lack of structural data from this organism, the structures with the greatest degree of sequence homology are shown. FtsZ is colored alternately in shades of green to denote filament formation, FtsA is shown in red, an antiparallel EzrA dimer is colored in shades of pink, SepF is shown in sand (note that the membrane-anchoring region of SepF was not resolved in its crystal structure analysis), a 2:2 complex of DivIB and DivIC is shown in blue and green, respectively, a GpsB hexamer is shown in orange, a representative class B PBP is shown in yellow and DivIVA in cyan

5.2 | The Z-ring

The best studied of the divisome proteins is FtsZ, and it is arguably the central protein to the function of the divisome in cell division. FtsZ, named after its mutants' abilities to cause *E. coli* cells to divide in a filamentous fashion at nonpermissive temperatures (*f*ilamentous *t*emperature *s*ensitive),[73] is a cytosolic protein known to accumulate at the site of division across all bacterial species.[74,75] The discovery of FtsZ set the groundwork for much of the research conducted on the divisome in the past ~25 years. The crystal structure of FtsZ provided the first definitive evidence of a bacterial cytoskeleton, as FtsZ is a clear structural homolog of tubulin despite sharing no significant amino acid sequence homology.[76] FtsZ polymerizes into filaments in a GTP-dependent manner rapidly "treadmilling"[77] in an agile and nimble ring-like structure, dubbed the "Z-ring," adjacent to the cytoplasmic face of the membrane. Prior to the observation of the treadmilling of FtsZ, the Z-ring was thought to represent a semicontinuous ring at the mid-cell which constricted during septum formation.[74,75] There are several molecular mechanisms that govern the placement of the Z-ring, for instance, the Min system functions in an inhibitory manner, preventing formation of the Z-ring away from midcell,[12] while Zap proteins function in a stimulatory manner, encouraging the formation of lateral interactions between filaments of FtsZ.[12,78] FtsZ acts as a scaffold onto which protein–protein interactions with other members of the divisome come together to stimulate division (Figure 4). A well-studied protein–protein interaction of FtsZ is with FtsA, a well-conserved "early" divisome component, which self-organizes with FtsZ and tethers it to the membrane.[79] The FtsA-mediated membrane tethering is essential to ensure constriction of the membrane at the septum, as FtsZ does not interact with the membrane of its own accord. ZipA works alongside FtsA in Gram-negative bacteria to tether FtsZ to the membrane[80]; however, no such homolog is present in Gram-positive bacteria, instead, SepF has been proposed to fulfil a similar function.[81] The combination of the polymerized FtsZ, along with SepF/ZipA and FtsA forms a structure called the proto-ring.[82]

5.3 | Recruitment of downstream proteins to the divisome

Following the formation of the proto-ring, the "late" division proteins start to assemble to promote downstream processes involved in the remodeling of the cell wall. Divisome assembly has perhaps been studied most extensively in *E. coli*; the proteins known to accumulate are FtsN, FtsI, FtsEX, FtsQ, FtsL, FtsB, FtsW, FtsK, and PBP2B.[83] However, the conservation of many of these components is not necessarily

maintained in Gram-positive bacteria, and the essentiality of the components is also not strictly conserved. One example of a widely conserved and essential subcomponent of the divisome is a trimeric complex of DivIB, DivIC, and FtsL in Gram-positives (FtsQ, FtsB, and FtsL in Gram-negatives, respectively). DivIB/FtsQ, DivIC/FtsB, and FtsL are transmembrane proteins, each with a single transmembrane helix, and form a complex independent of other divisome proteins in *E. coli* and *B. subtilis*.[84,85] DivIB/FtsQ interacts with PG through its extracellular PASTA domain and is required as a cell division checkpoint based on studies in *S. aureus*.[86] The extracellular portion of DivIB/FtsQ is also known to interact with PBPs, such as PBP2b in *B. subtilis*.[87] It appears that the DivIB/DivIC/FtsL (FtsQ/FtsB/FtsL) complex links the early intracellular stages of cell division with PG remodeling, which is predominantly an extracellular process.[88] The structure of *E. coli* FtsQ in complex with a fragment of FtsB has recently been solved.[89] Based on the essentiality of the interaction between FtsQ/DivIB with FtsB/DivIC, and their location of interaction on the outside surface of the cell, the structure of the complex should allow for the considered design of antibiotics, without a need to consider cell membrane traversal.

6 | REGULATORS OF CELL DIVISION AND PG REMODELLING

DivIVA is a member of the Gram-positive divisome with divergent roles in those bacteria that encode DivIVA orthologs. One feature common to all DivIVA homologs, however, is an apparent innate ability to sense membrane curvature.[90] The bulk of the published information about DivIVA comes from studies in *B. subtilis* where, among other things, it functions as a topological marker for the Min system,[12] a cell division inhibitor. X-ray crystallographic studies of the isolated N- and C-terminal domains of DivIVA revealed that it formed tetramers made up of an antiparallel arrangement of parallel coiled-coils.[91] This model clashes somewhat with earlier EM studies suggesting that DivIVA forms higher order oligomers; however, these studies were performed on mutants of DivIVA purposefully designed to alter oligomeric state and may not accurately represent the wild-type protein.[92] The crystal structure of the N-terminal domain of DivIVA also provided some insight into how membrane binding might be possible; a conserved Phe-Arg motif oriented outwards from the protein is positioned to form hydrophobic and electrostatic interactions with the membrane, respectively.[91] Since DivIVA interacts with several cytoplasmic proteins through its C-terminal domain, it may act somewhat promiscuously as a topological marker for several intracellular systems.[93] The situation is complicated as a result of DivIVA's divergent roles, for instance, *S. aureus* lacks MinC/D, and the interactions of DivIVA with divisome components in *S. aureus* have yet to be elucidated fully.

GpsB, a homolog of DivIVA present in Gram-positive organisms, is also involved in the coordination of PG synthesis at the septum. GpsB and DivIVA share sequence and structural homology at their N-termini; however, this homology between the two proteins decreases significantly in their C-terminal regions. The difference in C-terminal structure between the two proteins is responsible for the differences in oligomeric state between the two proteins.[91,94] Integrative structural and biochemical studies on GpsB from *Listeria monocytogenes* and *B. subtilis* revealed that GpsB binds the cytoplasmic microdomains of PBPs and forms a hexamer in solution, allowing for the generation of a model through which GpsB likely coordinates the activities of PBPs.[94,95] Interactions between GpsB and PBPs from a wider range of Gram-positive bacteria including *B. subtilis*, *L. monocytogenes*, and *S. pneumoniae* have since been interrogated structurally and biochemically, leading to the identification of motifs required for binding.[96] A greater mechanistic understanding of the interactions between GpsB and PBP homologs in various species has aided the identification of novel interactions between GpsB and the PG remodeling enzymes YpbE and YrrS, leading to the conclusion that GpsB acts as an adaptor protein.[96] Recent work on GpsB from *S. aureus* suggests a novel action of GpsB in the stimulation of lateral interactions between FtsZ filaments.[97] No interactions between FtsZ and GpsB have been detected in any other species of bacteria tested; therefore, this finding would suggest a divergent role for GpsB in *S. aureus*.[97]

Negative regulation is also necessary in order to prevent aberrant Z-ring formation; EzrA is an example of such a negative regulator in Gram-positive bacteria. EzrA was first identified in *B. subtilis*, and its colocalization with FtsZ first observed by fluorescence microscopy.[98] EzrA has a predicted TM helix at its N-terminus to link it, and potentially its interaction partners, to the membrane. *B. subtilis* EzrA inhibits the formation of FtsZ filaments in vitro and in vivo, and complete deletion of EzrA results in an increased frequency of FtsZ ring formation.[98–100] Recent studies in *S. aureus* and *B. subtilis* have implicated EzrA in the control of PG synthesis through direct interactions with PG synthases.[101,102] EzrA has been found by bacterial two-hybrid to interact with a multitude of divisome proteins in *S. aureus*, as well as the PG synthases PBP1, 2, and 3.[102] The crystal structure of EzrA from *B. subtilis* revealed that EzrA forms antiparallel dimers forming an overall crescent shape, with each monomer made up of repeating three-helical bundles that have structural homology to the spectrin repeat fold found in eukaryotic cytoskeletal proteins.[103] The space within the arch of the crescent is

sufficient to enclose an FtsZ filament, to sterically hinder the formation of lateral interactions between filaments.[103,104]

As stated above, ZipA is involved in the regulation of divisome assembly and Z-ring placement in Gram-negative bacteria.[105] ZipA has been studied most extensively in *E. coli*, where it is essential.[106] ZipA is predominantly cytoplasmic, with a single transmembrane helix and a microdomain in the periplasm. ZipA binds to FtsZ and tethers it to the cell membrane as well as FtsA.[80] The functional significance of ZipA was brought into question by a gain of function mutant of FtsA which allowed for the bypassing of ZipA[107]; however, more recent studies have suggested that ZipA functions by protecting FtsZ from degradation by cytoplasmic proteases, a role that cannot be substituted for by FtsA.[108] The stimulatory or inhibitory effects of ZipA on Z-ring formation and FtsZ bundling are currently unknown; while early studies on ZipA provided contradictory evidence for stimulatory[109] and inhibitory[79] roles of ZipA, more recent work suggests that ZipA has neither a stimulatory nor an inhibitory effect on lateral interactions between FtsZ filaments, and that it simply acts as a passive membrane tether for FtsZ.[105] More work is clearly required to elucidate the functional significance of ZipA for divisome formation in Gram-negative bacteria.

7 | ANTIBIOTICS TARGETING THE CELL DIVISION/PG SYNTHESIS MACHINERY

Beta-lactam antibiotics inhibit the transpeptidase action of PBPs by mimicking the structure of the terminal *D*-Ala-*D*-Ala residues of the glycan-attached peptide of PG, sequestering the active site serine in a covalent adduct and rendering the transpeptidase domain of the PBPs inactive.[110] The inhibition of the cell wall synthesis machinery ultimately results in the lysis of the cell due to the inability of the bacteria to generate new cell wall material to replace the parts it has degraded; this is the major cause of cell death by beta-lactam antibiotics.[110] Secondary mechanisms of cell death have also been observed, however, in which nonlytic cells undergo cell death as a result of futile cycles of PG precursor synthesis, for instance.[111] The introduction of beta-lactams ushered in a golden age of antibiotics, during which many diseases previously fatal became treatable. The overuse of antibiotics, combined with the short life cycle and rapid evolution of bacteria, has resulted in the generation of antibiotic-resistant strains of bacteria which, in certain clinical scenarios, often have fatal consequences.[3] PG homeostasis and regulation thus remain an attractive target for antibiotic drug design.

Two major mechanisms of resistance to beta-lactams have arisen: first, an accumulation of mutations in PBPs renders them insensitive to beta-lactams and second, enzymes capable of degrading beta-lactams, the beta-lactamases, have evolved. For instance, methicillin resistance in methicillin-resistant *S. aureus* (MRSA) is caused by the introduction of the *mecA* gene coding for PBP2a, where the active site serine is located in a pocket that is occluded from beta-lactams.[112] A multitude of new PBP2a-targetting antibiotics have been developed, including the cephalosporin subgroup of beta-lactams, ceftobiprole, and ceftaroline.[113] These molecules appear to target both the PBP2a active site as well as a putative allosteric site,[114,115] but resistance to these new drugs has already emerged.[112] Beta-lactam resistance is also caused by the evolution of new beta-lactamases, which form acyl-enzyme intermediates with beta-lactams as in PBPs; however, these enzymes can break open the beta-lactam ring to form products that do not inhibit PBPs.[116] Beta-lactamases were present in bacteria prior to the use of antibiotics in clinical and agricultural scenarios, but they have evolved into a very efficient beta-lactam resistance mechanism thanks to increased selection pressure from antibiotic overuse by mankind.[117,118] The somewhat unfortunately named New-Delhi metallo-beta-lactamases (NDMs) are one such example of this type of evolution; NDMs were first isolated and identified from a patient with a *Klebsiella pneumoniae* infection in 2009[119] and have since become a cause of global concern.[120] Novel antibiotics targeting NDMs are now necessary to combat the rise of superbugs which harbor these enzymes, and excellent progress is being made toward this end.[121]

The gap between antibiotic drug discovery and the development of antimicrobial resistance is becoming shorter with each iteration. In fact, the first report of penicillin resistance in *E. coli* appeared in 1940 *before* penicillin was in general public use.[122] Alternative means of disrupting cell division to fight infection are, therefore, an attractive method of sidestepping this problem and there is potential for divisome components to provide the necessary novel target. Inhibitors of divisome components have shown promising preliminary results against bacterial infections, specifically in the case of FtsZ. An inhibitor of FtsZ, PC190723, causes cell elongation in *B. subtilis*, and cell enlargement in *S. aureus*, and is effective against MRSA strains.[123] Computational ligand docking of PC190723 has identified a potential site of action at an allosteric site away from the nucleotide binding region of FtsZ.[124,125] This is the first viable mechanism found for alternative antibiotics targeting the divisome, but with the influx of structures becoming available for several divisome components, there is much promise for antibiotics targeting cell division to be developed to take back control from the march of infectious disease.

8 | CONCLUSION

Here, we have shown a brief overview of the complexities of the cell envelopes of Gram-negative and Gram-positive

bacteria. Although much progress has been made in the last decade or so in some areas, such as the atomic detail of PG synthesis, there is still much work to be done. Focus now should be turned to the molecular nuances of envelope modification during division and how environmental factors influence cell division and PG synthesis. From a translational standpoint, a lack of structural and functional information about lesser studied members of the divisome presents a stumbling block in the antimicrobial pipeline and is thus a potentially lucrative area of research.

ACKNOWLEDGMENTS

Research in the Lewis laboratory has been funded by Newcastle University in a studentship to S.B., the UK BBSRC and MRC, and the European Commission.

ORCID

Simon Booth https://orcid.org/0000-0001-5585-022X
Richard J. Lewis https://orcid.org/0000-0003-2641-8643

REFERENCES

1. Nikaido H. Outer membrane, Gram-negative bacteria. Encyclopedia of microbiology. 3rd ed. Academic Press, Cambridge Mass. USA, 2009; p. 439–452.
2. Silhavy TJ, Kahne D, Walker S. The bacterial cell envelope. Cold Spring Harb Perspect Biol. 2010;2:1–16.
3. Lobanovska M, Pilla G. Penicillin's discovery and antibiotic resistance: Lessons for the future? Yale J Biol Med. 2017;90: 135–145.
4. Vollmer W, Blanot D, De Pedro MA. Peptidoglycan structure and architecture. FEMS Microbiol Rev. 2008;32:149–167.
5. Turner RD, Vollmer W, Foster SJ. Different walls for rods and balls: The diversity of peptidoglycan. Mol Microbiol. 2014;91: 862–874.
6. Lovering AL, Safadi SS, Strynadka NCJ. Structural perspective of peptidoglycan biosynthesis and assembly. Annu Rev Biochem. 2012;81:451–478.
7. Egan AJF, Vollmer W. The physiology of bacterial cell division. Ann N Y Acad Sci. 2013;1277:8–28.
8. Lutkenhaus J. The regulation of bacterial cell division: A time and place for it. Curr Opin Microbiol. 1998;1:210–215.
9. Turner RD, Ratcliffe EC, Wheeler R, Golestanian R, Hobbs JK, Foster SJ. Peptidoglycan architecture can specify division planes in *Staphylococcus aureus*. Nat Commun. 2010;1:26.
10. Garcia PS, Simorre JP, Brochier-Armanet C, Grangeasse C. Cell division of *Streptococcus pneumoniae*: Think positive! Curr Opin Microbiol. 2016;34:18–23.
11. Männik J, Wu F, Hol FJH, et al. Robustness and accuracy of cell division in *Escherichia coli* in diverse cell shapes. Proc Natl Acad Sci U S A. 2012;109:6957–6962.
12. Rowlett VW, Margolin W. The bacterial Min system. Curr Biol. 2013;23:R553–R556.
13. Wu LJ, Errington J. Nucleoid occlusion and bacterial cell division. Nat Rev Microbiol. 2012;10:8–12.
14. Rowlett VW, Margolin W. The Min system and other nucleoid-independent regulators of Z ring positioning. Front Microbiol. 2015;6:478.
15. Adams DW, Wu LJ, Errington J. Cell cycle regulation by the bacterial nucleoid. Curr Opin Microbiol. 2014;22:94–101.
16. Rollauer SE, Sooreshjani MA, Noinaj N, Buchanan SK. Outer membrane protein biogenesis in Gram-negative bacteria. Philos Trans R Soc B Biol Sci. 2015;370:20150023.
17. Ruiz N, Kahne D, Silhavy TJ. Advances in understanding bacterial outer-membrane biogenesis. Nat Rev Microbiol. 2006;4: 57–66.
18. Achouak W. Multiple facets of bacterial porins. FEMS Microbiol Lett. 2001;199:1–7.
19. Cowan SW, Garavito RM, Jansonius JN, et al. The structure of OmpF porin in a tetragonal crystal form. Structure. 1995;3: 1041–1050.
20. Weiss MS, Schulz GE. Structure of porin refined at 1.8 Å resolution. J Mol Biol. 1992;227:493–509.
21. Glenwright AJ, Pothula KR, Bhamidimarri SP, et al. Structural basis for nutrient acquisition by dominant members of the human gut microbiota. Nature. 2017;541:407–411.
22. Egan AJF. Bacterial outer membrane constriction. Mol Microbiol. 2018;107:676–687.
23. Gray AN, Egan AJ, Van't Veer IL, et al. Coordination of peptidoglycan synthesis and outer membrane constriction during *Escherichia coli* cell division. Elife. 2015;4:e07118.
24. Vollmer W, Massidda O, Tomasz A. The cell wall of *Streptococcus pneumoniae*. Microbiol Spectr. 2019;7:1–25.
25. Brown S, Santa Maria JP, Walker S. Wall teichoic acids of Gram-positive bacteria. Annu Rev Microbiol. 2013;67:313–336.
26. Percy MG, Gründling A. Lipoteichoic acid synthesis and function in Gram-positive bacteria. Annu Rev Microbiol. 2014;68: 81–100.
27. Formstone A, Carballido-Lopez R, Noirot P, Errington J, Scheffers DJ. Localization and interactions of teichoic acid synthetic enzymes in *Bacillus subtilis*. J Bacteriol. 2008;190: 1812–1821.
28. Rausch M, Deisinger JP, Ulm H, et al. Coordination of capsule assembly and cell wall biosynthesis in *Staphylococcus aureus*. Nat Commun. 2019;10:1404.
29. Wanner S, Schade J, Keinhörster D, et al. Wall teichoic acids mediate increased virulence in *Staphylococcus aureus*. Nat Microbiol. 2017;2:16257.
30. Swoboda JG, Meredith TC, Campbell J, et al. Discovery of a small molecule that blocks wall teichoic acid biosynthesis in *Staphylococcus aureus*. ACS Chem Biol. 2010;4:875–883.
31. Farha MA, Leung A, Sewell EW, et al. Inhibition of WTA synthesis blocks the cooperative action of PBPs and sensitizes MRSA to β-lactams. ACS Chem Biol. 2013;8:226–233.
32. Meeske AJ, Riley EP, Robins WP, et al. SEDS proteins are a widespread family of bacterial cell wall polymerases. Nature. 2016;537:634–638.
33. Sanderson AR, Strominger JL, Nathenson SG, Sanderson R. Chemical structure of teichoic acid from chemical structure of teichoic acid from *Staphylococcus aureus*, strain Copenhagen. J Biol Chem. 1962;237:3603–3613.

34. Neuhaus FC, Baddiley JA. A continuum of anionic charge: Structures and functions of D-alanyl-teichoic acids in Gram-positive bacteria. Microbiol Mol Biol Rev. 2003;67:686–723.
35. Tsirigotaki A, De Geyter J, Šoštaric N, Economou A, Karamanou S. Protein export through the bacterial Sec pathway. Nat Rev Microbiol. 2017;15:21–36.
36. Palmer T, Berks BC. The twin-arginine translocation (Tat) protein export pathway. Nat Rev Microbiol. 2015;10:483–496.
37. Scott JR, Barnett TC. Surface proteins of Gram-positive bacteria and how they get there. Annu Rev Microbiol. 2006;60:397–423.
38. El Zoeiby A, Sanschagrin F, Levesque RC. Structure and function of the Mur enzymes: Development of novel inhibitors. Mol Microbiol. 2002;47:1–12.
39. Brown ED, Vivas EI, Walsh CT, Kolter R. MurA (MurZ), the enzyme that catalyzes the first committed step in peptidoglycan biosynthesis, is essential in *Escherichia coli*. J Bacteriol. 1995;177:4194–4197.
40. Sylvester DR, Alvarez E, Patel A, Ratnam K, Kallender H, Wallis NG. Identification and characterization of UDP-N-acetylenolpyruvylglucosamine reductase (MurB) from the Gram-positive pathogen *Streptococcus pneumoniae*. Biochem J. 2001; 355:431–435.
41. Van Nieuwenhze MS, Mauldin SC, Zia-Ebrahimi M, Aikins JA, Blaszczak LC. The total synthesis of lipid I. J Am Chem Soc. 2001;123:6983–6988.
42. de Kruijff B, van Dam V, Breukink E. Lipid II: A central component in bacterial cell wall synthesis and a target for antibiotics. Prostag Leukotr Ess Fat Acids. 2008;79:117–121.
43. Ruiz N. Lipid flippases for bacterial peptidoglycan biosynthesis. Lipid Insights. 2016;8:21–31.
44. Skarzynski T, Mistry A, Wonacott A, Hutchinson SE, Kelly VA, Duncan K. Structure of UDP-*N*-acetylglucosamine enolpyruvyl transferase, an enzyme essential for the synthesis of bacterial peptidoglycan, complexed with substrate UDP-*N*-acetylglucosamine and the drug fosfomycin. Structure. 1996;4:1465–1474.
45. Eschenburg S, Kabsch W, Healy ML, Schönbrunn E. A new view of the mechanisms of UDP-*N*-acetylglucosamine enolpyruvyl transferase (MurA) and 5-enolpyruvylshikimate-3-phosphate synthase (AroA) derived from X-ray structures of their tetrahedral reaction intermediate states. J Biol Chem. 2003;278:49215–49222.
46. Hrast M, Sosič I, Šink R, Gobec S. Inhibitors of the peptidoglycan biosynthesis enzymes MurA-F. Bioorg Chem. 2014;55:2–15.
47. Mohammadi T, van Dam V, Sijbrandi R, et al. Identification of FtsW as a transporter of lipid-linked cell wall precursors across the membrane. EMBO J. 2011;30:1425–1432.
48. Sham LT, Butler EK, Lebar MD, Kahne D, Bernhardt TG, Ruiz N. MurJ is the flippase of lipid-linked precursors for peptidoglycan biogenesis. Science. 2014;345:220–222.
49. Sieger B, Schubert K, Donovan C, Bramkamp M. The lipid II flippase RodA determines morphology and growth in *Corynebacterium glutamicum*. Mol Microbiol. 2013;90:966–982.
50. Boyle DS, Khattar MM, Addinall SG, Lutkenhaus J, Donachie WD. *ftsW* is an essential cell-division gene in *Escherichia coli*. Mol Microbiol. 1997;24:1263–1273.
51. Mohammadi T, Sijbrandi R, Lutters M, et al. Specificity of the transport of lipid II by FtsW in *Escherichia coli*. J Biol Chem. 2014;289:14707–14718.
52. Ruiz N. Bioinformatics identification of MurJ (MviN) as the peptidoglycan lipid II flippase in *Escherichia coli*. Proc Natl Acad Sci U S A. 2008;105:15553–15557.
53. Inoue A, Murata Y, Takahashi H, Tsuji N, Fujisaki S, Kato J. Involvement of an essential gene, *MviN*, in murein synthesis in *Escherichia coli*. J Bacteriol. 2008;190:7298–7301.
54. Taguchi A, Welsh MA, Marmont LS, et al. FtsW is a peptidoglycan polymerase that is functional only in complex with its cognate penicillin-binding protein. Nat Microbiol. 2019;4:587–594.
55. Emami K, Guyet A, Kawai Y, et al. RodA as the missing glycosyltransferase in *Bacillus subtilis* and antibiotic discovery for the peptidoglycan polymerase pathway. Nat Microbiol. 2017; 2:16253.
56. Caffrey M. Crystallizing membrane proteins for structure-function studies using lipidic mesophases. Biochem Soc Trans. 2011;39:725–732.
57. Kuk ACY, Mashalidis EH, Lee SY. Crystal structure of the MOP flippase MurJ in an inward-facing conformation. Nat Struct Mol Biol. 2017;24:24171–24176.
58. Kuk ACY, Hao A, Guan Z, Lee SY. Visualizing conformation transitions of the lipid II flippase MurJ. Nat Commun. 2019;10: 1736.
59. Zheng S, Sham LT, Rubino FA, et al. Structure and mutagenic analysis of the lipid II flippase MurJ from *Escherichia coli*. Proc Natl Acad Sci U S A. 2018;115:6709–6714.
60. Egan AJF, Biboy J, van't Veer I, Breukink E, Vollmer W. Activities and regulation of peptidoglycan synthases. Philos Trans R Soc B Biol Sci. 2015;370:20150031.
61. Peters K, Kannan S, Rao VA, et al. The redundancy of peptidoglycan carboxypeptidases ensures robust cell shape maintenance in *Escherichia coli*. MBio. 2016;7:e00819–e00816.
62. Marie A, Guilmi D, Dideberg O, Vernet T. Functional characterization of penicillin-binding protein 1b from *Streptococcus pneumoniae*. J Bacteriol. 2003;185:1650–1658.
63. Marie A, Guilmi D, Dessen A, Dideberg O, Vernet T. Bifunctional penicillin-binding proteins: Focus on the glycosyltransferase domain and its specific inhibitor moenomycin. Curr Pharm Biotechnol. 2010;3:63–75.
64. Sauvage E, Kerff F, Terrak M, Ayala JA, Charlier P. The penicillin-binding proteins: Structure and role in peptidoglycan biosynthesis. FEMS Microbiol Rev. 2008;32:234–258.
65. Kim SJ, Chang J, Singh M. Peptidoglycan architecture of Gram-positive bacteria by solid-state NMR. Biochim Biophys Acta. 2015;1848:350–362.
66. Schneider T, Sahl HG. An oldie but a goodie—Cell wall biosynthesis as antibiotic target pathway. Int J Med Microbiol. 2010; 300:161–169.
67. Moon TM, D'Andréa ÉD, Lee CW, et al. The structures of penicillin binding protein 4 (PBP4) and PBP5 from *Enterococci* provide structural insights into β–lactam resistance. J Biol Chem. 2018;293:18574–18584.
68. Vollmer W. Structural variation in the glycan strands of bacterial peptidoglycan. FEMS Microbiol Rev. 2008;32:287–306.
69. Zapun A, Philippe J, Abrahams KA, et al. In vitro reconstitution of peptidoglycan assembly from the Gram-positive pathogen *Streptococcus pneumoniae*. ACS Chem Biol. 2013;8:2688–2696.
70. Morlot C, Straume D, Peters K, et al. Structure of the essential peptidoglycan amidotransferase MurT/GatD complex from *Streptococcus pneumoniae*. Nat Commun. 2018;9:3180.
71. Walsh JC, Angstmann CN, Bisson-Filho AW, Garner EC, Duggin IG, Curmi PMG. Division plane placement in pleomorphic

archaea is dynamically coupled to cell shape. Mol Microbiol. 2019;112:785–799. https://doi.org/10.1111/mmi.14316.
72. den Blaauwen T, Hamoen LW, Levin PA. The divisome at 25: The road ahead. Curr Opin Microbiol. 2017;36:85–94.
73. Lutkenhaus JF, Wolf-Watz H, Donachie WD. Organization of genes in the *ftsA-envA* region of the *Escherichia coli* genetic map and identification of a new *fts* locus (*ftsZ*). J Bacteriol. 1990;142: 615–620.
74. Erickson H. FtsZ, a tubulin homologue in prokaryote cell division. Trends Cell Biol. 1997;7:362–367.
75. Lutkenhaus J, Addinall SG. Bacterial cell division and the Z ring. Annu Rev Biochem. 1997;66:93–116.
76. Löwe J, Amos LA. Crystal structure of the bacterial cell-division protein FtsZ. Nature. 1998;391:203–206.
77. Bisson-Filho AW, Hsu YP, Squyres GR, et al. Treadmilling by FtsZ filaments drives peptidoglycan synthesis and bacterial cell division. Science. 2017;355:739–743.
78. Buss JA, Peters NT, Xiao J, Bernhardt TG. ZapA and ZapB form an FtsZ-independent structure at midcell. Mol Microbiol. 2017; 104:652–663.
79. Loose M, Mitchison TJ. The bacterial cell division proteins FtsA and FtsZ self-organize into dynamic cytoskeletal patterns. Nat Cell Biol. 2014;16:38–46.
80. Pazos M, Peters K, Casanova M, et al. Z-ring membrane anchors associate with cell wall synthases to initiate bacterial cell division. Nat Commun. 2018;9:5090.
81. Hamoen LW, Meile JC, de Jong W, Noirot P, Errington J. SepF, a novel FtsZ-interacting protein required for a late step in cell division. Mol Microbiol. 2006;59:989–999.
82. Rico AI, Krupka M, Vicente M. In the beginning, *Escherichia coli* assembled the proto-ring: An initial phase of division. J Biol Chem. 2013;288:20830–20836.
83. Haeusser DP, Margolin W. Splitsville: Structural and functional insights into the dynamic bacterial Z ring. Nat Rev Microbiol. 2016;14:305–319.
84. Robson SA, King GF. Domain architecture and structure of the bacterial cell division protein DivIB. Proc Natl Acad Sci U S A. 2006;103:6700–6705.
85. Buddelmeijer N, Beckwith J. A complex of the *Escherichia coli* cell division proteins FtsL, FtsB and FtsQ forms independently of its localization to the septal region. Mol Microbiol. 2004;52: 1315–1327.
86. Bottomley AL, Kabli AF, Hurd AF, Turner RD, Garcia-Lara J, Foster SJ. *Staphylococcus aureus* DivIB is a peptidoglycan-binding protein that is required for a morphological checkpoint in cell division. Mol Microbiol. 2014;94: 1041–1064.
87. Angeles DM, Macia-Valero A, Bororquez LC, Scheffers DJ. The PASTA domains of *Bacillus subtilis* PBP2B stabilize the interaction of PBP2B with DivIB. bioRxiv. 2019; https://doi.org/10.1101/713677.
88. Boes A, Olatunji S, Breukink E, Terrak M. Regulation of the peptidoglycan polymerase activity of PBP1b by antagonist actions of the core divisome proteins FtsBLQ and FtsN. MBio. 2019;10:e01912–e01918.
89. Kureisaite-Ciziene D, Kureisaite-Ciziene D, Varadajan A, et al. Structural analysis of the interaction between the bacterial cell division proteins FtsQ and FtsB. MBio. 2018;9: e01346–e01318.
90. Lenarcic R, Halbedel S, Visser L, et al. Localisation of DivIVA by targeting to negatively curved membranes. EMBO J. 2009;28: 2272–2282.
91. Oliva MA, Halbedel S, Freund SM, et al. Features critical for membrane binding revealed by DivIVA crystal structure. EMBO J. 2010;29:1988–2001.
92. Stahlberg H, Kutejová E, Muchová K, et al. Oligomeric structure of the *Bacillus subtilis* cell division protien DivIVA determined by transmission microscopy. Mol Microbiol. 2004; 52:1281–1290.
93. Halbedel S, Lewis RJ. Structural basis for interaction of DivIVA/GpsB proteins with their ligands. Mol Microbiol. 2019; 111:1404–1415.
94. Cleverley RM, Rismondo J, Lockhart-Cairns MP, et al. Subunit arrangement in GpsB, a regulator of cell wall biosynthesis. Microb Drug Resist. 2016;22:446–460.
95. Rismondo J, Cleverley RM, Lane HV, et al. Structure of the bacterial cell division determinant GpsB and its interaction with penicillin-binding proteins. Mol Microbiol. 2016;99:978–998.
96. Cleverley RM, Rutter ZJ, Rismondo J, et al. The cell cycle regulator GpsB functions as cytosolic adaptor for multiple cell wall enzymes. Nat Commun. 2019;10:261.
97. Eswara PJ, Brzozowski RS, Viola MG, et al. An essential *Staphylococcus aureus* cell division protein directly regulates FtsZ dynamics. Elife. 2018;7:e38856.
98. Levin PA, Kurtser IG, Grossman AD. Identification and characterization of a negative regulator of FtsZ ring formation in *Bacillus subtilis*. Proc Natl Acad Sci U S A. 1999;96:9642–9647.
99. Land AD, Luo Q, Levin PA. Functional domain analysis of the cell division inhibitor EzrA. PLoS One. 2014;9:e102616.
100. Singh JK, Makde RD, Kumar V, Panda D. A membrane protein, EzrA, regulates assembly dynamics of FtsZ by interacting with the C-terminal tail of FtsZ. Biochemistry. 2007;46:11013–11022.
101. Claessen D, Emmins R, Hamoen LW, Daniel RA, Errington J, Edwards DH. Control of the cell elongation–division cycle by shuttling of PBP1 protein in *Bacillus subtilis*. Mol Microbiol. 2008;68:1029–1046.
102. Steele VR, Bottomley AL, Garcia-Lara J, Kasturiarachchi J, Foster SJ. Multiple essential roles for EzrA in cell division of *Staphylococcus aureus*. Mol Microbiol. 2011;80:542–555.
103. Cleverley RM, Barrett JR, Baslé A, et al. Structure and function of a spectrin-like regulator of bacterial cytokinesis. Nat Commun. 2014;5:5421.
104. Cleverley R, Lewis RJ. EzrA: A spectrin-like scaffold in the bacterial cell division machinery. Microb Cell. 2015;2:59–61.
105. Krupka M, Sobrinos-Sanguino M, Jiménez M, Rivas G, Margolin W. *Escherichia coli* ZipA organizes FtsZ polymers into dynamic ring-like protofilament structures. MBio. 2018;9:e01008–e01018.
106. Hale CA, de Boer PA. Direct binding of FtsZ to ZipA, an essential component of the septal ring structure that mediates cell division in *E. coli*. Cell. 1997;88:175–185.
107. Geissler B, Elraheb D, Margolin W. A gain-of-function mutation in *ftsA* bypasses the requirement for the essential cell division gene *zipA* in *Escherichia coli*. Proc Natl Acad Sci U S A. 2003; 100:4197–4202.
108. Pazos M, Natale P, Vicente M. A specific role for the ZipA protein in cell division. J Biol Chem. 2013;288:3219–3226.
109. Chen Y, Huang H, Osawa M, Erickson HP. ZipA and FtsA* stabilize FtsZ-GDP miniring structures. Sci Rep. 2017;7:3650.

110. Waxman DJ, Strominger JL. Penicillin-binding proteins and the mechanism of action of beta-lactam antibiotics. Annu Rev Biochem. 1983;52:825–869.
111. Cho H, Uehara T, Bernhardt TG. Beta-lactam antibiotics induce a lethal malfunctioning of the bacterial cell wall synthesis machinery. Cell. 2014;159:1300–1311.
112. Peacock SJ, Paterson GK. Mechanisms of methicillin resistance in *Staphylococcus aureus*. Annu Rev Biochem. 2015;84:577–601.
113. Foster TJ. Antibiotic resistance in *Staphylococcus aureus*. Current status and future prospects. FEMS Microbiol Rev. 2017;41:430–449.
114. Otero LH, Rojas-Altuve A, Llarrull LI, et al. How allosteric control of *Staphylococcus aureus* penicillin binding protein 2a enables methicillin resistance and physiological function. Proc Natl Acad Sci U S A. 2013;110:16808–16813.
115. Mahasenan KV, Molina R, Bouley R, et al. Conformational dynamics in penicillin-binding protein 2a of methicillin-resistant *Staphylococcus aureus*, allosteric communication network and enablement of catalysis. J Am Chem Soc. 2017;139:2102–2110.
116. Fernandes R, Amador P, Prudêncio C. β-Lactams: Chemical structure, mode of action and mechanisms of resistance. Rev Med Microbiol. 2013;24:7–17.
117. Bonomo RA. β-Lactamases: A focus on current challenges. Cold Spring Harb Perspect Med. 2017;7:a025239.
118. Hall BG, Barlow M. Evolution of the serine β-lactamases: Past, present and future. Drug Resist Updat. 2004;7:111–123.
119. Yong D, Toleman MA, Giske CG, et al. Characterization of a new metallo-lactamase gene, ^{bla}NDM-1, and a novel erythromycin esterase gene carried on a unique genetic structure in *Klebsiella pneumoniae* sequence type 14 from India. Antimicrob Agents Chemother. 2009;53:5046–5054.
120. Zmarlicka MT, Nailor MD, Nicolau DP. Impact of the New Delhi metallo-beta-lactamase on beta-lactam antibiotics. Infect Drug Resist. 2015;8:297–309.
121. Ma B, Fang C, Lu L, et al. The antimicrobial peptide thanatin disrupts the bacterial outer membrane and inactivates the NDM-1 metallo-β-lactamase. Nat Commun. 2019;10:3517.
122. Abraham EP, Chain E. An enzyme from bacteria able to destroy penicillin. Nature. 1940;146:837–837.
123. Andreu JM, Schaffner-Barbero C, Huecas S, et al. The antibacterial cell division inhibitor PC190723 is an FtsZ polymer-stabilizing agent that induces filament assembly and condensation. J Biol Chem. 2010;285:14239–14246.
124. Elsen NL, Lu J, Parthasarathy G, et al. Mechanism of action of the cell-division inhibitor PC190723: Modulation of FtsZ assembly cooperativity. J Am Chem Soc. 2012;134:12342–12345.
125. Haydon DJ, Stokes NR, Ure R, et al. An inhibitor of FtsZ with potent and selective anti-*Staphylococcal* activity. Science. 2008;321:1673–1675.

How to cite this article: Booth S, Lewis RJ. Structural basis for the coordination of cell division with the synthesis of the bacterial cell envelope. *Protein Science*. 2019;1–13. https://doi.org/10.1002/pro.3722